# UNDERSTANDING AND DEVELOPMENT OF MANUFACTURABLE SCREEN-PRINTED CONTACTS ON HIGH SHEET-RESISTANCE EMITTERS FOR LOW-COST SILICON SOLAR CELLS

A Thesis
Presented to
The Academic Faculty

by

Mohamed M. Hilali

In Partial Fulfillment
of the Requirements for the Degree
Doctor of Philosophy in
Electrical and Computer Engineering

Georgia Institute of Technology
August 2005

**UNDERSTANDING AND DEVELOPMENT OF MANUFACTURABLE SCREEN-PRINTED CONTACTS ON HIGH SHEET-RESISTANCE EMITTERS FOR LOW-COST SILICON SOLAR CELLS**

Approved by:

Dr. Ajeet Rohatgi, Advisor
College of Engineering
*Georgia Institute of Technology*

Dr. Thomas K. Gaylord,
College of Engineering
*Georgia Institute of Technology*

Dr. Ian Ferguson,
College of Engineering
*Georgia Institute of Technology*

Dr. Miroslav M. Begovic
College of Engineering
*Georgia Institute of Technology*

Dr. Meilin Liu
College of Engineering
*Georgia Institute of Technology*

Date Approved: June 27, 2005

This work is dedicated to

*my mother, Ms. Hidaya Selim for her love and support*

*my father, Dr. Mosaad Hilali for his love and support*

*my grandmother, Ms. Nazek Hafez for her love*

*my sister, Ms. Hend Hilali for her love*

# ACKNOWLEDGMENTS

First, I thank Allah the most merciful and compassionate for allowing me to complete this Ph.D. dissertation. I would like to thank my thesis advisor, Dr. Ajeet Rohatgi. He has contributed the most to my research and helped me develop critical thinking. He has not only provided scientific resources to do world-class research, but he also spent many hours with me in writing technical papers and developing presentation skills. I am also grateful to Dr. Thomas Gaylord for serving as committee chair of my dissertation proposal and my dissertation defense. I would like to thank Dr. Ian Ferguson for serving on my dissertation proposal and dissertation defense committee, and I also thank him for his sincere advice and recommendations. I also thank Dr. Miroslav Begovic for his careful reading of this dissertation as well as helpful comments. I would like to thank Dr. Meilin Liu at the Materials Science and Engineering department for serving as the external committee member of my dissertation defense. I am very grateful to Dr. Aziz Shaikh, Dr. Steve Kim, Dr. Sidharsan Sridharan, and Dr. Chandra Khadilkar at Ferro Corporation for providing research support and encouragement. I am also deeply indebted to Dr. Mowafak M. Al-Jassim, Dr. Helio Moutinho, and Dr. Sally Asher at the National Renewable Energy Lab (NREL), for substantial research support, helpful suggestions and encouragement. I also thank Bobby To and Robert C. Reedy at NREL for their assistance.

I would like to acknowledge all of the members of the University Center of Excellence for Photovoltaics Research and Education at Georgia Institute of Technology. Many thanks are given to Alan Ristow, Dr. Abasifreke Ebong, Dr. Dongseop Kim, Dr.

Vijay Yelundur, Brian Rounsaville, Vichai Meemongkolkiat, Kenta Nakayashiki, and Ajay Upadhyaya. I also thank Dean Sutter and Ms. Denise Taylor for their assistance. I would also like to express my thanks to previous UCEP members and colleagues: Dr. Ji-Weon Jeong, Dr. Ben Damiani, and Dr. Aleksandar Pregelj. I would also like to thank Dr. Stuart Bowden and Dr. Christiana Honsberg. Last but not least, I give my deepest respect and appreciation to my parents for their support, patience, and encouragement during my Ph.D. studies. I will always be indebted to them.

This research was supported by Ferro Corporation and the U.S. Department of Energy.

# TABLE OF CONTENTS

# LIST OF TABLES

# LIST OF FIGURES

# LIST OF SYMBOLS AND ABBREVIATIONS

| | |
|---|---|
| **PV** | Photovoltaics |
| **mc-Si** | Multicrystalline-Si |
| **a-Si** | Amorphous Si |
| **SP** | Screen-printed |
| **BC** | Buried contact |
| **PL** | Photolithography |
| **FF** | Fill factor |
| **FFs** | Fill factors |
| $\mathbf{V_{oc}}$ | Open-circuit voltage |
| $\mathbf{J_{sc}}$ | Short-circuit current |
| $\mathbf{V_{mp}}$ | Maximum power point voltage |
| $\mathbf{J_{mp}}$ | Maximum power point current density |
| **MPP** | Maximum power point |
| $\mathbf{R_s}$ | Series resistance |
| $\mathbf{R_{sh}}$ | Shunt resistance |
| $\rho_c$ | Specific contact resistance |
| **n factor** | Composite ideality factor for a single-diode model |
| $\mathbf{n_1}$ | First-diode ideality factor |
| $\mathbf{n_2}$ | Second-diode ideality factor |
| $\mathbf{J_{o2}}$ | Junction leakage current density |
| $\mathbf{J_{o1}}$ | Saturation current density |

**$J_{oe}$** Emitter saturation current density

**$J_{ob}$** Base saturation current density.

**BSRV** Back-surface recombination velocity

**FSRV** Front-surface recombination velocity

**ARC** Antireflection coating

**PECVD** Plasma-enhanced chemical vapor deposition

**IQE** Internal quantum efficiency

**SR** Spectral response

**R** Reflectance

**FGA** Forming gas anneal

# SUMMARY

Photovoltaics (PV) offers a unique opportunity to solve energy and environmental problems simultaneously because solar energy is unlimited and free and it can be converted into electrical energy by solar cells without any undesirable impact on the environment. The current cost of PV modules is $3-4/W, which needs to decrease to about $1/W to produce electricity at a rate of 6¢/kWh and compete with fossil fuels. Hence, the focus of this thesis is to develop low-cost high-efficiency on crystalline Si cells through fundamental understanding and low-cost technology development. This is done by understanding the formation of screen-printed (SP) contacts and then successfully fabricating high-efficiency SP solar cells on high sheet-resistance shallow emitters with improved surface passivation.

In the first phase of this research, device modeling was used to quantify the performance enhancement possible from the high sheet-resistance emitter for various cell designs. It was found that for performance enhancement from the high sheet-resistance emitter, certain cell design criteria must be satisfied. For example, it was established that fill factors (FFs) greater than 0.78 can be achieved on the high sheet-resistance emitter if the junction leakage current $J_{o2} \leq 25$ nA/cm$^2$, series resistance $R_s \leq 0.8$ Ω-cm$^2$, and shunt resistance $R_{sh} \geq 2000$ Ω-cm$^2$. In addition, model calculations showed that in order to achieve any performance enhancement over the conventional 40-45 Ω/sq emitter, the front-surface recombination velocity (FSRV) of the high sheet-resistance emitter cell must be less than ~120,000 cm/s. In fact, the front-surface recombination velocity should

be $<10^4$ cm/s to realize the full benefit of high sheet-resistance emitter cells. Moreover, lower base resistivity as well as lower back-surface recombination velocity (BSRV) help the enhancement in absolute cell efficiency resulting from the high sheet-resistance emitter. Similarly, a higher bulk lifetime was also to help the enhancement in open-circuit voltage ($V_{oc}$) and efficiency as a result of the high sheet-resistance emitter. This is because above changes make the cell performance more dependent on the emitter rather than on the base saturation current. Model calculations showed that a 100 Ω/sq emitter with an FSRV of ~7,000 cm/s can give ~0.7% enhancement in cell efficiency over a 45 Ω/sq emitter for a BSRV of 1,000 cm/s, base resistivity ~1 Ω-cm, and a bulk lifetime of 30 μs. Lowering the base resistivity, increasing the bulk lifetime, and lowering the BSRV were all found to enhance cell performance as a result of the high sheet-resistance emitter. These guidelines were used in the design and fabrication of cells in this research.

The next phase of this research involved the development of SP contacts to high sheet-resistance emitters. Initially, a selective emitter technique, which makes use of a self-doping paste, was employed. However, this technique was found to limit cell performance as well as the possibility of using >75 Ω/sq emitters because of the excessive diffusion of Ag from the paste during the self-doping diffusion process. Later on, using a mild glass frit paste in conjunction with the contact firing optimization, SP contacts directly to 100 Ω/sq emitters were achieved for the first time in this research. High-quality SP Ag contacts were obtained directly on high sheet-resistance emitters (100 Ω/sq) by rapid firing of DuPont PV168 Ag paste. Excellent specific contact resistance (~1 mΩ-cm$^2$) in conjunction with high fill factor (0.775) were obtained on 100 Ω/sq emitters by a 900° C spike firing of DuPont PV168 paste in a belt furnace. The

combination of the contact characteristics of the DuPont PV168 Ag paste and optimized single-step rapid low-thermal budget firing resulted in a cost-effective manufacturable process for high-efficiency Si solar cells. In addition, the co-fired 100 Ω/sq cell showed a noticeable improvement of ~0.5% in absolute efficiency over a conventional co-fired 45 Ω/sq-emitter cell. Lighter doping in the 100 Ω/sq-emitter cell resulted in better blue response compared to the conventional cell, contributing to ~1.3 mA/cm$^2$ improvement in short-circuit current. Improved surface passivation on a 100 Ω/sq emitter cell resulted in an additional 0.6 mA/cm$^2$ increase in short-circuit current ($J_{sc}$), 15 mV higher $V_{oc}$, and 0.6% increase in absolute cell efficiency. Front grid design optimization resulted in a FF of 0.780 with cell efficiency of 17.4% on 0.6 Ω-cm untextured float-zone (FZ) Si with bulk lifetime of >200 μs.

Physical and electrical properties of SP Ag thick-film contacts were studied and correlated to understand and achieve good-quality ohmic contacts to high sheet-resistance emitters for solar cells. Analytical microscopy and surface analysis techniques were used to study the Ag-Si contact interface of three different SP Ag pastes (A, B, and PV168) subjected to high (~835° C) and conventional (740-750° C) temperature firing conditions. At ~750° C firing, all three pastes failed on a 100 Ω/sq emitter either because of incomplete etching of the silicon nitride film (PV168), an irregular small distribution of re-grown Ag crystallites (paste A), or an excessive diffusion of Ag into the p-n junction (paste B). At a firing temperature of ~835° C, paste A failed partially and gave a lower open-circuit voltage because of the diffusion of Al from the glass frit into the emitter region. Paste B failed because of the formation of very large (0.3-1 μm) Ag crystallites that shunted the p-n junction. Of the three pastes, the PV168 paste from DuPont gave the

best contact quality on a 100 Ω/sq emitter, with a solar cell fill factor of 0.782 only after annealing in a hydrogen atmosphere, which was found to enhance the conductivity of the glass.

Scanning electron microscopy (SEM) studies revealed that there is very little or no direct contact between the Ag grid and Si emitter because of the presence of the glass layer. In addition, Ag crystallites were found to be embedded in the Si emitter underneath the glass layer. For optimizing the contact directly to the high sheet-resistance emitter without any self-doping technique, it was found necessary to optimize paste, firing, and device parameters to achieve the best results: (1) the high-sheet-resistance emitter profile (e.g., surface concentration and depth) and size and distribution of Ag crystallites that gives sufficient contact area fraction to achieve low specific contact resistance ($\rho_c$<3 mΩ-cm$^2$) and avoids junction shunting; (2) the glass frit aggressiveness to completely etch the silicon nitride film without the formation of large Ag crystallites and without excessive etching of the Si emitter; (3) the glass frit chemistry to achieve ultra-thin glass regions; (4) the composition and properties of the inorganic constituents of the paste to avoid excessive diffusion of impurities; and (5) spike firing at high temperatures (>700°C). It was found that small- to medium-sized Ag particles in a paste with a medium-high glass transition temperature, fired rapidly, can produce a large number of small Ag crystallites that can give ≤1 mΩ-cm$^2$ contact resistance and 0.78 FF on 100 Ω/sq sheet resistance emitters.

To achieve superior ohmic contact to high sheet-resistance emitters, research was conducted to optimize the properties of the inorganic constituents of the paste (glass frit and metal powder) and understand their influence on ohmic contact and solar cell

performance. First, the impact of the Ag particle (metal powder) size used for making the SP Ag paste was investigated on the quality of Ag thick-film ohmic contacts. Spherical particle size was varied in the range of 0.1–10 μm (ultra-fine to large). Ultra-thin (≤ 50 Å) glass regions between the Ag grid and Si emitter were achieved for the large particle size paste, giving very low specific contact resistance ($\rho_c$). However, secondary ion-mass spectroscopy (SIMS) measurements showed an unacceptably higher Ag concentration (>$10^{15}$ $cm^{-3}$) at the p-n junction, which increased the junction leakage current ($J_{o2}$) and decreased the $V_{oc}$ by ~7 mV and the FF by ~0.02. The paste with ultra-fine Ag particles generally produced a thick glass layer at the Ag–Si contact interface, which led to high $\rho_c$, an increase in series resistance ($R_s$) (≥1 Ω-$cm^2$), and a FF loss of ~0.03. Small- to medium-sized Ag particles in the paste produced the desirable results with very thin glass regions in conjunction with a large number of regularly distributed Ag crystallites at the contact interface. This resulted in low $R_s$ (<1 Ω-$cm^2$), high shunt resistance (60,558 Ω-$cm^2$), low $J_{o2}$ (~20 nA/$cm^2$), and high FF (0.781). Cell efficiencies of ~17.4% were achieved on untextured FZ Si with a 100 Ω/sq emitter by rapid co-firing of SP contacts in a lamp-heated belt furnace. A physical model based on competition between the sintering and dissolution of Ag by the glass frit is presented to explain how and why particle size can alter the structure of the contact interface.

After understanding the role of the Ag particle size in the SP paste, a study was conducted to understand the role of the glass frit chemistry on the physical and electrical properties of the ohmic contact behavior. The softening characteristics of the glass frit determine the firing scheme suitable for low contact resistance and high fill factors (FFs). It was found that the glass frit with a high glass-transition temperature ($T_g$) (less fluid)

results in a lower contact resistance to the Si emitter at conventional firing conditions (750° C/120 ipm) because of the formation of ultra-thin glass regions that help current transport via tunneling. Based on the above results, a fast crystallizing high $T_g$ glass was demonstrated to be better for enhancing the $V_{oc}$ and cell efficiency because of reduced shunting and junction leakage while achieving ultra-thin glass regions. This resulted in untextured FZ cell efficiencies as high as 17.4% with FFs greater than 0.78 on 95-100 Ω/sq emitters.

The above understanding of paste chemistry and firing scheme produced ~0.4% increase in absolute efficiency with cell efficiency >17.4% on FZ Si. Good contact quality was achieved on high sheet-resistance emitters even for low-cost multicrystalline and ribbon Si materials. This was achieved in conjunction with bulk lifetime enhancement. Lifetimes greater than 100 μs were achieved along with the FFs in excess of 0.76. The firing process was tuned for mc-Si, which involved a faster firing speed (120 ipm), but the peak temperature (~840° C) was similar to that for FZ Si cells. This prevented shunting and resulted in high lifetime, supporting enhanced passivation of defects resulting from the increased retention of hydrogen during this rapid firing process. Screen-printed cell efficiencies of 16.1% and ~16.2% on EFG ribbon substrates were achieved on high sheet-resistance emitters using PV168 Ag paste from DuPont and 33-456 Ag paste from Ferro Corporation, respectively.

After achieving high-efficiency cells on planar Si substrates, attempts were made to fabricate SP high-efficiency cells on textured substrates using 100 Ω/sq emitters and a rapid single-step firing process for further efficiency enhancement. High contact quality was achieved with low series resistance of 0.79 Ω-cm$^2$, high shunt resistance of 48,836

Ω-cm$^2$, and low junction leakage current of 2 nA/cm$^2$, yielding a high FF of 0.784 on a textured 100 Ω/sq emitter. These results were supported by the high-quality contact interface, which showed a large number of small Ag crystallites at the interface. In fact, pyramid texturing on the FZ Si surface enhanced the formation of a more regular distribution of Ag crystallites. Based on model calculations, a low resistivity FZ Si (0.6 Ω-cm), was used for the base to enhance the contribution of the high sheet-resistance emitter to $V_{oc}$. This resulted in a record-high screen-printed cell efficiency of 19.0% (confirmed by NREL) on textured 0.6 Ω-cm FZ Si with a single-layer antireflection coating. Extensive device modeling and characterization were performed on this 19% screen-printed Si cell to understand the reason for the high efficiency and to develop a roadmap for even higher efficiency. Device modeling revealed that without the effect of the metal grid on the front, the open-circuit voltage could have been ~668 mV. However, this decreased to ~650 mV because of the contact recombination associated with the metal grid.

Model calculations were extended to provide guidelines for achieving greater than 20% SP Si cells on high sheet-resistance emitter. Device modeling showed that by achieving a low back-surface recombination velocity (BSRV) of ~50 cm/s, in conjunction with a back-surface reflector of 95%, and an FSRV of 20,000 cm/s, efficiencies approaching 21% can be achieved on a textured FZ substrate.

# CHAPTER 1

# INTRODUCTION

## 1.1 Statement of Problem

Demand for energy is expected to grow rapidly in the 21st century. Access to sufficient affordable energy is critical for maintaining our standard of living. Currently, most of the world's energy (~80%) is provided by fossil fuels (Fig. 1.1) [1]. Nuclear energy, which provides ~7% of the world's energy, has many problems, including safety and cost. The world population is expected to double by the end of the 21st century in conjunction with the rapid depletion of fossil fuels. Consequently, providing sufficient commercial energy, let alone clean energy, is an immense task that demands urgent attention. Solar energy can play a significant role in securing an adequate global energy supply for the 21st century, especially as the limitation on carbon emissions becomes more stringent. Currently, photovoltaics (PV) accounts for less than 0.05% of the energy production, with more than 98% of solar cell production based on Si semiconductors in the form of single-crystal, multicrystalline or amorphous Si [2]. Crystalline silicon has been the workhorse of the PV industry since 1954 and is the second most abundant element in the earth's crust. Scalability, reliability, and performance are the reasons for the success of Si solar cells. Even though the cost of Si cells was reduced by more than a factor of 10 in the last two decades, it needs to decrease by another factor of two to four to compete with traditional energy sources for utility scale applications. Most cell manufacturers use screen-printed contacts, instead of photolithography contacts, in an

effort to keep the cost low. However, screen-printed contacts contribute to significant loss in cell performance and contribute to considerable scatter in commercial cell efficiencies. Therefore, the goal of this research is to improve the fundamental understanding of the formation of screen-printed contacts, understand the loss mechanisms associated with it, improve screen-printed technology, and demonstrate that very high-efficiency screen-printed cells can be achieved by optimizing the paste chemistry and firing conditions.

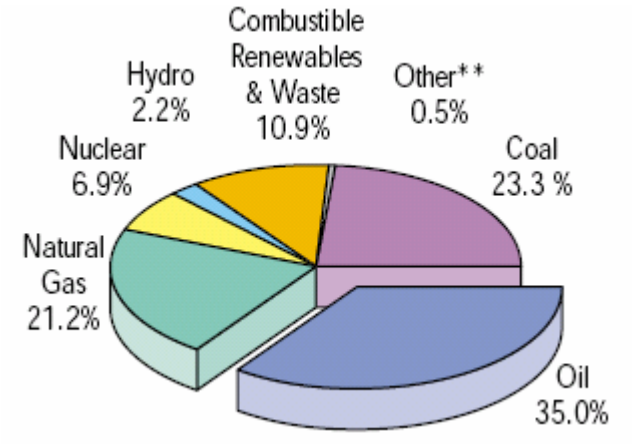


**Other includes solar, wind, heat, tidal

Figure 1.1. World energy consumption by energy source (2003) [1].

## 1.2 Opportunities and Challenge in Photovoltaics

Japan, Europe, and the United States lead the world in PV module shipments, with annual shipments of 602 MW, 314.4 MW, and 138.7 MW, respectively in 2004. PV is now a greater than $5 billion industry, with worldwide shipments [3] reaching 1.195 GW in 2004 (Fig. 1.2) [4]. The U.S. photovoltaic industry roadmap, published by the U.S. PV Industry, May 2001, projects a growth of 25%/yr for PV, resulting in annual worldwide production of 21 GW by 2020. As a result of different incentive programs, particularly in Europe and Japan, over the past six years the PV markets have grown by

about 35% per year, with about 60% growth in 2004 (Fig. 1.2) [4,5]. The demand for electrical energy is expected to grow rapidly because there are still two billion people in the world with little or no access to electricity and the world population may double by the end of this century. The potential for PV is huge in developing countries, where just the availability of electricity can play a major role in the economic development and standard of living. Many countries have vast areas where a significant fraction of the population lives in rural areas with no access to electricity because of the absence of an electric grid [6]. In those areas, PV already offers a cheaper energy option compared to running power lines over a long distance.

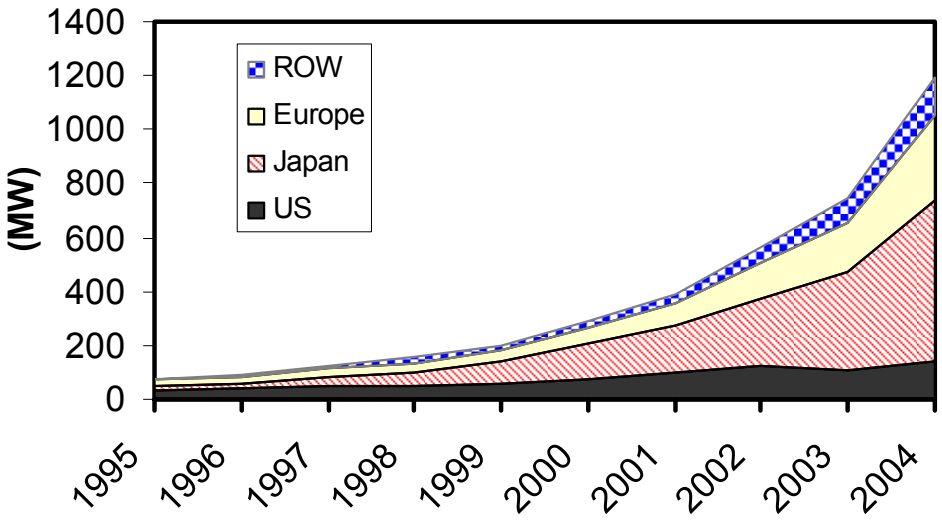


Figure 1.2. World PV module production (MW) [5].

Renewable energy sources collectively provide ~14% of the world's primary energy (Fig. 1.1), with the majority of the supply coming from biomass (~10%) and large (>10 MW) hydropower stations (~2%). Most of the major hydropower sites have already been exploited, and large-scale biomass energy production can have harmful ecological effects. Among the various renewable energy options available today, solar energy is

particularly attractive because it is free, unlimited, and not localized in any part of the world. The available capacity from solar energy is enormous. For example, large-scale PV systems located in major deserts of the world can generate 200 times the world's current total energy consumption of 118 trillion kWh [7], and the amount of solar energy incident in less than an hour on the United States exceeds its annual electrical energy consumption of 2.88 trillion kWh [8]. Solar energy does not compete with other renewable energy sources. For example, regions that are suitable for PV systems are generally not suitable for wind systems. Unlike some other renewable energy sources, PV offers a high technology approach to providing energy. PV technology has already been well established as a reliable, clean, and economical source of electricity in small, off-grid applications, far from urban areas. However, currently the application driving the PV market involves urban residential rooftop systems, which is expected to remain the most important commercial application for PV during the current decade [9]. Smart integration of PV into buildings, where PV modules replace the building materials, reduces the effective module costs and is expected to drive and reach widespread commercialization. It is already influencing building architecture and engineering in Europe and Japan [10]. Therefore, PV can create thousands of direct and indirect jobs during the coming decades.

There are several key advantages of PV: Solar energy is unlimited because the sun will be around for several billion years; PV systems are simple to install and maintain, they are modular and can be expanded depending on energy needs; they can be used with other energy sources; and most of all, PV systems do not produce heat or waste and are nonpolluting and safe [11]. There are no fundamental or scientific barriers

implementing the photovoltaic effect. When the PV production rate exceeds the consumption rate, it can be fed back into the grid or stored in the form of hydrogen produced by electrolysis from PV-generated electricity [12]. Since PV output varies continuously because of the change in the sun's position and ambient conditions, the effective use of energy from PV requires careful thinking and planning.

PV destined to make a significant contribution to the world energy supply because of the above reasons and the finite supply of fossil fuels as well as the increased awareness of their impact on the environment. However, for PV to become a major energy source, the cost of PV must become competitive with the cost of current primary energy sources. Since the early 1970s when PV was seriously considered as a terrestrial power source, the emphasis was on research to improve performance, lower costs, and increase reliability [13]. This is still the case today, as reflected in the United States as well as the European PV roadmaps which have set a cost goal of $1/Watt for PV modules from bulk crystalline Si solar cells. Figure 1.3 shows the ~80% learning curve for PV, i.e., the doubling of cumulative PV production leads to ~20% reduction in cost [14]. In the last couple of years, module sale prices ranged from $2.75/Wp-$3.5/Wp [3], with direct manufacturing cost approaching $2/Wp. Table 1.1 shows how the combination of cell efficiency and direct manufacturing cost ($/m$^2$) influences the final PV module cost in $/Watt [15]. It is obvious that higher cell efficiencies reduce module cost because it shrinks the size of a PV module for the same power output. Therefore, reducing the cost of electricity produced by PV is actually an optimization problem in which the direct manufacturing cost should be reduced, while the solar cell efficiency should be improved simultaneously. The research objectives in this thesis, described in the next section, are

entirely consistent with the goal of reducing manufacturing cost and achieving high-efficiency solar cells.

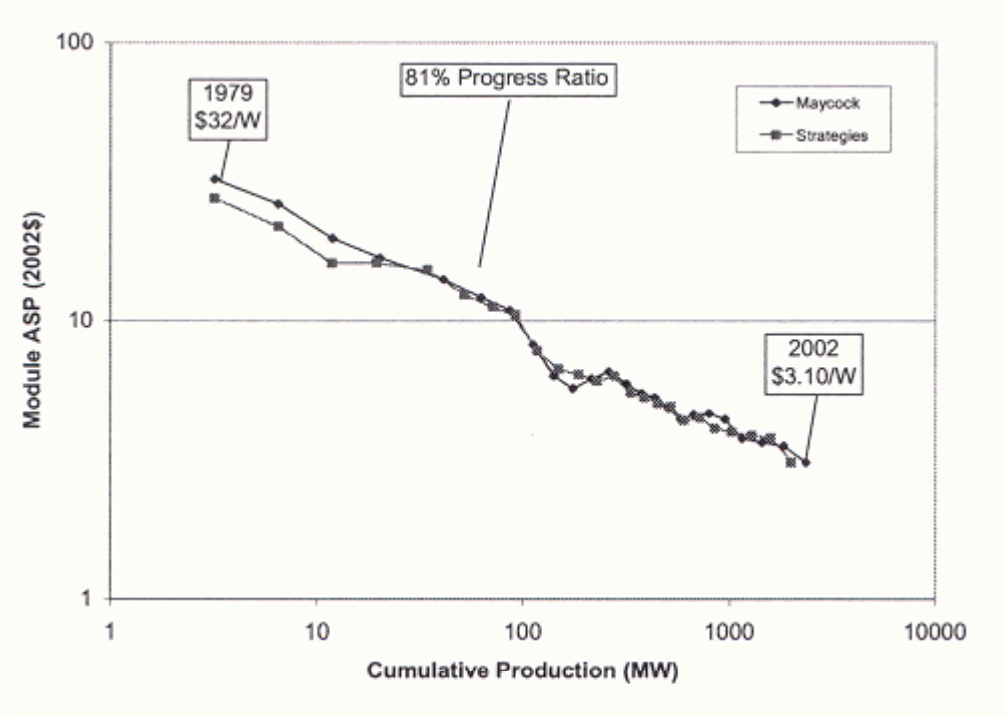


Figure 1.3. Historical plot of the module average selling price (ASP) showing classic learning or experience curve behavior [14].

Table 1.1: Impact of efficiency and direct manufacturing cost ($/m$^2$) on the final cost of the PV module ($/Wp) [15].

| **Cost** / **Eff.** | **$350/m$^2$** | **$ 300/m$^2$** | **$ 250/m$^2$** | **$ 200/m$^2$** | **$ 150/m$^2$** |
|---|---|---|---|---|---|
| **10%** | $ 3.5 | $ 3.0 | $ 2.5 | $ 2.00 | $ 1.50 |
| **12%** | $ 3.0 | $ 2.5 | $ 2.08 | $ 1.67 | $ 1.25 |
| **15%** | $ 2.33 | $ 2.0 | $ 1.67 | $ 1.33 | **$ 1.0** |
| **18%** | $2.05 | $1.67 | $ 1.39 | $ 1.11 | $ 0.83 |

## 1.3 Specific Research Objectives

The overall goal of this thesis is to reduce the cost of PV through the fundamental understanding and development of low-cost rapid technologies suitable for high-efficiency solar cells on single-crystal as well as multicrystalline silicon. Figure 1.4 shows that the cost of a silicon PV module can be divided into three parts: Si substrate (~40-45%), cell processing (~15%), and assembly of cells into the module (~40%) [16].

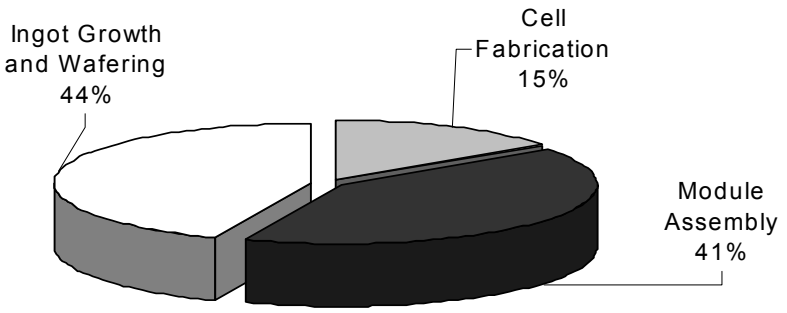


Figure 1.4. Cost breakdown of commercial PV modules [16].

Developing low-cost techniques without sacrificing cell efficiency reduces cell processing cost, and achieving higher efficiency cells reduces the use of Si and module assembly cost because fewer cells are required for a given power output. Contact formation has a very significant impact on the cost because it influences cell performance and throughput. Most cell manufacturers (more than 85%) use screen-printed (SP) contacts instead of photolithography contacts because screen printing is inexpensive, simple, and rapid. However, as shown in Figure 1.5, it can reduce the absolute cell

efficiency by ~1.7% because of a number of loss mechanisms associated with the heavily doped emitters (30-45 Ω/sq) currently used for screen-printed contacts. Heavily doped emitters are used in industry because SP metals do not produce acceptable ohmic contacts to high sheet-resistance emitters (80-100 Ω/sq). In addition, these shallow emitters can easily be shunted during contact firing. Therefore, a significant portion of this research focuses on the development of high-performance screen-printed contact metallization to the lightly doped emitter (~100 Ω/sq) for Si solar cells. The predominant technique in the photovoltaic industry involves the formation of ohmic contact to the 45 Ω/sq n-type Si emitter of on a Si substrate by screen printing Ag-based thick-film pastes followed by a firing process [17]. Even though the technique is simple, there is a considerable lack of understanding about the current transport, operation, and physics of screen-printed contacts. In this thesis, an attempt is made to investigate and understand the formation and operation of screen-printed contacts and apply that information to achieve high-efficiency screen-printed solar cells. Model calculations in Fig. 1.5 show that if 40-45 Ω/sq emitters are used with screen-printed contacts, a loss of ~0.5-1% in absolute efficiency can occur because of heavy doping effects, recombination in the emitter, and poor surface passivation of heavily doped emitters. The fill factor (FF) of a solar cell, which is also a measure of the "squareness" of the I-V curve, is frequently used as a figure of merit for the contact quality; the higher the FF, the better the quality of the contact. In fact, it is still a challenge to produce high-quality screen-printed contacts on heavily doped emitters (≤45 Ω/sq), which often give fairly low fill factors (FFs) of ≤0.75 in production as opposed to ≥0.8 for photolithography contacts. This contributes to another 0.5-1% loss in efficiency. Thus, the combination of heavy doping effects and

poor contacts result in 1-2 % loss in absolute efficiency of screen-printed cells (Fig. 1.5). Hence, this research addresses the challenge of achieving high-quality screen-printed contacts to lightly doped emitters (100 Ω/sq) with the fill factor target of ≥0.78. To accomplish this goal, untextured single-crystal silicon will be used first for cell fabrication to improve fundamental understanding and technology development. Emphasis will be placed on optimization as well as understanding the physical and electrical properties of screen-printed contacts. The optimized process and design will then be applied to low-cost multicrystalline Si materials as well as textured single-crystal Si in an attempt to achieve record high-efficiency cells. It is important to note that a 1.5% increase in absolute cell efficiency for 15%-efficient baseline cells corresponds to a 10% increase in production capacity, which translates into a $30 million dollar increase in revenue per year for a 100 MW production line and module sale price of $3/Watt.

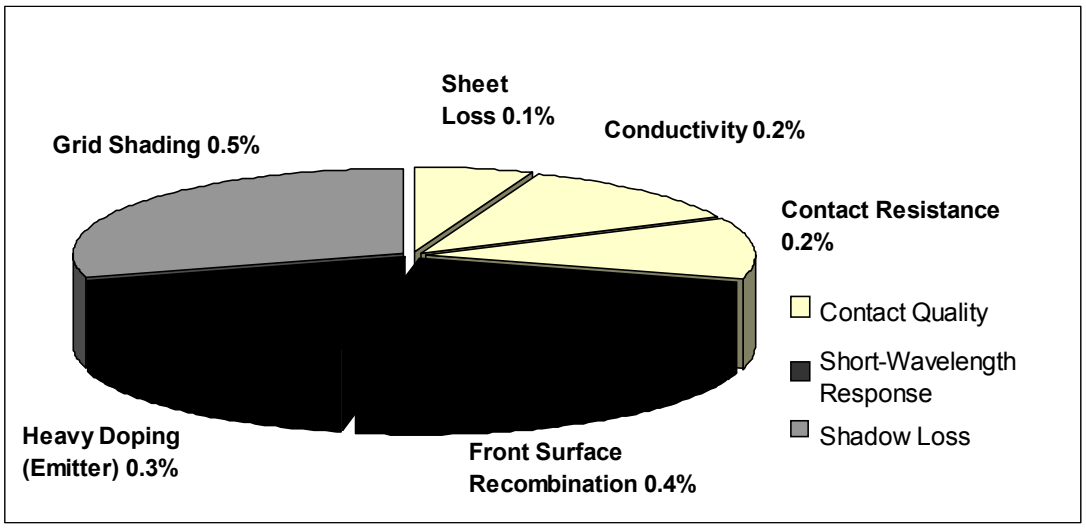


Figure 1.5. Loss mechanisms in 45 Ω/sq screen-printed cells compared to 90-100 Ω/sq photolithography cells.

The overall goal of this research is to develop high-quality screen-printed contacts to high sheet-resistance emitters for Si solar cells. The specific objectives are

divided into six tasks as follows: (1) model the impact of lightly doped emitters in screen-printed cells and establish the requirements for achieving maximum efficiency enhancement relative to conventional or heavily doped emitters; (2) understand and compare the electrical performance of Ag contacts using different pastes and develop a high-throughput firing process to achieve good-quality contacts to high sheet-resistance silicon emitters; (3) improve the fundamental understanding of contact formation and current transport using different characterization tools; (4) investigate the role of glass frit chemistry and metal powder to optimize paste composition and establish the criteria for good contact quality and cell performance; (5) fabricate high sheet-resistance cells on textured single-crystal Si to achieve high-efficiency cells; and (6) fabricate low-cost high-efficiency screen-printed multicrystalline and ribbon Si cells with high sheet-resistance emitters.

***Task 1: Modeling the Benefit of High Sheet-Resistance Emitter Cells***

Device modeling is performed in this task to understand and quantify the improvement in solar cell performance from the use of lightly doped emitters. Modeling is also used to establish cell design criteria for maximizing the benefit from high sheet-resistance emitters for screen-printed cells. Silicon solar cells with high sheet-resistance emitters (110 Ω/sq) are also compared to low sheet-resistance emitter cells (45 Ω/sq). The PC1D modeling program is used to quantify the performance enhancement resulting from the high sheet-resistance emitter for various cell designs. The impact of front-surface recombination velocity (FSRV), back-surface field (BSF), bulk lifetime, and base resistivity on the efficiency enhancement resulting from high sheet-resistance emitters is studied for screen-printed cells. Finally, modeling is performed to establish the

requirements for shunt resistance, junction leakage current, and series resistance to achieve fill factors approaching 0.79 on high sheet-resistance emitter cells.

***Task 2: Development of High Sheet-Resistance Screen-Printed Silicon Solar Cells with High Fill Factors***

In this task an attempt is made to develop a rapid, optimized firing process for selected pastes to achieve high-quality contacts (yielding high fill factors) on high sheet-resistance emitters. Firing time, temperature, and belt speed are optimized to achieve high fill factors.

***Task 3: Understanding the Formation of Screen-Printed Ag Contacts to High Sheet-Resistance Si Emitters***

In this task, characterization tools like SEM, AFM, and SIMS are used to obtain a better understanding of the contact interface and physical characteristics of different thick-film Ag contacts. The effect of firing temperature is studied to understand contact formation and tailor the contact interface. The contact interface structure is correlated with the electrical performance of the contacts and solar cells for different pastes to obtain guidelines for achieving good screen-printed contacts.

***Task 4: Investigation of the Effect of the Inorganic Constituents in the Screen-Printed Paste on Screen-Printed Contact Quality and Interface***

The thick-film Ag paste consists of a glass frit (lead oxide containing silicates), metal powder, organic binder, and a solvent. In this task the role of the inorganic constituents, i.e., glass frit and metal powder, is studied. The effect of different glass frit chemistries on contact quality is studied, along with the effect of the metal content, Ag particle size, shape, and morphology. These pastes will be prepared by one or more paste

manufacturers upon our request. The objective of this task is to guide the development of the paste and to find an optimum paste (or pastes) that can yield very high contact quality and fill factor on high sheet-resistance emitters.

### *Task 5: Fabrication of Textured Cells on High Sheet-Resistance Emitter Single-Crystal Silicon*

Surface texturing is known to reduce reflectance and promote light trapping; therefore, it can produce higher cell efficiency. However, screen-printed cells on shallow high sheet-resistance emitters may be vulnerable to junction shunting. Therefore, the objective of this task is to explore paste and firing schemes that can produce record high-efficiency textured FZ cells on ~100 Ω/sq emitters. A comparison will be made with the textured low sheet-resistance emitter (45 Ω/sq) cells that have a deeper junction. Cells will be analyzed to assess the impact of texturing on the front-surface recombination velocity (FSRV) and the effect of change in FSRV on the efficiency enhancement resulting from high sheet-resistance emitter.

### *Task 6: Fabrication of High-Efficiency High Sheet-Resistance Cells on Multicrystalline Si and Ribbon Si Substrates*

To fully realize the benefit of the process developed for high sheet-resistance emitters, screen-printed cells will be fabricated on widely used low-cost substrates in this task to take advantage of the lightly doped emitter and improved front-surface passivation. Low-cost multicrystalline materials rely on the silicon nitride antireflection coating (ARC) induced defect hydrogenation during contact firing. Better defect passivation leads to higher bulk lifetime. In this task, an attempt is made to tailor the firing conditions so that the hydrogen passivation of defects is not compromised during

contact firing. The objective of this task is to achieve record high-efficiency cells on selected low-cost materials to demonstrate that the high sheet-resistance emitter is also beneficial for defective materials.

# CHAPTER 2

# CHARACTERIZATION TOOLS

## 2.1 Characterization Tools for Understanding the Physical Structure of the Solar Cell Contact Interface

### 2.1.1 Atomic Force Microscopy

The atomic force microscope measures topography with a force probe. There are no lenses used for the scanning-probe system; thus, the probe size rather than diffraction effects limit the resolution. Microscope raster scans of the probe over the whole sample for measuring the surface property of a sample result in an image that resembles one on a television screen. The atomic force microscope (AFM) resembles the stylus profilometer. Nevertheless, it incorporates certain improvements that enable it to achieve atomic-scale resolution. These refinements include sensitive detection, flexible cantilevers, sharp tips, force feedback, and high resolution tip-sample positioning. The AFM technique works by measuring attractive or repulsive forces between the probe tip and the sample. This technique is well documented in the literature [18]. A conductive atomic force microscopy (CAFM) technique is also employed in this thesis to measure the cross-sectional conductivity of the screen-printed contacts across the Ag gridline-Si contact interface. This is done by contacting the back of the cell while a conductive probe passes along the contact cross-section.

In this research AFM measurements were used to scan the features of the contact interface underneath the screen-printed Ag gridline after firing. Thus, the gridline has to

be etched off before the measurement. The following sequence is used to etch the gridline, including the glass frit and Ag metal:

1- 70%-$HNO_3$ at 80° C for 10 minutes.

2- DI water rinse for 2 minutes.

3- 2.5%-HF at room temperature for 4 minutes.

4- DI water rinse for 2 minutes.

5- 70%-$HNO_3$ at 80° C for 10 minutes.

6- DI water rinse for 2 minutes.

Step 1 in the above sequence is responsible for etching the bulk of the Ag metal gridline, step 3 is responsible for etching the glass layer between the Ag bulk and the Si emitter, and step 5 is used to remove the Ag crystallites at the Si emitter surface. The above sequence is not the only way to remove the gridline and Ag crystallites. Alternatively, the sample can be dipped in 5% HF for 5-10 minutes (until the gridline is removed) at room temperature to remove the gridline by etching away the glass layer. The sample is then rinsed in DI water for 2 minutes, followed by a 70% $HNO_3$ for 10 minutes at room temperature. The sample is finally rinsed in DI water for 2 minutes. However, this technique is not preferred because of the use of high HF concentration and prolonged etching time.

### 2.1.2 Secondary Ion-Mass Spectroscopy

Secondary ion-mass spectroscopy (SIMS) makes use of sputtered material elements to determine the surface chemistry of a sample. A resolution of a monolayer and a sensitivity of one ppm are easily achievable using SIMS. The SIMS makes use of a

mass spectrometer to determine the material chemistry. The SIMS technique has been extensively documented in the literature [19-21].

SIMS is particularly well suited for depth profiling, as the sputtered particles reflect the true chemical composition of the solid. The sputtered particles largely originate from the top one or two atomic layers of a surface; hence, SIMS is a surface-specific technique. The secondary ions are extracted into a mass spectrometer, which uses electrostatic and magnetic fields to separate the ions according to their mass-to-charge ratio. The 'dynamic SIMS' technique, used in this thesis for depth profiling of elements in Si, makes use of a high incidence flux for bulk analysis involving high rates of material removal while providing extreme compositional sensitivity as well. The most obvious advantage of SIMS is the low detection limit. The CAMECA IMS-5f dynamic SIMS is used in this research for surface analysis has a detection limit of $\sim 10^{13}$ atoms/$cm^3$. An outstanding feature of SIMS is its ability to constantly monitor and obtain a depth profile of the surface composition with a resolution <10nm.

In this research SIMS is used for detecting elements in the Si emitter region. These elements include the emitter dopant (P), Ag diffusion from the paste during firing of the grid, and other elements such as Al, Bi, Zn etc. that may be present in the paste. For P detection, the silicon nitride coating was first completely etched in a 10:1 $H_2O_2$:HF solution. For P detection underneath the gridline only the metal is removed using HCl:$HNO_3$ 1:3 for ~10 minutes. This prevents P from being etched from the Si surface. This etching solution can also be used for detecting Ag in the emitter region, including precipitated Ag crystallites at the interface. For detecting impurities in the emitter region

without the effect of any metal precipitation on the surface, the etching steps used for the AFM analysis described in the previous subsection can also be used.

***Primary Ions used in SIMS Analysis***

*i- Use of Oxygen Ions for Boron and Transition Metals Analysis*

A beam of $O_2^+$, purified by a mass filter, was used as the source of the primary ions. The impact energy of the primary ion beam was 8.0 keV at an incident angle of 39° from the surface normal. The primary current was approximately 500 nA. The primary beam was focused into a spot approximately 40 μm in diameter that was raster-scanned over a 150 μm x 150 μm square area. Positive secondary ions generated from the sample were accelerated normal to its surface and were detected at 4.5 keV. Secondary ions were collected from a 60-μm diameter area in the center of the raster-scanned area to minimize effects from the crater walls. In the sample chamber, the working pressure was approximately $3x10^{-10}$ torr. An electron multiplier and Faraday cup detectors were used for counting the secondary ions. Oxygen ions were used for Ag analysis in selected samples, however, in most cases cesium ions were used for Ag analysis.

*ii- Use of Cesium Ions for the Analysis of Light Elements (H, C, N, O), Phosphorous, and Silver*

A beam of $Cs^+$, purified by a mass filter, was used as the source of the primary ions. The impact energy of the primary ion beam was 14.5 keV at an incident angle of 25° from the surface normal. The primary current was approximately 100 nA. The primary beam was focused into a spot approximately 40 μm in diameter that was raster-scanned over a 150 μm x 150 μm square area. Negative secondary ions generated from the sample were accelerated normal to its surface and were detected at 4.5 keV.

Secondary ions were collected from a 60-μm diameter area in the center of the raster-scanned area to minimize effects from the crater walls. In the sample chamber, a cryoshield at liquid nitrogen temperature was used, and the working pressure was approximately $3x10^{-10}$ torr. Secondary ions were counted by an electron multiplier and Faraday cup detectors.

### 2.1.3 Scanning Electron Microscopy

The scanning electron microscope is often the preferred starting tool for analytical microscopy because of its versatility and the wide range of information it can provide [22]. In scanning electron microscopy (SEM), a focused beam of high-energy electrons is scanned over the surface of a material. The electron beam interacts with the material, causing a variety of signals—secondary electrons, back-scattered electrons, X-rays, and photons-- each of which may be used to characterize a material with respect to specific properties. State-of-the-art SEMs provide remarkable analytical versatility and a wide magnification range from 20x to 650,000x. High-resolution JEOL-FE-SEM 6320 was used for this work.

The SEM technique is very well documented in reference [22]. The electron gun generates electrons and accelerates them in an energy range of 0.1-30 keV. For the SEM used in this work, the electron beam spot size was 20 nm while the accelerating voltage was 2 KeV.

Backscattered electrons (BSE) are electrons that escaped the sample and are useful for compositional contrast in the specimen. Secondary electrons are collected from all surfaces that the beam strikes. This results in a high collection efficiency of secondary

electrons from most surfaces, even partial collection from surfaces tilted away from the detector. Thus, secondary electrons are a tool for a topographical analysis of the specimen surface. Secondary electrons were used for most of the SEM images in this thesis.

In this thesis work SEM measurements were used to obtain cross-section images as well as top-view images of the features of the contact interface underneath the screen-printed Ag gridline after firing. To obtain a cross-section image of the contact interface, the sample was first prepared by making a notch with a diamond-tipped scribe at the edge of the wafer. Using a tweezer the fracture was propagated along the wafer and across the gridlines. SEM was then performed at the gridline/Si interface. For the top–view, images of the gridline were etched off before the measurement. The following sequence was used to etch the gridline, including the glass frit:

1- 70%-$HNO_3$ at 80° C for 10 minutes.

2- DI water rinse for 2 minutes.

3- 2.5%-HF at room temperature for 4 minutes.

4- DI water rinse for 2 minutes.

Step 1 in the above sequence is responsible for etching the bulk of the Ag metal gridline and step 3 is responsible for etching the glass layer between the Ag bulk and the Si emitter. The Ag precipitation on the Si emitter surface is not affected by the process and it can be viewed by the SEM.

### 2.1.4 Transmission Electron Microscopy

Diffraction and imaging high-energy electrons are important experimental techniques for determining structural details at atomic resolution. The transmission electron microscopy (TEM) technique was originally based on the principle that magnetic lenses [23] can focus charged particles. Because of its atomic resolution, TEM is currently one of the key characterization tools in characterizing condensed matter.

In TEM an electron beam from an electron gun illuminates the sample, usually through an illuminating system of lenses. This radiation interacts with the sample and is scattered. The scattered radiation is brought to focus by an objective lens. Further magnification is needed to obtain an image of a convenient size [24].

Electrons have a much stronger interaction with a solid (interacting with electrons and nuclei in a crystal) compared to X-rays or neutrons. Thus, multiple scattering effects are always present in electron diffraction. An electron beam can only pass through a very thin film, even though it is usually accelerated by potentials greater than 100 kV [25]. Hence, during the TEM process, a thin (<200 nm) sample is bombarded by a highly focused beam of single-energy electrons. The beam has enough energy for the electrons to be transmitted through the sample. The transmitted electron signal is greatly magnified by a series of electromagnetic lenses. Direct electron images yield information about the microstructure of the material and about its defects. The TEM used in this work is the Philips CM-30. TEM analysis in this thesis involves direct electron images only. Energy dispersive spectrometry (EDS) performs qualitative or quantitative compositional analysis for elements.

Before the TEM analysis, the sample is first prepared as follows:

1- Standard mechanical polishing down to about 50 μm followed by dimple polishing down to a thickness around 5μm.

2- Ion-beam milling: The samples were then ion beam milled to a thickness of ~100-500 nm using a Gatan precision ion polishing system (PIPS) at low energy and low angle. Samples were milled using argon ions at room temperature.

### 2.1.5 Energy Dispersive Spectrometry

The chemical analysis of the transmission electron microscope as well as the scanning electron microscope is normally obtained by measuring the energy and intensity distribution of the generated X-ray signal using a focused electron beam. The X-rays pass into a cooled reverse biased p-i-n Si Li-doped crystal, which is the detector. The liquid nitrogen is used to keep the Si Li-doped detector at liquid nitrogen temperature, as Li is mobile at room temperature. The operation of the energy dispersive spectrometer (EDS) involves the absorption of an X-ray photon, which leads to the ejection of a photoelectron [22]. Thus, electron hole pairs are generated. Holes and electrons are separated by the electric field because of the applied reverse bias voltage and are collected at the p and n electrodes, respectively. This results in a charge pulse that is converted into a voltage by a charge-to-voltage converter circuit (also called a pre-amplifier) that makes use of a capacitor for charging and discharging as well as a field-effect transistor (FET) to convert the charge into voltage.

## 2.2 Characterization Tools for Understanding the Electrical Properties of the Contacts and Solar Cells

A solar cell is an optoelectronic device that works as a result of the interaction of sunlight with the device material or semiconductor. When sunlight is incident on the surface of a semiconductor with a *p*-*n* junction, a built-in field at the junction separates the electron-hole pairs generated by the absorbed photons in the bulk. A voltage is generated across the junction as electrons go to the *n*-region and holes to the *p*-region, resulting in charge separation. The process of generating a voltage from incident photons is called the photovoltaic effect. When an external load is connected across the photovoltaic device under illumination, a current flows through the load. Figure 2.1 illustrates the I-V characteristics in the dark and under illumination.

There are three important output parameters of the *p*-*n* junction solar cell: the short-circuit current ($J_{sc}$), the open-circuit voltage ($V_{oc}$), and the fill factor (FF), as shown in Figure 2.1. These three parameters determine the conversion efficiency ($\eta$) of the solar cell, which is given by

$$\eta = \frac{J_{sc} \cdot V_{oc} \cdot FF}{P_{in}}, \tag{2.1}$$

where $P_{in}$ represents the incident power on the cell. The FF is a measure of the 'squareness' of the solar cell's I-V curve and is given by

$$FF = \frac{V_{mp} I_{mp}}{V_{oc} I_{sc}} \tag{2.2}$$

where $V_{mp}$ and $I_{mp}$ are the voltage and current at the maximum power point. $V_{oc}$ can be expressed as

$$V_{oc} = \frac{kT}{q} \cdot \ln\left(\frac{J_{sc}}{J_{o1}} + 1\right) \tag{2.3}$$

where $J_{o1}$ is the saturation current density for a single-diode model that results from the recombination of minority carriers within the emitter and base regions.

where

$$J_{o1} = J_{oe} + J_{ob} = qn_i^2\left[\frac{D_p}{N_D L_p}F_p + \frac{D_n}{N_A L_n}F_n\right] \tag{2.4}$$

and

$$F = \frac{SL/D + \tanh\frac{W}{L}}{1 + \frac{SL}{D}\tanh\frac{W}{L}} \tag{2.5}$$

$D$ is the diffusivity of the minority carriers in Si, $n_i$ is the intrinsic carrier concentration, $W$ is cell thickness, $L$ is the minority-carrier diffusion length, and $S$ is the surface recombination velocity (SRV). $N_D$ and $N_A$ in Eq. (2) represent the emitter and base doping, respectively.

To represent the single-junction solar cell more accurately, a two-diode model is used. In this model the junction leakage current ($J_{o2}$) represents the saturation current density of the second diode, which results from recombination in the space-charge region.

The FF is strongly dependent on the series resistance ($R_s$), shunt resistance ($R_{sh}$), $V_{oc}$ and $J_{o2}$. It is important to note that the unit of the series and shunt resistances is Ω-cm$^2$.

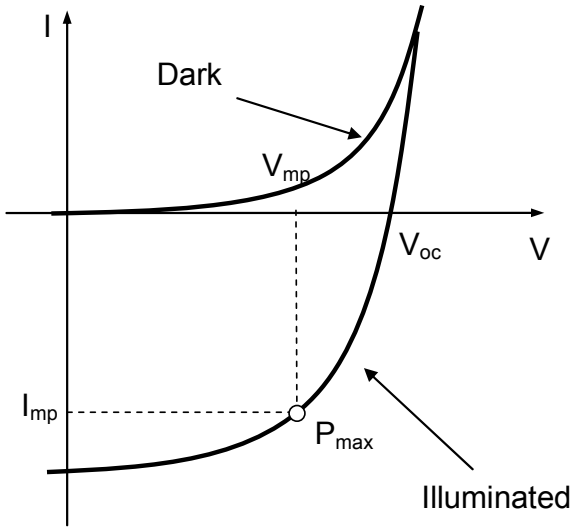


Figure 2.1. Current-voltage characteristics of the solar cell in the dark and under illumination.

### 2.2.1 Light-IV Measurement and Analysis

The solar cell is measured under normal one-sun conditions. This gives the $V_{oc}$, $J_{sc}$, FF and conversion efficiency of the solar cell. The light I-V measurement and analysis used in this research to extract cell parameters including resistances is illustrated in Figure 2.2. The schematic of the equivalent of a circuit solar cell is shown in Figure 2.3, assuming a one-diode model. The open circles are the measured data points. The three points, shown in Fig. 2.2, on the fully illuminated curve are measured during the normal (1 sun) IV curve measurement (0.1 sun). The only extra data needed for the determination of $R_s$ are the cell $V_{oc}$ and $I_{sc}$ under shading. The point in the reverse bias is measured for obtaining $R_{sh}$. Since superposition is valid for a solar cell device, the shaded light I-V curve can be translated by the difference between the one-sun (under full light) curve and the 0.1-sun curve with shading. The shaded curve is then translated by $I_{sc(full)}$-$I_{sc(shaded)}$. Shading of 10% or 0.1 sun is used to achieve a measurement of the series resistance ($R_s$) close to the operating point or maximum power point of the solar cell. The

voltage on the actual measured one-sun curve corresponds to $V_A$ at $I_{sc(full)}$-$I_{sc(shaded)}$. $V_A$ and the 0.1-sun curve are shown in Figure 2.2 below. This light IV analysis has been illustrated in [26].

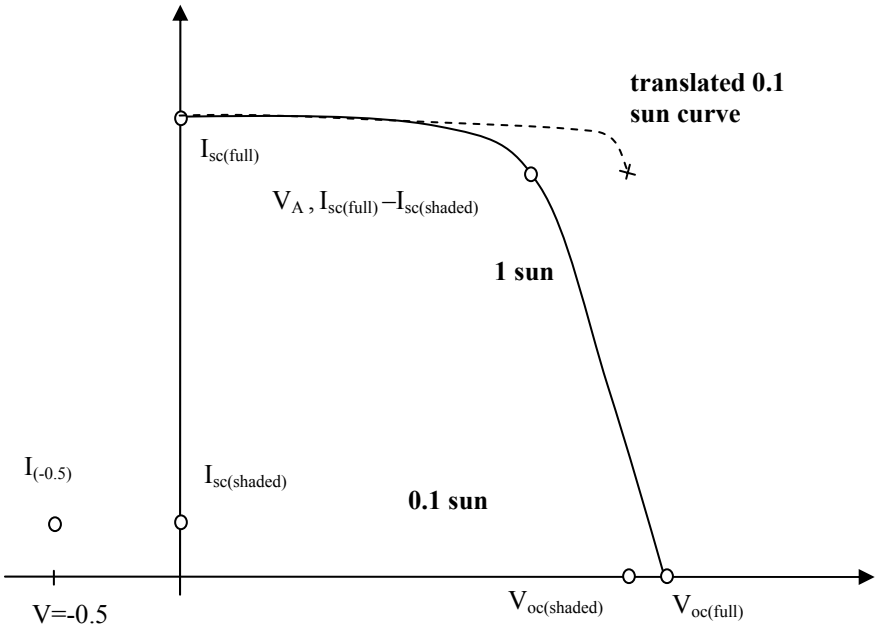


Figure 2.2. Light I-V measurement analysis [26].

The light I-V parameters can be obtained as shown by the equations below:

$$R_s = \frac{V_{oc\,(shaded)} - V_A}{I_{sc\,(full)} - I_{sc\,(shaded)}} \tag{2.6}$$

Assuming a single-exponential diode model, $I_{sc}=I_o\exp[qV_{oc}/nkT]$ : hence,

$$n = \frac{V_{oc\,(full)} - V_{oc\,(shaded)}}{\ln\left(I_{sc\,(full)}\right) - \ln\left(I_{sc\,(shaded)}\right)} \cdot \frac{q}{kT} \tag{2.7}$$

$$R_{shunt} = \frac{0.5}{I_{(-0.5)} - I_{sc\,(shaded)}} \tag{2.8}$$

$$FF_0 = \frac{v_{oc} - \ln(v_{oc} + 0.72)}{v_{oc} + 1} \tag{2.9}$$

$$v_{oc} = \frac{qV_{oc\ (full)}}{nkT} \tag{2.10}$$

In this light I-V analysis a single-diode model is assumed for the solar cell device. This is illustrated in Figure 2.3. $FF_o$ is the fill factor of the cell without the influence of $R_s$ and $R_{sh}$. The FF resulting from series resistance is calculated as follows [27]:

$$FF_s = FF_o(1 - r_s) \tag{2.11}$$

where $r_s = R_s/R_{CH}$ and

$$R_{CH} = \frac{V_{oc}}{I_{sc}} \tag{2.12}$$

The effect of the shunt resistance on the FF is calculated as follows [27]:

$$FF = FF_o\left(1 - \frac{(v_{oc} + 0.7)}{v_{oc}}\frac{FF_o}{r_{sh}}\right) \tag{2.13}$$

where $r_{sh}$ is defined as the normalized shunt resistance, which is expressed as $R_{sh}/R_{CH}$.

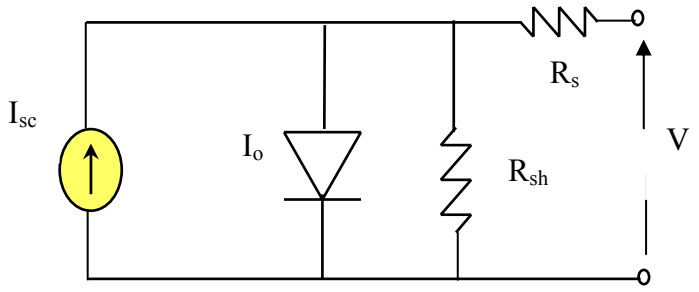


Figure 2.3. Single-diode solar cell equivalent circuit.

To determine the overall FF of the solar cell device resulting from the effects of both series and shunt parasitic resistance, equation 2.13 is used, however, in this case, $FF_o$ is replaced by $FF_s$ calculated from equation 2.11.

### 2.2.2 Dark I-V Measurement and Analysis

Cell parameters such as $R_s$, $R_{sh}$, $J_{o1}$, and $J_{o2}$ can also be obtained from the dark I-V measurement and analysis. For the dark I-V analysis, a two-diode model is assumed to represent the solar cell [28]. The circuit representing the solar cell in this case is shown in Figure 2.4. The solar cell is measured in the dark by applying a bias voltage from 0 to 0.8 V, and the current $J_d$ is measured as a function of the applied voltage. The measured dark I-V response is shown in Figure 2.5. The experimental data is fitted to equation 2.14 using the least-squares method (see Appendix F) and five pertinent variables: the saturation current density ($J_{o1}$), the junction leakage current ($J_{o2}$), the shunt resistance ($R_{sh}$), the series resistance ($R_s$), and the second-diode ideality factor $n_2$. The first-diode ideality factor $n_1$ for bulk recombination is always set to one.

At low bias, the shunt resistance effect dominates the dark I-V curve. At voltages below the maximum power point, the junction leakage current (second diode) starts to influence the dark I-V curve, and at slightly higher voltages the bulk saturation current strongly affects the dark I-V curve. At higher voltages the series resistance strongly affects the dark I-V curve.

$$J_d = J_B + J_j + J_{sh} = J_{o1}\left[\exp\left(\frac{q\{V+JR_S\}}{n_1 kT}\right)-1\right]+J_{o2}\left[\exp\left(\frac{q\{V+JR_S\}}{n_2 kT}\right)-1\right]+\frac{(V+JR_S)}{R_{sh}} \qquad (2.14)$$

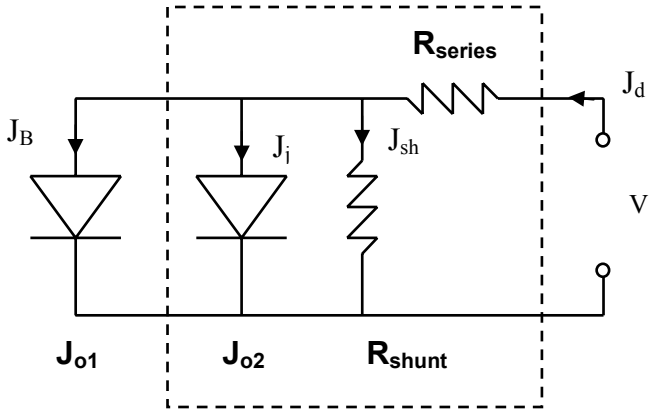


Figure 2.4. A two-diode model equivalent circuit of a solar cell in the dark.

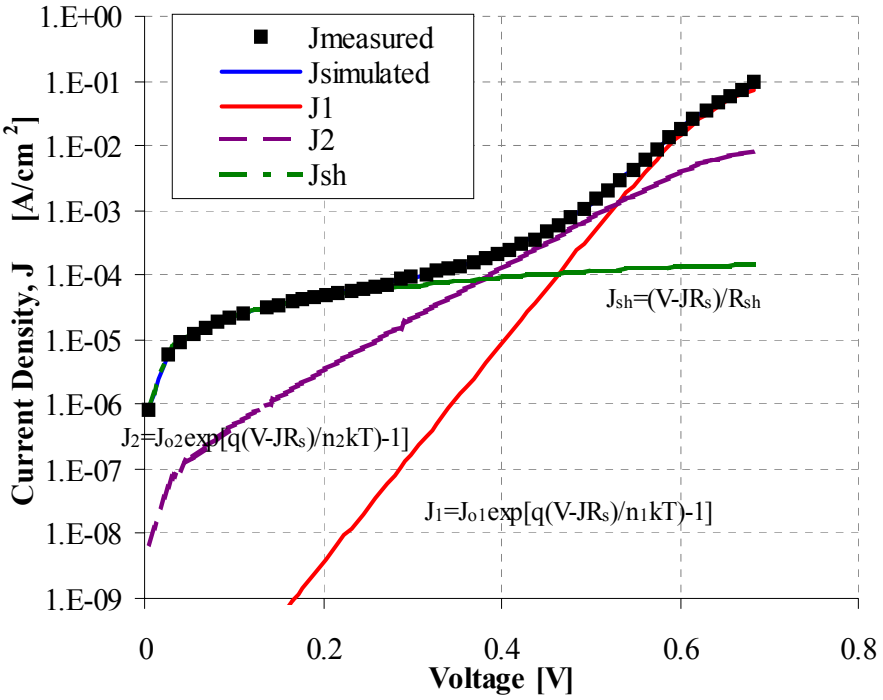


Figure 2.5. Measured and simulated dark J-V responses.

### 2.2.3 Suns-$V_{oc}$ Measurement Technique

The suns-$V_{oc}$ measurement gives a $J_{sc}$-$V_{oc}$ curve by obtaining the $V_{oc}$ for different suns or illumination intensity using a quasi-steady-state light pulse from a flash lamp (Fig. 2.6) [29]. This curve is obtained from the flash pulse, which gives suns (implied $J_{sc}$)

as a function of time as well as the corresponding $V_{oc}$ as a function of time (Fig. 2.7). The inputs for the suns-$V_{oc}$ measurement are the short-circuit current ($J_{sc}$) and the shunt resistance ($R_{sh}$) obtained from the light-IV measurement described previously in Section 2.2.1. The suns-$V_{oc}$ measurement gives the base saturation current density ($J_{o1}$), the junction leakage current ($J_{o2}$), and a pseudo-FF without the series resistance effect. A pseudo-efficiency, without the effect of $R_s$, can also be obtained by this technique to assess the impact of $R_s$. The schematic representation of the solar cell measured under suns-$V_{oc}$ conditions is shown in Figure 2.8. The advantage of suns-$V_{oc}$ over the dark-IV measurement is that the effect of series resistance on the voltage is excluded and, therefore, more accurate results of junction leakage can be obtained at the maximum power point (MPP), which is the most important regime because this is where the cell operates. The difference between the illuminated IV curve and the suns-$V_{oc}$ IV curve is a good measure of the effect of series resistance on the cell. The equation used to fit the suns-$V_{oc}$ $J_{sc}$-$V_{oc}$ curve is shown below. At the open-circuit voltage conditions, the output current is zero: $J = J_L - J_D = 0$, where $J_L$ is the photocurrent ($J_{sc}.suns$) and $J_D$ is the dark current without $R_s$.

$$J_{sc}\,sun = J_{01}\left[\exp\left(\frac{qV}{n_1 kT}\right)-1\right] + J_{02}\left[\exp\left(\frac{qV}{n_2 kT}\right)-1\right] - \frac{V}{R_{sh}}. \qquad (2.15)$$

where $J_{sc}$ is the short-circuit current of the cell at one sun illumination. The suns-$V_{oc}$ data can be analyzed either by floating $n_2$ in equation 2.15 or by fixing $n_2$ to 2 assuming a mid-gap trap [30]. The fitting is done by a least-squares method described in Appendix F to obtain $J_{o1}$, $J_{o2}$ and $n_2$.

The measurement setup is similar to that of the lifetime PCD tester, which is described in Section 2.2.5, with some modifications. There is no RLC circuit so the wafer does not have to be matched to the RLC resonant circuit and hence no coupling of the sample is needed. However, there is a full area backside contact to the Al backside of the cell as well as a probe connecting to the front grid of the cell (Fig. 2.9). There is also a reference cell from which the value of the sun (intensity) is obtained. It is useful to select a flash lamp that can give the required range of suns to cover the MPP (e.g., 0.1 to 1 sun for our measurements). The flash lamp used in for the suns-$V_{oc}$ measurements is the Quantum-X2 with 8 ms decay time. The input parameters for the suns-$V_{oc}$ analysis are obtained from the light I-V measurement; these are the shunt resistance ($R_{sh}$), the cell short-circuit current ($J_{sc}$), and the first-diode ideality factor, $n_1$, which is set to 1.

An implied $V_{oc}$ is obtained from the suns-$V_{oc}$ measurement by constructing an implied illuminated I-V curve. This is done by using the superposition principle. At each $V_{oc}$ point, the implied terminal current is given by $J_{terminal} = J_{sc} - J_D = J_{sc}(1\text{-}suns)$ [29]. The light I-V curve is obtained without the effect of series resistance. A pseudo-FF can be obtained from the $J_{terminal}$ versus $V_{oc}$ curve, which will not include series resistance. The bulk minority-carrier lifetime of the finished cell may also be obtained from the $V_{oc}$ measured by the suns-$V_{oc}$ technique [31].

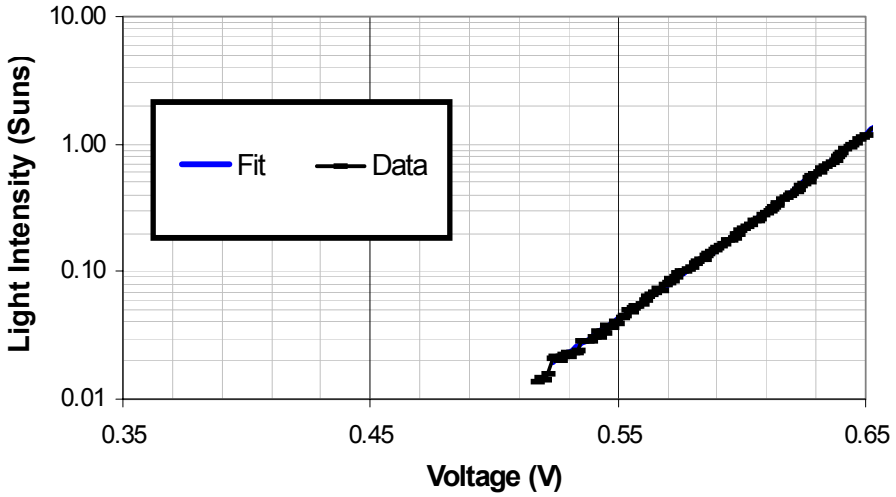


Figure 2.6. The generated $J_{sc}$-$V_{oc}$ curve from the suns-$V_{oc}$ measurement.

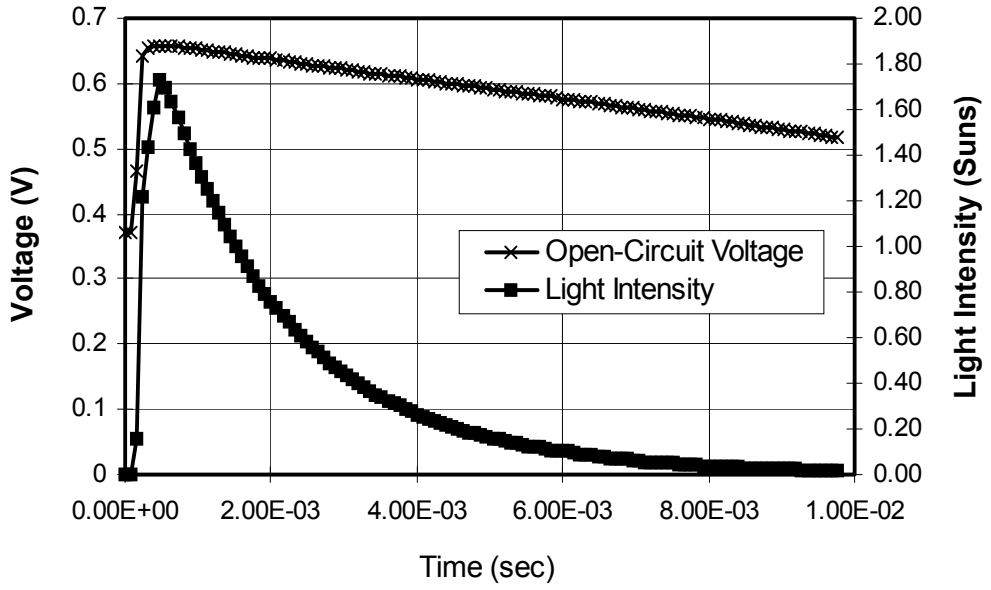


Figure 2.7. $V_{oc}$ and implied $J_{sc}$ as a function of time.

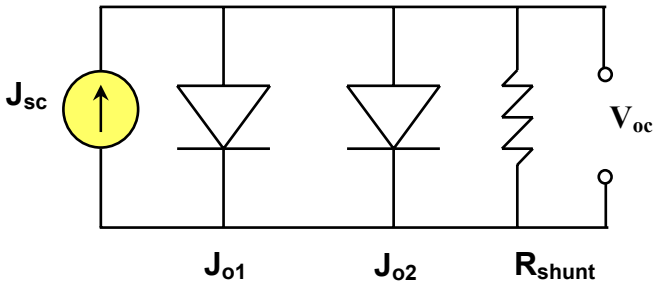


Figure 2.8. A two-diode model equivalent circuit of a solar cell under $V_{oc}$ condition.

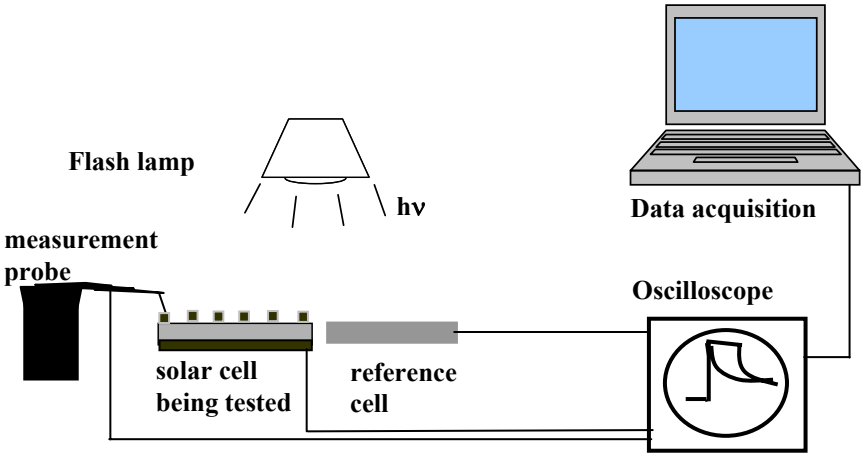


Figure 2.9. Schematic of the suns-$V_{oc}$ measurement apparatus.

### 2.2.4 Determination of the Specific Contact Resistance using the Transfer Length Method

The transfer length is a characteristic variable of the current path. The transfer length method (TLM) technique was originally proposed by Shockley [32]. The measurement structure consists of more than three contacts with varying spacing, as shown in Figure 2.10 [33].

. Figure 2.11 shows a current flow through the emitter into the grid. It is important to note that current does not flow over the entire width of the grid. The area underneath the grid that picks up the current is a function of the specific contact resistance ($\rho_c$): if $\rho_c$

is very small, the current travels mainly along the edge of the grid finger. On the other hand, if $\rho_c$ is high the current path into the metal grid finger is expanded [30]. The resistance network in Fig. 2.12 explains this behavior. The voltage U at the metal finger is zero since it is grounded (Fig. 2.12).

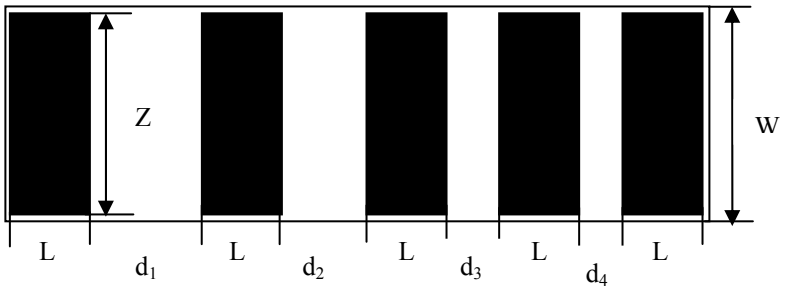


Figure 2.10 A transfer length method test structure.

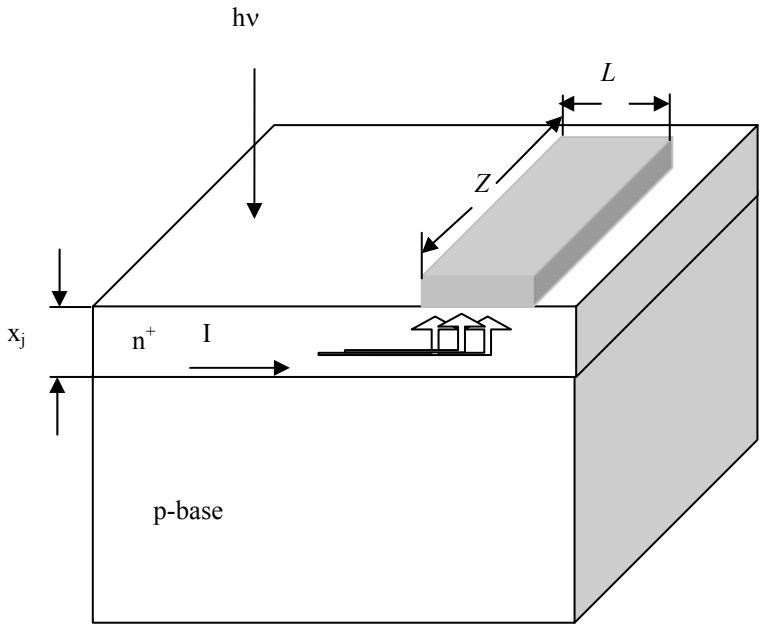


Figure 2.11. Current path under the metal finger: *L* is the width of the finger, *Z* is the length of the finger, and I is the electric current [30].

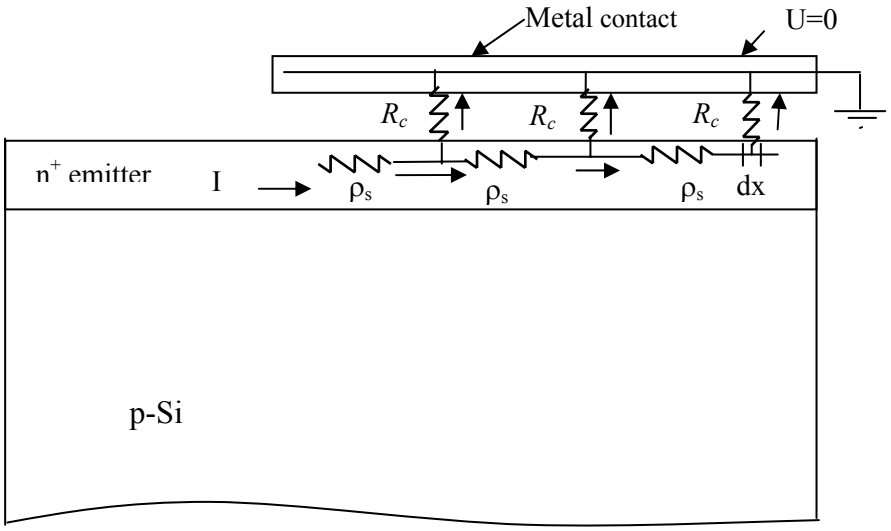


Figure 2.12. Distributed resistance network for metal-semiconductor contact resistance [30].

The current path in the emitter is assumed to be homogeneous. In the layer dx the contact resistance can be determined from the following relationship: $dR_c=\rho_c/Z\mathrm{d}x$. Further mathematical analysis that requires the solution of differential equations is needed [34]. The voltage distribution under the gridline (Fig. 2.13) can be expressed as [30]

$$U(x) = U_0 \exp\left[-\left(\frac{x}{\sqrt{\rho_c/\rho_s}}\right)\right] \tag{2.16}$$

where the transfer length ($L_T$) is designated as

$$L_T = \sqrt{\rho_c/\rho_s} \tag{2.17}$$

Thus, the voltage drops by 1/e after a distance $L_T$ and the current drops correspondingly.

For a grid width of $L$, the contact resistance can then be expressed as [30]

$$R_c = \frac{\rho_c}{ZL_T}\coth\left(\frac{L}{L_T}\right) \tag{2.18}$$

For $L \geq 1.5L_T$, $coth(L/L_T) \sim 1$ and equation 2.18 simplifies to

$$R_c = \frac{\rho_c}{L_T Z} \tag{2.19}$$

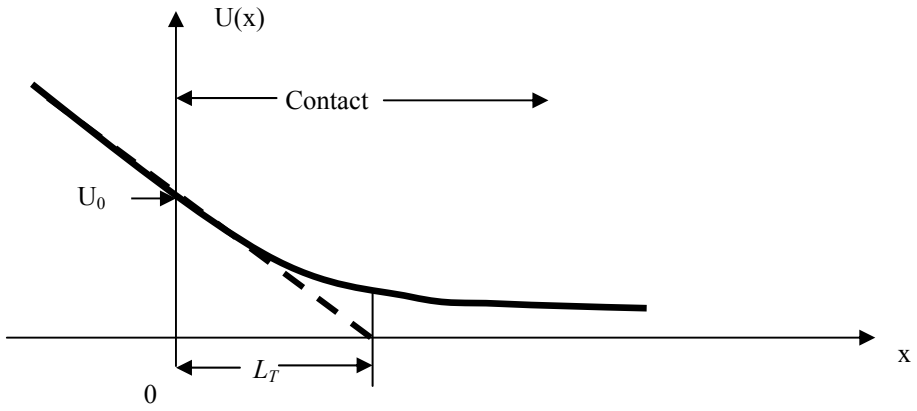


Figure 2.13. Voltage distribution under the gridline [30].

Each measurement between adjacent contacts with spacing $d_i$ would result in a total series resistance expressed as

$$R_{Ti} = \frac{\rho_s d_i}{Z} + 2R_c \tag{2.20}$$

Each measurement results in a data point as shown in the graph in Figure 2.13. For thick-film contacts, $L \geq 1.5L_T$ and equation (2.19) maybe substituted into equation (2.20), which gives the following equation for the total resistance to give the characteristics of a straight line for all the measured data points as previously shown in Figure 2.14.

$$R_T = \frac{\rho_s d}{Z} + 2\frac{\rho_s L_T}{Z} \tag{2.21}$$

Thus, the above equation represents the total resistance for various contact spacing *d*. Plotting $R_T$ as a function of d gives the plot in Figure 2.14. There are three parameters that could be extracted from the plot: the slope $\Delta(R_T)/\Delta(d)=\rho_s/Z$, which gives the sheet resistance, where the contact width Z is independently measured. The intercept at $d$=0 is $R_T$=2$R_c$, which gives the contact resistance. Finally, the intercept at $R_T$=0 gives $d$=2$L_T$, which gives the specific contact resistance with $\rho_s$ known from the slope of the plot. The transfer length method is often used for contact resistance measurements. However, there are some disadvantages. One problem with the transfer length method is that incorrect values of $\rho_c$ may be obtained if $L_T$ is not very distinct. However, probably the most serious problem or disadvantage of this technique is the uncertainty in the sheet resistance underneath the contacts. In equation (2.21), $\rho_s$ is assumed constant across the whole emitter region. However, the sheet resistance underneath the contact may be different from the sheet resistance between the contacts because of the effects of the contact formation process itself. This can be the case for screen-printed contacts since molten frit can etch part of the Si surface, as is shown in Chapter 5. However, the assumption of a uniform emitter sheet resistance would yield more conservative or higher $\rho_c$ values.

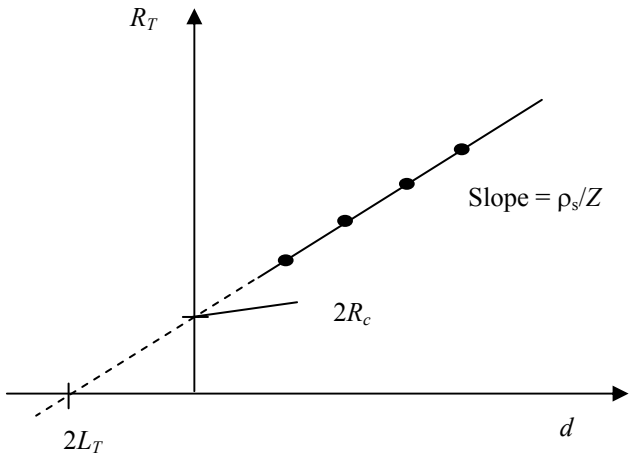

Figure 2.14. Plot of the total resistance as a function of contact spacing *d*.

### 2.2.5 Measurement of the Minority-Carrier Lifetime

Figure 2.15 is an illustration of a photo-conductance measurement system. It includes a radio-frequency RLC circuit that exhibits a high quality factor at the resonant frequency [35]. An oscillating magnetic field is generated when a sinusoidal voltage is applied across the inductor coil. When a Si sample is brought in close proximity to the inductor coil, the oscillating magnetic field gives rise to eddy currents in the sample. The power dissipation in the sample lowers the effective quality factor of the RLC resonant circuit. The coupling between the inductor coil and the sample is directly proportional to the conductivity of the sample. When a pulse of light exposes the sample on the coil, the photo-generated excess carriers are injected and increase the conductivity of the sample, which is detected by the resonant circuit as a change in quality factor (Q). Additional circuitry is needed to detect the change in quality factor as a voltage signal.

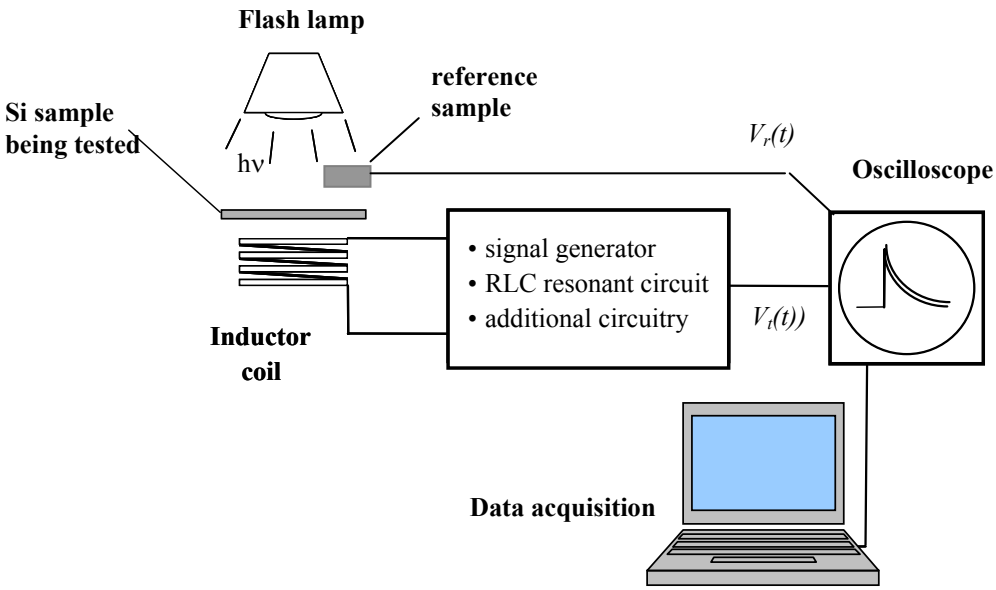


Figure 2.15. An illustration of the photo-conductance measurement system.

### 2.2.5.1 Fundamentals of the Lifetime Measurement Setup

Starting with Faraday's law of induction, the electromotive force (emf) is expressed as [36]

$$\oint \vec{E} \bullet dl = -\frac{d\Phi_B}{dt}. \tag{2.22}$$

The flux is given as [36]

$$\Phi_B = B\left(\pi r_{coil}^{\,2}\right) \tag{2.23}$$

where $r_{coil}$ is the radius of the inductive coil, $E$ is the electric field, $B$ is the magnetic field, and $\Phi_B$ is the magnetic flux. The magnetic flux results in an induced electromagnetic field, which results in eddy current losses. For a sample with thickness $W$ the current

$$I = J.\left(r_{coil} W\right) \tag{2.24}$$

The current density $J$ for a sample with conductivity $\sigma$ is given as

$$\vec{J} = \sigma \bullet \vec{E} \tag{2.25}$$

The voltage can be obtained from the electric field as shown in the following equation:

$$\vec{E} = \frac{dV}{d\vec{l}} \Rightarrow V = 2\pi r_{coil}.E \tag{2.26}$$

The power loss resulting from the sample is

$$P_{loss} = \frac{V^2}{R_{loss}} \tag{2.27}$$

where

$$R_{loss} = \frac{V}{I} = \frac{E(2\pi r)}{\sigma E[rW]} = \frac{2\pi}{\sigma W} \tag{2.28}$$

This results in

$$P_{loss} = \frac{V^2}{R_{loss}} = \frac{[2\pi r_{coil}.E]^2}{2\pi} \cdot (\sigma W) \tag{2.29}$$

where $\sigma W$ is the conductance of the sample.

A high photo-conductance results in a high power loss ($P_{loss}$) and a low Q factor. The circuit in Figure 2.16 relates $Q(t)$ to the output voltage $V_{out}(t)$. The schematic in Figure 2.16 shows the matching of the resonant frequency and the difference in voltages between the test sample and reference sample.

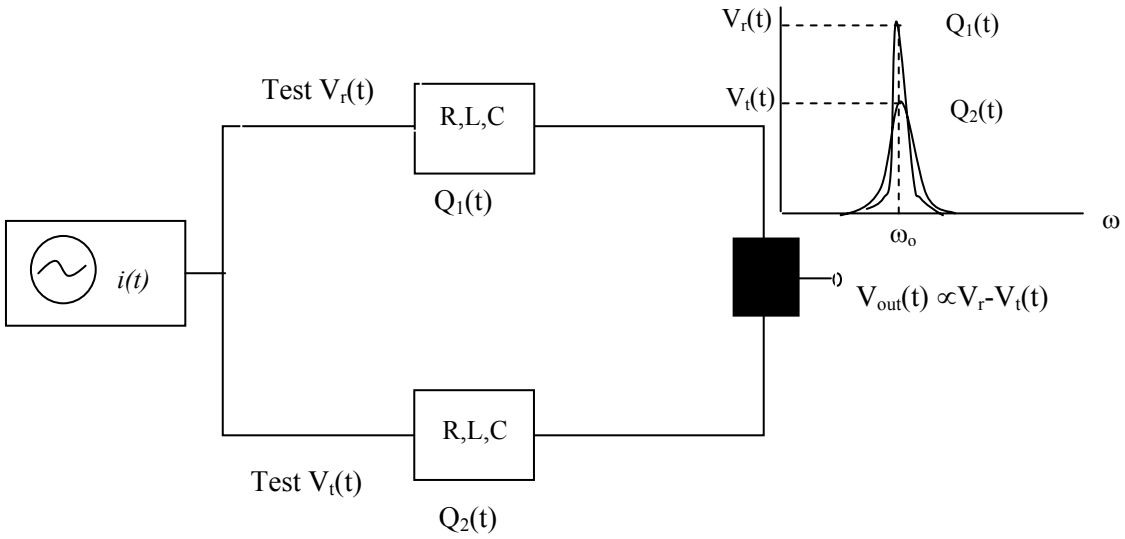


Figure 2.16. A schematic explaining the process of matching the resonant frequency of the reference and test cell used for the PCD measurement.

### 2.2.5.2 Fundamentals of the Photo-conductance Lifetime Measurement

Two modes operate the minority-carrier lifetime measurement: one is by using a transient method and the other is using a steady-state photo-conductance method [37]. The transient method involves measuring the photo-conductance decay (PCD) transients after a very short light pulse from a flash lamp. The effective lifetime is obtained from the decaying curve:

$$t_{eff} = -\frac{\Delta n}{d(\Delta n)/dt} \tag{2.30}$$

The transient technique works best for minority-carrier lifetimes greater than 50 μs and is therefore not suitable to measure low minority-carrier lifetimes of as-grown or processed multicrystalline wafers.

The other method for lifetime testing involves measuring the photo-conductance under steady-state illumination [38]. Using this method, minority-carrier lifetimes <50 μs can be measured. The photo-generated excess carriers result in an increase in the wafer conductance:

$$\Delta\sigma = q\left(\Delta n\mu_n + \Delta p\mu_p\right)\mathrm{W} \tag{2.31}$$

where W is the thickness of the wafer. If the effect of electron or hole trapping is small and charge does not build up in the wafer under illumination, then $\Delta n=\Delta p$ holds [39]. Hence, equation (2.31) becomes

$$\Delta\sigma = q\Delta n\left(\mu_n + \mu_p\right)\mathrm{W} \tag{2.32}$$

The electron and hole mobility, $\mu_n$ and $\mu_p$, respectively, are a function of both doping and injection level. The above equation can be iterated to find both $\Delta n$ and $(\mu_n+\mu_p)$. In steady-state illumination, the rates of electron-hole pair generation and recombination are equal. The generation current ($J_{ph}$) and recombination current ($J_{rec}$) are equal:

$$J_{ph} = J_{rec} = \frac{q\int_0^W \Delta n dx}{\tau_{eff}} = \frac{\mathrm{q}\Delta\mathrm{n}_{\mathrm{avg}} W}{\tau_{eff}} \tag{2.33}$$

Substituting the sheet wafer conductance for Δn gives

$$\tau_{eff} = \frac{\Delta\sigma}{\left(J_{ph}\left(\mu_n + \mu_p\right)\right)} \tag{2.34}$$

The conductance and the photo-generated current are measured by placing the test sample on the coil and using a reference solar cell to obtain the bulk lifetime from the PCD

tester. The photo-conductance measurement as a function of time gives lifetime as a function of the injection level. The minority-carrier lifetime is determined at a specific injection level. For multicrystalline cells with significant traps, the lifetime is measured at a high injection ($\geq 10^{15}$ $cm^{-3}$) to avoid the effect of trapping. Figure 2.17 shows the measured lifetime versus minority-carrier density obtained from the photo-conductance measurement.

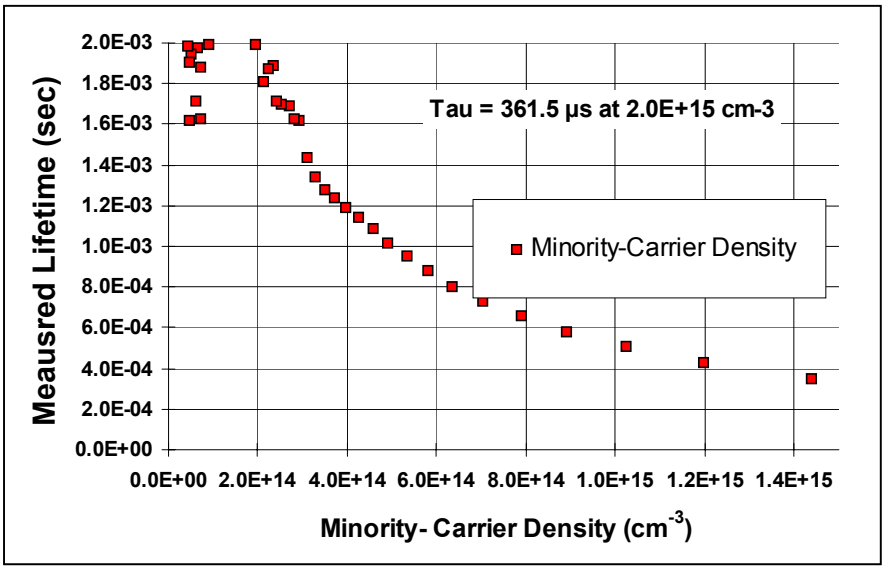


Figure 2.17. Measured lifetime versus minority-carrier density.

## 2.2.6 Measurement of the Saturation Current Density

The emitter saturation current density ($J_{oe}$) is an important parameter for solar cells that determines the degree of recombination in the emitter region. Since this thesis deals mainly with high-sheet resistance emitters, the measurement of $J_{oe}$ was frequently performed to determine the degree of recombination for different emitters (100 versus 40 Ω/sq) with different silicon nitride passivation quality. The emitter saturation current

density can also be obtained from transient photo-conductance decay measurement [40]. The setup is identical to that of Figure 2.15.

The continuity equation and the diffusion current equation after generation has stopped, can be written as

$$\frac{dn}{dt} = -\frac{n}{\tau_b} + D_n \frac{d^2 n}{dx^2} \tag{2.35}$$

To extract $J_{oe}$, the test wafer is identically diffused and/or passivated on both sides and illuminated under transient condition. It can be shown [40] that the effective lifetime can be expressed in terms of bulk and surface recombination according to

$$\frac{1}{\tau_{eff}} = \frac{1}{\tau_b} + \frac{2J_{oe}n_{av}}{qWn_i^2}, \tag{2.36}$$

where $n_i$ is the intrinsic carrier concentration, $\tau_{eff}$ is the effective minority-carrier lifetime, $\tau_b$ is the bulk (or base) minority-carrier lifetime of the sample, and $n_{av}$ is the average minority-carrier concentration in the sample.

The transient PCD measurement gives the inverse of the minority-carrier lifetime versus the average minority-carrier density (Fig. 2.18). According to equation (2.36) the intercept gives the bulk lifetime, while the slope of the curve gives $J_{oe}$.

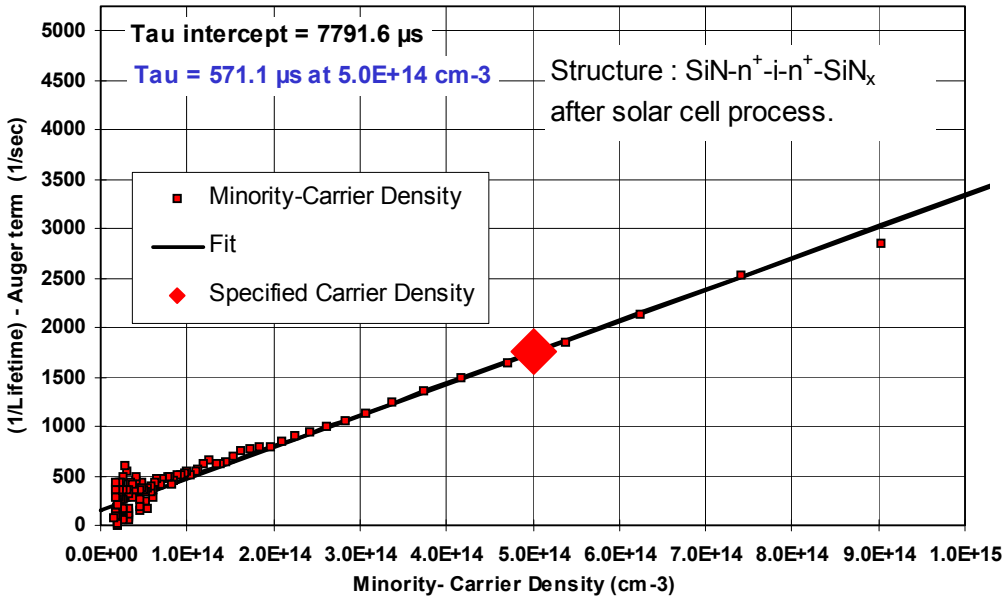


Figure 2.18. Inverse minority-carrier lifetime versus minority-carrier density for extracting the saturation current.

## 2.2.7 Determination of the Internal Quantum Efficiency and Total Reflection of the Solar Cell

### 2.2.7.1 Spectral Response and Reflectance Measurements

To measure the spectral response of a solar cell, the cell is mounted on a stage and electrically connected to the solar cell detector support module (DSM). The stage itself acts as the back contact for the solar cell, while a probe is connected to the grid for the front contact. The measurement consists of a light source, a monochrometer, an attachment for the sample, and a detector (Si or Ge) (Fig. 2.19). The detector is only used for calibration and specular reflectance measurement.

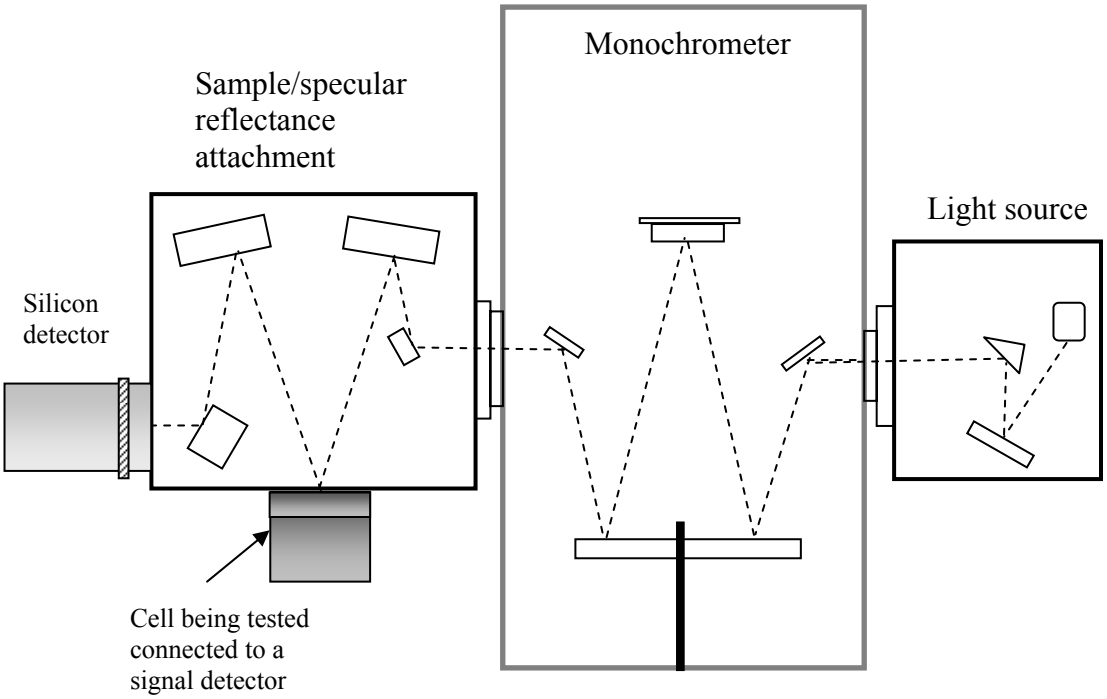


Figure 2.19.The spectral response measurement system.

### 2.2.7.2 The Monochrometer Operation

A mirror focuses white light entering through the entrance slit onto a rotating diffraction grating. The exit slit allows only a portion of the diffraction pattern to pass to the detector. The general grating equation is given as follows [41]:

$$d\left(\sin\theta + \sin\beta\right) = m\lambda \tag{2.37}$$

where $m$ is the optical order; the angles $\theta$, and $\beta$ are described in Figure 2.20. Higher diffraction orders become less intense because of the angular dispersion. The angular dispersion for a fixed incident angle ($\theta$) is given as [41]

$$\frac{\partial\beta}{\partial\lambda} = \frac{m}{d\cos\beta} \tag{2.38}$$

The different optical orders are diffracted at different angles. The absolute efficiency of a grating in a given wavelength range and order is the ratio of the diffracted light energy to the incident light energy in the same wavelength range [41]. Blazed gratings are used so that the diffraction envelope maximum shifts into another order. The blaze angle depends on the incident angle, so that various geometries requiring different blaze angles are possible. Thus, the grating is blazed for a wavelength $\lambda$ and order $m$. However, orders may overlap one another; in this case the undesired wavelengths from other orders can be filtered out.

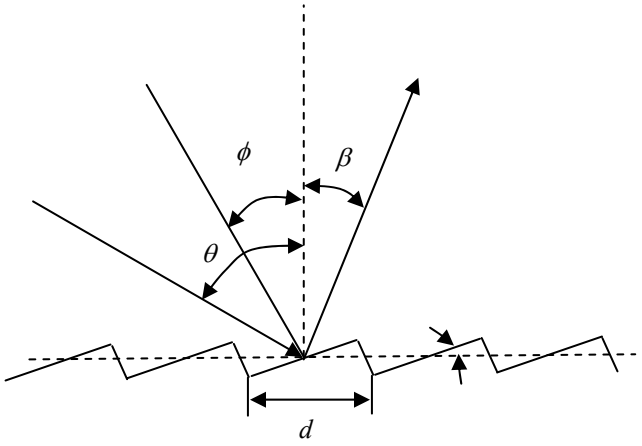


Figure 2.20. Blazed grating diffraction.

### 2.2.7.3 The Internal Quantum Efficiency of the Solar Cell

The monochromatic light generates electron-hole pairs in the semiconductor with a spatial distribution given by [27]

$$G = (1 - R)\alpha N e^{-\alpha x} \tag{2.39}$$

where $N$ is the incident photon flux, $R$ is the fraction reflected, and $\alpha$ the absorption coefficient. The absorption is large for short wavelengths (UV light), and light is

absorbed quickly when entering the semiconductor material. Conventional solar cells are not very effective at collecting light close to the surface. The internal quantum collection efficiency (IQE) is defined as the ratio of the current photogenerated carriers to the photon flux incident just inside the light incident boundary of that particular layer, i.e., after accounting for reflection. It is very low for UV light. The absorption is smaller for intermediate wavelengths (~500-900 nm); a large part of the generated carriers is created where the collection probability is high; and therefore, the IQE is high. For long – wavelengths, light absorption is weak and only a small portion of the light is absorbed in the active region of the solar cell. Thus, the IQE is decreases and drops to zero when the photons have insufficient energy to create electron-hole pairs.

The IQE is independent of the reflectance. However, it is necessary to measure the reflectance of the solar cell to obtain the IQE from the measured spectral response. For the solar cell samples, the diffuse reflectance is measured since this represents the reflectance of the imperfect or rough surface; this measurement requires an integrating sphere. The theory and operation of an integrating sphere for diffuse reflectance measurements is well documented in reference [42].

# CHAPTER 3

# A REVIEW OF SI SOLAR CELL CONTACTS AND TECHNOLOGY

## 3.1 Solar Cell Metallization Techniques

Solar cell metallization is a major efficiency-limiting and cost-determining step in solar cell processing [43]. High-quality high-performance photolithography/evaporated contacts are frequently used in the laboratory to achieve high-efficiency solar cells. This technique is too expensive for low-cost production. For cost reasons, the most common metallization technique used for Si solar cell production is screen-printing of thick-film Ag contacts. Another competing technology for solar cell production is buried-contact technology, which involves laser grooving and metal plating. These metallization techniques are briefly discussed in the following subsections.

### 3.1.1 Photolithography Contacts

Most world record high-efficiency laboratory cells are fabricated with photolithography contacts, which allows for more accurate prediction of solar cell behavior. In this technology, metal-Si specific contact resistance is generally very low ($1\times10^{-5}$ $\Omega$-cm$^2$) [44], with very narrow gridlines (~8 μm) and no junction shunting. Therefore, photolithography cells have the highest fill factors and the highest cell performance. However, this technology is time consuming and expensive because of the use of photo-resist mask patterning and metal e-beam evaporation. This has led to the

investigation, development, and use of other simpler metallization techniques for solar cell applications. Photolithography (PL) contacts on the front have also been used with screen-printed back contacts using rapid-thermal processing technologies to achieve high efficiency [45]. Recently, record high-efficiency EFG (edge-defined film-fed growth) and string ribbon cells with photolithography front-grid metallization were fabricated at Georgia Tech using rapid thermal processing with efficiencies of 18.2% and 17.8%, respectively [46]. World record efficiencies of 24.7% on single-crystal Si [47] and 20.3% on cast multicrystalline Si [48] have also been achieved with photolithography contacts.

### 3.1.2 Buried-Contact Technology

The buried-contact (BC) technology was developed at the University of New South Wales to overcome screen-printing metallization limitations, including the inability to produce fine lines, obtain high aspect ratios, and achieve good metal conductivity and low contact resistance [49]. The contact grooves are made either mechanically or by a laser. Contact metallization is achieved by electroless Ni/Cu plating and sintering [50]. The advantage of buried-contact cells is that the conducting contacts are buried deeply in heavily doped grooves, reducing resistive losses and recombination at the contacts. This results in higher fill factor, open-circuit voltage, and current. This technology also allows for contacting lightly doped emitters, thus lowering surface recombination and enhancing the "blue response." Laser-grooved buried-contact solar cells with surface texturing, lightly diffused emitter, and oxide passivation have been fabricated with efficiencies of ~19.8% on 12-$cm^2$-area cells [51]. High-efficiency (17.5%) buried-contact cells have

been reported on large-area multicrystalline wafers using mechanical V-grooves and electroless plating of Ni and Cu [52].

Low-cost selective-emitter techniques have also been investigated for buried-contact solar cells. P-doped spin-on dopants (SOD) and screen-printed dopant paste have been used for selective-emitter formation [53].

### 3.1.3 Screen-Printing Technology

Screen-printed (SP) contact technology, which is the focus of this research, is much more rapid and cost effective compared to photolithography and buried-contact technologies. The screen-printing equipment is robust, simple, and inexpensive, and the screen-printing technique can also be easily automated with a throughput exceeding 1,000 wafers per hour. It produces a small amount of chemical waste with little environmental impact and is modular for actual production facilities [54]. Screen printing is truly a cost-effective option for large-scale solar cell manufacturing, provided high-quality contacts with FF≥0.77 can be achieved in production.

Figure 3.1 shows a schematic of the screen-printing process. During the actual printing, a squeegee moves the paste across the screen. This action causes a decrease in the viscosity of the paste, which in turn allows the paste to pass through the patterned areas onto the substrate. As the squeegee passes, the screen peels off and the paste viscosity returns to normal. Factors that affect the screen peel are the paste and its viscosity, the area of the print, the tension of the screen, the squeegee speed, and the snap-off distance between the sample and the screen. The screen is made of an interwoven mesh kept at high tension, with an organic emulsion layer defining the printing pattern. A disadvantage of screen printing is the cost of the metal paste since

controlled micro-sized high purity silver particles are required, with a paste composition designed for solar cell processing [51]. However, screen printing is the most widely used metallization technique for Si solar cells because of the above mentioned advantages. A solar cell contact has to meet certain requirements [55]:

1- Low contact resistance to Si,

2- Low line resistance,

3- Negligible effect on the Si substrate,

4- Good line resolution,

5- Good solderability,

6- Good adhesion,

7- Low cost.

The firing of a thick-film paste on the diffused and antireflection-coated front-side of the wafer is a technique similar to soldering, which requires wetting the surface without leaching.

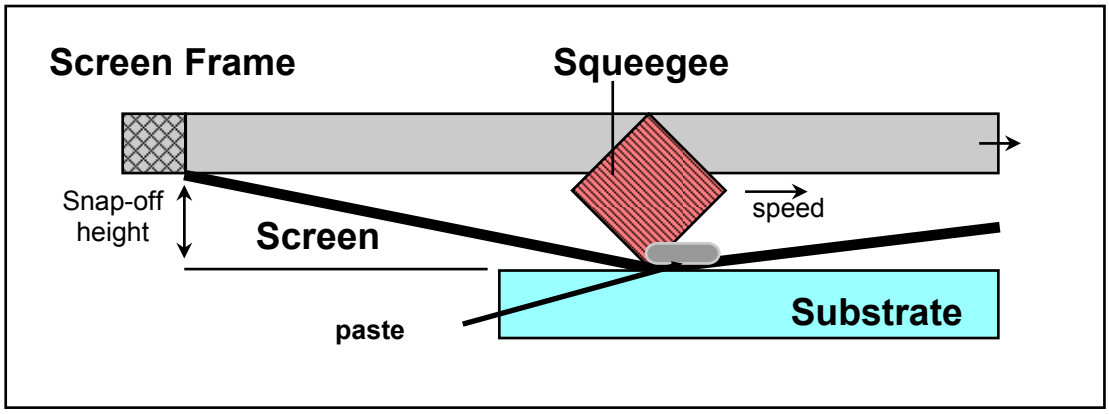


Figure 3.1. The screen-printing process.

### 3.1.3.1 The Composition of Screen-Printing Pastes

The paste is composed of four different materials: metal powders, glass frit and modifiers, solvent, and non-volatile polymers or resin, which are blended together [56]. The role of these ingredients is described below:

1- Functional phase, which consists of the metal powder (e.g., Ag in the case of conductive metal pastes for printing the front grid), and is responsible for providing the current conduction;

2- Binder phase, which holds the paste to the substrate, dissolves the metal powder and sticks to the substrate or provides adhesion during high-temperature firing. It also affects the sintering kinetics. This is also called glass frit, which is a mixture of metal oxides and silicon dioxide melted to form a uniform glass. Before being added to the paste, the glass is milled to a thin sheet and crushed. Normally, lead oxide is the most important ingredient, which is added in amounts of 2-5% for the sintering action. Other components can be bismuth, boron, aluminum, copper, and titanium. Phosphorus can also be added to improve the contact with the n-type emitter.

3- Vehicle, which acts as a carrier for the powders and consists of both volatile solvents and non-volatile polymers. These substances evaporate during the drying and burn-off steps before the actual firing step. The vehicle is also responsible for pseudoplastic behavior and adhesion of the paste to the substrate during printing.

4- Modifiers, which are small amounts of additives that are proprietary to the paste manufacturer. These additives control the behavior of the paste before and after

processing. The modifiers include combinations of elemental metals such as Ge, Bi, Pb, Li, Cd, In, and Zn [57].

The front-side paste typically contains about 70% silver. Silver can be present as very fine spherical particles of 1-2 μm, or as flakes that are about 5 μm in size. The flakes are normally in very small quantities; they are important for good contact (low contact resistance) to the Si during sintering and they also prevent blistering of the fired silver lines.

The rhoelogical behavior of the thick-film paste depends on its composition and the nature of the ingredients. The screen-printing process requires that the printed paste be in a certain range of viscosity. This is determined by the rheological properties of the paste like the inorganic powders (e.g., Ag powder) in the paste. Most paste formulations generally involve more than one type of solid powder with different characteristics, such as size, distribution, and surface area. For a dilute dispersion of solid particulates, the viscosity of the suspension increases linearly with solid phase volume fraction according to the following Einstein relationship [58]:

$$\nu_{rel} = \frac{\nu_s}{\nu_o} = 1 + 2.5\phi, \tag{3.1}$$

where $\nu_s$ is the suspension viscosity, $\nu_o$ is the viscosity of the suspending medium (solution), and $\phi$ is the volume fraction of particles. At high particle concentrations, the viscosity of the suspension increases more rapidly than predicted by the above equation because of inter-particle interactions. As the fractional volume of solids is further increased, a point will come when flow will not occur, where viscosity approaches

infinity. This is called the maximum packing fraction $\phi_m$, which depends on particle shape, size, distribution, etc… [58].

The composition of the paste needs to be sufficiently dense to produce continuous lines during printing. Moreover, to be able to produce continuous lines, the viscosity of the paste must be sufficiently low during printing. This is to ensure that the paste is properly transferred onto the substrate through the screen openings. The paste must therefore have a pseudoplastic behavior, i.e., the viscosity should decrease with an increasing shear stress. It must also be thixotropic, meaning that it should maintain its low viscosity for a given time.

#### 3.1.3.2 The Fabrication of the Screen

The screen design is important for achieving the desired metal thickness and resolution. Therefore, it is useful to understand what is involved in making a screen. First, the screen used for printing is fabricated by stretching a stainless steel wire mesh cloth across the screen frame. The frame is normally made from aluminum and can vary in size (12 in. x 12 in., 8 in. x 10 in., or others). The mesh is attached and kept at high tension (Fig. 3.2). Then an organic light-sensitive emulsion layer is spread over the entire mesh filling all the open areas. The emulsion is basically an organic material that acts as a gasket between the screen and substrate. The emulsion is also used to define the printing pattern. First, a uniform photo-resist layer is deposited on the substrate side and pressed into the wire gauze. A positive transparency (metal pattern is black) is laid on the emulsion layer and illuminated with a powerful UV lamp. The exposed areas become hard and the grid pattern is washed away. Next, the area to be screen printed is patterned on the screen. The emulsion thickness is an important factor in improving the height of

the metal fingers. The minimum emulsion thickness required is about 8 μm [59]. The maximum amount of paste that can be deposited on the wafer depends on the volume between the wire gauze of the mesh and the volume in the emulsion layer. By using thinner wires or increasing the wire separation, the deposited metal paste uniformity can be improved and also the paste can have a better chance of being released from the screen more easily. However, the strength of the wire gauze decreases and significantly reduces the lifetime of the screen and maximum squeegee pressure that can be applied.

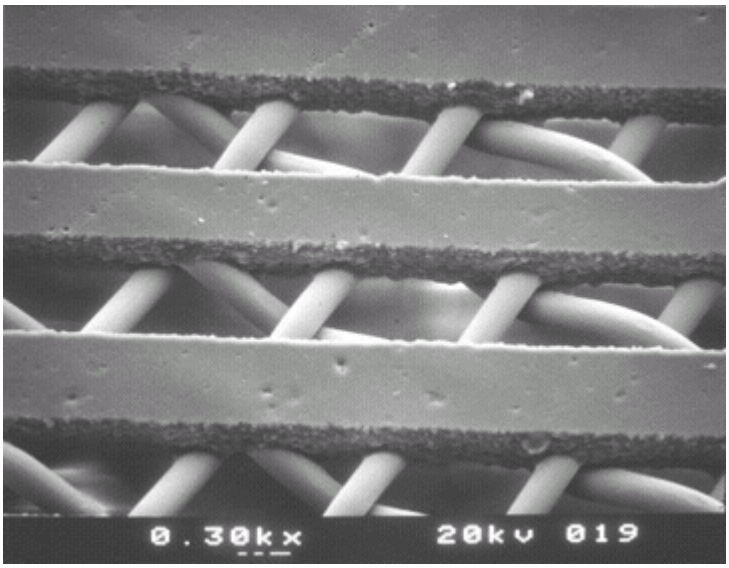

Figure 3.2. Emulsion and mesh (360) for a fine-line (2-mil line) screen.

The mesh weaves are normally standard counts of 290, 325, 400, and 500 wires per inch, the wire diameter ranges between 0.7-0.9 mils, and the mesh angle for the front Ag line printing is 22.5° for higher resolution, while that for the full Al back is 45° [60]. The mesh counts and wire types are used to allow different combinations of appropriate opening areas for paste flow, to minimize printed line width, and screen cost if possible. The mesh count is basically the number of wires per inch in the screen mesh.

### 3.1.3.3 The Screen Printing Process

During the actual printing a squeegee moves the paste across the screen. This action causes a decrease in the viscosity of the paste, which in turn allows the paste to pass through the patterned areas onto the substrate. As the squeegee passes, the screen peels off and the paste viscosity returns back to normal. Factors that affect the screen peel are the paste viscosity, the area of the print, the tension of the screen, the squeegee speed, and snap-off distance of the screen.

After the completion of the printing by the squeegee, the viscosity must increase so that minimal flow occurs when the emulsion gasket is removed [59]. The pastes used in solar cell screen printing are of pseudoplastic rheology; thus, low viscosity is produced under high shear and high viscosity elsewhere. High shear rates are obtained by printing the paste at ≥25 cm/s (10 in/s) while using a high mesh count [59]. Figure 3.3 shows the shear rate versus the screen mesh count per inch for different squeegee speeds.

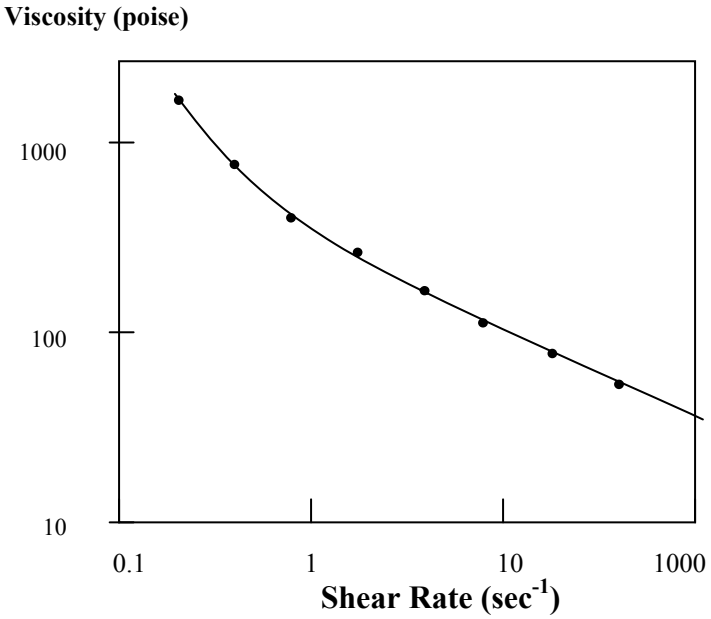


Figure 3.3. Pseudoplastic rheology of the paste [59].

The most important parameters that need to be set during the printing process include the following:

1 - the snap-off distance,

2 - the squeegee pressure,

3 - the squeegee speed.

The snap-off distance determines the upward movement of the screen when the squeegee passes by. The force exerted as a result of this motion lowers the viscosity of the paste and allows it to release from the wire gauze. If the snap-off distance is too small, the paste will not be released from the screen. On the other hand, if it is too large the squeegee pressure required to push the screen downward to the wafer must be excessively high; this would decrease the tension of the screen and hence its lifetime.

The squeegee is basically rubber (polyurethane) that normally has a square cross-section and is mounted on a 45° angle so that the sharp edge touches the screen (Fig. 3.1). The squeegee and the screen must be mounted parallel to the wafer. The squeegee should not be too soft or too hard. If it is too soft it follows the shape of the screen exactly and would then push the paste out of the fingers. If the squeegee is too hard, it would not accommodate the roughness of the wafer and the paste would not be supplied uniformly, or even worse, the wafer might break during the printing process. The squeegee speed determines the amount of paste being deposited. The squeegee speed that can be applied depends on the thixotropic behavior of the metal paste and also determines the amount of paste that can be deposited. If the speed is too high, the paste has little time to fill the openings in the screen and can therefore cause discontinuous printing of the lines because

of the short release time from the screen. At very high velocities ~25 cm/s, the viscosity of the paste decreases greatly and it becomes easy to fill the openings [61].

The squeegee must apply a downward force to make up for the snap-off distance and push the paste through the openings. The squeegee pressure needs to be increased for thicker emulsion layers. The squeegee pressure must not be too high, as this could cause the paste to be removed from the screen openings, the emulsion layer to become compressed, and the screen lifetime to be reduced; also, the wafer can break. On the other hand, if the squeegee pressure is too low, the paste might not be released through the screen holes consistently and it might dry there, causing clogging during printing. The screen would then need to be cleaned and the printing process would need to start all over again, which is not desirable for high-throughput screen-printing industrial processes.

#### 3.1.3.4 High-Resolution Screen Printing

This subsection describes the effects of the different elements involved in the screen-printing process to obtain high-resolution printing. These elements include screen type, the wire diameter, the deposited thick-film composition, the emulsion thickness (emulsion gasketing), and the printing dynamics. Fine-line resolution is achievable by optimizing and combining the effects of the different elements involved in the screen-printing process. Fine-line screen-printing techniques have been described in a concise technical paper [59].

When optimizing the printing resolution, the first element to consider is the screen, which needs to be imaged to the required printing pattern and resolution. The screen mesh count and wire size should be determined. The mesh count and the wire

diameter set a limit to the print resolution regardless of the paste rheology or the printing technique. To achieve high-resolution printing, a smooth emulsion is required. A 400-mesh count screen with small diameter wire and thin emulsion thickness will give a relatively lower printed paste thickness. Fine lines of 50, 75, 100, and 125 μm in width can be obtained using a 400-mesh screen with 0.75 mil wire diameter and 0.4 mil emulsion thickness.

For the best line resolution, the hydraulic pressure should be concentrated at the point after the emulsion is in contact with the substrate. There are several ways to bring the hydraulic pressure closer to the squeegee tip. These methods include

1- lowering the viscosity of the paste,

2- printing at the maximum printing speed using a high mesh count screen,

3- limiting the amount of paste in front of the squeegee tip.

The maximum printing speed is defined as the highest possible speed where the screen can still peel with ease. The line resolution can be significantly increased by increasing the printing speed to the maximum possible corresponding to the viscosity of the paste. Choosing a harder squeegee (60-80 Shore) can also help obtain well-defined line edges for fine-line printing.

#### 3.1.3.5 The Screen-Printed Paste Firing Process

Following the printing of the cell, the metal paste is fired. This is done in a radiation lamp-heated belt furnace in an industrial production environment. The firing is basically a three-step process:

1. Drying: Drying is performed to evaporate all the solvents in the paste, which otherwise cause gas bubbles at higher temperatures and result in cracking of the

metallization. Drying is done at ~150° C.

2. Burn-out: The burn-out process is done at temperatures in the range of 300-400° C to drive out the organic binders.
3. Firing: The firing step is also called the sintering step during which the Ag metal grid adheres to the underlying Si. Conventional firing is done at temperatures in the range of 700-800° C. As a rule, it is best to fire fast and hot [28].

The profiles of these three steps are described in Figure 3.4. Cracking in the metallization can happen if the outside surface of the paste is dried too fast, forming a crust that cannot be permeated by the solvent.

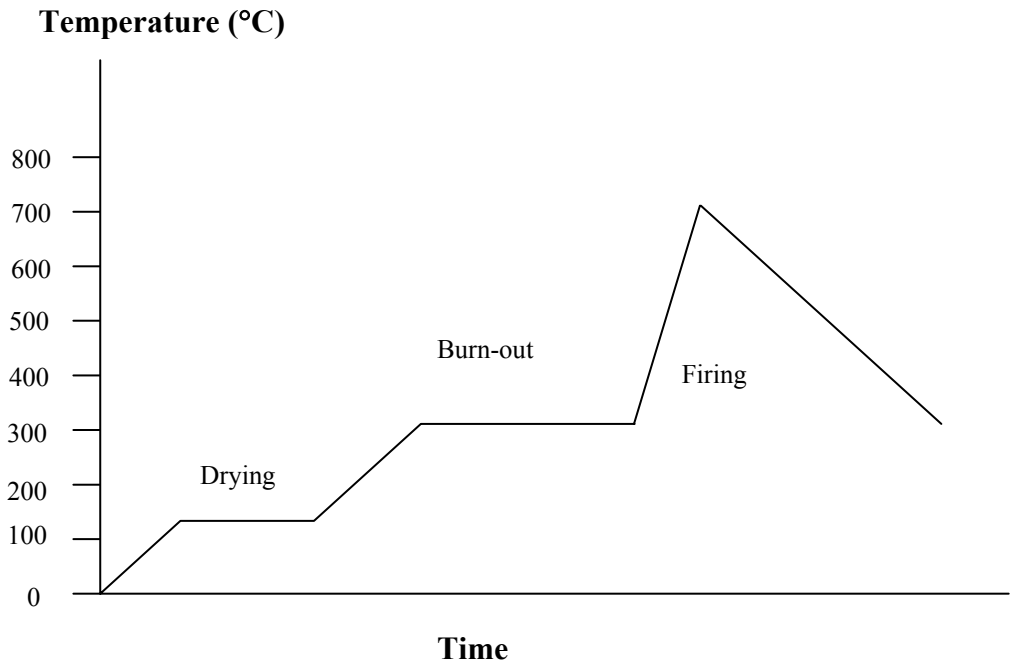


Figure 3.4. A schematic of the temperature profile in a belt furnace.

During the burnout process, sufficient airflow must be present to have complete oxidation of the organic components; otherwise, carbon will be present in the paste and

can diffuse into the junction during firing. The thermogravimetric analysis (TGA) gives the temperature at which all the organic constituents in the paste are burnt out; this depends on the type of polymers used. However, excessive burn-out is not critical and should be avoided since gas bubbles can give cracks in the metallization.

The firing step is also called the sintering step. The upward slope of the firing profile can be set to 50° C/s, while the downward slope can be set to slower rates to obtain better adhesion of the Ag to the Si and prevent detachment as a result of differences in the expansion coefficients. A value of -10° C/s has been deemed the best cooling rate in terms of specific contact resistance [62]. The cell stays around 30-60 s at a temperature less than 50° C from the peak. Conditions with the high belt loading of cells, an insufficient air injection, and rapid firing may produce a net reducing atmosphere in the local environment of the thick-film conductor, which is capable of converting the lead oxide (and bismuth oxide if present in the glass) contained in the glass to metallic lead (and bismuth) [63].

During the firing process the silicate glass systems, such as the ones used for solar cell thick-film contacts, form a viscous glass at the firing temperature, and a major part of densification results from the viscous flow under the pressure caused by the fine pores. In other words, vitrification takes place and is responsible for forming a bond for the thick-film contact. The processes or steps that take place during the firing cycle are shown in Figure 3.5. Ag is screen printed on top of the silicon nitride antireflection coating and then fired. Between 100-200° C, the solvent evaporates; from 200-400° C the polymer or resin burns out; from 400-600° C the glass frit starts to melt and Ag particles start to coalesce and sinter; from 600-800° C molten glass with some amount of dissolved Ag

etches the silicon nitride antireflection coating and reaches the Si surface where it reacts and etches a very thin layer of Si. Ag in the glass then precipitates onto the Si surface in the form of crystallites.

Contact formation can influence series resistance, shunt resistance, and junction leakage current, which in turn can degrade the fill factor. Optimizing the firing process means finding the temperature profile where $V_{oc}$ is unaffected and a good fill factor ($\geq$0.78) is achieved. The optimum firing condition depends on the frit composition and the emitter profile. Firing fast and hot generally gives optimum results because the impurities do not get a chance to diffuse and the sintering is effective. The activation energy for the impurities to diffuse into the emitter region is generally lower than that used for the sintering [56].

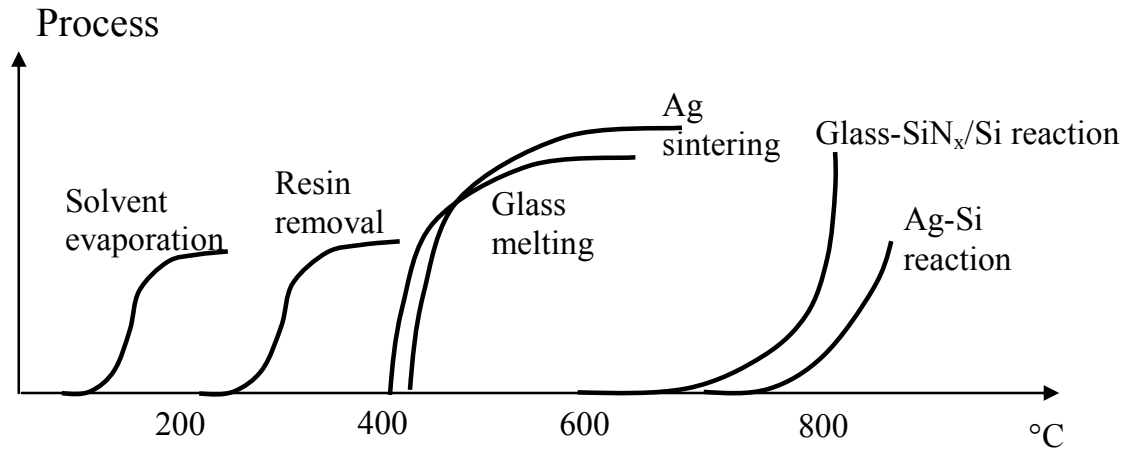


Figure 3.5. Processes occurring during the firing cycle.

### 3.1.3.6 The Glass Frit in the Thick-Film Paste

Successful thick-film metallization on Si solar cells requires forming a contact without penetrating the emitter too deeply; this is largely dependent on the glass frit used

in the paste. The reactive molten glass frit etches through the antireflection coating (ARC) and a very thin silicon surface layer. Upon cooling, the silicon that has been incorporated into the liquid state recrystallizes epitaxially. This recrystallized silicon layer under the contacts also influences the final solar cell parameters [57]. The etching of the silicon surface by the frit is a function of crystal orientation, firing temperature, and the percentage and composition of the glass frit.

A lower glass frit concentration is recommended in the Ag paste when used on multicrystalline Si material. This is because the glass frit etches grain boundaries more rapidly compared with single-crystal material. Grain boundaries have impurities that segregate during high-temperature processing. Pastes with a high glass frit content dissolve much of the Si and preferentially etch grain boundaries and defects, which have high impurity concentrations. These impurities enter the liquid phase and can degrade the junction region by causing junction shunting and recombination. Hence, lower frit content is desirable for multicrystalline silicon to reduce this effect. Also, for lower glass frit Ag pastes, higher-temperature firing is recommended to enhance the glass frit etching of the silicon. The etching of the silicon surface by the glass frit can also be controlled by the addition of modifiers, which can absorb a fraction of the molten glass, thus reducing the amount that is available for surface etching [57].

The glass frit in the Ag paste is the most important parameter for controlling the contact resistance, silicon surface etching, and the overall cell performance. The glass frit is required for good electrical and mechanical performance (adhesion and forming a bond in the thick-film). However, the type and amount of glass frit is responsible for open-

circuit voltage and fill factor degradation at higher paste firing temperatures. If a glass frit is too aggressive, molten glass alone can etch 3-4 μm Si [64].

The most important characteristic of molten glass is the viscosity. This is particularly important for screen-printed contacts, especially its behavior as a function of temperature. The viscosity ($\nu$) of glasses decreases rapidly and monotonically from $>10^{22}$ poise to $\sim 10^{2}$ poise with an increase in temperature from 300-1400° C [65]. The viscosity-temperature behavior of glasses has an Arrhenius form:

$$\nu = \nu_0 \exp\left(\Delta H / RT\right) \tag{3.2}$$

where $\nu_0$ is the pre-exponential constant, $R$ is the gas constant, $T$ the absolute temperature (Kelvin scale), and $\Delta H$ is the activation energy for viscous flow.

When discussing glasses, an important concept is the glass transition temperature ($T_g$), which is the temperature of the intersection between the curve of the glassy state and that of the super-cooled liquid (Fig. 3.6(a)) [66]. There are also four important viscosity reference temperature points [65]:

1- The working point temperature: the temperature where the glass viscosity is $10^4$ poise;

2- The softening point (Labino softening point): the temperature at a viscosity of $10^{7.6}$ poise. At this point the glass starts to flow by its own weight;

3- The annealing point: the temperature where the glass viscosity is $10^{13}$ poise. Stresses in the glass are relieved at this point within minutes;

4- The strain point: the temperature at which the glass viscosity is $10^{14.5}$ poise. Stresses that form in the glass are relieved at this point within hours.

The latter two points are in the lower half of the glass transition range (Fig. 3.6(b)). The glass softening point is actually the temperature point where the glass frit flows and adheres to the Si emitter.

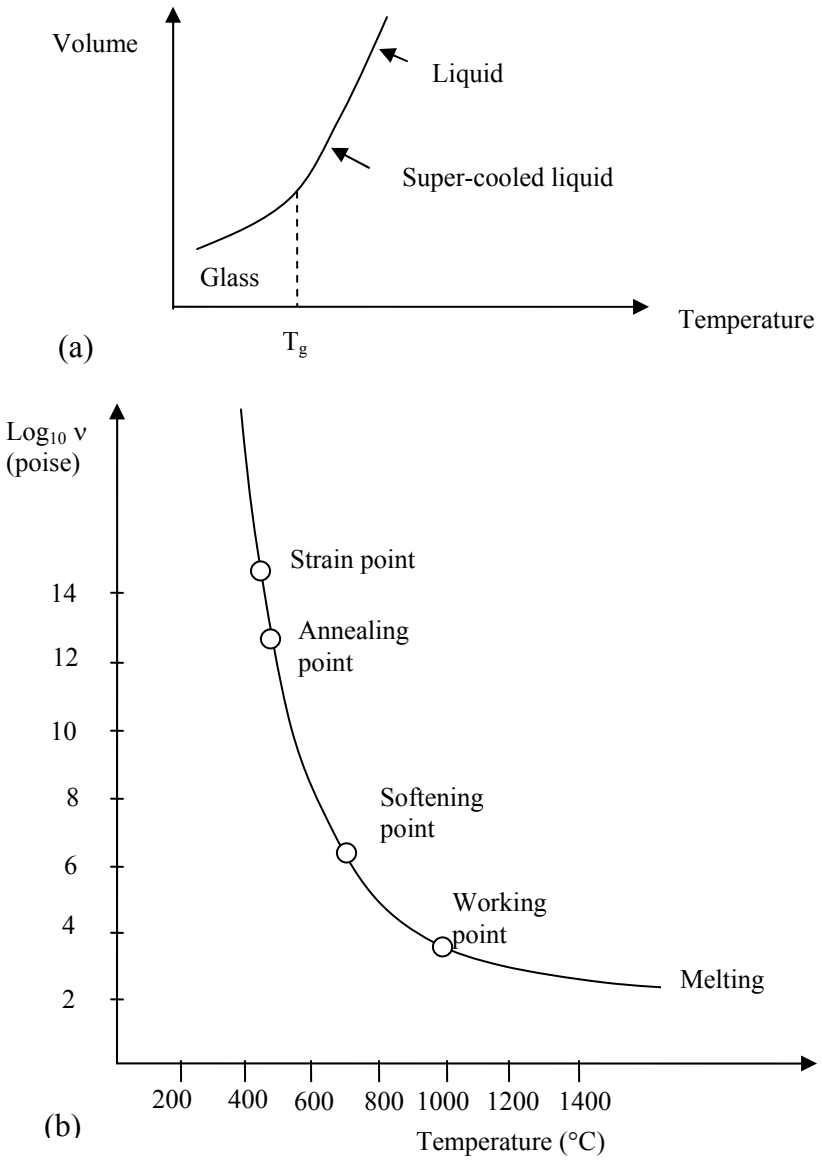


Figure 3.6. (a) A schematic of the specific volume-temperature relationship for glasses, (b) viscosity ν versus temperature for a silicate glass [65].

### 3.1.3.7 Sintering of Ag Particles in the Thick-Film Paste

After printing and drying, the metal particles are in intimate contact. As the temperature increases during the firing cycle, several forces lead to densification and compaction. This process is referred to as sintering. During the firing process, the changes that occur involve a change in the size and shape of particles or grains, change in pore shape, and changes in pore size. Both the size and shape of the pores change during the firing process, the pores becoming spherical in shape and smaller in size as the firing continues. The compact metal powder initially has between 25 and 60% porosity by volume [66]. For enhancing properties such as strength and thermal and electrical conductivity, it is desirable to eliminate as much porosity as possible. The fundamental sintering process leads to pore shrinkage and elimination (Fig. 3.7). The free-energy change that gives rise to densification is the decrease in the surface area and the lowering of the surface free energy by eliminating solid-vapor interfaces [66].

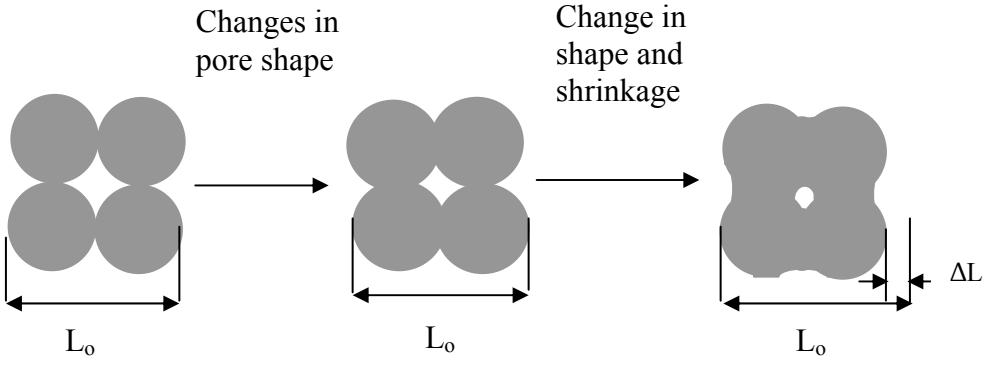


Figure 3.7. Changes in pore shape and shrinkage.

Material transfer is affected by pressure differences and changes in free energy across the curved surface. If the particle size or radius of curvature is small, these effects will have a significantly high magnitude [66].

The variables that affect the metal powder sintering are listed below [67]:

1- Temperature: Since the vapor pressure increases exponentially with temperature, the process of vapor phase sintering is strongly temperature dependent. Thus, increasing the temperature significantly increases the rate and magnitude of any changes occurring.

2- Particle size: All other factors being equal, a decreasing particle size or radius is a strong driving force for sintering, as it increases surface area and surface energy. However, it is also important to consider the distribution of powders when discussing the particle size effect. Models of sintering assume a homogeneous geometry. However, in real powder systems there is a distribution in particle size, number of contacts per particle, and contact flattening as a result of compaction. Generally, finer particle sizes will show faster neck growth and need less sintering time or lower sintering temperature to achieve a similar degree of sintering [68]. Larger particles will sinter more slowly and will require higher sintering temperatures or longer times.

3- Time: The degree of sintering increases with the increase in time; however, the effect is small compared to that of the temperature effect.

4- Particle shape, surface area, and topography: Changes that result in greater intimate physical contact among particles and increase in internal surface area promote sintering. These changes include increased surface roughness and decreased sphericity to increase the surface energy.

5- Particle composition and surfactant treatment: impurities at the metal powder surface may either increase or decrease sintering. Oxidation normally decreases

surface energy and decreases sintering. Also, variations in the sintering structure depend on the surfactant treatment type of the powders [69-72].

6- Packing efficiency (green density): The rate of sintering and the magnitude of changes resulting from it increase with decreasing packing efficiency because this signifies an increasing amount of internal surface area. However, the sintered density remains highest for the higher packing efficiency material.

During the sintering process there is a tendency for material transfer because of the differences in the surface curvature and therefore the differences in vapor pressure at different parts of the system [66]. Initially the particles are in point contact; however, as the temperature increases, necks are formed and the particles join (Fig. 3.8).

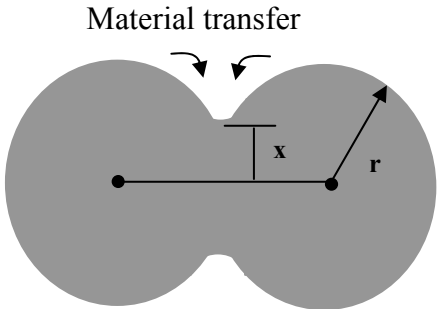


Figure 3.8. Initial stages of sintering by evaporation and condensation.

The relationship for the rate of growth of the bond area between particles is given as

$$\frac{x}{r}=\left(\frac{3\sqrt{\pi}\gamma M^{3/2}p_0}{\sqrt{2}R^{3/2}T^{3/2}d^2}\right)^{1/3} r^{-2/3}t^{1/3} \tag{3.3}$$

where $\gamma$ is the interfacial or surface free energy, $d$ is the theoretical density, $p_o$ is the vapor pressure, $M$ is the molecular weight of the material, $t$ is the time of sintering, $T$ is the absolute temperature, and $R$ is the gas constant.

Other than evaporation and condensation, there are several methods by which the transport can occur [73]:

1- Diffusion along the surface from regions of high surface energy to regions of low surface energy;
2- Diffusion of atoms via regions of disordered atomic structure such as grain boundaries;
3- Material transfer via vacancy diffusion, which involves the movement of vacant atomic sites in the crystal lattice of the metal, and hence the metal atoms diffuse in the opposite direction;
4- Sintering in the presence of fluid glass frit (Liquid phase): Material transfer takes place by solution in high-energy regions followed by precipitation in low- energy regions. Another method of material transfer is compound formation and decomposition at the particle surface.

In the absence of the liquid phase, at lower temperature firing transport takes place mainly via surface and grain boundary diffusion; however, as the temperature is increased, vacancy diffusion becomes the predominant mode [73]. For Si solar cell screen-printed contacts, sintering does not take place in the presence of metal particles only. The sintering takes place in the presence of a reactive liquid, which is the glass frit. Upon firing, the glass frit melts and forms a semi-continuous network of glass/metal

composites [73]. For densification to take place rapidly, it is important to have the following three conditions [58, 66]:

1- an appreciable amount of liquid phase,

2- wetting of the solid by the liquid,

3- an appreciable solubility of the solid in the liquid.

The driving force for densification is the capillary pressure of the liquid present between the fine solid particles. During this sintering process, the solid phase dissolves in the glass and is transported to the low-energy neck region where precipitation of the solid phase results in increased grain size and densification. The presence of glass frit has been shown to help increase the sintering rates of silver-palladium compositions [73]. However, it is important to control the viscosity of the glass frit for optimum densification; nevertheless, heating rates, peak firing temperature, and glass compositions are also critical for optimum densification [65].

## 3.2 History and Motivation for this Research

This section describes the current understanding of screen-printed (SP) contacts for solar cells in four areas: (a) screen-printed contact formation, (b) loss mechanisms associated with screen-printed contacts, (c) current transport in screen-printed contacts, and (d) rapid thermal firing of screen-printed contacts for solar cells. These areas are reviewed with the objective of defining and supporting the research goals outlined in Chapter 1.

### 3.2.1 Loss Mechanisms in Screen-Printed Contacts

The main drawbacks of the screen-printing technology for high-performance solar cells are summarized below:

1- Line width of screen-printed contacts is typically 125-150 μm wide, which gives rise to high shading losses.

2- Fill factors of screen-printed cells are generally low (~0.75) because of the higher contact resistance and lower metal conductivity of screen-printed contacts. The resistances that can contribute to the fill factor (FF) loss mechanisms associated with SP metallization are shown in Figure 3.9. The contact resistance and gridline resistivity both depend on the firing cycle and the properties of the inorganic constituents of the SP paste. For SP solar cells, the source of high series resistance is the Ag thick film/Si contact interface [74]. The junction leakage and shunting characteristics depend mainly on the emitter profile, firing cycle, and paste constituents.

3- An effective emitter surface passivation is practically difficult because a high emitter surface concentration is used to obtain reasonable specific contact resistance (≤ 3 mΩ-cm$^2$). This also results in a poor short-wavelength response because of the heavy doping effects and increased Auger recombination in the heavily doped emitter region.

As a result of the above factors, the efficiency of screen-printed cells is typically ~2% lower than that of cells with photolithography contacts [75]. Figure 3.10 shows the breakdown of these losses, which are divided into three categories: contact quality, short-wavelength response, and reflectance. The contact quality is inferior because of the high specific contact resistance, lower conductivity of the screen-printed Ag gridline bulk, and emitter sheet-resistance loss resulting from the wider grid spacing for the SP contacts. The short-wavelength response is low because of the higher front-surface recombination velocity and heavy doping effects in the heavily doped emitter compared to the lightly doped emitters used for PL cells. Finally, higher reflectance losses are mainly due to the high shading from the wider SP grid. Laboratory PL cells are also fabricated with a double- layer antireflection coating (ARC), typically $MgF_2$/ZnS, which gives about 0.3% enhancement in absolute efficiency compared to single-layer silicon nitride coated cell in production. Table 3.1 shows a comparison of contact quality and parameters for the PL, BC, and SP cells.

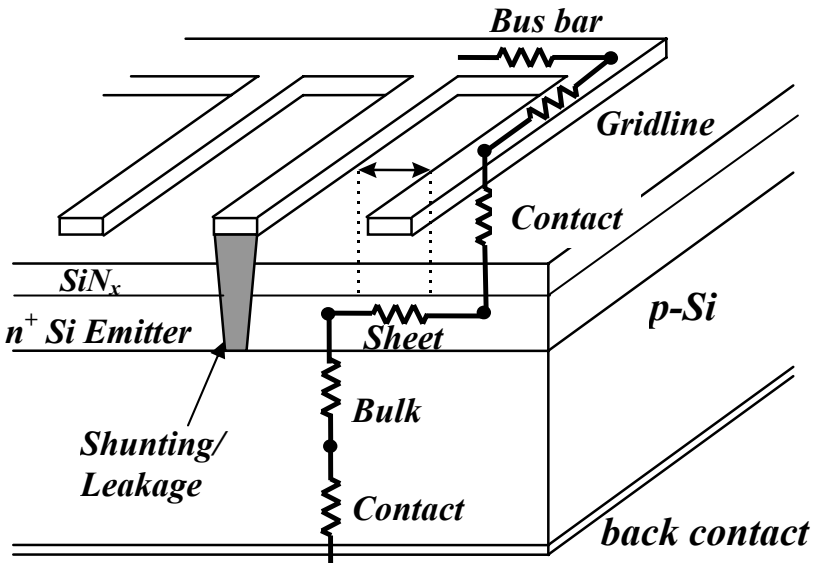


Figure 3.9. Si solar cell cross-section diagram showing FF loss mechanisms [74].

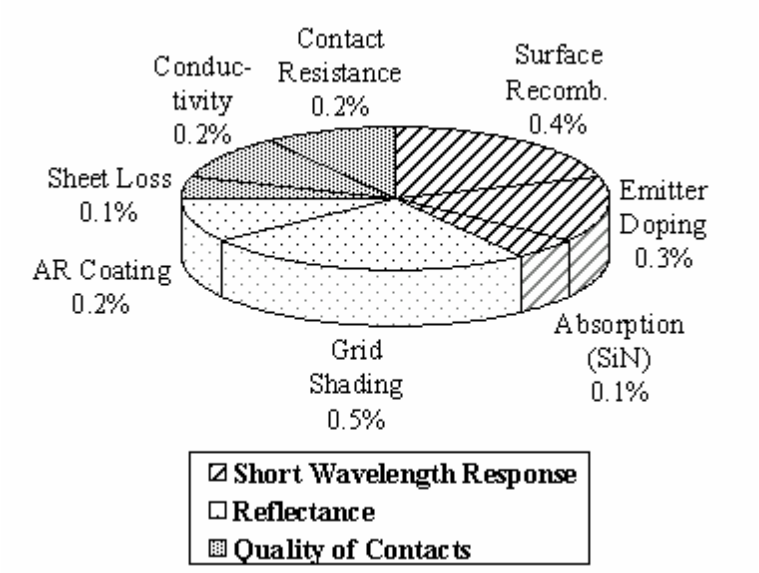


Figure 3.10. Loss mechanisms that account for the 2% efficiency difference between screen-printed and photolithography cells [75].

Table 3.1: Comparison of SP, BC, and PL contacts.

| Parameter | SP Cell | BC cell | PL cell |
|---|---|---|---|
| finger thickness | 14 μm | 50 μm | 8 μm |
| finger width | 100-135 μm | 20 μm | 20 μm |
| specific contact-resistance | 0.3-3 mΩ-cm$^2$ | 3-6 μΩ-cm$^2$ | 0.01 mΩ-cm$^2$ |
| metal resistivity | 3 μΩ-cm | 1.7 μΩ-cm | 1.7 μΩ-cm |
| Fill Factor | 0.75-0.77 | 0.78-0.79 | 0.81-0.82 |

The inferior quality of screen-printed contacts compared to buried-contact and photolithography contacts provided the motivation to improve the screen-printed contact quality and reduce the gap between screen-printed and buried-contact and photolithography cells. This is done in this thesis through fundamental and applied research involving the understanding of the loss mechanisms, role of paste chemistry, firing cycle, and impact of emitter sheet-resistance and doping profile. The next sub-section illustrates the current understanding of screen-printed contact formation and the metallurgical reasons why it may have inferior current transport compared to photolithography and buried contacts.

## 3.2.2 Current Understanding of the Contact Formation and Current Transport in the Screen-Printed Contacts

### 3.2.2.1 Contact Formation Mechanism

During solar cell processing, a Ag grid is generally screen printed on top of the $SiN_x$ antireflection coating and fired through the $SiN_x$ film onto the emitter surface. The contact formation occurs when the screen-printed thick film experiences elevated temperatures (>650° C) during the firing process. Upon heating, the glass frit fluidizes and wets the $SiN_x$ surface, dissolving the silver and etching the silicon nitride [64, 76]. The etching of $SiN_x$ takes place by a redox reaction, $xSi+2MO_{x,glass} \rightarrow xSiO_2+2M$ [77],

where *M* is the metal in the glass frit. This behavior has been supported by the presence of metal precipitates observed in the glass after firing [78, 79]. Figure 3.11 shows an SEM/EDS image demonstrating the presence of lead precipitates in the glass after firing. Subsequently, the glass frit also etches or dissolves a small amount of the Si surface. This has been demonstrated by Schubert et al. in Fig. 3.12, where significant Si etching was observed by a paste which contained only glass frit with no Ag. Upon cooling, the excess Si contained in the glass frit crystallizes epitaxially on the substrate [57]. This mechanism is shown in Figure 3.13. However, this model has not been validated experimentally; dissolved Si could alternatively become oxidized and precipitate in the glass layer. Excess Ag in the molten glass re-crystallizes epitaxially at the Si surface in the shape of inverted pyramid-like Ag crystallites [80].

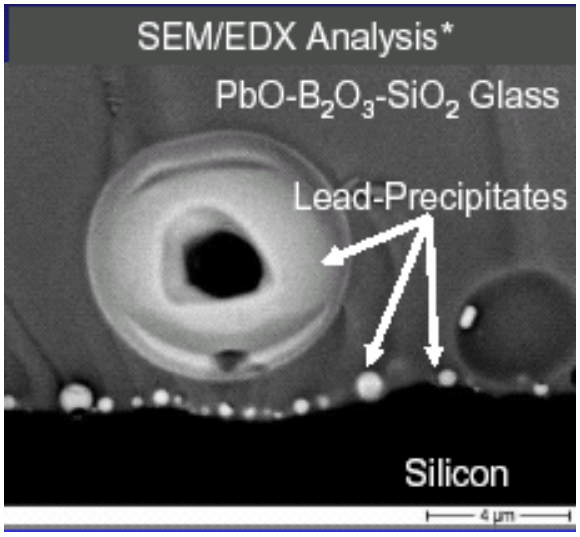


Figure 3.11. Presence of lead precipitates in the fired glassy layer [79].

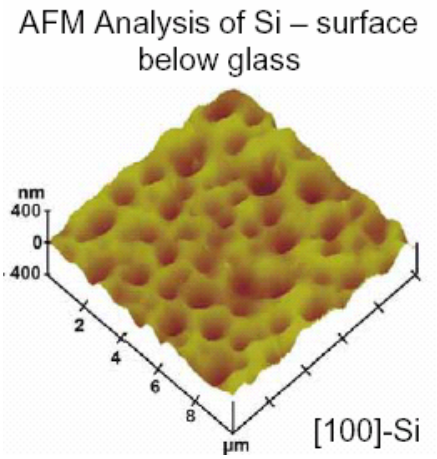


Figure 3.12. AFM image showing etched Si surface by the glass frit only [17].

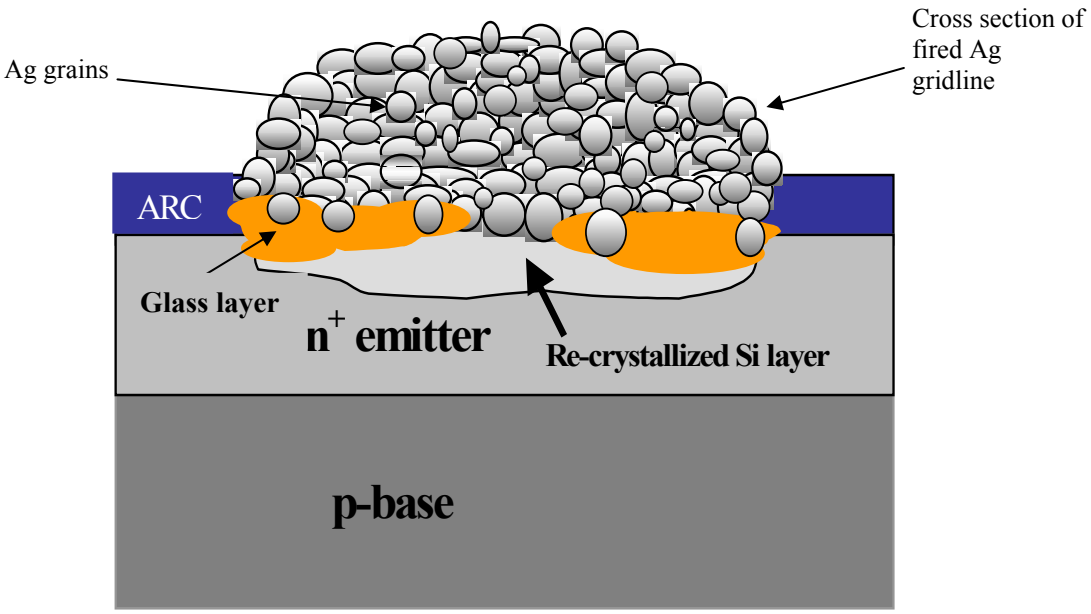


Figure 3.13. Re-crystallization of Si upon cooling.

A model for contact formation has been proposed in the literature [81]. Five steps in Figure 3.14 pictorially summarize this model for the contact formation. Figure 3.14(a) shows that the screen-printed Ag gridline contains the inorganic constituents (Ag particles, glass frit, and modifiers). Figure 3.14(b) shows that, upon heating, the glass frit

starts to melt at temperatures >450° C. The glass frit wets the surface and then starts to etch or react with the $SiN_x$ layer underneath (Fig. 3.14(c)). In addition, the Ag particles begin to sinter and dissolve in the glass frit. Once the glass frit etches through the $SiN_x$ film, it starts to etch or dissolve the Si surface underneath the $SiN_x$ at temperatures ~670-700° C. (Fig. 3.14(d)). Upon cooling, the excess Si in the glass frit crystallizes epitaxially, and some of the dissolved Ag in the frit precipitates as Ag crystallites, which get embedded into the Si surface at the Ag-Si interface, forming a direct contact with the Si emitter to provide a path or interconnection for current transport [78] (Fig. 3.14(e)). Finally, lead and possibly other metals also precipitate in the glass layer.

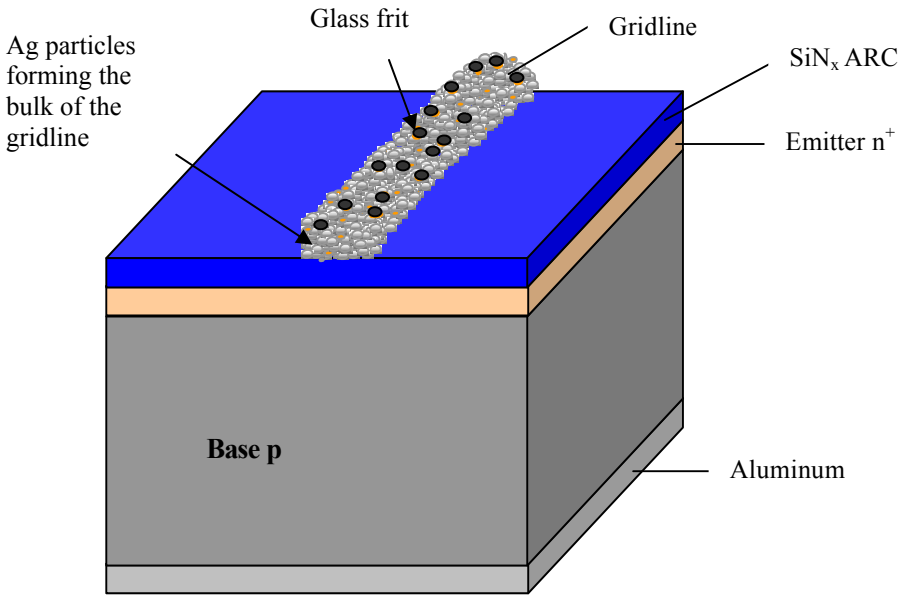


(a) Screen-printed Ag gridline.

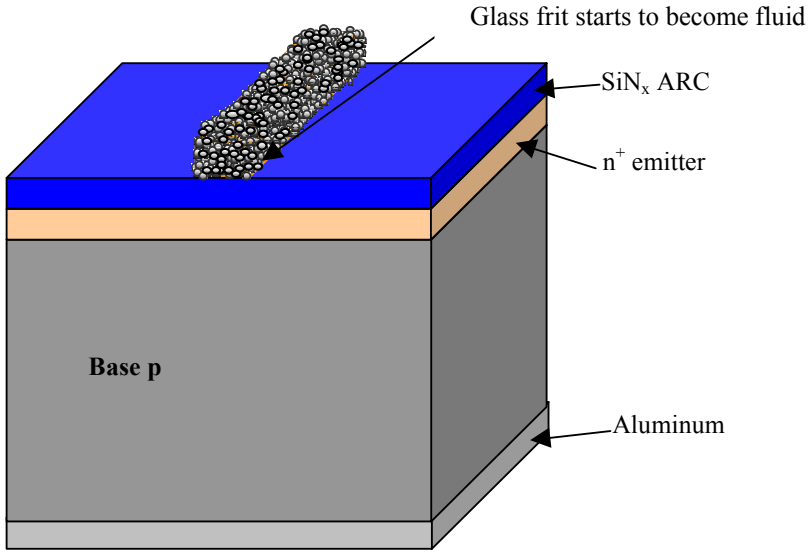


(b) Glass frit starts to become fluid upon heating during the contact firing process.

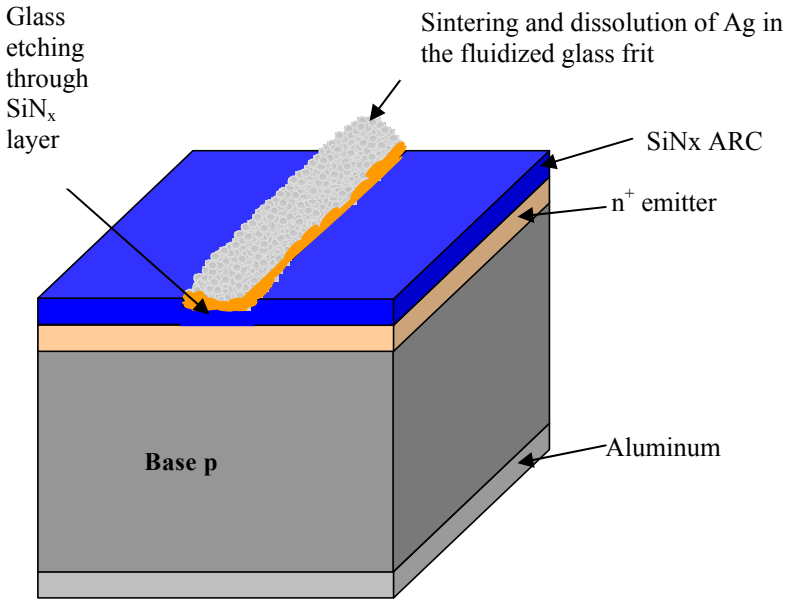


(c) Etching of $SiN_x$ layer by the glass frit and sintering of Ag.

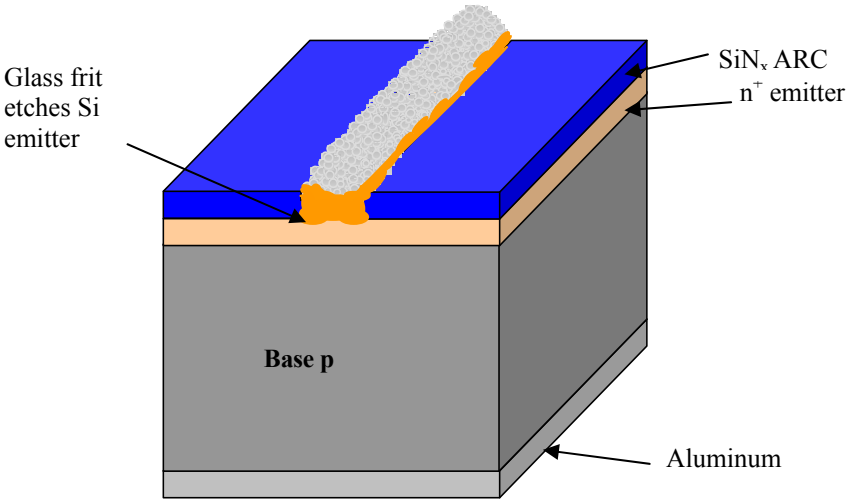


(d) Etching of the Si emitter by the glass frit.

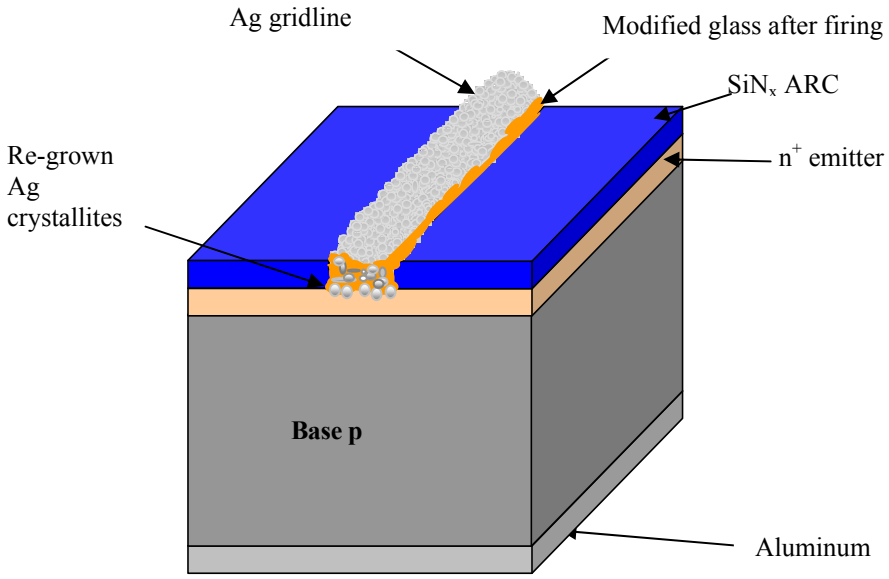


(e) Re-growth of Ag crystallites through the glass layer.

Figure 3.14. Screen-printed contact formation.

High series resistance is often a problem with screen-printed contacts on solar cells. This is because glass within the Ag paste flows preferentially toward the Ag-Si interface during firing. This creates a glass barrier between the Ag contact and the Si, causing it to be a region of high series resistance in the solar cell [82]. The glassy layer is very continuous and hence the area fraction where Ag grid directly contacts Si is a very small compared to the full area of grid metallization. Low-resistivity contacts can be obtained when the glass does not have sufficient time to flow and collect at the interface during a very short infrared (IR) firing cycle. This would leave a greater number of silver particles at the silicon surface across the entire contact. However, the smaller amount of glass at the interface can cause the IR-fired contacts to have adhesion problems. Even though these ideas are known, no systematic study has been conducted in the literature about controlling or improving the contact interface by tailoring the paste constituents and firing cycle. This provided the motivation in this research to study the role of particle size and glass transition temperatures in tailoring the thickness of the glass layer and size and distribution of Ag crystallites. In addition, special emphasis is placed on rapid thermal firing to constrain the flow of the glass layer to obtain thin regions of glass layers in between Ag crysallites and the Ag grid to promote tunneling.

#### 3.2.2.2 Current Transport Mechanisms

Current transport through the SP contacts is very complex and poorly understood at this time. Several models have been proposed regarding the current transport mechanism for screen-printed contacts to the Si emitter. Higher series resistance is generally observed for screen-printed contacts compared to evaporated or plated contacts for solar cells because glass acts as a resistive barrier between the Ag grid and the Si.

Firor et al. in 1982 first proposed that the current transport occurs via direct Ag-Si interconnections (Fig. 3.15(a)) [82]. However, in 1983 Nakajima et al. observed that annealing of the fired screen-printed contacts in hydrogen reduced the contact resistance of the solar cell [83]. He therefore proposed that the current transport occurs not by direct connection but via tunneling through the fired glass layer between the Ag bulk (grid) and the underlying Si emitter (Fig. 3.15(b)).

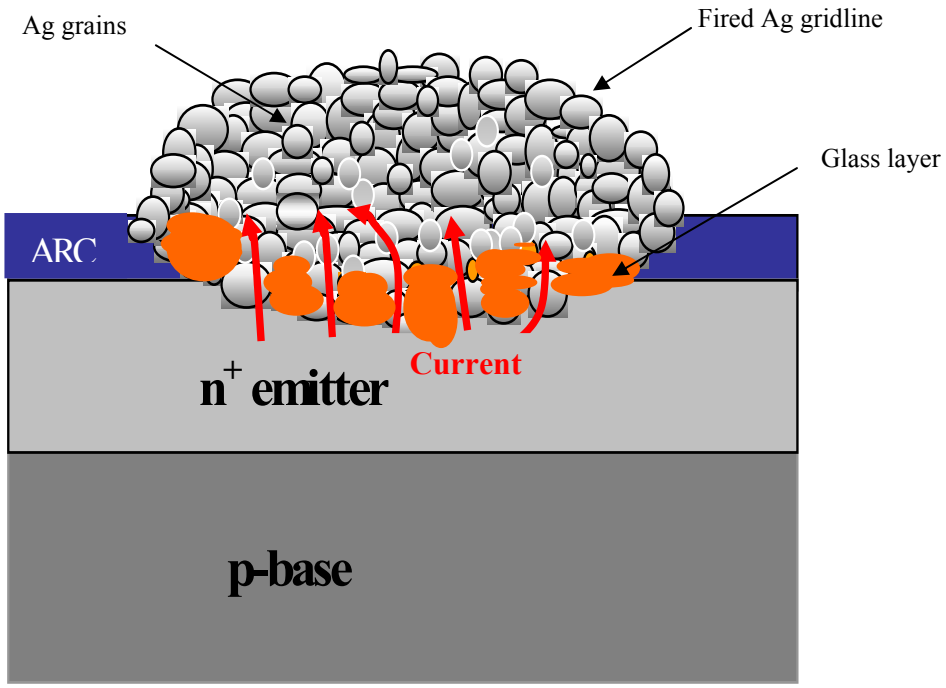


(a) Current transports via direct connection to the bulk of the gridline.

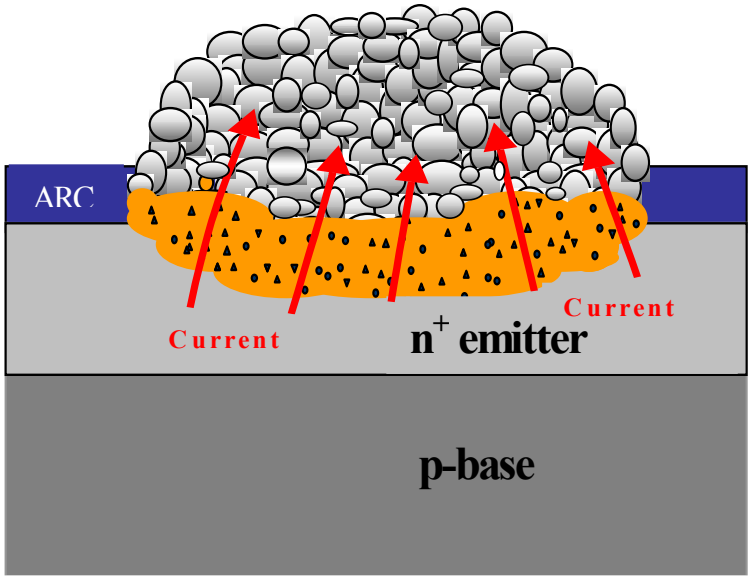


(b) Current transport via tunneling through the glassy layer.

Figure 3.15. Current transport mechanism in screen-printed contacts.

It has been recently shown by transmission electron microscopy that the Si-Ag interface of a fired commercial Ag paste is composed of 200-500 nm-diameter Ag crystallites penetrating the Si by up to 130 nm [80]. These crystallites are surrounded by a quasi-continuous layer of modified glass. A transfer of Ag through a glassy interface has been reported by Schubert et al. [79]. Using conductive cross-sectional atomic-force microscopy (AFM), the contact resistivity between the Ag crystallites and the Si emitter was measured to be ~$2\times10^{-7}$ Ω-cm$^2$ on average, which is low compared to the typical macroscopic value of contact resistance of $10^{-3}$ Ω-cm$^2$ for the whole contact [78]. The interface crystallites are covered by several tens of nanometers of glass frit. This glass frit layer (lead borosilicate glass) has resistivities higher than $10^9$ Ω-cm, which is too high for any conduction through the glass to take place. Thus, he proposed that only a limited fraction of the interface crystallites contributes to the current flow out of the emitter. The conduction thus takes place at isolated spots by two possible mechanisms: (1) by direct

metal silicon contact or (2) through ultra-thin regions of a glassy layer via tunneling, with the latter being the more likely situation. Figure 3.16 shows an SEM image of an actual screen-printed and fired Ag contact with glass frit. The glass frit covers a large area at the Ag-Si interface and around the Ag crystallites. Figure 3.17 shows a TEM image of actual screen-printed and fired Ag contact with glass frit. The glass frit covers a large area at the Ag-Si interface, and around the Ag grains and metal precipitates are observed in the glass. A schematic of the cross-section of the fired screen-printed contact is shown in Figure 3.18 along with the possible current transport mechanisms. There is still a considerable lack of understanding of the contact mechanism and current flow in the screen-printed contacts. This provided the motivation to study and correlate the contact interface structure to contact resistance and electrical properties of the contact. In this thesis, the contact interface was varied by altering the paste chemistry and firing conditions, and physical and electrical properties were correlated by a combination of structural and electrical measurements.

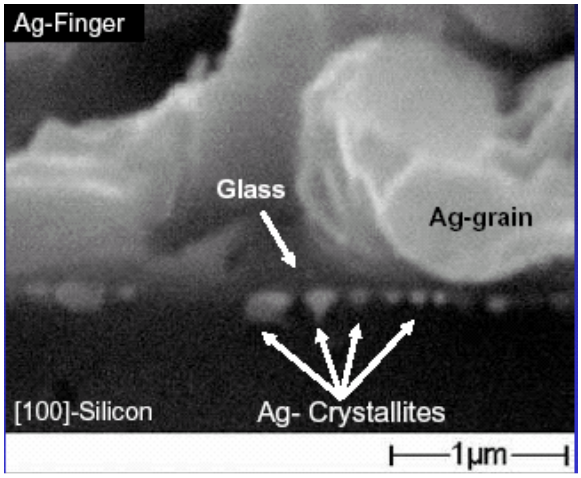


Figure 3.16. Ag crystallites re-grown at the interface [17].

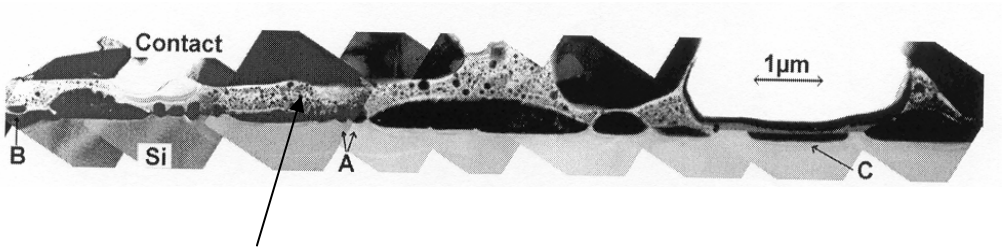


Figure 3.17. TEM cross-section image of the screen-printed contact interface: A, B, and C are regions of re-grown Ag crystallites [80].

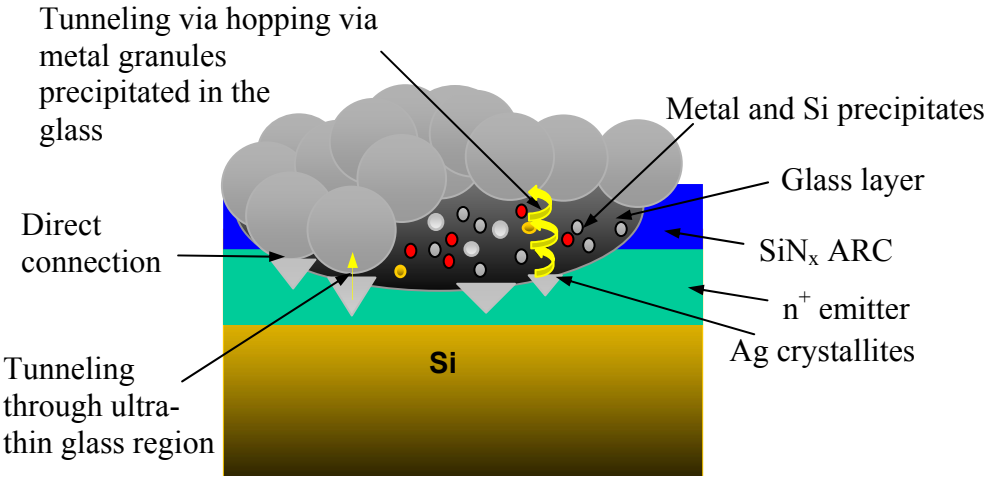


Figure 3.18. Fired screen-printed contact cross-section interface structure showing the possible current transport mechanisms.

### 3.2.3 Rapid Thermal Processing of Screen-Printed Si Solar Cells

Rapid thermal processing (RTP) is used extensively in the microelectronics industry to minimize the thermal budget that a wafer experiences during processing. RTP is also used in this research in conjunction with screen-printed contacts. In RTP, processing times are kept very short, and extremely steep temperature ramps are used to avoid unwanted diffusion or oxidation. RTP processing has been investigated in the past few years for Si solar cells. RTP has been successfully demonstrated for industrial-sized

Si solar cells along with screen-printed metallization. A simple process involving rapid-thermal diffusion and oxidation (each <1 min long) with screen-printed front and rear contacts fired in an RTP furnace resulted in 16% efficient 100 $cm^2$ Cz-Si cells [84]. Large-area RTP cells with efficiency of 15.6% have been made on multicrystalline Si (mc-Si) [85]. Screen-printed contacts require deeper emitters (>0.3 μm) than laboratory RTP solar cells to prevent shunting and a high surface concentration of P (>$10^{20}$ $cm^{-3}$) to achieve low contact resistance. A throughput of >1,200 wafers/hr is required for all processing steps to meet production line requirements, and hence conventional RTP systems that are designed for single-wafer processing will not meet these requirements. Therefore, continuous RTP systems or belt furnaces have to be designed for the industrial production of Si solar cells. Some manufacturers are currently attempting that [86]. Figure 3.19 illustrates a conventional belt-line furnace. A novel open quartz diffusion system, which combines the advantages of continuous processing of a belt furnace and the cleanliness of closed quartz tube furnaces, is being commercialized [87].

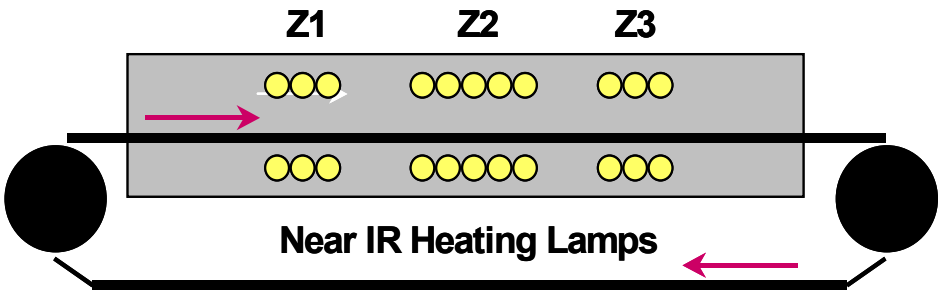


Figure 3.19. Belt-furnace processing.

It has been shown that fast ramp-up rates (≥50 °C/s) in RTP produce a good quality, uniform screen-printed Al back-surface field (BSF) [88, 89]. Rapid thermal

processing has also been shown to be effective in lifetime and cell efficiency enhancement in low-cost materials because the rapid firing and fast cooling rates enhance the $SiN_x$ induced hydrogen passivation of defects [90].

This provided the motivation to explore screen-printed contacts formed by rapid belt speeds in conventional belt furnaces. A systematic study is conducted to see how the belt speed influences not only the contact quality, but also the contact interface structure, including the glass layer thickness, Ag crystallite size and shape, etc.

### 3.2.4 Screen-Printed Selective-Emitter Cells and Technologies

Figure 1.5 in Chapter 1 showed that a 0.7% loss in absolute efficiency can be eliminated by using high sheet-resistance emitters (100 Ω/sq instead of 45 Ω/sq) because of the removal of heavy doping effects in the emitter and improved front-surface recombination technology. This can be done either by making selective emitters or by forming direct screen-printed contacts to the high sheet-resistance emitter.

#### 3.2.4.1 Selective-Emitter Cells Fabricated by Masking and Etching

A selective emitter involves two different doping levels, with higher doping (≤40 Ω/sq) underneath the grid to achieve good ohmic contact and low doping between the grid to minimize the heavy doping effect in the emitter. Many different attempts have been made to fabricate selective-emitter solar cells using industrial processes and materials. One technique involves the fabrication of a selective emitter on low-cost polycrystalline silicon by applying a wet etch-back of a heavily doped emitter in the cell area between the gridline fingers. A screen-printed polymeric paste protects the metal fingers during etch-back. The advantages of this process include the use of a full screen-

printing technology, phosphorus gettering, and self-alignment. It has been shown that this process can provide improvements of 17 mV in $V_{oc}$, 1.5 mA/cm$^2$ in $J_{sc}$ and 1% absolute in efficiency [91]. Another selective-emitter process involves a screen-printed mask after a deep diffusion step (16 Ω/sq), followed by surface texturing combined with etch-back of the emitter [92]. The mask is then removed and a second shallow diffusion is formed (80 Ω/sq) by screen-printing phosphorus paste. This is followed by surface oxidation for passivation purposes, ARC deposition, and metal gridline printing and firing. It is crucial to align the front gridline pattern to the area with the deep emitter without surface texturing. This is achieved with a screen printer with optical alignment. Using a similar principle, another selective-emitter process with a plasma-etch-back technique was developed. In this case, standard commercial screen-printed gridlines are used as a mask for the plasma etch-back of the emitter [93]. A PECVD $Si_3N_4$ layer is subsequently deposited for AR coating and good surface and bulk passivation. This process was applied on mc-Si material and a 5% absolute increase in cell efficiency was reported. Similarly, selective-emitter cells have been fabricated on multicrystalline Si using the front metal contacts themselves as masks during hydrogen plasma etches [94]. The plasma also provides diffusion of hydrogen (hydrogenation) while etching, which increases bulk lifetime.

#### 3.2.4.2 Selective-Emitter Cells Fabricated using Self Alignment without Masking and Etching

In 1997, for the first time, a process was introduced that could form the selective emitter with only one diffusion step and without additional etching or masking steps [95]. This process involves the selective printing of a phosphorus paste as the front gridline

pattern followed by the diffusion process. During the diffusion the P heavily dopes the printed regions, while a shallow high sheet-resistance emitter is formed between the gridlines via auto-doping of the P atoms that are present in the surrounding gas atmosphere as a result of the printed P grid (Fig. 3.20). An ARC layer is deposited ($Si_3N_4$ or $TiO_2$) next. Finally, the front-contact metallization is aligned to the P printed pattern and the front and back contacts are co-fired through the dielectric layer. A similar process has been used to realize selective-emitter structures by selective diffusion from a SP P-dopant paste fired in an RTP system [96].

The above processes are time consuming and require several steps or the use of alignment to form the selective emitter. This emphasizes the need to investigate novel techniques for fabricating selective emitter structures or to find ways to make good ohmic contacts to high sheet-resistance emitters.

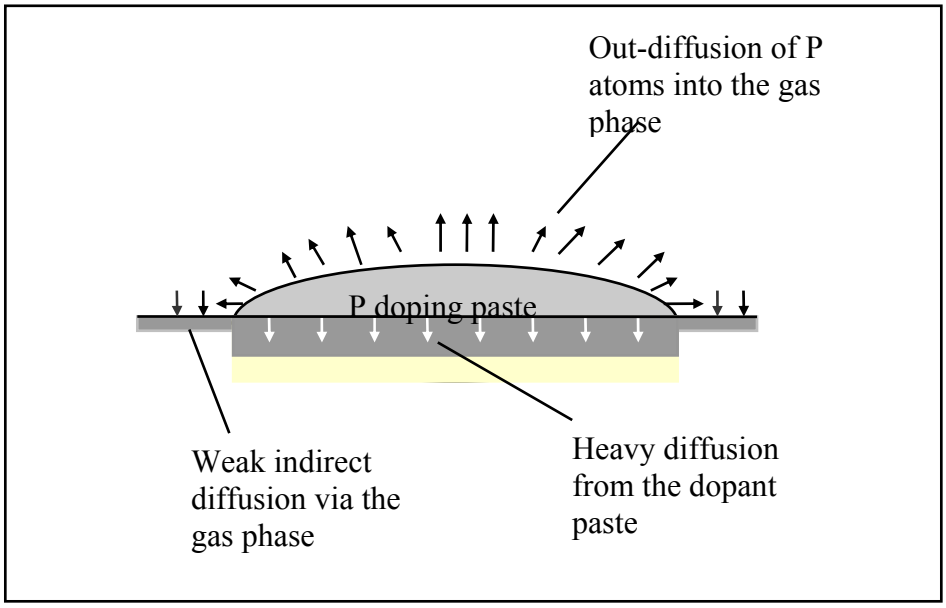


Figure 3.20. Screen-printed selective-emitter cells using alignment.

### 3.2.4.3 Selective-Emitter Cells Fabricated using Self-Aligned Self-Doping Ag Paste

This technique involves silver that is coated with a layer of dopant and alloyed with silicon. Hence, using this technique, the underlying Si is doped and a low-resistance ohmic contact is formed simultaneously [97]. This concept has been verified by using evaporated Ag with commercially available phosphorus and boron liquid dopants. It was found that the processing temperature should exceed the Ag-Si eutectic temperature of 835° C. This contact system was also implemented using fritless screen-printing Ag paste with self-doping P. It is also possible using a Ag paste with integral P and with a frit to punch through the SiN ARC in a belt furnace to contact $n^+$ layers of up to 100 Ω/sq. Such a contact system is applicable to conventional cell structures like selective emitters and to more complex structures such as interdigitated-back-contact solar cells [98].

As reported in [17] there are two possible routes to achieve good-quality ohmic contacts on lightly doped emitters. First is through self-doping techniques [99] and the second is via optimization of the Ag paste and firing to achieve good ohmic contact directly to a 100 Ω/sq emitter. Since the diffusivity of Ag [100] is greater than that of P [101], the self-doping technique like the one discussed in this subsection involves the risk of junction shunting or introducing an excessive amount of Ag into the emitter region for a longer firing time, which could degrade the open-circuit voltage. Initially the path taken for this thesis research was to employ self-doping pastes; however, it was found that the performance of the p-type FZ cells was limited to 75-80 Ω/sq emitters with low fill factors of ≤0.765. This motivated the research task in this thesis involving the

optimization of firing as well as Ag paste inorganic constituents to achieve good screen-printed ohmic contacts directly to high sheet-resistance (100 Ω/sq) emitters.

# CHAPTER 4

# MODELING THE INFLUENCE OF SOLAR CELL PARAMETERS ON PERFORMANCE ENHANCEMENT FROM THE HIGH SHEET-RESISTANCE EMITTER

## 4.1 Introduction

This section involves computer modeling and quantitative investigation of the criteria for cell design to maximize the effectiveness of the high sheet-resistance emitter in improving cell performance. This is because bulk lifetime, base resistivity, and front and back-surface recombination velocities can influence the relative improvement from incorporating the high sheet-resistance emitter. If the cell design is not appropriate, the high sheet-resistance emitter can actually degrade cell efficiency. Therefore, it is important to know the cell design criteria before implementing the high sheet-resistance emitter for performance enhancement. The PC1D device-modeling program [102] is used to calculate the performance enhancement from the high sheet-resistance emitter for various cell designs. Table 4.1 shows the key material and device inputs used in the PC1D for these calculations. It is important to note that PC1D is a one-dimensional model; therefore, it can only be used to model the emitter with homogeneous sheet-resistance with a constant FSRV. A low minority-carrier lifetime of 30 μs, as opposed to >100 μs, was intentionally used in these initial calculations to assess the potential for efficiency improvement for widely used low-cost low-lifetime silicon substrates.

Modeled efficiencies are therefore lower than what they would be for a high-quality single-crystal FZ Si cell where minority-carrier bulk lifetime is generally in excess of 200 μs. In the simulations, the contact quality is assumed to be the same for both high (~100 Ω/sq) and low (40-45 Ω/sq) sheet-resistance emitters, i.e., the series resistance ($R_s$), shunt resistance ($R_{sh}$), and junction leakage current ($J_{o2}$) are assumed to be the same for both emitters, which will be shown to be nearly true experimentally in later chapters.

Table 4.1: Modeling parameters for the $n^+$-p-$p^+$ solar cells.

| Device Parameter | | PC1D Input |
|---|---|---|
| Thickness | | 300 μm |
| Resistivity | | 1.3 Ω-cm |
| BSRV | | 1000 cm/s |
| FSRV | 40 Ω/sq.-conventional cell | 200 000 cm/s |
| | 110 Ω/sq.-selective emitter | 7000 cm/s |
| Series Resistance | | 0.6 Ω-cm$^2$ |
| Shunt Resistance | | 3333 Ω-cm$^2$ |
| $J_{02}$ | | 5 nA/cm$^2$ |
| $n_2$ | | 2.1 |
| Front Surface Reflectance | | Single Layer ARC: t = 790 Å, n = 2.0 |
| Grid Shadowing | | 5% |
| Texturing | | None |
| Rear Internal Reflectance | | 45 % Diffuse |
| Lifetime (τ) | | 30 μs |

## 4.2 Device Modeling Results

### 4.2.1 Effect of Base Resistivity on Performance Enhancement Resulting from the High Sheet-Resistance Emitter

The model calculations in Figure 4.1 show the improvements in $V_{oc}$ and in the short-circuit current ($J_{sc}$) from the lightly doped emitter, relative to a conventional 40 Ω/sq emitter cell, as a function of base resistivity. Absolute efficiency for the 110 Ω/sq

emitter cell as a function of base resistivity is also shown. Lifetime is assumed to be independent of resistivity in these calculations. It is important to note that in these calculations, the back-surface recombination velocity (BSRV) was reduced appropriately for the higher resistivity Si because of the increase in the doping step height ($N_A^+/N_A$) of the high-low junction. Figure 4.2 shows that for a 30 μs lifetime and 1.3 Ω-cm resistivity material, used in most current industrial cells, a high sheet-resistance emitter of 110 Ω/sq can produce ~0.7% increase in absolute efficiency. A high sheet-resistance emitter (110 Ω/sq instead of 40 Ω/sq) increases the cell efficiency from 15.8% to 16.5% for cell design inputs shown in Table 4.1. Figure 4.3 indicates that the modeled internal quantum-efficiency (IQE) shows an appreciable enhancement in the short-wavelength response, which also supports the expected increase in the short-circuit current ($\Delta J_{sc}$) from the high sheet-resistance emitter.

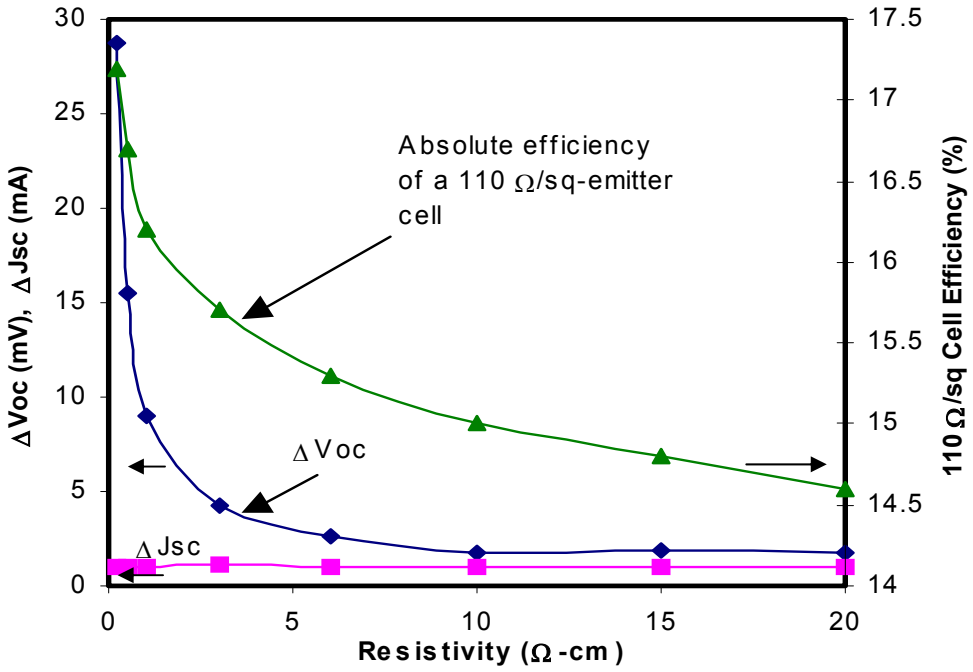


Figure 4.1. The absolute efficiency of a high sheet-resistance emitter solar cell and the change in open-circuit voltage and short-circuit current (relative to a 40 Ω/sq emitter cell) as a function of base resistivity.

Figure 4.2 shows that for base resistivities of less than 1 Ω-cm, the improvement in efficiency (Δη) resulting from the high sheet-resistance emitter is very rapid. For resistivities between 1 Ω-cm and 10 Ω-cm, there is almost a linear improvement in efficiency with the decrease in resistivity. However, for resistivities greater than 10 Ω-cm, the efficiency improvement saturates at 0.4% absolute (for the 30 μs bulk lifetime case).

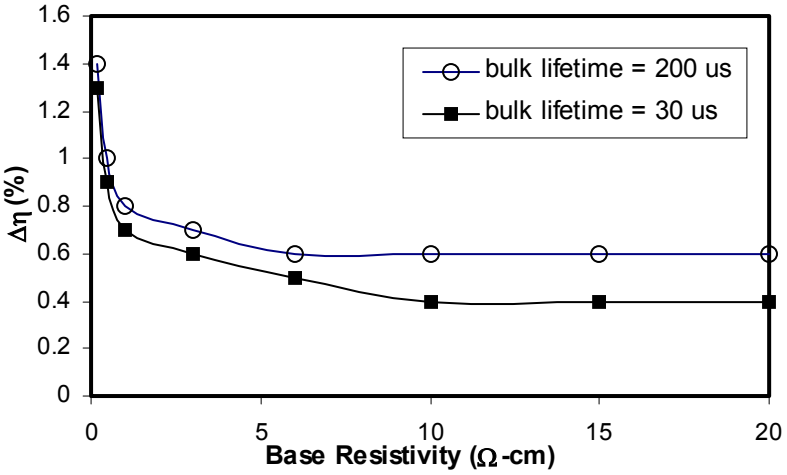


Figure 4.2. Improvement in cell efficiency resulting from the high sheet-resistance emitter relative to the conventional 40 Ω/sq emitter.

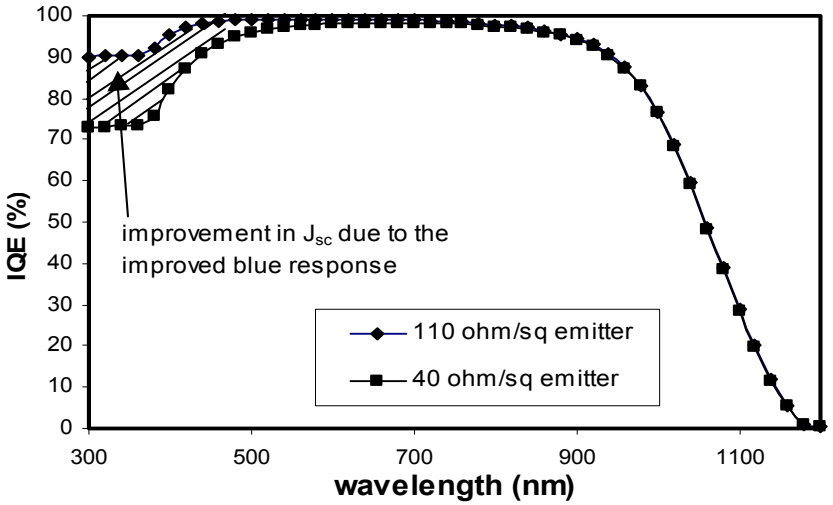


Figure 4.3. PC1D-modeled IQE plots for high- and low-sheet-resistance emitters.

The efficiency enhancement starts to saturate starting at lower base resistivities (6 Ω-cm) for the higher bulk lifetime case. This is because the effect of the base recombination starts to become more dominant for higher minority-carrier diffusion lengths, where minority carriers become more sensitive to the recombination in the base. The emitter and base saturation current densities ($J_{oe}$ and $J_{ob}$, respectively) in Figure 4.4 reveal that above 10 Ω-cm resistivity, $J_o$ ($=J_{oe}+J_{ob}$) is dominated by $J_{ob}$, which is the same for both high and low sheet-resistance emitters cells. Therefore, $J_o$, $V_{oc}$, and efficiency do not change with base resistivity, and the efficiency enhancement becomes saturated and limited only by the increase in short-circuit current ($J_{sc}$) due to the reduced Auger recombination in the emitter.

Model calculations were extended further to extract the emitter and base component of the saturation current density, i.e., $J_{oe}$ and $J_{ob}$. Figure 4.4 shows that above 10 Ω-cm resistivity, $J_{ob}$ is much greater than the $J_{oe}$ of the high and low sheet-resistance emitter. Therefore, the open-circuit voltages of both cells are virtually identical. As we lower the base resistivity below 10 Ω-cm, $J_{ob}$ decreases. Since the $J_{oe}$ of the 40 Ω/sq emitter cell is higher than that of the 110 Ω/sq emitter cell and is not negligible relative to the $J_{ob}$, $J_o = J_{oe} + J_{ob}$ of the conventional cells becomes higher, while the $J_o$ of the high sheet-resistance-emitter cell remains $\approx J_{ob}$. As a result, the efficiency enhancement resulting from the high sheet-resistance emitter rises as we decrease the resistivity below 10 Ωcm (Fig. 4.2). It should be noted that the bulk lifetime was maintained at 30 μs for all resistivities in these calculations.

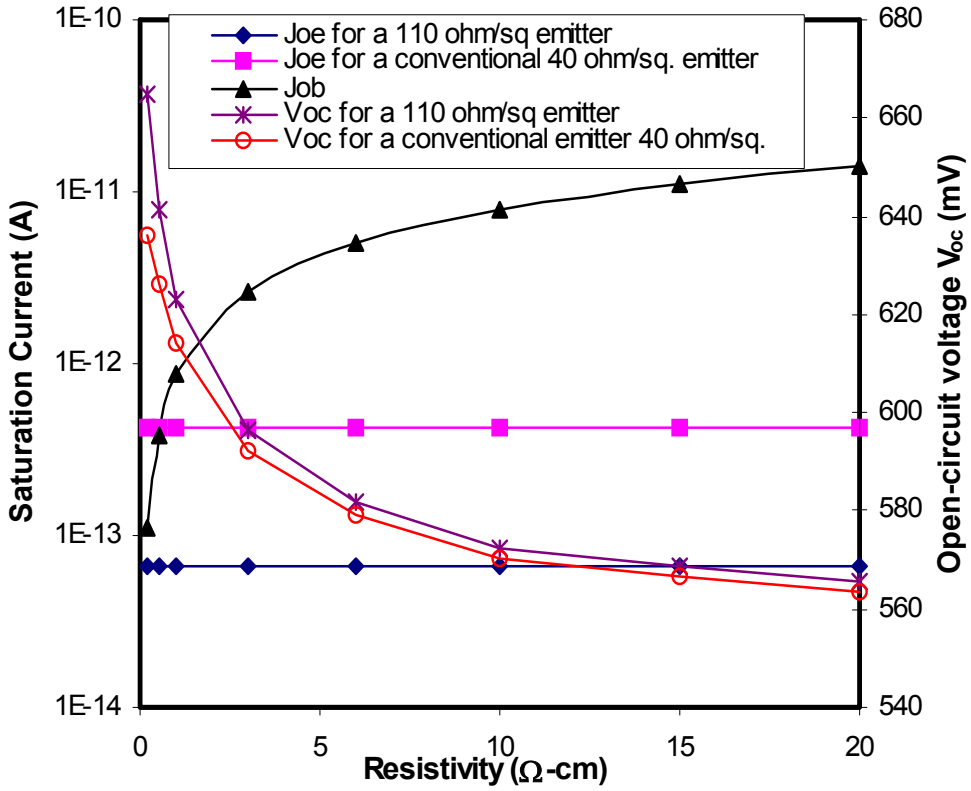


Figure 4.4. Plots of the leakage currents ($J_{oe}$ and $J_{ob}$) and open-circuit voltage ($V_{oc}$) for the high and low sheet-resistance emitters.

### 4.2.2 Effect of Front-Surface Passivation on Performance Enhancement Resulting from the High Sheet-Resistance Emitter

The model calculations in Figure 4.5 show that the front-surface recombination velocity (FSRV) is also very critical in realizing the full benefit of the high sheet-resistance emitter. In these calculations, bulk lifetime, BSRV, and base resistivity were fixed at 30 μs, 1,000 cm/s, and 1.3 Ω-cm, respectively. The FSRV of the conventional cell was fixed at 200,000 cm/s, while the FSRV for the 110 Ω/sq emitter cell was varied from $10^3$-$10^6$ cm/s. The calculations indicate that for an FSRV greater than 120,000 cm/s, the high sheet-resistance emitter actually under performs the conventional cell because a transparent emitter (emitter thickness < 3 × diffusion length) with high

FSRV lowers the $V_{oc}$ and $J_{sc}$. However, if the FSRV of the 110 Ω/sq emitter can be lowered to 10,000 cm/s, the role reverses and the 110 Ω/sq emitter increases the performance by 0.60% absolute. The crossover point is a function of the FSRV selected for the conventional 40 Ω/sq emitter ($2\times10^5$ cm/s used in these calculations). If the FSRV value for 40 Ω/sq emitter is increased from 200,000 cm/s to 500,000 cm/s, the curve becomes almost asymptotic with the FSRV axis, with the crossover point approaching $10^6$ cm/s. The FSRV value for the 40 Ω/sq emitter was fixed at 200,000 cm/s in these calculations, while the FSRV for the 110 Ω/sq emitter was varied because heavily doped emitters are less sensitive to the front-surface passivation [103]. The FSRV of 200,000 cm/s also represents typical passivation for conventional screen-printed $SiN_x$-coated 40 Ω/sq emitter cells. Model calculations also showed that the improvement in efficiency from the high sheet-resistance emitter for a FSRV<120,000 cm/s results from (1) the improvement in $V_{oc}$ because of a lower $J_{oe}$, and (2) higher $J_{sc}$ because of reduced Auger recombination. This is shown Figure 4.6.

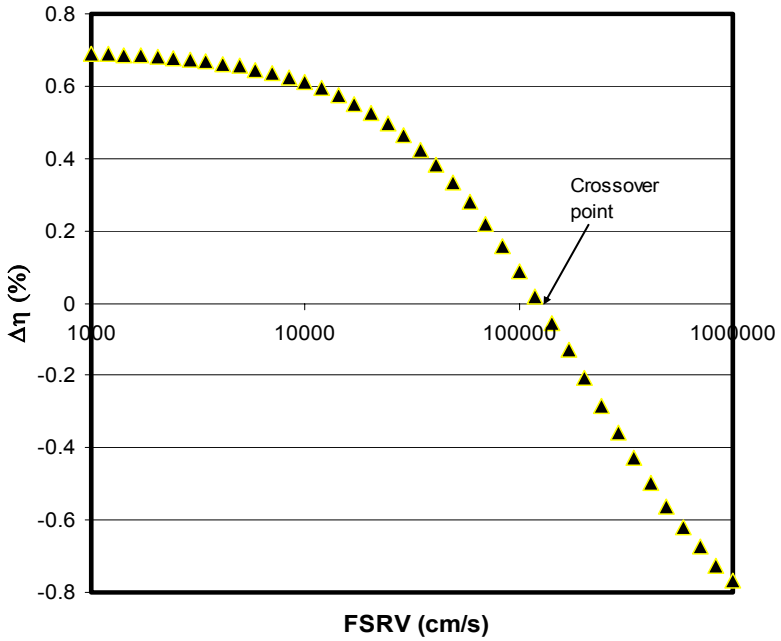


Figure 4.5. Improvement in efficiency of the high sheet-resistance emitter cell relative to the 40 Ω/sq conventional emitter cell as a function of FSRV. The FSRV of the conventional emitter cell was fixed at 200.000 cm/s.

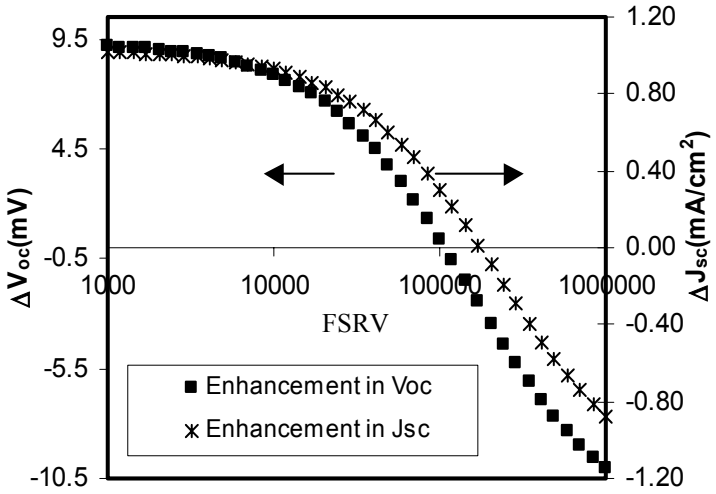


Figure 4.6. Improvement in $V_{oc}$ and $J_{sc}$ of the high sheet-resistance emitter cell, relative to the 40 Ω/sq conventional emitter cell as a function of FSRV. The FSRV of the conventional emitter cell was fixed at 200,000 cm/s.

### 4.2.3 Effect of the Bulk Lifetime and Back-Surface Recombination Velocity on the Performance Enhancement Resulting from the High Sheet-Resistance Emitter

The model calculations in Figure 4.7 show the efficiency resulting from a high sheet-resistance emitter (compared to a conventional 40 Ω/sq-emitter cell) as a function of back-surface recombination velocity (BSRV) and bulk lifetime. It is clear that a lower BSRV of 600 cm/s compared to 15,000 cm/s, provides a much greater enhancement in efficiency because of the high sheet-resistance emitter. This is attributed to the lower $J_{ob}$, resulting from the lower BSRV, which amplifies the significance of $J_{oe}$. The cell becomes limited by $J_{oe}$ rather than $J_{ob}$ for a low BSRV of 600 cm/s. Thus, a lower BSRV cell shows a more pronounced improvement in efficiency resulting from the lightly doped high sheet-resistance emitter, which has a lower $J_{oe}$. Figure 4.7 also shows that the use of high lifetime FZ Si with lifetime greater than 150 μs and good BSF can enhance the benefit of the high sheet-resistance emitter. This is because for a minority-carrier diffusion length greater than the substrate thickness, the back-surface recombination velocity (BSRV) becomes more significant. Thus, if the BSRV is low, the improvement in $V_{oc}$ and in cell efficiency resulting from the high sheet-resistance emitter increases with higher minority-carrier lifetime. However, if the BSRV is high, the improved minority-carrier lifetime would not show much improvement in $V_{oc}$ and cell efficiency.

Based on the above calculations and analysis, in this thesis low resistivity (0.6 Ω-cm) high bulk lifetime FZ Si was used with a full back screen-printed Al BSF, which produces low BSRV. All these material parameters promote the positive effect of high sheet-resistance emitters.

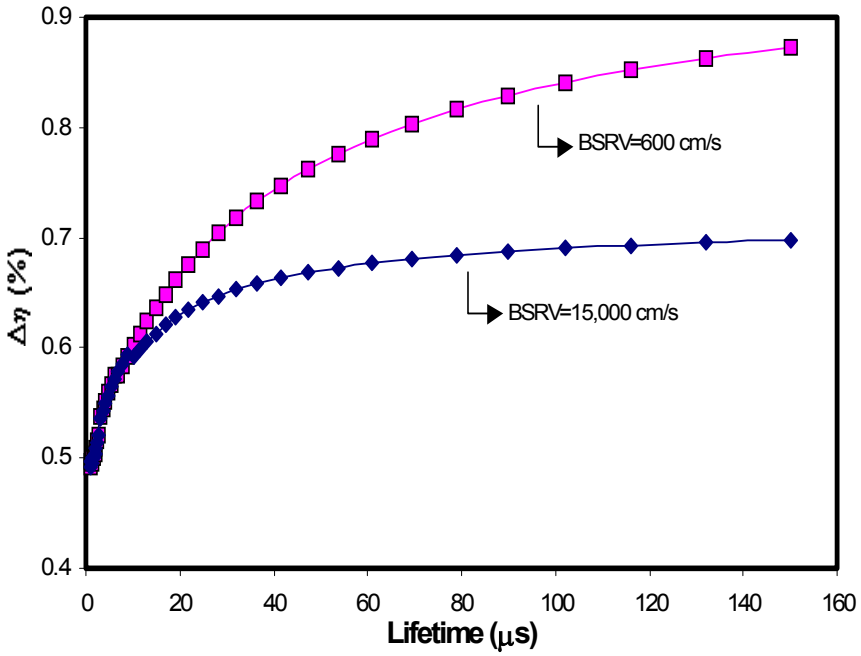


Figure 4.7. Improvement in efficiency as a function of lifetime resulting from a 110 Ω/sq emitter (compared to a conventional 40 Ω/sq emitter cell) cell for a BSRV of 600 cm/s and 15,000 cm/s.

### 4.2.4 Guidelines for Achieving High-Quality Contacts on High Sheet-Resistance Emitters

To achieve high fill factors on high sheet-resistance emitters, certain requirements for the contact parameters have to be satisfied. Since junction leakage current ($J_{o2}$) and the series ($R_s$) and shunt ($R_{sh}$) resistances control the fill factor (FF) of a solar cell, PC1D device modeling calculations were performed to determine the requirements of these contact parameters to achieve FFs in excess of 0.78. Figures 4.8 and 4.9 show that for a $J_{o2} \cong 10$ nA/cm$^2$, $R_s$ should be less than 0.8 Ω-cm$^2$ (Fig. 4.8) and $R_{sh}$ should be greater than 2,000 Ω-cm$^2$ (Fig. 4.9) to achieve FFs of >0.78. The series resistance of a screen-printed Si solar cell is often dictated by the front-contact resistance [82] for screen-printed cells. Thus, the effect of the specific contact resistance on the loss in FF was also calculated using the grid model in [104] for comb-like front Ag grid design on a 2×2 cm$^2$ solar cell.

The derivation and calculation for the specific contact resistance induced loss in FF is given in Appendix C.1.

Calculations in Figure 4.10, reveal that the specific contact resistance needs to be below 3 mΩ-cm$^2$ to avoid any appreciable loss in FF. A specific contact resistance greater than 10 mΩ-cm$^2$ significantly increases the loss in FF.

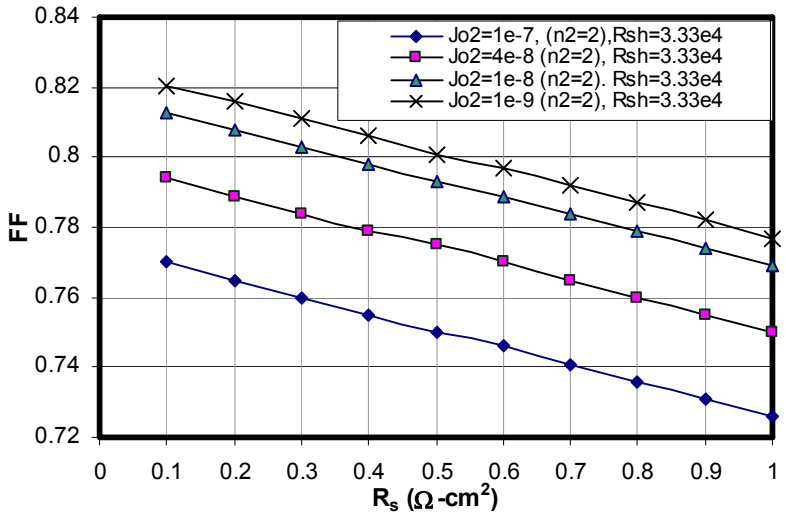


Figure 4.8. The effect of $R_s$ and $J_{o2}$ on FF.

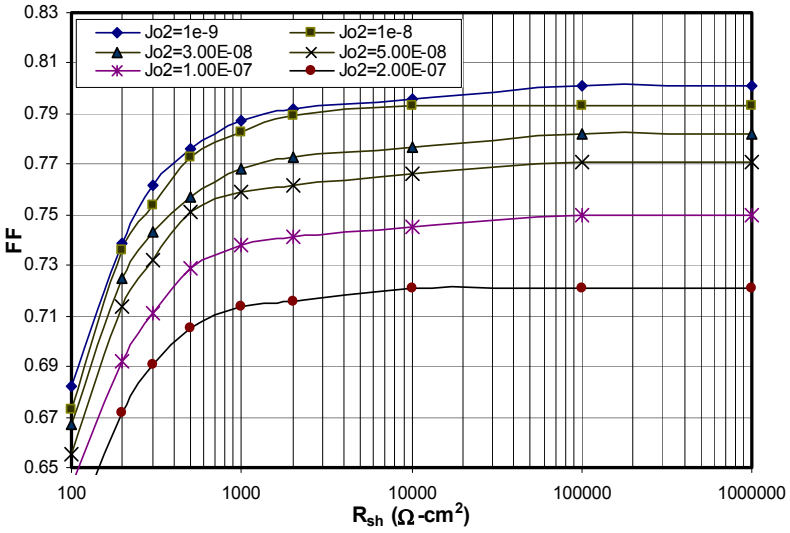


Figure 4.9. The effect of $R_{sh}$ and $J_{o2}$ on FF. $R_s$ is set to 0.6 Ω-cm$^2$.

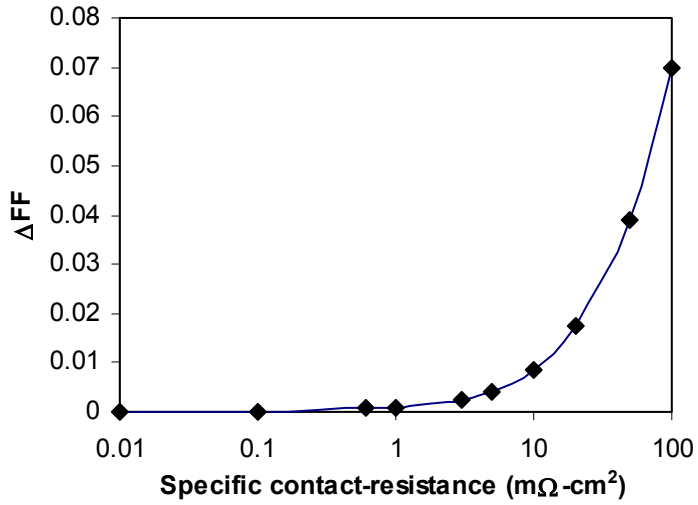


Figure 4.10. The effect of specific contact resistance on the loss in FF.

## 4.3 Conclusions

Model calculations were performed in this chapter to provide guidelines for achieving maximum benefit from the high sheet-resistance emitter. In addition, requirements for contact parameters were established for achieving FFs in excess of 0.78. These calculations and guidelines are used to design the experiments in the following chapters. Model calculations revealed that the front-surface recombination velocity should be $<10^4$ cm/s to realize the full benefit of high sheet-resistance emitter cells. In addition, lower base resistivity as well as a lower BSRV help the enhancement in absolute cell efficiency resulting from the high sheet-resistance emitter. Similarly, a higher bulk lifetime also helps the enhancement in $V_{oc}$ and efficiency as a result of the high sheet-resistance emitter. This is because these changes make the cell performance more dependent on the emitter rather than on the base saturation current. The model calculations showed that if we reduce the base resistivity of the cells from 1-2 Ω-cm to

0.6 Ω-cm, lower the FSRV to <10,000 cm/s, and lower the BSRV to 600 cm/s, a high sheet-resistance (~110 Ω/sq) emitter on a 30 μs lifetime material can improve the absolute efficiency by 0.7%. Detailed analysis showed that the performance enhancement due to high sheet-resistance emitter cells decreases with the increase in front-surface recombination velocity and if it is too high, it could actually degrade cell performance. Model calculations showed that to achieve fill factors greater than 0.78 on the high sheet-resistance emitter, the series resistance needs to be ≤0.8 Ω-cm$^2$, the shunt resistance >2,000 Ω-cm$^2$, the junction leakage current ~10 nA/cm$^2$, and the specific contact resistance below 3 mΩ-cm$^2$.

# CHAPTER 5

# DEVELOPMENT OF SCREEN-PRINTED SILICON SOLAR CELLS WITH HIGH FILL FACTORS ON 100 Ω/SQ EMITTERS

## 5.1 Introduction

Good-quality front contacts are critical for achieving high-efficiency screen-printed solar cells. As described in Section 3.1, photolithography and buried-contact technologies are known to give excellent contact quality, but they are time consuming and expensive compared to screen printing, which is simple, rapid, and cost effective. In addition, screen-printing technology is widely used for commercial silicon solar cell production [105]. However, currently, high throughput is realized at the expense of fill factor and cell performance. In addition, commercial screen-printed cells are fabricated on 35-50 Ω/sq emitters because it is difficult to achieve good screen-printed ohmic contacts on high sheet-resistance emitters. The model calculations in Chapter 4 also showed that a lightly doped emitter with appropriate cell design and good surface passivation can improve cell efficiency significantly (~0.7%).

The model calculations in the previous chapter showed appreciable performance enhancement from the high sheet-resistance emitter because reasonably good contact parameters ($R_s$, $R_{sh}$, and $J_{o2}$) were assumed. However, contacting the high sheet-resistance (~100 Ω/sq) emitter is a major challenge preventing the widespread use of such emitters in production today. Even on 30-45 Ω/sq emitters, the fill factors (FFs) are only

approximately 0.75 in commercial screen-printed cells because of the high series resistance and/or junction shunting. As illustrated in Section 3.2, high sheet-resistance cells can also be made by forming selective emitters. However, these techniques generally involve two separate P diffusions, alignment [95], and masking and etching steps [93], which make them expensive and time consuming. In this chapter an attempt is made to develop a simple and rapid technology to form good-quality screen-printed contacts directly on high sheet-resistance shallow emitters using a combination of a special commercial Ag paste (PV168 from DuPont) and a novel firing scheme. Previous studies have shown that a reasonably low contact resistance can be attained using the DuPont PV168 Ag paste if the firing temperature is kept above the Ag-Si eutectic temperature of 835° C [97,99]. Contact resistances of 0.26 mΩ-cm$^2$ and 12 mΩ-cm$^2$ were previously reported on 73 Ω/sq and 93 Ω/sq emitters [97] using PV168 Ag paste. However, these studies involved n-base Si with interdigitated back-contact (IBC) or PhosTop cells involving prolonged high-temperature firing [98, 99, 106], which is impractical for conventional p-base devices with shallow junctions.

In this chapter the firing of PV168 through the PECVD silicon nitride ($SiN_x$) antireflection (AR) coating is optimized to simultaneously achieve good series resistance, blue response, and back-surface field (BSF) for p-base $n^+$-p solar cells. The study combines the PV168 Ag alloying characteristics with a rapid, cost-effective, and manufacturable co-firing scheme to achieve high FFs and cell efficiency on 100 Ω/sq emitters. In addition, the effectiveness of the DuPont PV168 Ag paste along with this firing scheme is demonstrated by comparing its performance with two other commercial Ag pastes.

## 5.2 Experimental Method

Screen-printed $n^+$-p-$p^+$ solar cells (4 $cm^2$) were fabricated on high-quality single-crystal FZ Si using different Ag pastes and firing conditions on a 100 Ω/sq emitter as well as widely used 45 Ω/sq emitters. Based on the modeling results and guidelines established in the previous chapter, P-type, 300-μm thick (100) float-zone (FZ) substrates with a low base resistivity of 0.6 Ω-cm and a high bulk lifetime of >200 μs are used for all the experiments in this chapter to maximize the enhancement in absolute cell efficiency using a high sheet-resistance emitter. Silicon wafers were first chemically cleaned, followed by $POCl_3$ diffusion to form the $n^+$-emitter. The diffusion temperature used for the 45 Ω/sq emitter was 889° C, while that for the 100 Ω/sq emitter was 857° C. All other parameters were kept the same for both diffusions. After the phosphorus-glass removal and another clean, a PECVD $SiN_x$ AR coating was deposited on the emitter. The optimization study was done for the 100 Ω/sq emitter using a high-frequency (13.56 MHz) direct PECVD $SiN_x$ passivation layer deposited at 300° C. A low-frequency (50 KHz) direct PECVD $SiN_x$ film deposited at 430° C, which gives superior surface passivation, was also used for comparison. Next, an Al paste was screen printed on the back side and dried at 200° C. The Ag grid was then screen printed on top of the $SiN_x$ film and Ag and Al contacts were co-fired (single firing step) in a lamp-heated belt furnace. The Radiant Technology Corp. model LA-310 belt furnace used in this study has three heating zones, with lengths of 7.5, 15, and 7.5 inches, respectively, totaling 30 inches for all three hot zones. The cells were then isolated using a dicing saw and annealed in forming gas at 400° C for ~15 min. No surface texturing was used for these cells. In addition to the PV168 Ag paste from Dupont, two additional commercial Ag

pastes (A and B) were also investigated, which are widely used in production for low sheet-resistance emitter cells. All three pastes contain phosphorus dopant. In addition to the 100 Ω/sq emitter cells, conventional cells with a 45 Ω/sq emitter were also fabricated using an optimized co-firing scheme for each paste. To understand and compare the quality of contacts for the three different pastes (A, B, and PV168) on the low and high sheet-resistance emitters, current voltage (I-V) and internal quantum efficiency (IQE) measurements were taken to extract cell parameters and the short- and long-wavelength response. Suns-$V_{oc}$ measurements [29] were used to evaluate the junction leakage current ($J_{o2}$), which is generally attributed to the recombination centers in the depletion region [107]. $J_{o2}$ was determined by fixing the second-diode ideality factor ($n_2$) to two. Since high-quality monocrystalline FZ Si, which has very few dislocations and impurities, was used in this study, the degradation in $J_{o2}$ primarily attributed to the recombination centers created in the depletion region by the paste and firing conditions.

SIMS measurements were performed on selected samples to determine the Ag and P concentration profiles in the silicon directly underneath the Ag grid using a CAMECA IMS-5F ion microscope. The Ag grid was etched in HCl prior to the SIMS measurements to prevent any Si etching. The samples were bombarded with 5.5 KeV $O_2^+$ primary ions for analysis of Ag, while 14.5 KeV $Cs^+$ primary ions were used for P. The primary ion beam was rastered over an area of 150 μm × 150 μm. Positive or negative secondary ions were collected from a ~20 μm diameter area in the center of the rastered crater for Ag and P, respectively. Spreading resistance measurements were made to determine the electrically active P concentration profile in the emitter. Finally, the contact resistance measurements were made using transfer-length method (TLM) patterns

[33], which were printed during cell fabrication. Since screen-printed (SP) contacts are not full area metal-Si contacts, the TLM of measurement gives a macroscopic specific contact resistance ($\rho_{cm}$) for SP contacts. The actual temperature of the wafer was measured as it was fired through the belt by attaching a fast-response K-type thermocouple with a closed-end tip loosely touching the surface of the wafer. This is because set temperature and sample temperature are quite different in a belt furnace. Table 5.1 shows the approximate peak firing temperatures for the corresponding set temperature and belt speed for the different firing cycles used in this study.

Table 5.1: Set temperature, belt speed and the approximate peak temperature experienced by the cell.

| Set temperature (°C) | Belt speed (ipm) | Approximate peak temperature (°C) |
|---|---|---|
| 435/585/750°C | 15 | 720 |
| 825/825/825°C | 80 | 750 |
| 850/850/850°C | 80 | 780 |
| 900/900/900°C | 80 | 835 |
| 900/900/900°C | 60 | 850 |
| 900/900/900°C | 15 | 895 |

## 5.3 Results and Discussion

### 5.3.1 Determination of the 45 and 100 Ω/sq Emitter Doping Profiles

The emitter profile can greatly influence solar cell characteristics such as junction shunting, grid contact resistance, and short-wavelength IQE response [104]. For example, the specific contact resistance ($\rho_c$) and emitter sheet resistance ($\rho_s$) are inversely proportional to the surface dopant concentration ($N_D$), while for a well-passivated surface, $J_{oe}$ and the photo-current loss are directly proportional to $N_D$ and the doping profile. The junction depth also influences the junction shunting ($R_{sh}$) for screen-printed contacts, with a shallow junction being more vulnerable to contact firing-induced

degradation. Thus, there are competing factors in designing the emitter region for high-efficiency cells. Therefore, to gain a better understanding of the cell performance results, emitter-doping profiles were first determined by spreading resistance measurements. Figure 24 shows the phosphorus doping profiles for the 100 and 45 Ω/sq emitters formed in this study. The 100 Ω/sq emitter had a surface concentration of ~$1.5\times10^{20}$ $cm^{-3}$ with a junction depth of 0.277 μm, while the 45 Ω/sq emitter had a surface concentration of ~$2.3\times10^{20}$ $cm^{-3}$ with a junction depth of 0.495 μm. With a good surface passivation, the 100 Ω/sq emitter should lead to higher current because of the thinner heavily doped dead layer compared to the 45 Ω/sq emitter (Figure 4.5). On the other hand, shallow emitters are more prone to junction shunting or leakage because of the incorporation of impurities from the paste into the junction, especially if the frit in the paste strongly etches the Si surface to allow the Ag metal to reach the junction. Junction shunting lowers the open-circuit voltage ($V_{oc}$) and the FF of the cell, as shown by the model calculations in the previous chapter.

According to the literature [108, 109], a surface dopant concentration of $>10^{19}$ $cm^{-3}$ is required for an evaporated and full-area ohmic contact to an n-type Si region. However, it has been shown by SEM and TEM studies that full-area metal-Si contact is not achieved for the screen-printed grid because of the presence of a quasi-continuous glass frit layer (Figs 3.16 and 3.17 in Chapter 3). It is conjectured that carriers have to tunnel through the glass layer [17, 78, 80]. That is why it is difficult to achieve excellent ohmic contacts using screen-printing technology. Figure 5.1 shows that both the 45 Ω/sq and 100 Ω/sq emitters used in this study have high surface concentrations greater than $1\times10^{20}$ $cm^{-3}$. However, the challenge is to develop an appropriate firing condition that

will provide adequate area coverage for the contact points (Ag crystallites) to the 100 Ω/sq emitter without shunting or degrading the junction. Therefore, a study was conducted to optimize contact firing conditions that can yield good contact quality for both 45 and 100 Ω/sq emitters using three different commercial pastes A, B, and PV168. These three pastes have been evaluated with the goal of achieving a performance enhancement from the 100 Ω/sq emitter over the 45 Ω/sq emitter, in addition to establishing the requirements for paste composition for achieving good contacts to high sheet-resistance emitters.

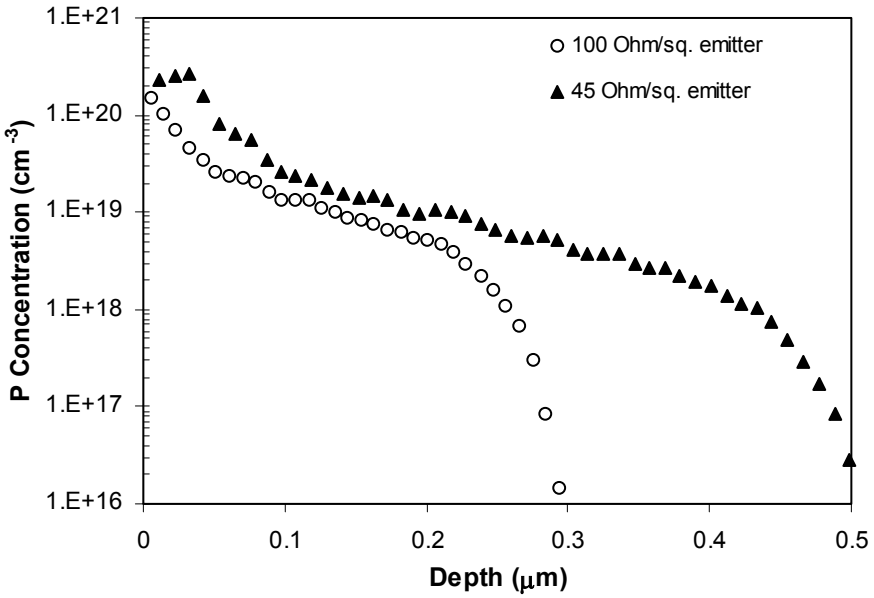


Figure 5.1 Spreading resistance profiles of $POCl_3$ diffused 100 Ω/sq and 45 Ω/sq emitters.

Achieving a good ohmic contact between the Ag and the high sheet-resistance Si emitter is a challenge because it has a lower P doping (Fig 5.1), resulting in higher specific-contact resistance for a tunneling-based carrier transport process described by the following equation [110]:

$$\rho_c \propto \exp\left(\frac{2\sqrt{\varepsilon_s m^*}}{\hbar}\left(\frac{\phi_{Bn}}{\sqrt{N_D}}\right)\right) \tag{5.1}$$

where $N_D$ is the doping concentration ($\geq 10^{19}$ cm$^{-3}$), $m^*$ is the effective mass of the charge carriers, $\varepsilon_s$ is the semiconductor permittivity, $\hbar$ is the reduced Planck constant, and $\phi_B$ is the Schottky barrier height. The surface doping for both the 45 and 100 Ω/sq emitters used in our cell process is greater than $10^{19}$ cm$^{-3}$. However, the high sheet-resistance emitter is shallower (0.277 μm) than the low sheet-resistance emitter (0.495 μm). Hence, the challenge is to achieve good ohmic contacts without degrading or shunting the p-n junction. This requires the technology development and optimization of the glass frit, Ag powder in the paste, and contact firing, which are described in the following sections.

## 5.3.2 Optimization of Ag Paste Firing to Achieve Good Contacts on a 100 Ω/sq Emitter

### 5.3.2.1 Effect of Conventional Firing of Commercial Pastes A and B on the Performance of 45 Ω/sq and 100 Ω/sq Emitter Cells

Before investigating the PV168 paste from Dupont, we studied the two widely used commercial Ag pastes, A and B. Both pastes are expected to give good-quality contacts to 45 Ω/sq emitters. Complete cells were fabricated and characterized. Light and dark I-V and Suns-$V_{oc}$ data is summarized in Table 5.2, which confirms that conventional co-firing of pastes A and B at 700-750° C peak temperature gives excellent FFs, exceeding 0.785 for the 45 Ω/sq emitter cells, with efficiencies approaching 16%.

Table 5.2: I-V data for cells fabricated with commercial pastes A and B using co-firing processes on a low sheet-resistance (45 Ω/sq) emitter.

| Paste | Co-firing Process | $V_{oc}$ (mV) | $J_{sc}$ (mA/cm²) | FF | Eff (%) | n factor | $R_s$ (Ω-cm²) | $R_{sh}$ (Ω-cm²) | $\rho_{cm}$ (mΩ-cm²) | $J_{o2}$ (nA/cm²) |
|---|---|---|---|---|---|---|---|---|---|---|
| A | 435/585/750°C 15 ipm | 623 | 31.80 | 0.792 | 15.7 | 1.04 | 0.61 | 22,541 | 0.12 | 13 |
| B | 850/850/850°C 80 ipm | 627 | 32.6 | 0.785 | 16.0 | 1.09 | 0.64 | 188,040 | 0.38 | 29 |

Currently, no cell manufacturer uses high sheet-resistance emitters (≥ 60 Ω/sq) because it is difficult to achieve good screen-printed ohmic contact using conventional Ag pastes. Thus, different firing conditions were used to investigate the performance of pastes A and B on the 100 Ω/sq emitter. To understand the significant difference in efficiency and FFs for the two sheet resistances, specific-contact resistance ($\rho_c$) measurements were taken by the TLM method. It is important to recall that the model calculations in Chapter 4 revealed that the specific-contact resistance should be below 3 mΩ-cm$^2$ to achieve good FFs. In addition, $J_{o2}$ and series resistance ($R_s$) should be below 50 nA/cm$^2$ and 1 Ω-cm$^2$, respectively, to achieve FFs≥0.77. It was found that both commercial pastes worked well for the 45 Ω/sq emitter, but failed on the 100 Ω/sq emitter for various firing schemes (Table 5.3). This was the result of very high contact resistance at lower firing temperatures and high junction-leakage current and lower $V_{oc}$ at higher firing temperatures (Table 5.3). This indicates that the composition of pastes A and B is not adequate to make good ohmic contacts to the high sheet-resistance emitter, regardless of the firing scheme. Therefore, as explained in the next section, we acquired a less aggressive special paste (PV168) from DuPont that allowed us to go to higher firing temperatures without causing junction shunting.

Table 5.3: I-V data for cells fabricated with commercial pastes A and B using co-firing process on a high sheet-resistance (100 Ω/sq ) emitter for different firing temperatures.

| Paste Firing Temperature (°C) | $V_{oc}$ (mV) | $J_{sc}$ (mA/cm²) | FF | Eff (%) | n factor | $R_s$ (Ω-cm²) | $R_{sh}$ (Ω-cm²) | $\rho_{cm}$ (mΩ-cm²) | $J_{o2}$ (nA/cm²) |
|---|---|---|---|---|---|---|---|---|---|
| **Paste A** 435/585/750° C15 ipm | 612 | 32.1 | 0.704 | 13.9 | 1.09 | 2.41 | 1,707 | 33.00 | 10 |
| 825°C/80 ipm | 633 | 32.3 | 0.268 | 5.5 | 1.31 | 13.39 | 644 | 12.51 | 11 |
| 850°C/80 ipm | 618 | 33.5 | 0.740 | 15.3 | 1.07 | 1.78 | 1,247 | 7.21 | 106 |
| 900°C/80 ipm | 620 | 33.2 | 0.761 | 15.6 | 1.10 | 1.05 | 5,092 | 1.14 | 29 |
| **Paste B** 825°C/80 ipm | 626 | 18.7 | 0.231 | 2.7 | 1.42 | 29.70 | 6,658 | 200 | 15 |
| 850°C/80 ipm | 291 | 32.7 | 0.479 | 4.6 | 2.02 | 1.11 | 3,071 | 1.53 | 120,000 |
| 900°C/80 ipm | 572 | 32.9 | 0.536 | 10.1 | 2.62 | 3.21 | 15,078 | 2.30 | 697 |

#### 5.3.2.2 Optimization of Firing Conditions for PV168 Ag Paste to Achieve Good Contacts on 100 Ω/sq Emitters

The paste composition and firing cycle can significantly influence series resistance, junction leakage, and FF. The previous section showed that the widely used commercial pastes failed on the 100 Ω/sq emitter over a wide range of practical firing conditions. Therefore, PV168 paste was used in which the composition, shape, and size of the frit and Ag particles were tailored to reduce the etching of Si at high temperatures. Exact details about the paste chemistry are proprietary. The following sections describe the understanding and optimization of firing temperature and belt speed that led to the firing conditions, which eventually produced **for the first time** good contacts directly to the 100 Ω/sq emitter.

First, the effect of firing temperature on FF was examined using a high belt speed (≥80 ipm), referred to as spike firing in this thesis. Table 5.4 shows that specific-contact

resistance ($\rho_c$) decreases with higher firing temperature and reaches ~1 mΩ-cm$^2$ at a set temperature of 900° C, resulting in a high FF of 0.775. Notice that the $V_{oc}$ did not degrade even for such a high set temperature. This is supported by very low junction leakage current ($J_{o2}$) of 10 nA/cm$^2$. It is important to realize that the actual sample temperature is generally lower than the set temperature (Table 5.1), especially for high belt speeds. Temperature profiling showed that the sample experienced a peak temperature in the range of 830-840° C for a few seconds during the spike firing cycle of 900° C/80 ipm.

Table 5.4: I-V data for cells fabricated with PV168 Ag paste using co-firing process (80 ipm belt speed) on a high sheet-resistance (100 Ω/sq ) emitter for different firing temperatures.

| Set Temperature (°C) | $V_{oc}$ (mV) | $J_{sc}$ (mA/cm²) | FF | Eff (%) | n factor | $R_s$ (Ω-cm²) | $R_{sh}$ (Ω-cm²) | $\rho_{cm}$ (mΩ-cm²) |
|---|---|---|---|---|---|---|---|---|
| 825°C | 626 | 19.8 | 0.249 | 3.1 | 1.46 | 27.16 | 2,951 | 45.00 |
| 850°C | 572 | 32.9 | 0.536 | 10.1 | 2.62 | 3.21 | 15,078 | 4.71 |
| 900°C | 627 | 33.9 | 0.775 | 16.5 | 1.01 | 1.00 | 3,353 | 1.06 |

Since the combination of the set temperature and belt speed dictates the thermal budget of the sample, we also examined the role of belt speed on contact formation. Table 5.5 shows that increasing the belt speed from 15 to 80 ipm at a fixed set temperature of 900° C lowered $J_{o2}$ by a factor of 100. The reduction of $J_{o2}$ agreed well with the improvement in the FF and $V_{oc}$, also shown in Table 5.5. The optimum firing condition for the PV168 paste was found to be 80 ipm at 900$^o$ C, which gave a FF of 0.775 and the best cell performance of 16.5% with a $V_{oc}$ of 627 mV. The firing cycle optimization was done up to a set temperature of 900° C because of the limitations of the

Radiant Technology Corp. model LA-310 belt furnace used in this study, which could not maintain set temperatures greater than 900° C for speeds of 80 ipm or higher.

Table 5.5: I-V data for cells fabricated with PV168 Ag paste using co-firing process (900°C set temperature) on high sheet-resistance (100 Ω/sq ) emitters for different belt speeds.

| Belt speed (ipm) | $V_{oc}$ (mV) | $J_{sc}$ (mA/cm²) | FF | Eff (%) | n factor | $R_s$ (Ω-cm²) | $R_{sh}$ (Ω-cm²) | $\rho_{cm}$ (mΩ-cm²) | $J_{o2}$ (nA/cm²) |
|---|---|---|---|---|---|---|---|---|---|
| 15 | 578 | 32.8 | 0.564 | 10.7 | 3.63 | 0.65 | 13,316 | 2.78 | 1,070 |
| 60 | 623 | 33.4 | 0.759 | 15.8 | 1.03 | 1.27 | 979,127 | 4.67 | 15 |
| 80 | 627 | 33.9 | 0.775 | 16.5 | 1.01 | 1.00 | 3,353 | 1.06 | 10 |

### 5.3.2.3 SIMS Analysis to Understand and Explain the Success of PV168 Ag Paste in Forming Good Ohmic Contact to 100 Ω/sq Emitter

Secondary ion mass spectroscopy (SIMS) was performed to determine the extent of Ag migration into Si by obtaining Ag profiles into the Si emitter. The SIMS data in Figure 5.2 show that Ag indeed penetrates into Si and could be a problem for junction shunting. It was found that slow belt-speed firing (15 ipm) at a set temperature of 900° C resulted in a much higher concentration of Ag in the underlying Si, while fast firing (80 ipm) introduced a much lower amount of Ag at or near the p-n junction. Recall that spreading resistance measurements gave a junction depth of 0.277 μm for the 100 Ω/sq emitter (Fig. 5.1). Ag concentrations at the $n^+$-p junction (0.277 μm) were found to be $6\times10^{18}$ $cm^{-3}$, $2\times10^{17}$ $cm^{-3}$, and $2\times10^{16}$ $cm^{-3}$ for belt speeds of 15, 60, and 80 ipm, respectively. This indicates that faster firing decreases the Ag concentration near the junction edge, which in turn reduces junction leakage current and gives higher $V_{oc}$. This is consistent with the work of Van Craen et al. [111], who showed that solar cell efficiency decreases with the increase in Ag concentration near the junction.

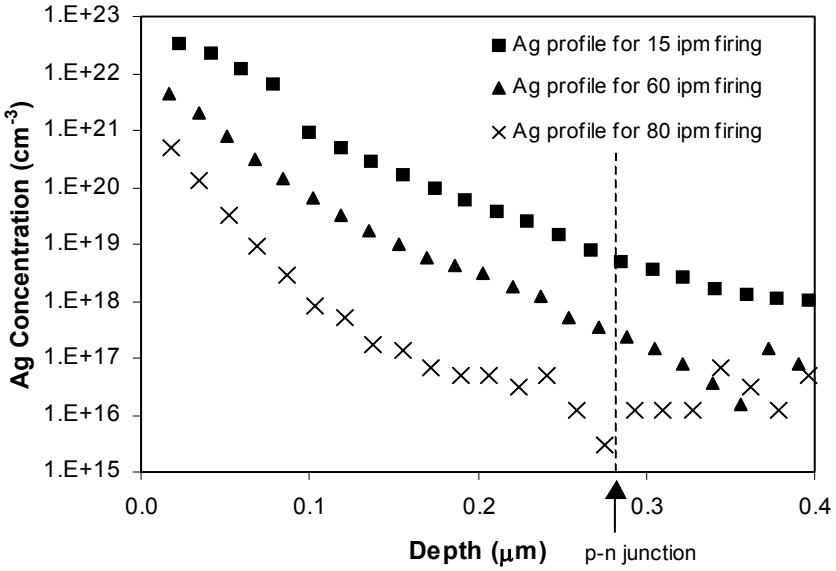


Figure 5.2. SIMS profile of PV168 Ag paste fired at different belt speeds.

In Section 5.3.2.1 it was shown that pastes A and B did not show a performance enhancement with the 100 Ω/sq emitter for various firing conditions. Instead, cell performance degraded because of either high contact resistance or excessive junction leakage current. On the other hand, in Section 5.3.2.2 it was demonstrated that the PV168 Ag paste is capable of producing high FFs and cell efficiencies on 100 Ω/sq emitters, provided spike firing is performed at a high set temperature, resulting in sample peak temperatures in the range of 830-840° C for a very short time (a few seconds). PV168 is made by DuPont using a proprietary technology involving a somewhat different Ag particle morphology, Ag content, and frit composition. The SIMS analysis is illustrated in this section to complement cell data to understand and explain why, in contrast to PV168 paste, pastes A and B were not able to achieve high FFs on the 100 Ω/sq emitter. To improve the understanding further, more cells were fabricated on the 100 Ω/sq emitter using pastes A, B, and PV168 and the same co-firing condition (900°

C/80 ipm). Table 5.6 shows that the $V_{oc}$ and FF decrease, while $J_{o2}$ increases monotonically for cells made from pastes PV168, A, and B, respectively. The lowest $J_{o2}$ value of 10 nA/cm$^2$ for the PV168 paste indicates much less junction shunting compared to the other two pastes. This was supported by SIMS analysis showing the Ag concentration at the junction edge (Table 5.6) to be $1.24\times10^{16}$ cm$^{-3}$, $2.50\times10^{17}$ cm$^{-3}$, and $1.20\times10^{18}$ cm$^{-3}$. Thus, the Ag penetration into Si is reduced significantly because of the PV168 paste chemistry, permitting high-temperature firing to reduce contact resistance without increasing the $J_{o2}$ value for the shallow 100 Ω/sq emitter.

Table 5.6: Correlation of $V_{oc}$, FF, and $J_{o2}$ with Ag concentration at the junction for pastes PV168, A, and B using co-firing process (900° C set temperature and 80 ipm belt speed) on high sheet-resistance (100 Ω/sq ) emitters.

| Paste | $V_{oc}$ (mV) | FF | $J_{o2}$ (nA/cm$^2$) | Ag concentration at the junction (cm$^{-3}$) | $\rho_{cm}$ (mΩ-cm²) |
|---|---|---|---|---|---|
| PV168 | 627 | 0.775 | 10 | $1.24\times10^{16}$ | 1.06 |
| A | 619 | 0.761 | 29 | $2.50\times10^{17}$ | 1.14 |
| B | 572 | 0.536 | 697 | $1.20\times10^{18}$ | 2.30 |

To improve the understanding of the series resistance effect of the three pastes, specific-contact resistance measurements were made. Table 5.6 shows that the macroscopic specific-contact resistance for all three pastes was less than 3 mΩ-cm$^2$ on the 100 Ω/sq emitter, which is acceptable for screen-printed contacts and should not degrade the FF. For the 100 Ω/sq-emitter cells, PV168 gave the lowest specific-contact resistance (1.06 mΩ-cm$^2$), followed by paste A (1.14 mΩ-cm$^2$) and paste B (2.3 mΩ-cm$^2$). These results indicate that, contrary to the original concern, the problem with conventional pastes A and B is not the contact resistance to the 100 Ω/sq emitter. Instead,

when we go to high temperatures (set temp. ~900° C) to achieve reasonable contact resistance, the Ag penetration into the junction becomes excessive, which increases the $J_{o2}$ and lowers the $V_{oc}$ (Table 5.3). On the other hand, if we stay at lower temperatures (set temp.≤ 850° C) to prevent excessive Ag penetration, the contact resistance becomes too high and degrades the FF and cell performance as shown in Table 5.3. The composition of PV168 is such that at higher firing temperatures (830-840° C), good ohmic contact is achieved, probably because of the larger number and/or size of Ag crystallites in contact with the emitter surface. In addition, the frit content and composition are such that PV168 is able to etch through the $SiN_x$ AR coating without excessive etching of the Si emitter underneath the grid. In the case of the PV168 paste, Ag penetration into Si is somewhat arrested because of the right combination of frit content and composition and the Ag particle morphology. The contact formation mechanism [64, 76] for widely used commercial pastes generally involves lower temperature firing (700-800° C), heating-induced fluidization of the glass frit, and surface wetting, followed by etching of the AR coating and the Si emitter surface. Higher firing temperature results in deeper etching of Si and higher Ag penetration. It appears that in the case of PV168, the etching of Si by the frit is minimal and the contact formation takes place via a very thin eutectic region or Ag-Si alloy.

SIMS measurements were also taken to obtain the phosphorus profiles before and after the grid formation and gain a better understanding of the success of PV168 screen-printed contacts on 100 Ω/sq emitters. Ag metal was etched off prior to the SIMS measurements. For the optimized firing condition of PV168, SIMS measurements showed no apparent addition of P from the paste to the original 100 Ω/sq emitter profile

(Fig. 5.3), even though the paste contains some source of phosphorus. This indicates that the injection of P from the paste did not play a major role in the ohmic-contact formation to the 100 Ω/sq emitter. However, to establish this with more certainty we did the contact firing on the undiffused wafer; we found that after firing, some additional P does come from the paste, but the profile is very shallow, with a surface concentration of only ~$4\times10^{18}$ $cm^3$, resulting in a sheet resistance of ~5000 Ω/sq. Thus, there is no indication of selective-emitter formation. SIMS measurements of the P profiles were taken underneath the Ag grid and underneath the silicon nitride coating to get an idea of the extent of Si emitter etching during contact formation. The difference between the two profiles shown in Figure 5.3 reveals a penetration depth of ~55 nm for the PV168 Ag paste fired at 900° C/80 ipm, which could also be a measure of the average penetration depth of the Ag crystallites into Si. This is much less than the average penetration depth of 130 nm for the Ag crystallites formed in conventional pastes [78].

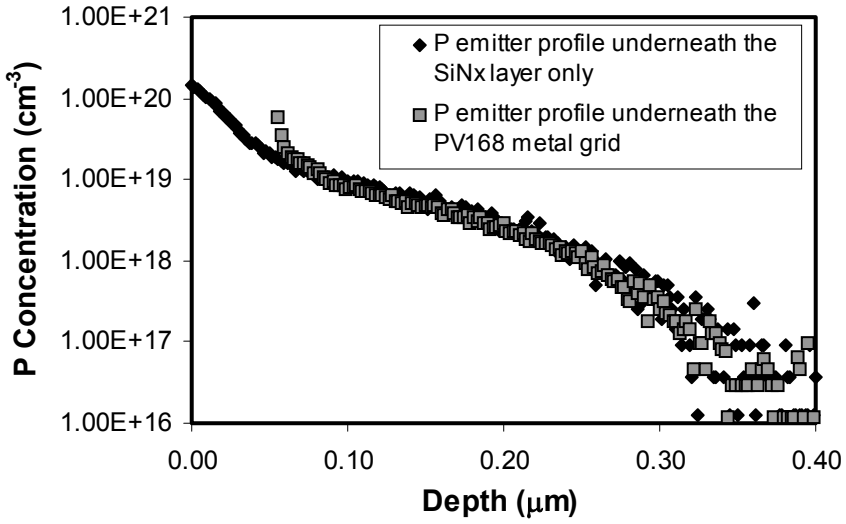


Figure 5.3 P emitter 100 Ω/sq profiles underneath the $SiN_x$ layer only and underneath the PV168 Ag metal contact grid after contact firing.

## 5.3.3 Quantitative Assessment and Enhancement of $Si_3N_4$-induced Front- Surface Passivation on 45 and 100 Ω/sq Emitters

### 5.3.3.1 Internal Quantum Efficiency (IQE) Analysis to Support Current Enhancement Due to the High Sheet-Resistance Emitter

In the previous sections, we successfully demonstrated for the first time that good-quality screen-printed contacts can be directly achieved on a 100 Ω/sq emitter with good ohmic contact, fill factor, and cell efficiency. Figure 5.4 shows the internal quantum efficiency (IQE) plots of a conventional 45 Ω/sq cell fabricated using silver paste B (Cell 1), and the 100 Ω/sq emitter cell co-fired using PV168 paste (Cell 2). The short-wavelength response of Cell 2 is superior because the 0.277 μm deep lightly doped emitter reduces the dead layer thickness, Auger recombination, and the heavy doping effects. The extraction of $J_{sc}$ via photon flux weighted integration of the IQE curve in Figure 5.4 showed that the difference in the short-wavelength response accounts for the great majority of the observed 1.3 mA/cm$^2$ improvement in $J_{sc}$ for the two cells. There is a slight difference in the long-wavelength response in favor of the 100 Ω/sq emitter cell fired at higher temperature. Since co-firing is normally performed at lower temperatures, around ~750° C, for conventional 45 Ω/sq cells to avoid junction shunting, a slightly lower-quality back-surface field (BSF) may result. This may explain why the long-wavelength response for Cell 2 is slightly superior to that of Cell 1. By matching the experimental and calculated long-wavelength IQE, using the PC1D model [102], effective BSRVs were estimated to be 600 cm/s and 900 cm/s for the co-fired 100 Ω/sq- and 45 Ω/sq emitter cells, respectively. A similar analysis for the short-wavelength response gave an effective FSRV of 250,000 cm/s and 450,000 cm/s for the 100 and 45 Ω/sq emitters, respectively. Thus, co-firing with PV168 Ag paste on the 100 Ω/sq emitter

at a set temperature of 900° C with a high belt speed of 80 ipm accomplishes reduced FSRV, reduced emitter recombination, an effective BSF, and a good ohmic contact to 100 Ω/sq emitters. Model calculations show that a BSRV of 600 cm/s can limit the maximum possible $V_{oc}$ to ~662 mV for a 0.6 Ω-cm material with a bulk lifetime of 250 μs when the effect of FSRV or $J_{oe}$ on $V_{oc}$ is completely neglected ($V_{oc}=(kT/q).\ln[(J_{sc}/(J_{oe}+J_{ob}))+1]$). The cell data in Figure 5.4 also show that the efficiency difference of ~0.5% between the co-fired 45 Ω/sq cell and the 100 Ω/sq cell is mainly due to higher short-wavelength response or $J_{sc}$.

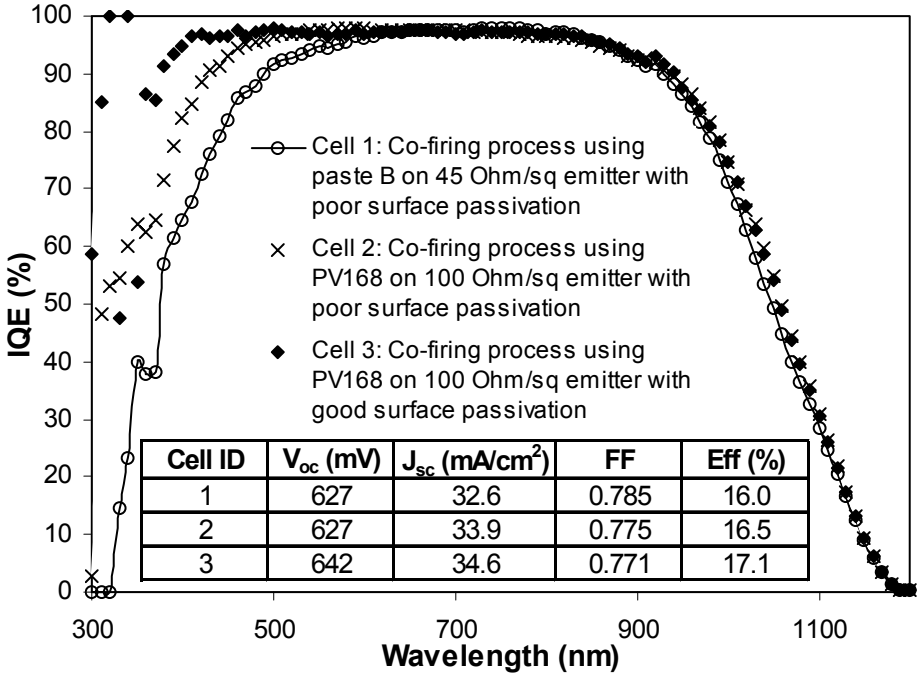


| Cell ID | $V_{oc}$ (mV) | $J_{sc}$ (mA/cm$^2$) | FF | Eff (%) |
|---|---|---|---|---|
| 1 | 627 | 32.6 | 0.785 | 16.0 |
| 2 | 627 | 33.9 | 0.775 | 16.5 |
| 3 | 642 | 34.6 | 0.771 | 17.1 |

Figure 5.4. IQE plots for co-fired 45 Ω/sq emitter (using paste B) and 100 Ω/sq emitter cells using PV168 paste with good and poor front-surface passivation.

### 5.3.3.2 Further Enhancement in the Performance of 100 Ω/sq-Emitter Cell with Higher Quality Front-Surface Passivation

All the cells reported in the previous sections had a $SiN_x$ film deposited in a high-frequency (HF) PECVD reactor, which resulted in an effective FSRV of ~250,000 cm/s on the 100 Ω/sq emitter and ~450,000 cm/s on the 45 Ω/sq emitter. These FSRV values were obtained by matching the measured and PC1D-simulated IQEs in the short-wavelength range (0.3-0.5 μm). The actual emitter doping profile was used with the default bandgap narrowing model of PC1D. According to the model calculations in Chapter 4, these FSRV values are too high to obtain maximum benefit from the high sheet-resistance emitter. To enhance the understanding of this aspect and increase the efficiency gap between the 100 and 45 Ω/sq- emitter cells, we improved the surface passivation by depositing a low-frequency (LF) PECVD $SiN_{x,}$. The deposition condition (430-435°C) was used to achieve better passivation. The IQE/PC1D analysis showed that the LF $SiN_x$ lowered the effective surface recombination velocity of the 100 Ω/sq emitter from ~250,000 cm/s to ~40,000 cm/s. This should lower $J_{oe}$ and give higher $V_{oc}$ [$=kT/q \cdot \ln(J_{sc}/J_{o1} + 1)$] because $J_{o1} = J_{oe} + J_{ob}$. Recall that in this study, low-resistivity Si was selected to reduce the base saturation current density ($J_{ob}$), which made $V_{oc}$ more sensitive to $J_{oe}$. Figure 5.4 shows that indeed the co-fired 100 Ω/sq cell using PV168 Ag paste (Cell 3) with good surface passivation gave ~1% higher cell efficiency with a much higher blue response of 2.0 mA/cm$^2$, higher $J_{sc}$, and 15 mV higher $V_{oc}$ compared to the co-fired 45 Ω/sq cell with poor surface passivation. It also gave ~0.6% improvement in absolute efficiency over the poorly passivated 100 Ω/sq cell. The FSRV for the well-passivated (LF $SiN_x$) cell was comparable to that of Kerr et al., who reported an FSRV of

~25,000 cm/s for an emitter with a surface concentration of $1.8x10^{20}$ $cm^{-3}$ [112]. It has been shown in [113] that annealing at 500° C causes $J_{oe}$ to decrease by a factor of two for 100 Ω/sq emitters passivated with LF direct-plasma $SiN_x$ film, while the $J_{oe}$ for the HF direct-plasma $SiN_x$ film increases during annealing. It is important to note that because of our HF PECVD machine limitations, the HF $SiN_x$ deposition conditions were not optimum for a good FSRV. The conditions for better HF $SiN_x$ passivation include higher deposition temperature of 400° C (the deposition temperature of our HF PECVD machine is 300°C) and higher gas flows [31]. The beneficial effect of the LF $SiN_x$ is especially pronounced after rapid high-temperature firing. This is supported by the measured $J_{oe}$ values, which showed a drop from 580 $fA/cm^2$ to 66 $fA/cm^2$ after firing. This result is close to the $J_{oe}$ values below 60 fA/cm obtained for good surface passivation using optimized remote or HF PECVD $SiN_x$ for surface concentrations up to $10^{20}$ $cm^{-3}$ (without annealing) [114].

The short-wavelength response can be further enhanced by using a stack oxide/nitride front-surface passivation since a thermal oxide is known to passivate defects and dangling bonds at the surface. Figure 5.5 shows a higher IQE short-wavelength response for a stack 100 Å rapid thermal oxide (RTO)/LF PECVD $SiN_x$ film (see Appendix D for the oxide growth process conditions) compared to a LF $SiN_x$ film only. The lowest $J_{oe}$ (54 $fA/cm^2$) was measured for the stack RTO/$SiN_x$ front-surface passivation, which supports the higher short-wavelength response.

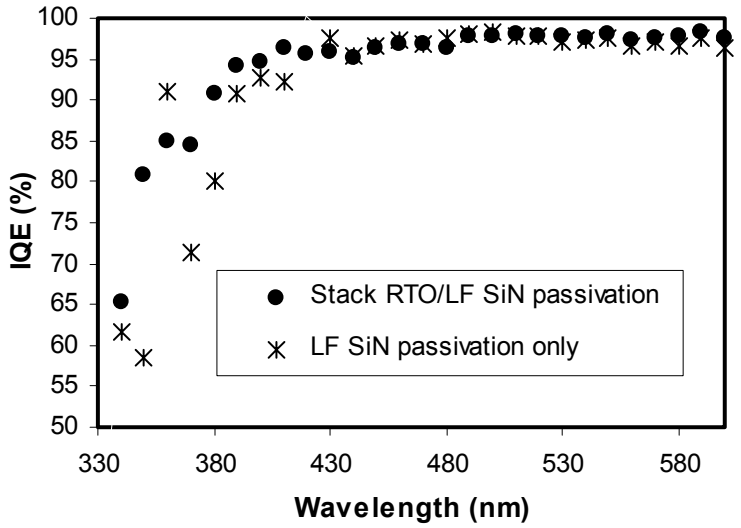


Figure 5.5: Short-wavelength IQE response for 100 Ω/sq co-fired cells with LF PECVD $SiN_x$ only and RTO/LF $SiN_x$.

### 5.3.4 Optimization of the Grid Design to Further Enhance the Fill Factor of the 100 Ω/sq Emitter Cells

In the previous sections, the firing condition was optimized and the front-surface passivation was improved to enhance the benefit from the high sheet-resistance emitter. However, all the previous cells were fabricated using the same screen and grid design that was optimized for the 45 Ω/sq emitter. An increase in sheet resistance to 100 Ω/sq cells requires re-optimization of the grid design, with narrower spacing to minimize the sheet resistance loss. The metal grid design used in this study had one tapered busbar with a 500 × 800 μm pad and eight gridlines for the 45 Ω/sq emitter and 2 cm x 2 cm cells. The finger width is 75-80 μm in the case of the fired PV168 Ag gridlines. In this section, the grid model presented in [104] is used to optimize the grid design, taking into account resistance and shading losses (see Appendices A and B). This resulted in the addition of two gridlines to the original grid design to have a total of 10 gridlines with a

grid spacing of 0.2 cm as opposed to 0.25 cm. The grid optimization gives a fractional power loss of 0.0793 because of the eight-line grid, while that for the 10-line grid is 0.0753 on the 100 Ω/sq emitter. Hence, the total fractional power loss is higher for the eight-line grid on the 100 Ω/sq emitter compared with the 10-line grid because of the high sheet-resistance loss, even though the shading loss is lower for the eight-line grid. Therefore, the grid optimization led to a decrease in the series resistance by ~0.2 Ω-cm$^2$ coupled with an enhancement in the FF of 0.008-0.009. This is consistent with [74] where the resistance associated with the sheet resistance and gridline spacing is given by $R_e=(\rho_s b^2)/12$, where $\rho_s$ is the sheet resistance in Ω/sq and $b$ is the gridline spacing in cm. The contribution to the series resistance from the diffused 100 Ω/sq sheet is 0.52 Ω-cm$^2$ for 0.25-cm spacing and 0.33 Ω-cm$^2$ for 0.2-cm spacing. Thus, $R_e$ is improved by 0.19 Ω-cm$^2$ because the new grid design. Since each 1 Ω-cm$^2$ in series resistance causes a decrease of ~0.042 in FF (assuming a reasonably high shunt resistance, see Appendix C.2) [115], the total expected improvement in FF is ~0.008. This is consistent with data in Table 5.7, where the FF improved by 0.009, from 0.771 to 0.780, because of a decrease in the series resistance from 1.02 Ω-cm$^2$ to 0.79 Ω-cm$^2$ as a result of the new grid design. This resulted in further enhancement in cell efficiency from 17.2% to 17.4%. The FF and efficiency can be further improved on high sheet-resistance emitters if finer gridlines can be screen printed with the corresponding optimum grid design. Thus, grid design optimization is also important in maximizing the benefit from the high sheet-resistance emitter.

Table 5.7: I-V data for cells with and without optimized grid design fabricated with PV168 Ag paste using co-firing process (900° C/80 ipm) on high sheet-resistance (100 Ω/sq ) emitters with LF-$SiN_x$ AR coating.

| Cell Grid | | $V_{oc}$ (mV) | $J_{sc}$ (mA/cm²) | FF | Eff (%) | n factor | $R_s$ (Ω-cm²) | $R_{sh}$ (Ω-cm²) |
|---|---|---|---|---|---|---|---|---|
| 8-line (not optimized) | Best | 645 | 34.6 | 0.771 | 17.2 | 1.08 | 1.02 | 495,500 |
| | Average | 645 | 34.4 | 0.759 | 16.8 | 1.08 | 1.33 | 87,255 |
| 10-line (optimized) | Best | 646 | 34.5 | 0.780 | 17.4 | 1.09 | 0.79 | 281,975 |
| | Average | 645 | 34.4 | 0.777 | 17.2 | 1.09 | 0.89 | 742,029 |

The highest $V_{oc}$ of 648 mV was obtained for a LF-$SiN_x$/RTO stack passivated cell with a planar 100 Ω/sq emitter. This cell gave an efficiency of 17.5% with the optimized grid design.

## 5.4 Conclusions

In this chapter, a combination of modeling and deeper, fundamental understanding and technology development led to a 1.5% increase in absolute cell efficiency. Screen-printed solar cells are generally made on 30-60 Ω/sq emitters because of the challenge of achieving good screen-printed contacts to high sheet-resistance emitters. The use of low sheet-resistance emitters results in appreciable loss in cell performance because of the heavy doping effects and high emitter saturation current density. The research in this chapter demonstrated for the first time that it is possible to obtain high fill factors on 100 Ω/sq emitters using a manufacturable single-step firing scheme in conjunction with an appropriate Ag paste like PV168 from DuPont. A combination of fundamental understanding and process optimization, involving rapid firing at ~830-840° C, resulted in high fill factors of ≥0.775 on a 100 Ω/sq emitter. Two conventional commercial Ag pastes gave inferior contact quality on the same 100 Ω/sq

emitter when fired using the same conditions because of significant Ag penetration near the p-n junction. This is attributed to excessive Si etching at higher firing temperatures by the frit used in those pastes. At lower or conventional firing temperatures (~750°C), when Ag penetration is not excessive, high contact resistance becomes the problem for the conventional pastes on 100 Ω/sq emitters. IQE analysis of the co-fired 45 Ω/sq- and 100 Ω/sq-emitter cells showed an appreciable improvement in the short-wavelength response because of the lightly doped emitter. The rapid co-firing process developed in this research using the PV168 also gave good BSF or back-surface velocity at no additional cost because of the higher firing temperature used. An absolute efficiency improvement of ~0.5% (from 16% to 16.5%) was achieved for the 100 Ω/sq cell over the 45 Ω/sq cell, even with poor front-surface passivation on both devices. An additional efficiency enhancement of ~0.6% (from 16.5% to 17%) was achieved by improving the front-surface passivation or FSRV of the high –sheet-resistance emitter cells from 250,000 cm/s to 40,000 cm/s. This was accomplished by using a low-frequency $SiN_x$ deposited at ~430° C. This resulted in planar FZ cell efficiencies in excess of 17% on a 100 Ω/sq emitter, demonstrating ~1% increase in absolute efficiency over the co-fired 45 Ω/sq-emitter cell with inferior surface passivation. Finally, optimization of the front-contact metal grid improved the FF from 0.771 to 0.780, resulting in a cell efficiency of 17.4%. Thus, a combination of high sheet-resistance emitter, improved front-surface passivation, and optimized grid design raised the cell efficiency from 16% to 17.4%. A stack oxide/silicon nitride front surface passivation further improved the 100 Ω/sq emitter cell performance due to the enhanced short-wavelength response.

# CHAPTER 6

# UNDERSTANDING THE FORMATION OF AG-SI CONTACT INTERFACE AND CURRENT TRANSPORT THROUGH IT IN SCREEN-PRINTED AG CONTACTS TO HIGH SHEET-RESISTANCE EMITTERS

## 6.1 Introduction

After establishing the technology of making good screen-printed contacts to high sheet-resistance emitters in Chapter 5, a detailed study was conducted on the three pastes, PV168, A, and B, using two different firing conditions. The contact interface structure was correlated with the electrical properties of ohmic contacts and solar cell performance. This chapter focuses on understanding the contact interface and possible current transport mechanisms. First, the quality of the screen-printed (SP) contact is assessed in terms of the specific-contact resistance, junction leakage current, and shunting and is then compared with the contact interface structure, with the objective of correlating the physical and electrical properties of the screen-printed contacts. Contact parameters were determined by light and dark I-V, Suns-$V_{oc}$, and TLM measurements. The contact interface was examined by AFM, SEM, TEM, and SIMS measurements.

The specific-contact resistance is strongly dependent on the surface doping ($N_s$) for the tunneling regime ($N_s$>$10^{19}$ $cm^{-3}$) and is given as [30]

$$\rho_c = \frac{k}{qTA^*}\exp\left[\frac{4\pi\sqrt{\varepsilon_{Si}m^*}}{h}\frac{\Phi_{Bn}}{\sqrt{N_s}}\right] \tag{6.1}$$

where $q$ is the elementary charge, $h$ is the Planck constant, $\varepsilon_s$ is the semiconductor permittivity, $\Phi_{Bn}$ is the barrier height between the metal and semiconductor, $m^*$ is the effective mass of the charge carriers, $k$ is the Boltzmann constant, $T$ is the temperature in $^oK$, and $A^*$ is the effective Richardson constant. The derivation of the above equation is given in Appendix G. Shallow high sheet-resistance emitters have a lower surface doping compared with lower sheet-resistance emitters. Hence, it is harder to achieve a low specific-contact resistance (< 3 m$\Omega$-cm$^2$) on the higher sheet-resistance emitter. Since screen-printed contacts are not full-area contacts, a macroscopic specific contact resistance needs to be defined: $\rho_{cm}=\rho_c/A_f$ , which is a function of the contact-area fraction, $A_f$, and the microscopic specific contact resistance, $\rho_c$.

The first requirement for achieving low-resistivity ohmic contact to the Si emitter is to punch through the $SiN_x$ layer during the contact firing process [77]. Second, the paste and firing combination must result in a metal-Si contact area fraction that is sufficient for low contact resistivity. Third, the fired or modified glass layer should be thin enough for tunneling and/or it should be conductive to allow for current transport. In addition, the 100 $\Omega$/sq emitter is more prone to shunting since it has a shallower p-n junction compared to the 45 $\Omega$/sq. This adds another constraint to the chemistry of the glass frit and metallic constituents of the paste to prevent shunting and excessive impurity diffusion.

The above concepts have been used in conjunction with new findings from this study to explain why, of the three Ag pastes studied in the previous chapter, PV168 paste from DuPont gave the highest fill factors (FFs) while the other two pastes did not work as well on 100 Ω/sq emitters. To gain a better understanding of the interface structure requirements for achieving good-quality screen-printed ohmic contact to a 100 Ω/sq emitter, the same three commercial thick-film Ag pastes (pastes PV168, A, and B), studied in Chapter 5, are examined in more detail in this chapter in an attempt to correlate the electrical and physical properties of screen-printed contacts. To understand the temperature dependence of the contact interface and its quality, two different firing conditions were examined for each paste.

## 6.2 Experimental Method

Screen-printed $n^+$-p-$p^+$ solar cells (4 $cm^2$) were fabricated on single-crystal Si using different Ag pastes and firing conditions on a 100 Ω/sq emitter. P-type, 0.6 Ω-cm, 300-μm-thick (100) float-zone (FZ) substrates were used for all the experiments. The cell processing sequence, as well as the process conditions, are shown in Table 6.1. Silicon wafers were first chemically cleaned, followed by $POCl_3$ diffusion to form the $n^+$-emitter. After the phosphorus-glass removal and another clean, a plasma-enhanced chemical vapor deposited (PECVD) $SiN_x$ antireflection (AR) coating was deposited on the emitter. Next, an Al paste was screen printed on the back side and dried at 200° C. An Ag grid was then screen printed on top of the $SiN_x$ film and then dried. Ag and Al contacts were co-fired (single firing step) in a lamp-heated three-zone belt-line furnace (RTC LA-310). The actual sample temperature profile was measured by using a fast

response K-type thermocouple with a closed-end tip loosely attached to the surface of the wafer as it travels through the belt furnace  Nine  4 $cm^2$ cells on large-area wafers were then isolated using a dicing saw and then exposed to ~15 min forming gas anneal (FGA).

Table 6.1: Process sequence and conditions used for fabricated cells.

| Process | Process/Cell conditions |
|---|---|
| 1- Wafer cleaning | 1- DI $H_2O$ rinse :  3 min |
| | 2- 2.5% HF dip (hydrophobic surface) |
| | 3- DI $H_20$ rinse:  3 min |
| | 4- 2:1:1 $H_2O$:$H_2O2$:$H_2SO_4$: 10 min |
| | 5- DI $H_20$ rinse:  3 min |
| | 6- 2.5% HF dip (hydrophobic surface) |
| | 7- DI $H_20$ rinse:  3 min |
| | 8- 2:1:1 HCl:$H_2O_2$:$H_2O$ :  10 min |
| | 9- DI $H_20$ rinse:  3 min |
| | 10- 2.5% HF dip (hydrophobic surface) |
| | 11- DI $H_20$ rinse:  30 sec |
| 2- Phosphorus diffusion | Deposition time: 20 min |
| | Drive-in tme: 12 min |
| | T = 877°C for the ~0.5-μm 45 Ω/sq emitter, $N_s$=2.6x$10^{20}$ $cm^{-3}$ |
| | T = 847°C for the ~0.28-μm 100 Ω/sq emitter, $N_s$=1.48x$10^{20}$ $cm^{-3}$ |
| 3- Phosphorus glass removal | 1- 2.5% HF dip (hydrophobic surface) |
| | 2- DI $H_2O$ rinse: 30 sec |
| 4- PECVD $SiN_x$ | Low-frequency (50 KHz) direct plasma ~435°C wafer deposition temperature |
| 5- Al screen printing | ~35 μm Al thickness after firing |
| 6- Ag screen printing | ~10-14 μm gridline height |
| | PV168 gridline width ~75-80 μm |
| | 4948 gridline width ~100 μm |
| | 3349 gridline width ~110 μm |
| 7- Contact organic burnout | 350-400°C for ~45 sec |
| 8- Contact co-firing | Actual peak temperature: ~ 746°C for ~1 sec or ~835°C for ~1 sec |
| 9- Forming gas anneal | 10:1 $N_2$:$H_2$ for ~15 min at 400°C |

Cross-sectional scanning electron microscopy (SEM) (JEOL FE-SEM-6320F) and plane-view atomic force microscopy (AFM) (DI 3100) measurements were performed to study the structure of the Ag-Si interface. Cross-sectional conductive AFM (CAFM)

images were taken to investigate the conductivity through the bulk of the PV168 Ag gridline for high and low firing temperatures. The CAFM technique uses a bias voltage applied between a highly conductive tip and the Al back contact as the tip passes over the cross-sectional area of the grid. No etching was found necessary for the cross-sectional SEM and CAFM measurements. However, the Ag grid was etched prior to the AFM using HF, $HNO_3$, and HF acids in sequence to remove the metal and the glass to delineate the footprints of the etched Ag crystallites into the Si surface. The plane-view AFM images of the surface morphology were acquired in intermittent tapping mode. Cross-sectional TEM (Philips CM-30) was performed on selected samples. The sample preparation for the TEM measurement involved standard mechanical polishing down to about 50 μm, followed by dimple polishing down to a thickness of around 5μm. The samples were then ion beam milled using a Gatan precision ion polishing system (PIPS) at low energy and low angle. Secondary ion mass spectroscopy (SIMS) measurements were taken on selected samples to determine the Ag and P concentration profiles in the silicon directly underneath the Ag grid using a CAMECA IMS-5F ion microscope. The Ag grid was etched in HCl for the SIMS measurements to prevent any Si etching. The samples were bombarded with 5.5 KeV $O_2^+$ primary ions for the analysis of Ag and Al, whereas14.5 KeV $Cs^+$ primary ions were used for P. The primary ion beam was raster scanned over a square area of 150 μm × 150 μm. Positive or negative ions were collected from ~20 μm diameter area in the center of the rastered crater for Ag and P, respectively.

Specific-contact resistance was determined by using the transfer-length method (TLM) pattern [33], which was printed simultaneously with the grid. The cell parameters were measured by light I-V for determining the open-circuit voltage ($V_{oc}$), short-circuit

current ($J_{sc}$), FF, and cell efficiency, as well as the series ($R_s$) and shunt resistances ($R_{sh}$) [26]. Suns-$V_{oc}$ [29] was used for evaluating the junction leakage-current ($J_{o2}$) at a second-diode ideality factor ($n_2$) of 2.

## 6.3 Results and Discussion

In the previous chapter, paste PV168 was found to work best on the high sheet resistance-emitter mainly because the glass frit used in this paste is mild in terms of aggressiveness in etching the $SiN_x$ and the Si emitter. Because of this characteristic, higher temperatures (>810° C) in the belt furnace had to be used to make good ohmic contact, as opposed to conventional firing temperatures of 700-750° C. To understand the impact of glass frit chemistry and firing temperature on the interface structure, the interface was examined for all three pastes for high and low firing temperatures.

### 6.3.1 Investigation of the Lower-Temperature Firing (746°C/1 sec)

Commercial pastes are generally fired at sample temperatures around 700° C [56]. This process works well for the 45 Ω/sq emitter. As shown in Table 6.2, pastes A and B gave reasonably low $R_s$ (~0.8 Ω-cm$^2$) and $J_{o2}$ (~25 nA/cm$^2$), along with high $R_{sh}$ (>7 kΩ-cm$^2$) on the 45 Ω/sq emitter, producing fill factors (FFs) greater than 0.780 and cell efficiency >16.7% on FZ Si. As expected, the lowest specific-contact resistance values were obtained for the 45 Ω/sq emitters. Also, as shown in Table 6.2, both pastes failed on the 100 Ω/sq emitter for the 746° C firing condition, as no improvement over the 45 Ω/sq cells was achieved. Thus, to understand the reasons for the poor

performance on the high sheet-resistance emitter, the contact behavior for each paste was investigated in detail in this section for the low-temperature firing case.

Table 6.2: The electrical performance of contacts and Si solar cells formed with the three pastes (PV168, A, and B) on a conventional 45 Ω/sq emitter and on a 100 Ω/sq emitter using low- (conventional) and high-temperature firing. Macroscopic specific- contact resistance ($\rho_{cm}$) values are shown after FGA.

| Paste | Peak Temp. (°C) | Emitter (Ω/sq) | $V_{oc}$ (mV) | $J_{sc}$ (mA/cm²) | FF | Eff (%) | n factor | $R_s$ (Ω-cm²) | $R_{sh}$ (Ω-cm²) | $\rho_{cm}$ (mΩ-cm$^2$) | $J_{o2}$ (nA/cm$^2$) |
|---|---|---|---|---|---|---|---|---|---|---|---|
| A | 746 | 45 | 631 | 33.10 | 0.782 | 16.3 | 1.10 | 0.802 | 7,838 | 0.24 | 25 |
| B | 746 | 45 | 634 | 33.74 | 0.782 | 16.71 | 1.09 | 0.880 | 96,782 | 0.43 | 26 |
| A | 746 | 100 | 639 | 33.82 | 0.730 | 15.77 | 1.08 | 2.067 | 11,454 | 4.11 | 27 |
| B | 746 | 100 | 582 | 34.19 | 0.575 | 11.44 | 3.59 | 0.449 | 43,518 | 0.40 | 2,678 |
| A | 835 | 100 | 634 | 34.18 | 0.771 | 16.69 | 1.17 | 0.753 | 77,750 | 0.30 | 26 |
| B | 835 | 100 | 555 | 34.55 | 0.528 | 10.11 | 3.82 | 0.490 | 5,740 | 0.59 | 16,139 |
| PV168 | 746 | 100 | 643 | 34.75 | 0.643 | 14.37 | 1.06 | 4.391 | 148,900 | 45.59 | 14 |
| PV168 | 835 | 100 | 646 | 34.48 | 0.782 | 17.42 | 1.08 | 0.854 | 131,404 | 1.06 | 15 |

The plane-view AFM image in Figure 6.1(a) shows that the 746° C firing of paste A produced a highly irregular distribution of Ag crystallites ~100 nm in depth. In addition, the contact area is quite small (~10%), which may not be suitable for high sheet-resistance emitters. This observation is consistent with the results of Ballif et al. [78] for this conventional paste and firing conditions. It was shown by model calculations in Chapter 4 that a specific-contact resistance of ≤3 mΩ-cm$^2$ is required to achieve FFs above 0.78. It is important to note that the TLM method (Chapter 2) gives a macroscopic specific-contact resistance ($\rho_{cm}$) for screen-printed contacts, which is inversely proportional to the contact area fraction $A_f$ ($\rho_{cm}=\rho_c/A_f$). Table 6.2 shows that the same firing condition produced a macroscopic specific-contact resistance of 0.24 mΩ-cm$^2$ on the 45 Ω/sq emitter. However, a higher macroscopic specific-contact resistance of ~4 mΩ-cm$^2$ is measured for the 100 Ω/sq emitter contact (Table 6.2), indicating the need for a higher contact area fraction of Ag crystallites embedded into Si for high sheet-

resistance emitters. The SEM image in Figure 6.1(b) shows the contact interface cross-section with thin glass regions for the 746° C/1 sec firing for paste A.

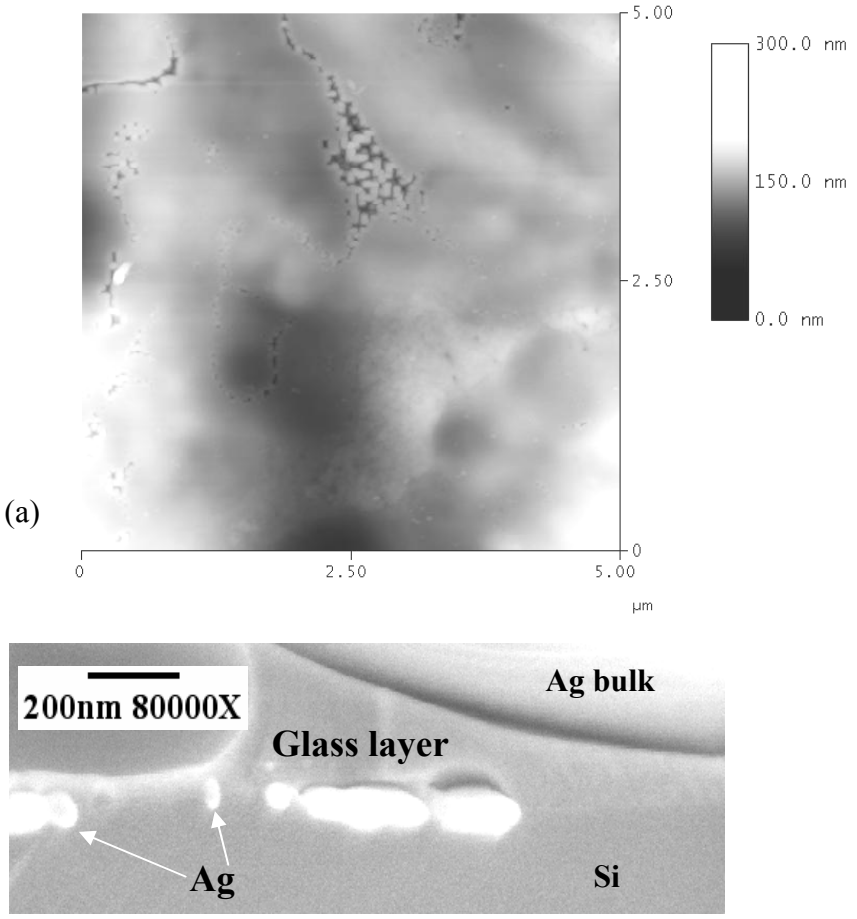


Figure 6.1 (a) AFM plane-view image of the contact interface after removing the glass frit and Ag and (b) SEM cross-section of the contact interface for paste A fired at 746°C/1 sec.

The AFM image in Figure 6.2(a) shows that paste B behaves quite differently than paste A for the 746° C firing. Paste B showed a fairly uniform and large distribution of small Ag crystallites (~25 nm in width). A regular distribution of small Ag crystallites is better for lower contact resistance compared to an irregular distribution of larger Ag crystallites that are localized in certain regions only. The SEM image in Figure 6.2(b)

reveals that most Ag crystallites formed at the Ag-Si interface for paste B are on the order of ~25 nm, but some Ag crystallites as large as ~100 nm in size are also present. The SEM micrograph in Figure 6.2(c) shows that ultra-thin glass regions that are suitable for carrier tunneling can occur for paste B for the 746° C/1 sec firing condition.

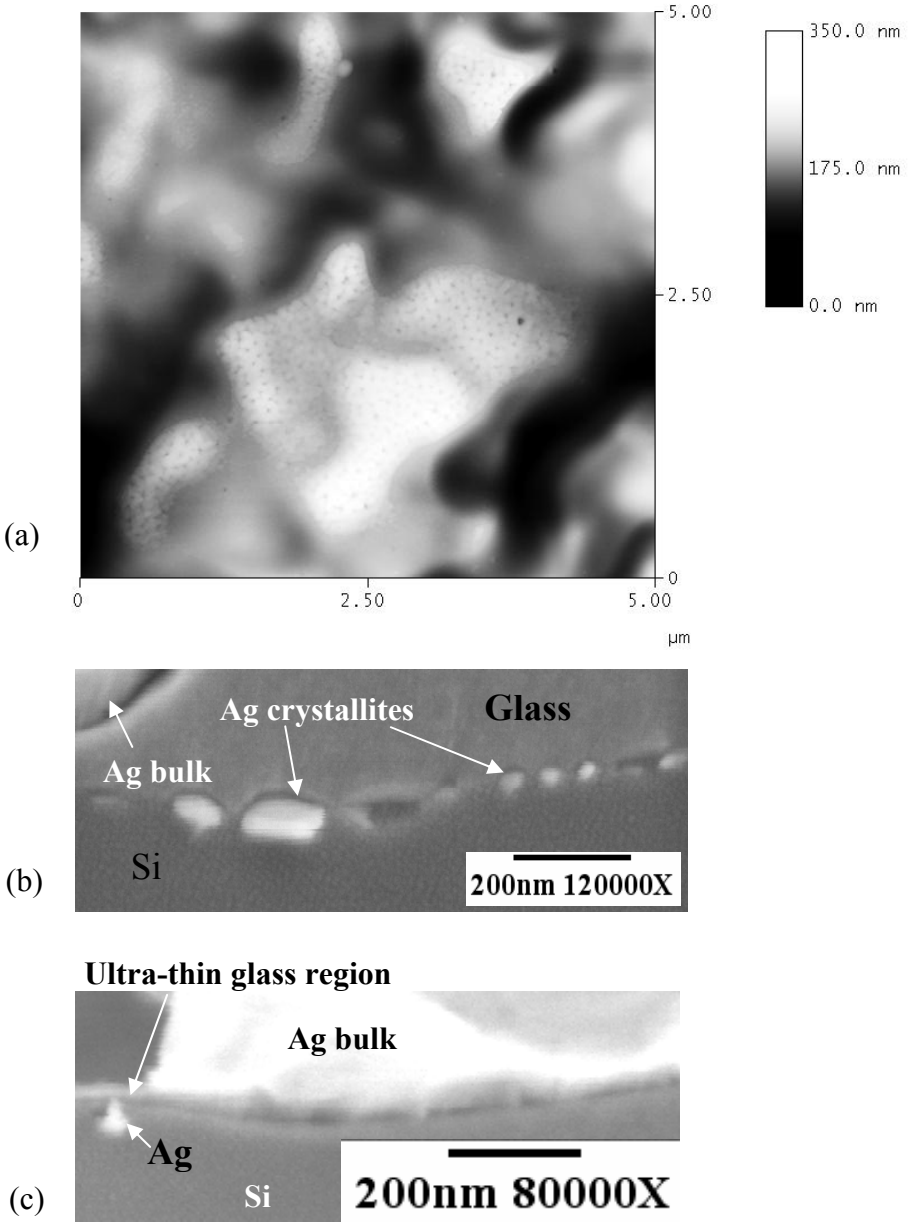


Figure 6.2 (a) AFM plane-view image of the contact interface after removing the glass frit and Ag, (b) SEM cross-section of the contact interface, and (c) SEM cross-section showing ultra-thin glass layer for paste B fired at 746° C/1 sec.

Another striking difference between pastes A and B is that the variation in the surface depth is much greater for paste B across the whole scanned surface, as seen from the AFM photographs in Figure 6.2(a) and Figure 6.1(a). These variations are up to 200 nm in depth for paste B. On the other hand, paste A has only a non-uniform distribution of the Ag crystallites. Thus, even at conventional 746° C/1 sec firing, paste B displays the aggressiveness of its glass frit, which probably enhances more Ag migration closer to the p-n junction. This was confirmed by the SIMS measurements in Figure 6.3, which revealed the presence of ~$3\times10^{17}$ $cm^{-3}$ Ag at or near the $n^{+}$-p junction located ~0.28 μm below the surface. This concentration is comparable to the emitter doping at the p-n junction and greater than the base doping. This increased the junction leakage current to 2678 $nA/cm^2$ (Table 6.2) and reduced the FF to 0.635.

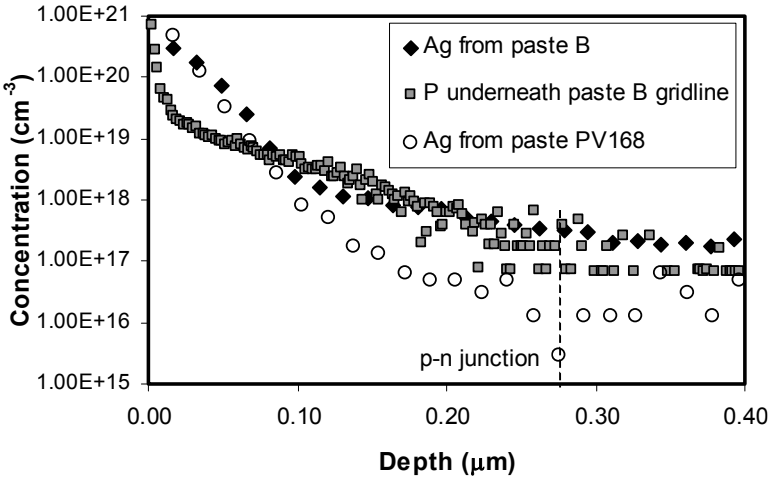


Figure 6.3. SIMS of the Ag and P concentration underneath paste B gridline after firing at 746° C/1 sec. Ag from paste PV168 fired at 835° C/1 sec is shown for comparison.

PV168 Ag paste, which has a less aggressive glass frit and finer Ag particle size compared to paste B, was also used for making contact to the 100 Ω/sq emitter using the

~750° C conventional firing. It is clear from Table 6.2 that the low-temperature (746° C) co-firing of PV168 paste resulted in unacceptably high specific-contact resistance (45 mΩ-cm$^2$) in conjunction with low FF (0.643) and poor cell efficiency (14.37%). To understand this behavior, TEM analysis was performed on the 746° C/1-sec fired sample. Figure 6.4(a) reveals that the thickness of the lead oxide glass varies extensively and the layer was not etched properly with the thickness of the SiNO layer ~65 nm in many regions, which is too thick for tunneling to take place. There were few regions where the SiNO is completely etched at this firing temperature. This explains the high contact resistance observed for the PV168 Ag paste when fired at a conventional firing temperature of 746° C/1 sec. This also indicates a much less aggressive glass frit chemistry in PV168 compared to conventional pastes A and B. Pastes A and B achieved good-quality contacts at 746°C/1 sec firing on the 45 Ω/sq emitter, as shown in Table 6.2, which indicates that the silicon nitride film is completely etched.

Figure 6.4(b) shows the cross-sectional conductive AFM images of the bulk of the PV168 Ag gridline and the Si beneath it for the ~750° C firing temperature. This technique can probe the variation in the conductivity of the gridline. The presence of a glass layer in the grid or at the interface can lower the grid conductivity in those regions. The bright contrast shows high conductivity or high current between the probes for the probing voltage applied between the back Al and the probing point within the grid. The absolute conduction through the bulk of the PV168 gridline was low (~18 nA current at 200 mV). The CAFM measurements also confirmed that ~750° C firing still gives a non-rectifying ohmic contact because similar current values were obtained when the applied voltage polarity was switched.

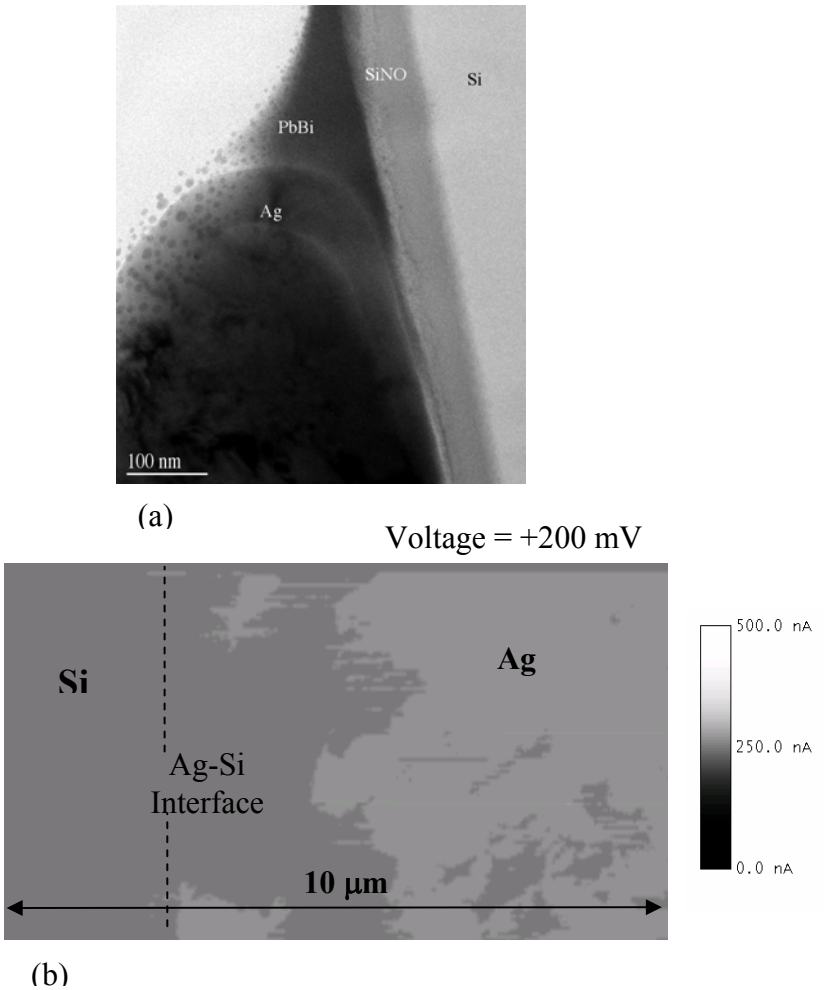


Figure 6.4 (a) Cross-section TEM image and (b) cross-section CAFM image of the PV168 Ag-Si contact fired at 746° C/1 sec.

## 6.3.2 Investigation of the Higher-Temperature Firing (835° C/1 sec)

Having established that conventional ~750° C/1 sec firing failed to achieve high-quality SP contacts for pastes A, B, and PV168, a higher-temperature firing condition was investigated. This higher-temperature firing condition has been used to completely punch through the SiNO film and achieve a low resistivity contact with the PV168 paste. Table 6.2 summarizes the electrical performance of contacts and solar cells fabricated with higher-temperature (835° C/1 sec) firing. For the PV168 paste, the 835° C firing

produced excellent ohmic contacts, with a specific-contact resistance of less than 2 mΩ-cm$^2$ and series resistance of 0.854 Ω-cm$^2$, resulting in a FF of 0.782 on a 100 Ω/sq emitter and a FZ Si cell efficiency of 17.4%.

Higher-temperature firing increases the aggressiveness of the etching reaction between the glass frit and the SiNO layer. Thus, for the ~835° C/1 sec firing condition, the SiNO is completely etched (except at very few regions where it is much thinner than the SiNO layer for the 750° C firing condition), allowing the glass frit with dissolved Ag to reach the underlying Si. Ag recrystallizes upon cooling, giving rise to the epitaxial growth of the Ag crystallites observed in Figure 6.5(a). The AFM conductivity is higher for both the Ag and glass regions at the 835° C firing (Figure 6.5(b)) compared to the ~750° C firing in Figure 6.4(b). This explains why the effective series resistance for the 835° C firing is 0.854 Ω-cm$^2$ as opposed to 4.39 Ω-cm$^2$ for the ~750° C firing (Table 6.2). Figures 6.4(b) and 6.5(b) support that the limited current transport between the Si emitter and the Ag bulk is the main reason for the high contact resistance for the 746° C/1 sec fired cell because of the incomplete etching of the dielectric SiNO layer. Hence, the higher-temperature (835° C) firing results in better current transport at the Ag-Si contact interface to give a current of 534 nA at 200 mV measured by CAFM (Figure 6.5(b)) compared with the 18 nA at 200 mV for the ~750° C firing. The higher-temperature firing-induced increase in CAFM current by a factor of 20-30 times agrees well with the 23 times decrease in specific contact resistance decrease from ~46 mΩ-cm$^2$ to ~2 mΩ-cm$^2$. To achieve similar current for the ~750° C-fired grid, the voltage applied to the grid had to be increased significantly from 200 mV to 1000 mV. The observed non-homogeneous conductivity of the Ag gridline in Figure 6.5(b), particularly near the Ag-Si

interface, is attributed to the presence of varying thickness of high-resistivity glass between Si and the Ag grid. The relative poor conductivity of the darker regions near the Ag-Si interface in Figure 6.5(b) is indicative of glass conductivity, which is lower than that of the Ag.

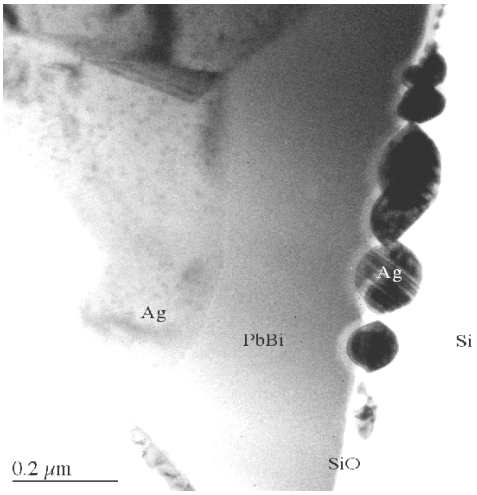


(a)

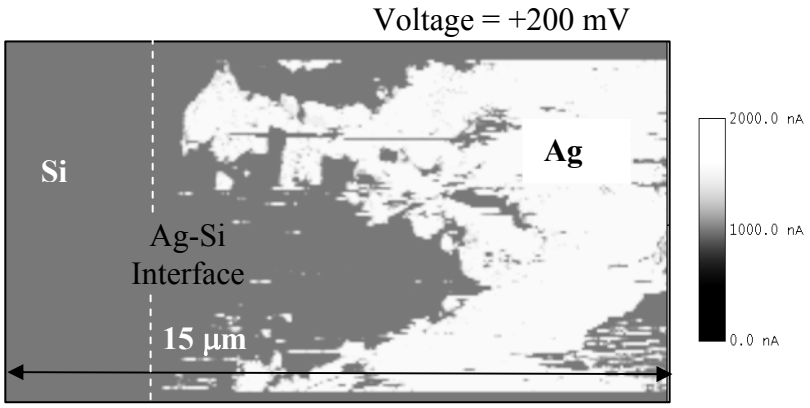


(b)

Figure 6.5 (a) Cross-section TEM image and (b) cross-section CAFM image of the PV168 Ag-Si contact fired at ~835° C/1 sec.

The SEM cross-section (Figure 6.6(a)) of the Ag-Si contact interface fired at 835° C revealed the presence 50-80-nm wide re-grown Ag crystallites for PV168 paste;

however, some larger conjugated Ag crystallites ~150 nm in width were also observed. Figure 6.6(b) shows the AFM image of the plane view of the same sample (fired at 835° C) after etching the Ag and the glass frit. Distributed pits observed in the AFM image are indicative of the footprints of the re-grown Ag crystallites into Si, which were removed during the Ag etching prior to AFM. The AFM image in Figure 6.6(b) also reveals that the depth of these crystallites in the Si is on the order of 60 nm (notice that the depth scale goes from 0-100 nm), which is much smaller than the junction depth of ~0.28 μm for the 100 Ω/sq emitter. This is in good agreement with the slight shift observed in the SIMS phosphorus profiles for regions with and without the gridline, which showed a displacement of ~55 nm, approximately (Fig. 5.3 in Section 5.3.2) equal to the penetration depth of the Ag crystallites for the PV168 paste. The Ag crystallite penetration depth of only ~60 nm also explains why there was no appreciable shunting in the case of the PV168 paste even after the 835° C firing. The shunt resistance and junction leakage current values were very reasonable (131.4 kΩ-cm$^2$ and 15 nA/cm$^2$, respectively), contributing to the observed high FF of 0.782 (Table 6.2).

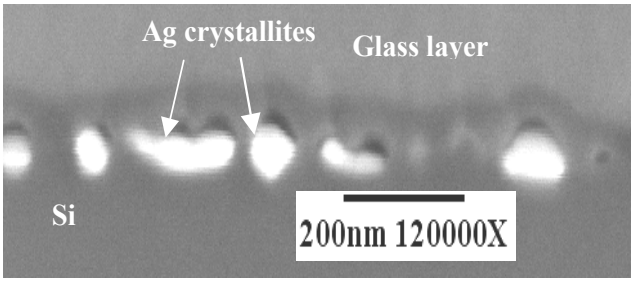


(a)

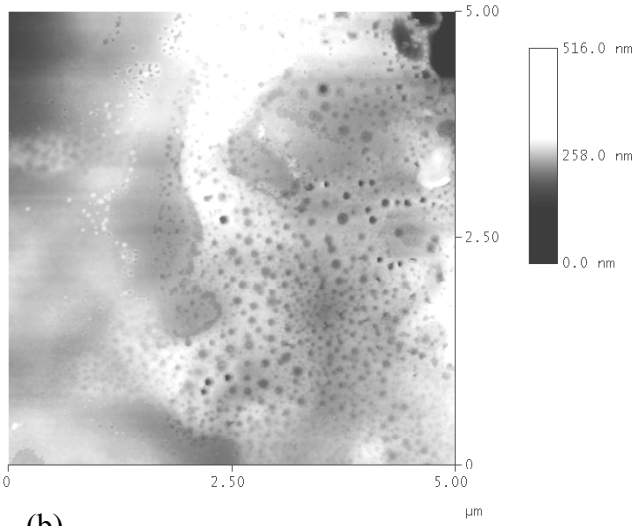


(b)

Figure 6.6 (a) Cross-section SEM image of the PV168 contact interface and (b) plane-view AFM image of the contact interface after removal of the glass frit and Ag for 835° C/1 sec firing.

The AFM image in Figure 6.6(b) also reveals a fairly uniform and larger distribution of Ag crystallites, much more than that for paste A (Figure 6.1(a)) and more than reported by Ballif et al. for a conventional paste and firing scheme [78]. The area coverage of the Ag crystallites is estimated at ~50% for the PV168 paste. The regular transfer of dissolved Ag through the glassy layer to the Si surface results in a uniform distribution of a large number of Ag crystallites (Figures 6.6(a) and (b)). The higher-temperature firing (835° C) dissolves more Ag into the glass frit, which reaches super

saturation upon cooling, and the excess Ag precipitates onto the Si emitter surface as crystallites.

The PV168 paste composition is such that even at ~835° C firing, which was necessary to achieve acceptable contact and series resistance, Ag crystallites are small enough (less than the 0.28 μm junction depth) to avoid junction shunting. This was the key to achieving high FF on a 100 Ω/sq emitter with PV168 paste. At the higher firing temperature of 835° C, PV168 produced Ag crystallites of similar size to those of paste B fired at ~750° C. This also demonstrates that the glass frit in paste B is much more aggressive than that of PV168. Moreover, the Ag profile of the PV168 paste showed a much lower Ag concentration even when fired at ~835° C compared to the ~750° C firing for paste B (Fig. 6.3). This demonstrates the ability of the PV168 glass frit to inhibit Ag from excessively migrating into the emitter region compared to paste B.

For the PV168 paste, Ag grain growth in the Ag bulk of the grid, above the glass layer, of up to ~4.5 μm was observed after the 835° C firing as opposed to ~2.1 μm for the ~750° C firing. In addition, the grains formed at 835° C firing showed a very compact structure. This yielded a lower gridline resistivity of ~1.9 μΩ-cm, which is close to the resistivity of pure Ag (~1.7 μΩ-cm). The gridline resistivity after the ~750° C firing was ~2.5 μΩ-cm. It has been shown that the Ag grain growth of thick-film contacts increases with firing temperature [69], yielding denser films, causing the sheet resistivity of the Ag thick films to decrease with higher sintering temperatures in the range of 450° C -800° C. However, this is a very minor factor compared to the contact-resistance effect in determining the observed decrease in the overall cell resistance at 835° C.

The final step in applying this methodology to explain the difference in performance of the three screen-printed contacts involved studying the contact interface resulting from the 835° C firing of pastes A and B. The solar cell and contact data in Table 6.2 show that, unlike paste PV168, paste B failed again at 835° C, with the ideality factor (n) rising above three, in conjunction with very high leakage current exceeding 14,000 nA/cm$^2$. At 835° C, paste A gave very good contact resistance of ~0.3 mΩ-cm$^2$ in conjunction with series resistance of ~0.75 Ω-cm$^2$, but it also failed and gave a lower $V_{oc}$ compared with the PV168 paste on the 100 Ω/sq emitter (Table 6.2) because of shunting.

The SIMS measurements (Fig. 6.7) detected the presence of Al from the glass frit of paste A at a high concentration deep into the emitter region. The Al concentration profile shown in Figure 6.7 is believed to be responsible for the lower $V_{oc}$ shown in Table 6.2. The Al is a component in the glass used to make better adhesion and contact as Al wets the Si surface at lower temperatures than the contact co-firing temperature. The Al melts at 635° C and forms a eutectic with Si at 577° C with a doping concentration that depends on the firing temperature and a depth that depends on the original Al content [116]. For deep low sheet-resistance emitters and lower-temperature contact co-firing, the Al is probably fully compensated by the P and may have very minor negative effects. However, for the 0.28-μm deep 100 Ω/sq emitter, this is probably not the case. The $V_{oc}$ is pinned down to ~634 mV compared to 646 mV for the PV168 paste, possibly because of the Al diffusion that may result in a second p-n junction. The Ag concentration, as well as that of other metal impurities detected for paste A, is less than both the base doping and P concentration at the p-n junction. Thus, $J_{o2}$ is not high (~26 nA/cm$^2$).

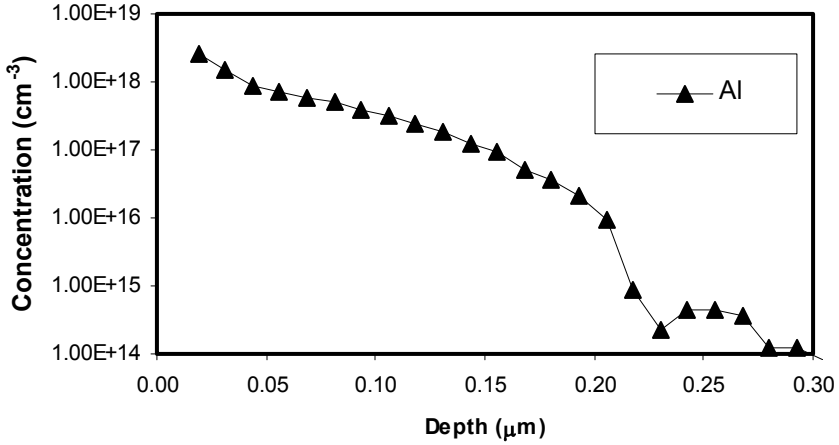


Figure 6.7. SIMS analysis of Al in the emitter region from paste A. The glass layer has been removed for this measurement.

Cell data showed that paste B failed again because of the excessive shunting after the 835° C firing. This is supported by the SEM image in Figure 6.8, which showed a significant increase in the size of Ag crystallites approaching 0.3-1 μm. Since this is even larger than the junction depth of ~0.28 μm, cells were badly shunted. A comparison of Figures 6.2 and 6.8 shows that the Ag crystallites grew almost 10 times in size (~100 nm⇒ ~1000 nm) when the paste B firing temperature was raised from ~750° C to 835° C. This is probably because the glass frit in paste B to dissolves a lot more Si and Ag at the higher temperature and becomes highly supersaturated, producing large precipitates or crystallites at the interface upon cooling. Figure 6.9 also confirms this shunting effect by showing a very high Ag concentration (greater than the P emitter concentration) in the emitter region and p-n junction.

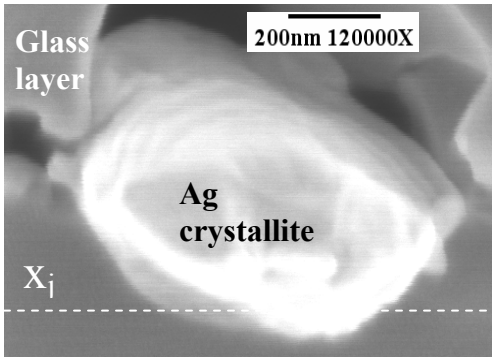


Figure 6.8 Cross-section SEM images of the Ag-Si interface for paste B fired at 835° C/1 sec. $X_j$ is the 100 Ω/sq emitter p-n junction depth of ~0.28 μm.

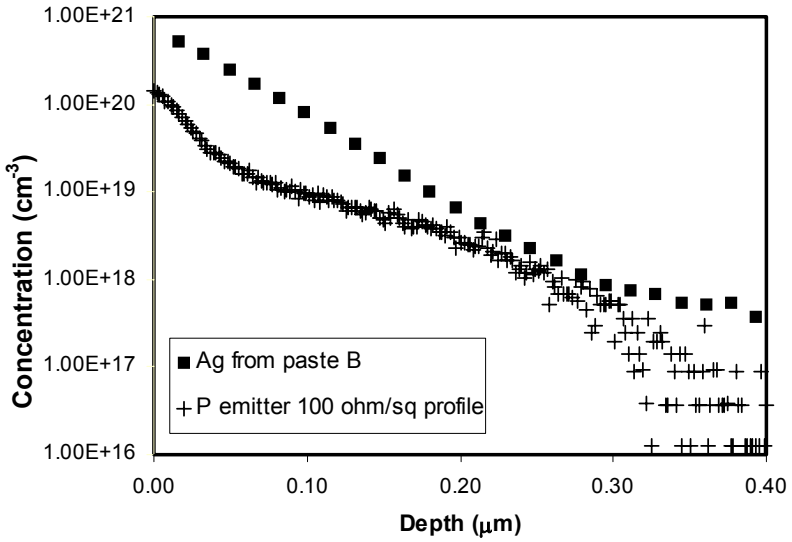


Figure 6.9 SIMS analysis of the Ag profiles in the Si emitter region underneath the Ag gridline for paste B fired at 835° C/1 sec. Ag crystallites have not been removed for this measurement.

### 6.3.3 Investigation of Phosphorus Injection from the Pastes

Since these pastes also had phosphorus**,** SIMS measurements were performed to investigate the possibility of the formation of a selective emitter resulting from the injection of P underneath the gridlines. This was determined by printing and firing the three pastes on an undiffused wafer (no emitter) with $SiN_x$ coating.

Figure 6.10 shows that all the pastes introduced only a limited amount of P into the Si, resulting in a sheet resistance of 900-5000 Ω/sq even for the higher-temperature (835° C/1 sec) firing condition used in this study. More important, the self-doping P concentration is much smaller than the P concentration associated with the diffusion of the 100 Ω/sq emitter (Fig. 6.10). Figure 6.10 also shows that the PV168 paste introduces much less P into Si compared to pastes A or B when fired at high temperatures. The glass frit of paste PV168 probably inhibits the P diffusion from the Ag powder coating since the fritless PV167 paste, which has the same P content as PV168, showed more P diffusion. Since the injected P concentration does not alter the net P concentration underneath the grid, selective-emitter formation can be precluded. Thus, self-doping can be ignored as the basis for any similarities and differences between the contacts formed by these pastes. However, if the injected P from pastes A and B in the frit few atomic layers of the Si emitter surface (Fig. 6.10) is electrically active, it could contribute significantly to lowering the specific contact resistance.

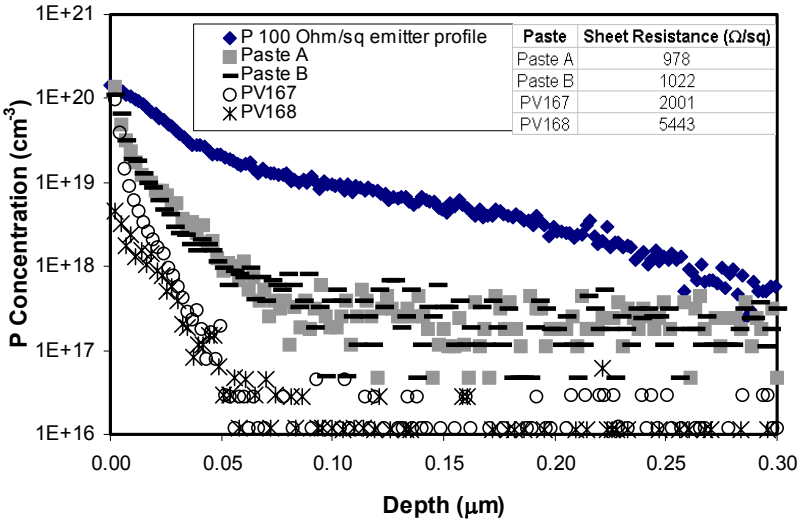


Figure 6.10 SIMS profiles of P detected in Si after ~835°C/1 sec firing of pastes A, B, PV67, and PV168 on undiffused Si. P profile for the 100 Ω/sq emitter is also shown for comparison.

### 6.3.4 The Role of the Glass Frit

To understand the role of the frit at the 835° C/1 sec firing condition, another paste was investigated, PV167 from DuPont, which is analogous to PV168 but without the glass frit. Even though more P diffusion was detected by SIMS for the PV167 paste compared with the PV168 paste, proper adhesion was not achieved with the PV167 paste when fired at the 835° C/1 sec condition on the bare Si emitter. This suggests that, for the fast firing condition, the presence of the glass frit plays a very important role in achieving proper contact, even at the Ag-Si eutectic temperature of 835° C [117]. This might be because the eutectic alloy between Ag and Si is difficult to form for fast firing conditions because phase equilibrium is not achieved. Therefore, glass frit provides the adhesive bond phase when no eutectic bond is formed. The glass frit also helps in dissolving enough Ag at the Ag-Si eutectic temperature to produce a large and relatively uniform distribution of Ag crystallites. This is why the PV168 performs well around the Ag-Si eutectic temperature and fails at the low firing temperature for high sheet-resistance emitters.

The eutectic reaction is not necessary for thick-film contacts to the Si emitter, since pastes A and B develop Ag crystallites below the eutectic temperatures. The reason that PV168 works at 835° C/1 sec firing is because the SiNO is completely etched at this firing condition. It is probably not a coincidence that PV168 makes an ohmic contact around the Ag-Si eutectic temperature of 835° C, since this paste was originally designed to act as a self-doping paste at temperatures ≥835° C by making use of a Ag-Si alloy [97, 118].

### 6.3.5 Investigation of the Possible Current Transport Mechanism at the Contact Interface

Since the contact interface consists of Ag crystallites embedded into the Si surface with a lead oxide glass layer in between the crystallites and Ag grid, it is not well understood how the carriers flow from the Si emitter to the grid. Since very few or no direct connection paths are observed between the Ag grid and silicon emitter in SEM, tunneling through the glass via metal precipitates is one possibility. The other is that the glass layer becomes conductive. To understand this, some observation and calculations are performed in this section. Figure 6.11 shows the modeling of the macroscopic specific-contact resistance as a function of surface concentration for different Ag-Si area coverage using equations 6.1 and 6.2 with an Ag-Si barrier height of 0.78 eV [110]. Figure 6.11 shows that at $N_s$=1.48×10$^{20}$ cm$^{-3}$ for the 100 Ω/sq emitter; the microscopic specific contact resistance ($\rho_c$) is calculated to be ~0.36 mΩ-cm$^2$ for a full-area contact. This translates to macroscopic specific contact resistance ($\rho_{cm}=\rho_c$/area) of ~0.72 mΩ-cm$^2$ for 50% area coverage and 3.6 mΩ-cm$^2$ for 10% area coverage, which are close to the ones measured for pastes A and PV168, respectively, after 400° C forming gas anneal (FGA), as shown in Figure 6.12 and Table 6.2**.** Comparing experimental results for $\rho_{cm}$ with the modeling results for pastes A and B (~750° C/1 sec firing) and paste PV168 (835° C/1 sec firing), it appears that after FGA the entire Ag crystallite-Si contact area begins to participate in the current transport and not just the regions where the glass layer is ultra-thin. This suggests that the glass becomes more conductive after FGA

Figure 6.12 shows that before FGA, paste PV168 has the highest $\rho_{cm}$ (~24 mΩ-cm$^2$) compared with the other two pastes. This drops substantially to less than 2 mΩ-cm$^2$

after FGA. This indicates an enhancement in the conduction of the lead oxide glass layer, which separates the Ag crystallites and the Ag bulk of the grid, as shown in Figure 6.5(a) for the 835° C firing. This lead oxide glass layer is generally much thicker (>200 nm) than the lead oxide glass layer after the ~750° C firing (Fig. 6.4(a)). Although a few direct interconnections between the Ag crystallites and the Ag bulk might exist, none were observed using both the high magnification SEM and TEM for the PV168 paste. Therefore, for the 835° C-fired PV168 contact, the main current transport mechanism probably involves conduction via tunneling through the discontinuous metal granules [119] in the glassy layer. Paste B also shows a significant drop in $\rho_{cm}$ after FGA (~6 mΩ-cm$^2$ to ~0.4 mΩ-cm$^2$). However, in Figure 6.12, paste A does not show as big a drop (~8 mΩ-cm$^2$ to ~3.5 mΩ-cm$^2$) in specific contact resistance as the DuPont paste PV168 and paste B, probably because of the different elements and composition of the frit.

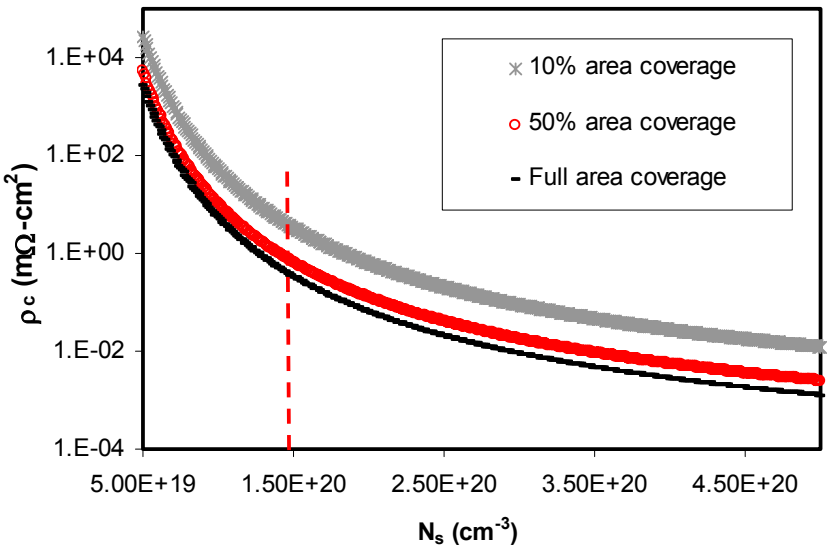


Figure 6.11 Modeling of the specific contact resistance versus the surface doping concentration of the Si emitter for a Ag-Si contact with different contact area fractions.

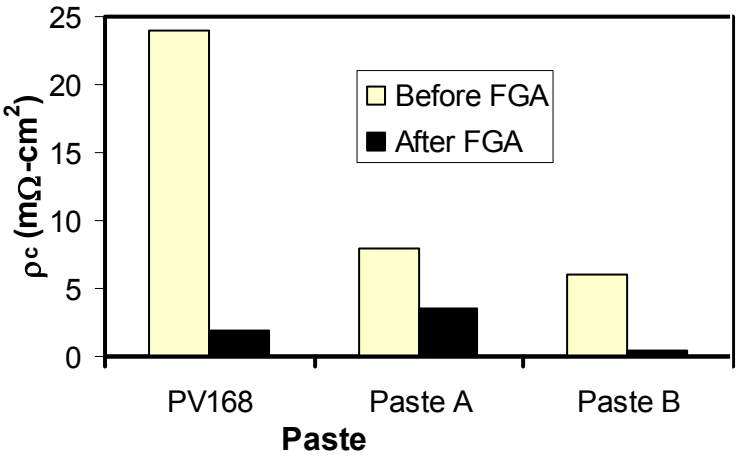


Figure 6.12 The effect of FGA on paste A and B fired at 746° C/1 sec and paste PV168 fired at 835° C/1 sec.

Annealing in a hydrogen atmosphere has been shown to enhance the conduction of the fired glass layer of thick-film silver contacts for solar cells [79, 83]. Significant conductivity of the lead silicate glass has been observed when metal precipitates take part in the conduction after reduction in a hydrogen atmosphere [119]. However, Pb atoms in the glass usually agglomerate into large Pb crystallites, and thus it is less probable for tunneling to occur. It has been suggested that Bi ions significantly increase the conductivity of lead-silicate glasses because they act as tunneling centers after reduction in a hydrogen atmosphere [119]. Bi was detected in the glass frit of PV168 Ag paste as well as in the fired glass layer formed between crystallites and the Ag grid (Figs. 6.4(a) and 6.5(a)), which might explain the significant reduction in the specific-contact resistance for the DuPont PV168 glass frit after the forming gas anneal.

Current transport probably takes place by (a) conduction through some moderately thick glass layer regions via multi-step tunneling involving metal precipitates

[79, 120] and (b) by direct tunneling through ultra-thin glass regions. Ultra-thin glass regions were found to occur for conventional pastes (A and B), Figures 6.1(b) and 6.2(c). However, for the PV168, ultra-thin glass regions were not observed for the 835° C firing temperature. Hence, the current transport probably takes place via multi-step tunneling through the glass layer, which explains the need for FGA, which helps the formation of small metal precipitates, to achieve low contact resistivity for the PV168 paste.

### 6.3.6 Understanding the Effect of Forming Gas Anneal (FGA) on the Physical Behavior of the Glass Layer

An attempt is made in this subsection to understand the physical effect of the forming gas anneal on the glass structure. As mentioned previously, conduction in the glass layer is believed to take place by a tunneling or hopping mechanism via metallic granules or precipitates in the glass. It is believed that hydrogen treatment reduces the metal precipitates in the glass along with the spacing between them [79].

The structure of the glass and Ag crystallites was analyzed using high-resolution TEM of the contact interface shown in Figure 6.13. It is clear from the figure that the Ag crystallites precipitate from the glass layer into the Si emitter surface. The glass layer has mainly Pb and Bi detected by EDS after firing. Other elements like Ag, O, Si, and N were also present. The white spots shown in Figure 6.13 are believed to be Pb/Bi/Ag precipitates of ~5 nm size. The PV168 contact in Figure 6.13 was fired at ~840º C for ~1 sec with no forming gas anneal.

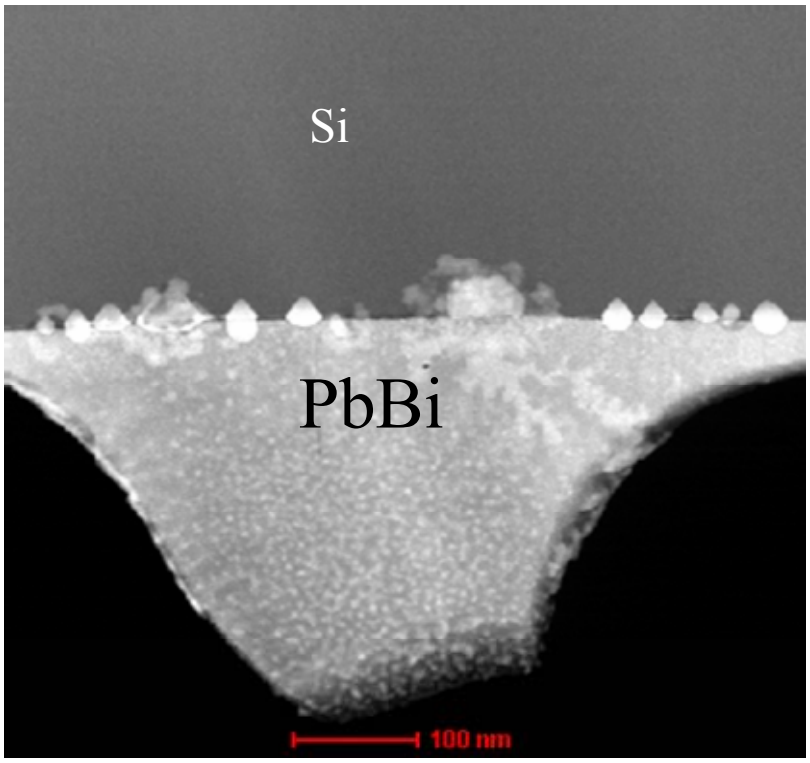


Figure 6.13 TEM cross-section image showing the structure of the fired glass layer.

Figure 6.14 shows the same screen-printed contact after the forming gas anneal at 400° C for ~15 min. It is interesting to note that the metal precipitates are much smaller now (white spots) after the forming gas anneal. These metal precipitates are roughly on the order of 5 Å and have undergone ~10 times reduction in size by FGA. This is attributed to the presence of hydrogen in the forming gas ambient because annealing in nitrogen ambient showed no reduction in the specific-contact resistance or enhancement in the fill factor [79]. Hydrogen anneal works because it can diffuse through the screen-printed contact and glass regions to act as a reducing agent for the metal oxides present in the glass layer [121].

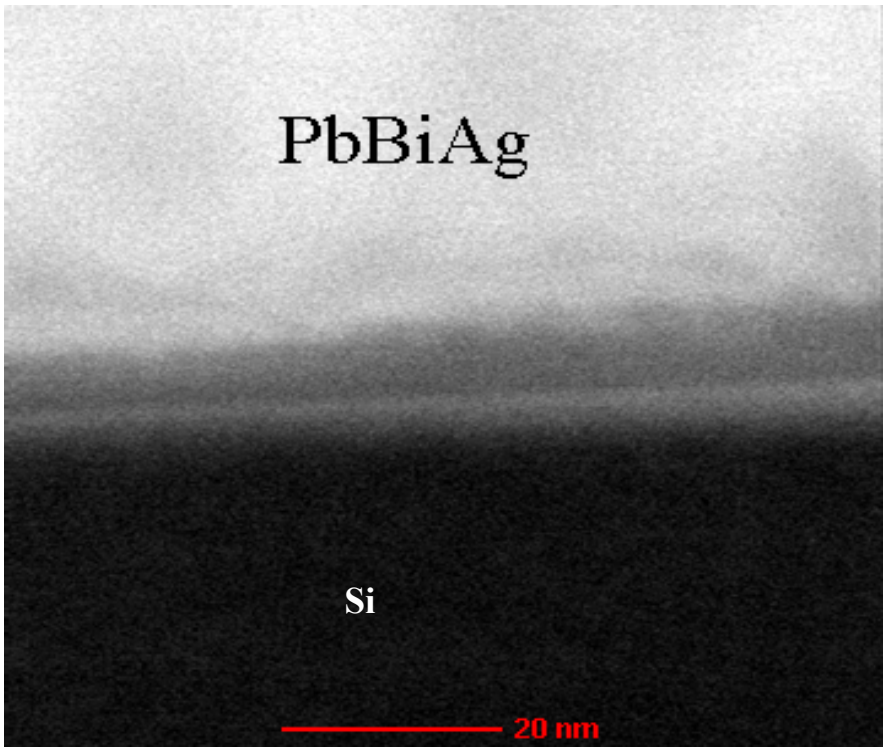


Figure 6.14 High magnification TEM cross-section image showing the glass layer of the thick-film contact after firing and after a forming gas anneal.

An attempt was made to calculate the tunneling probability through a glass region sandwiched between metal precipitates. According to the literature [110], for tunneling through a lead borosilicate glass layer in contact with the Pb or Ag metal precipitates, a barrier height of ~0.79 eV can be assumed due to the image lowering effect, which is half of the bandgap (1.58 eV) of the lead borosilicate glass [122]. For an incoming electron of energy equal to the metal Fermi level or metal work function, which is 4.25 eV for Pb, the tunneling probability can be calculated for a parabolic potential barrier using the following equation derived from the WKB approximation [110] (see Appendix H):

$$\Theta = \exp\left(-\frac{\pi\sqrt{qm^*}(\phi_B)^{3/2}}{2\sqrt{2}\hbar\xi}\right) \tag{6.2}$$

where $q$ is the elementary charge, $m^*$ is the mass of an electron, $\hbar$ is the reduced Planck constant, $\phi_B$ is the barrier height, L is the barrier width, and $\xi$ is the electric field. The detailed derivation of this equation is given in Appendix H.

The calculated results are plotted in Figure 6.15, which show that a spacing or glass thickness between metal precipitates less than ~60 Å is necessary for tunneling to occur. The Pb/Bi/Ag metal precipitates in the glass layer of PV168 contact satisfy the tunneling probability requirement because according to Figure 6.15, metal granules are only ~5 Å apart and seem to be evenly dispersed throughout the glass layer.

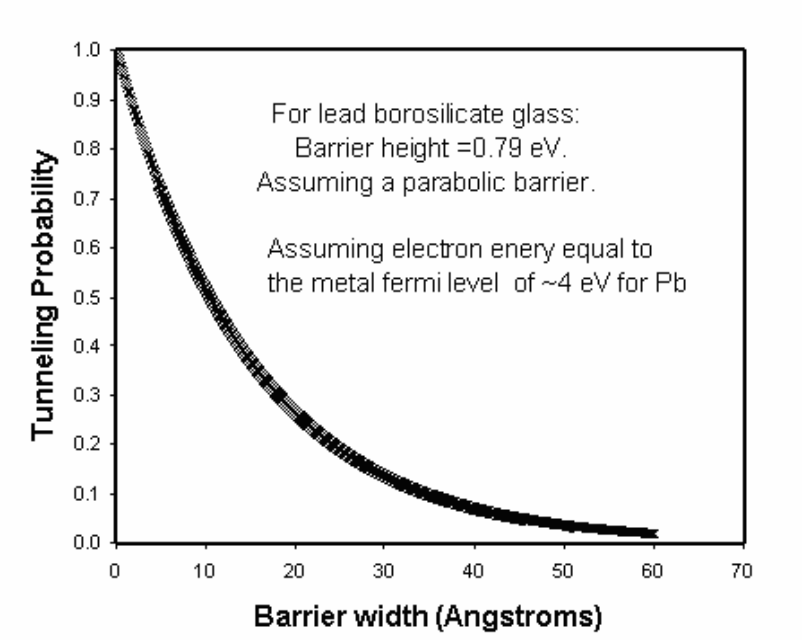


Figure 6.15 The tunneling probability as a function of the barrier width. L.

## 6.4 Conclusions

Because of the considerable lack of understanding of the current transport in screen-printed contacts, an attempt was made in this chapter to correlate the electrical and physical behavior of the screen-printed contacts to high and low sheet-resistance emitters. It is found that higher firing temperature enhances the etching reaction of the glass frit, which dissolves more Ag to produce larger Ag crystallites along with a thicker glass layer between the Ag crystallites and Ag bulk. Proper glass frit chemistry can allow for the complete etching of the $SiN_x$ layer, needed for low contact resistance, while arresting the diffusion of Ag into the junction, which is also necessary for high FF. Regions with very thin glass layer help improve the current transport via tunneling or by facilitating a direct connection between the Ag crystallites and Ag bulk. This study shows that it is important to optimize the following to achieve the best results: (1) high sheet-resistance emitter profile (e.g., surface concentration and depth) to obtain <3 $m\Omega\text{-}cm^2$ macroscopic specific contact resistance, (2) combination of paste and rapid firing scheme to precipitate a large number of small Ag crystallites to avoid shunting; (3) the glass frit aggressiveness to etch through the silicon nitride film without excessive etching of the Si emitter and to prevent the formation of very large Ag crystallites; (4) the glass frit chemistry to achieve ultra-thin glass regions to promote direct tunneling; (5) the composition and properties of the inorganic constituents of the paste to avoid excessive diffusion of Ag and other impurities into the Si emitter.

# CHAPTER 7

# UNDERSTANDING AND DEVELOPMENT OF SILVER PASTES FOR SILICON SOLAR CELLS WITH HIGH SHEET-RESISTANCE EMITTERS

## 7.1 Introduction

In the previous chapters it was shown through contact interface analysis how and why different Ag pastes gave good- or bad-quality contacts on high sheet-resistance emitters. In this chapter, we will make an attempt to understand how to control the contact quality by tailoring the key constituents of the paste. The understanding of contact interface structure and electrical performance of contacts and cells, developed in previous chapters, is used to explain the impact of paste constituents on the quality of the contacts. This is challenging, partly because the paste constituents and characteristics are generally proprietary to the paste manufacturing company and also because the exact behavior of the glass frit and Ag during firing is complex. However, understanding the roles of the inorganic constituents and their optimization in the Ag paste can help achieve good-quality thick-film ohmic contacts [78]. This is particularly important when dealing with high sheet-resistance emitters. In Chapters 5 and 6, high-quality screen-printed contacts to 100 Ω/sq emitters were achieved using PV168 Ag paste from DuPont. However, this paste only worked for higher than conventional firing temperatures (>810° C instead of 750° C). In this section we study the effects of key components of the paste,

glass frit and Ag particles, on the electrical characteristics of the cell. In particular, the impact of glass frit chemistry and Ag particle size and morphology is investigated to help in the development of an Ag paste for high sheet-resistance emitters using normal firing conditions.

## 7.2 Experimental Method

In this study, many screen-printed cells were fabricated by co-firing the contacts either at a conventional temperature of ~750° C or at a higher temperature of ~840° C (over-fired) for several carefully formulated pastes with different chemistry. Table 1 shows the formulation of nine different pastes studied. These pastes have different glass frit chemistry to control the glass transition temperature ($T_g$) (below which the glass frit becomes hard and brittle) and aggressiveness (etching of the $SiN_x$ and Si layers). For the glass frits investigated in this chapter, the $T_g$ and glass softening point (where the glass starts to flow by its own weight) ranged from ~400° C to 600° C. The pastes also contain different Ag particle sizes and morphology. The spherical particle size ranged from ~0.1 to 10 μm, with small particle size designated to be ~0.8 μm, medium particle size ~1.5 μm, and large particle size ~2.5 μm. The ultra-fine particle size is in the tens of nanometers (~0.1 μm) and the fine particle size is a few hundred nanometers. Table 1 summarizes the key differences and characteristics of each Ag paste. All the pastes used were specially manufactured by Ferro Corporation for this study. Pastes 33-462 and 33-456 have self-doping properties (contain P), whereas pastes 33-452, 33-455, and 33-460 have no P in the paste. Solar cells were fabricated using each paste and then electrical performance was correlated with the contact interface and the paste constituents.

Table 7.1: Description of the different pastes investigated in this study.

| Paste | Ag Powder Size | Ag Powder Morphology | Glass frit | Other |
|---|---|---|---|---|
| 33-460 | blend | spherical | lowest $T_g$, less aggressive (GF1) | no self-doping |
| 33-452 | blend | spherical | medium $T_g$, more aggressive(GF2) | no self-doping |
| 33-462(A) | ultra-fine | spherical | medium-high $T_g$, more aggressive (GF3) | self-doping |
| 33-462(B) | fine | spherical | medium-high $T_g$, more aggressive (GF3) | self-doping |
| 33-462(C) | small | spherical | medium-high $T_g$, more aggressive (GF3) | self-doping |
| 33-462(D) | regular | spherical | medium-high $T_g$, more aggressive (GF3) | self-doping |
| 33-462(E) | large | spherical | medium-high $T_g$, more aggressive (GF3) | self-doping |
| 33-456 | large | flake | medium-high $T_g$, ,more aggressive (GF3) | self-doping |
| 33-455 | blend | spherical | high $T_g$, less aggressive (GF4) | no self-doping |

## 7.3 Results and Discussion

### 7.3.1 The Effect of Ag Particle Size in Thick-Film Ag Paste on the Electrical and Physical Properties of Screen-Printed Contacts and Si Solar Cells

#### 7.3.1.1 Correlation between Particle Size and Electrical Performance of Contacts and Solar Cells

Figure 7.1 shows that for contact firing at 840° C with a belt speed of 120 inches per minute (ipm), the macroscopic specific-contact resistance as well as series resistance decreased with the increase in Ag particle size in the paste. However, the lowest ideality factor (n) factor was achieved for the small- to medium-sized Ag particles. Higher composite ideality factors are indicative of an increase in junction leakage current, which can degrade both $V_{oc}$ and FF of the solar cell. It is important to note that $R_s$ close to 0.5 $\Omega$-cm$^2$ and an n factor close to unity are desirable for high FF and $V_{oc}$. The combined effect of the particle size induced change in $R_s$ and n factor (Fig. 7.1) on the $V_{oc}$ and FF of the cells is depicted in Figure 7.2. The $V_{oc}$ was highest for the ultra-fine particle size and lowest for the largest particle size for the 840° C firing. However, the FF was optimum (>0.78) around the small particle size because of the trade-off between $R_s$ and n

factor. Both $R_s$ and n factor showed a decrease initially with an increase in the particle size, but for the larger particle size, the n factor starts to increase, while $R_s$ continues to decrease (Fig. 7.1).

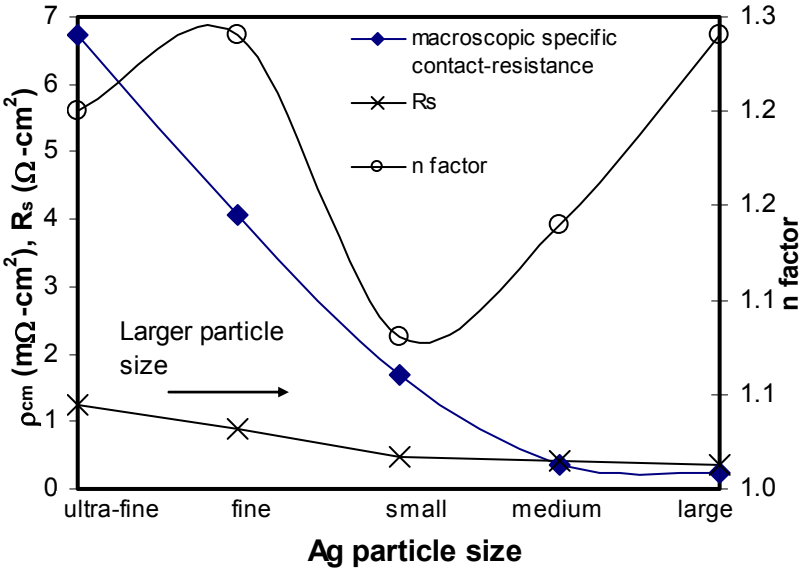


Figure 7.1. Effect of Ag particle size on macroscopic specific contact resistance, series resistance, and n factor for contacts fired at 840º C / 120 ipm.

For the 750° C firing, the FF was found to peak at the small particle size and was lowest for the fine to ultra-fine particle size (Fig. 7.3). The $V_{oc}$ peaked for the fine and small particle size. Table 7.2 shows that the cell performance, which is proportional to the product of $J_{sc}$, $V_{oc,}$ and FF, peaked in the range of small- to medium-sized Ag particles for the rapid firing used in this study.

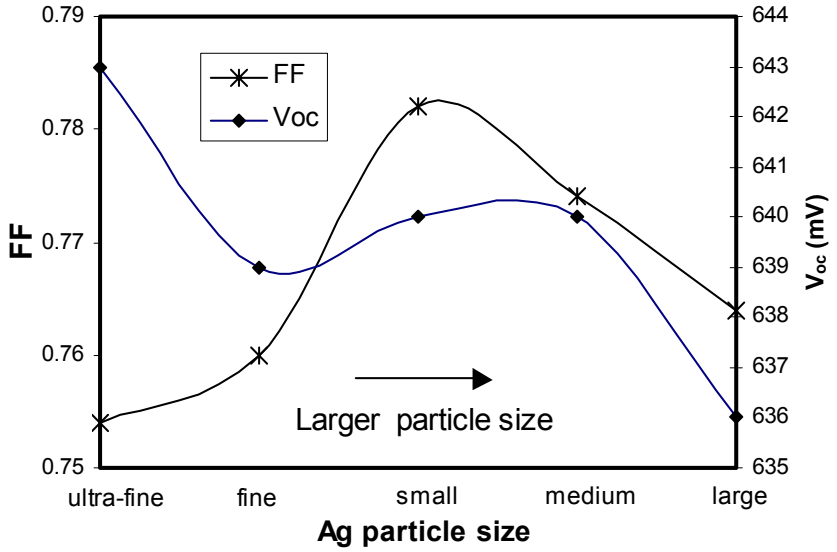


Figure 7.2. Effect of Ag particle size on $V_{oc}$ and FF at 840º C/120 ipm.

Table 7.2: Cell Efficiency (%) for the different particle size pastes for rapid (120 ipm) 750° C and 840° C firing.

| Firing Condition | ultra-fine | fine | small | medium | large |
|---|---|---|---|---|---|
| 750°C/120 ipm | 16.29 | 16.02 | 17.0 | 16.8 | 16.6 |
| 840°C/120 ipm | 16.8 | 16.3 | 17.4 | 17.3 | 16.6 |

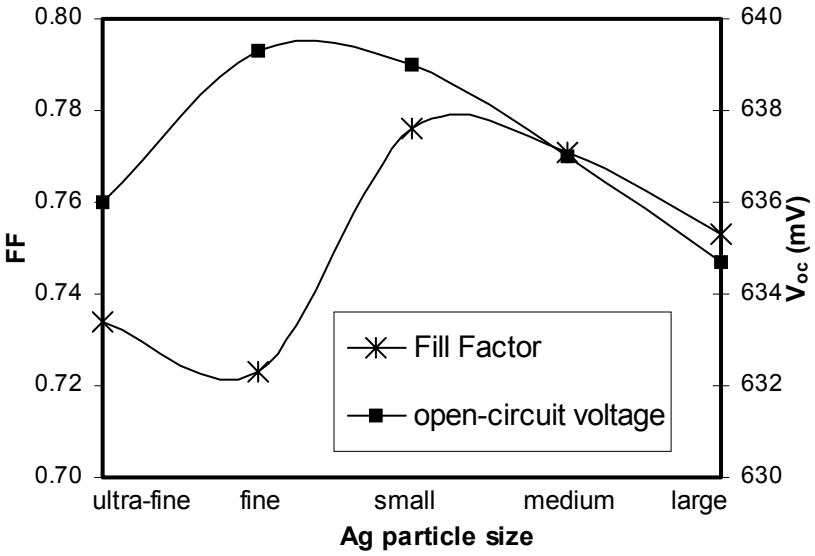


Figure 7.3. Effect of Ag particle size on $V_{oc}$ and FF at 750º C/120 ipm.

#### 7.3.1.2 Correlation between Particle Size and Contact Interface Structure

Cross-section SEM of the contact interface and SIMS measurements were performed to understand and explain the above trends in contact parameters, $V_{oc}$ and FF. Figure 7.4 shows the SEM images of the Ag-Si contact interface formed at 840° C/120 ipm using pastes with ultra-fine, small, and large Ag particles. SEM images again showed that the bulk of the Ag grid and the Si emitter surface is separated by a glass layer of varying thickness. In addition, there are Ag crystallites embedded into the Si surface. These Ag crystallites are formed during the cool-down stage when the dissolved Ag in the glass layer precipitates onto the Si surface. It has been suggested in the literature that Ag crystallites serve as current pick-up points, and conduction from the Ag crystallites to the bulk of the Ag grid takes place via tunneling through an ultra-thin glass layer above some of these crystallites [78]. As a result, the size, number, and distribution of these Ag crystallites, as well as the thickness of the glass layer, play a critical role in determining contact, series, and shunt resistances of the cell. For example, very few or non-uniformly distributed Ag crystallites with a thick glass layer would increase $R_s$. Similarly, if the size of the crystallites becomes too large and starts to approach or exceeds the p-n junction depth, then it could increase $J_{o2}$ and decrease $R_{sh}$, $V_{oc}$, and FF of the cell. In the following section, an attempt is made to correlate the particle size and interface structure to the electrical performance of the contacts and solar cells.

Figure 7.4(a) shows that the use of ultra-fine Ag particles gives rise to a denser Ag gridline bulk with a fairly uniform and thick (generally ~200-nm thick) glass layer between the Ag gridline and the Si surface in most regions. In addition, spherical Ag particles were found to be suspended in the glass layer. The presence of a thick glass

layer resulted in high macroscopic specific contact resistance (≥7 mΩ-cm$^2$), high series resistance (1.4 Ω-cm$^2$), and lower FF (~0.75) for this paste. In addition, Ag crystallites were not observed in some regions. Ultra-fine particles cause the particles to coalesce or sinter rapidly during firing, which may reduce the dissolution of Ag into the glass frit, resulting in a more dense Ag bulk and reduced super-saturation and precipitation of Ag upon cooling.

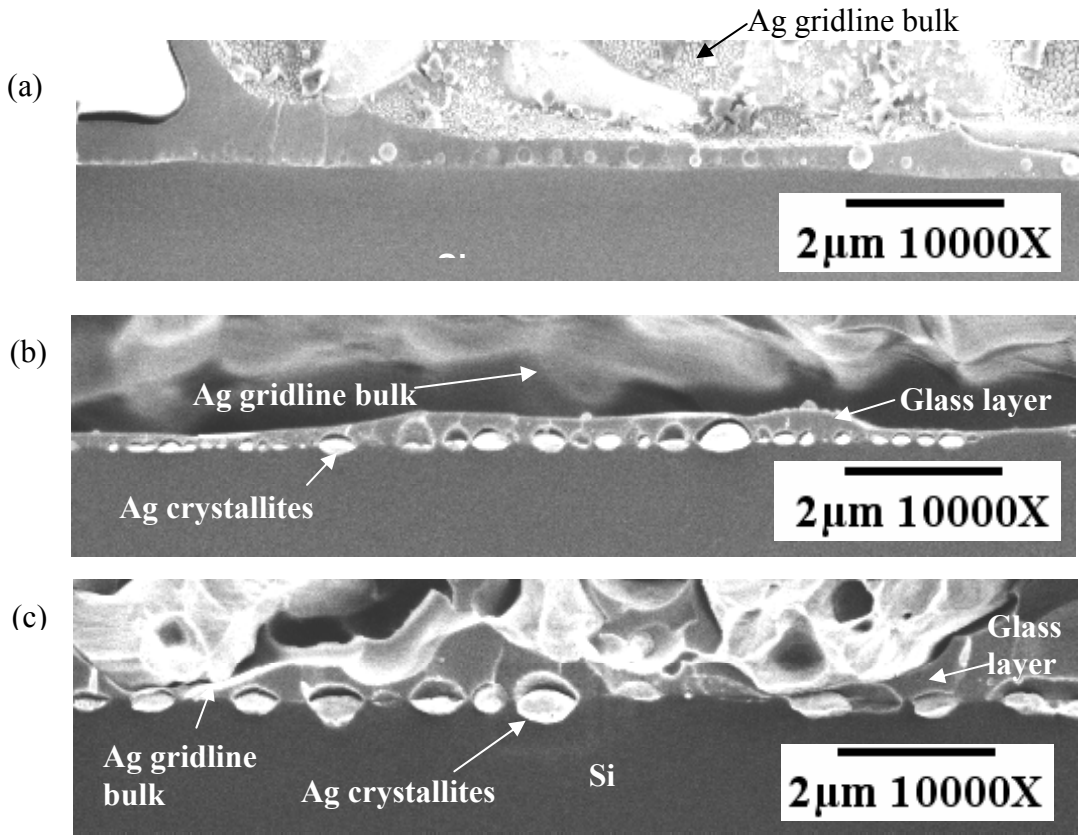


Figure 7.4. SEM images of the Ag-Si contact interface for (a) ultra-fine Ag particle paste, (b) small Ag particle paste, and (c) large Ag particle paste. The contacts were fired at 840° C/120 ipm.

Figure 7.4(b) shows that a small Ag particle size gave a large number of small Ag crystallites (~80 nm) embedded into the Si emitter surface along with a very thin glass layer (~20 nm) in many regions. A large number of Ag crystallites increases the contact

area fraction and a thin glass layer improves the probability of tunneling from Ag crystallites to the Ag grid. This may explain why small particle size gave good ohmic contact ($\rho_{cm}$=1.7 mΩ-cm$^2$), contributing to low $R_s$ (~0.5 Ω-cm$^2$) and a high FF of 0.782. Notice that because the penetration depth of the Ag crystallites into the emitter is small (~80 nm), relative to the 0.3 μm deep junction, the shunt resistance was highest (~75,000 Ω-cm$^2$) and $J_{o2}$ was lowest (~22 nA/cm$^2$) for this paste.

Figure 7.4(c) shows that larger Ag particles gave rise to large Ag crystallites at the contact interface with a widely varying thickness of the glass layer (very thin in some regions and thick in others) between the Ag gridline and the Si emitter. Unlike most pastes, there were also few direct Ag bulk/Ag crystallite connections at the interface for this large particle sized paste. Large particle size slows the sintering process, resulting in more dissolution of Ag into the glass, which in turn leads to a large number of larger Ag precipitates or crystallites at the interface. These factors should increase the tunneling probability and current transport, which explains the observed low specific-contact resistance of (0.24 mΩ-cm$^2$) for this paste. However, it does not explain the somewhat lower fill factor (0.76 as opposed to ≥0.78 for small Ag particle size). Larger Ag crystallites could also increase the Ag penetration and diffusion into the emitter. These two factors may explain the observed higher $J_{o2}$ (~85 nA/cm$^2$) and somewhat lower FF for larger Ag particle size.

#### 7.3.1.3 Physical Model to Explain the Correlation between Particle Size and Contact Interface Structure

During the firing process, the lead silicate glass softens and melts first and then starts dissolving the Ag particles. Upon further heating, this mixture (lead oxide + silver)

fluidizes and starts to etch the silicon nitride layer via a redox reaction [77]. Finally, upon cooling, silver and lead separate according to the phase diagram and Ag crystallizes at the Si surface [78, 81]. During the firing cycle, Ag particles in the paste also start to sinter or coalesce via the inter-diffusion of atoms between the metal particles that are in contact, resulting in neck formation between the spherical particles [73]. Good sintering results in the formation of solid blocks of Ag and a more compact structure, which tends to decrease the dissolution of Ag in the glass because a smaller surface area would be available for dissolution. The smaller the particle size, the easier the inter-diffusion of atoms and the quicker the sintering, resulting in smaller dissolution of Ag into the molten glass layer. In the case of ultra-fine particles, the dissolution is much less, reducing the super-saturation and precipitation of Ag upon cooling. Therefore, very few or no Ag crystallites were detected at the interface.

According to the above model, the dissolution of Ag should increase when the particle size is increased from ultra-fine to small in the paste. This produced a large number of small (~80 nm in depth) Ag crystallites at the Ag-Si contact interface at the end of the firing cycle. For this paste, the crystallites were embedded within a shallow depth (≤ 100 nm) of the surface of the Si emitter, indicating a very mild etching of Si by the PbO glass-Ag melt. In addition, the glass was not thick in many regions and Ag crystallites were distributed quite uniformly and were frequently observed across most of the Ag-Si interface. This explains the acceptably low contact resistance (Fig. 7.1) with no appreciable junction shunting.

Based on the sintering model, larger particles should lead to even more Ag dissolution in the glass frit, and consequently the re-grown Ag crystallites were found to

be larger for the larger Ag particle paste, both laterally (≤500 nm) and in depth (~0.21 μm). This makes the device more vulnerable to shunting for high sheet-resistance shallow emitters. Notice that most variation in the glass layer thickness at the interface was observed for the larger particle sized contact (Figure 7.4(c)), even though the glass frit chemistry was the same for all the pastes. In addition, the bulk of the Ag gridline at a few locations was found to be in direct contact with the Si emitter with ultra-thin or virtually no glass layer in between.

SIMS measurements were taken through the emitter region and Ag concentration was measured at and near the p-n junction. Figure 7.5 confirms that the Ag concentration increased by more than an order of magnitude around the p-n junction for the large particle sized paste, supporting the reason for the highest $J_{o2}$ value (~85 nA/cm$^2$). These results also agree well with Van Craen et al. [111], who showed that a Ag concentration of greater than $10^{15}$ cm$^{-3}$ at the p-n junction starts to cause a degradation in cell performance.

Based on the above results and observations, a physical model for contact formation is proposed to explain the difference in contact interface structure for the different Ag particle sizes. The proposed model is based on the competition between Ag sintering and Ag dissolution in the glass frit during the firing process, which seems to explain the effect of particle size on cell parameters. In general, finer particles will show faster neck growth and need less sintering time [68]. Coalesced Ag particles of the Ag bulk sintered into compact, almost round structures were only observed for the ultra-fine Ag particle sized paste for ~740-750° C/120 ipm contact firing. Hence, in the case of the ultra-fine particles, Ag sintering and surface inter-diffusion between particles occurs

rapidly before appreciable amount of Ag could dissolve in the glass frit. Less dissolved Ag reduces the super-saturation required to re-grow the Ag crystallites into the Si emitter surface during cooling. In the case of the large Ag particle size, sintering takes longer because surface inter-diffusion is not as rapid as in the case of very fine particles. This provides more time, surface area, and opportunity for Ag dissolution in the glass frit before solid blocks of Ag are formed and sintering takes effect. As a result, the glass frit is adequately supersaturated to allow the precipitation and re-growth of a large number of Ag crystallites (Fig. 7.4(c)). This model also explains why particle size can influence the glass layer thickness. For example, in the case of ultra-fine particles, rapid and more complete sintering leads to a more compact and less porous Ag grid block above the glass layer. As the Ag particles sinter, voids between the particles shrink and eventually disappear, causing more of the liquid glass trapped in these voids to seep down to the contact interface, resulting in a thicker and uniform glass layer. Because of the rapid sintering of the ultra-fine particles, less Ag surface area is available to dissolve in the glass frit. Thus, less Ag will precipitate (also irregularly distributed) at the contact interface, as observed in Figure 7.4(c). Suns-$V_{oc}$ measurements indicate that the ultra-fine paste Ag grid results in ~100 fA/cm$^2$ decrease in the saturation current density ($J_{o1}=J_{oe}+J_{ob}$). This indicates a lower emitter saturation current density ($J_{oe}$) since the base saturation current density ($J_{ob}$) is the same for all the cells (i.e., the same base resistivity and Al back-surface field). This result is consistent with the observed fewer Ag crystallites (Figs. 7.6(a) and 7.7(a)) and the lack of direct bulk Ag-Si emitter contact (Fig. 4(a)) for the ultra-fine Ag particle sized paste, because it reduces metal induced emitter recombination and produces the highest $V_{oc}$. However, some ultra-fine particles may not

sinter during the fast firing process and they remain trapped or suspended in the glass layer, as observed in Figure 7.4(a). In the case of the large Ag particles, sintering is slow and a more porous Ag grid is formed. Since the larger Ag particles do not sinter into a compact structure, some glass may be trapped in the pores, resulting in a more non-uniform glass layer thickness at the Ag-Si interface The glass is therefore thin in regions where Ag particles are in close contact with each other or with the Si surface, and it is thick where there are voids. To observe the Ag crystallites from the top view, the Ag grid was first etched in nitric acid, followed by etching the glass layer in a HF acid dip without affecting the Ag crystallites embedded into the Si emitter. Optical microscopy was performed at 5,000X to see the top view.

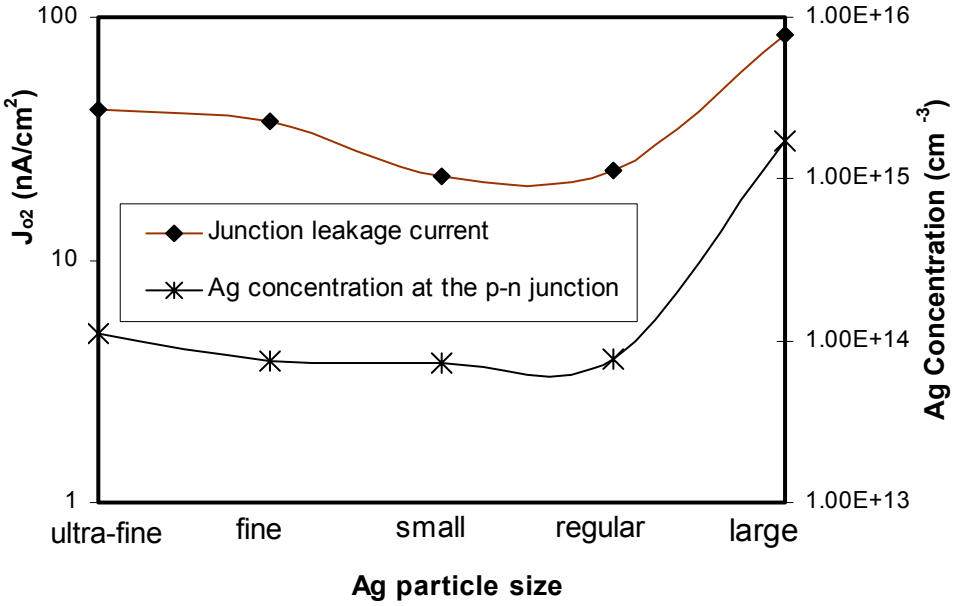


Figure 7.5. Junction leakage current and Ag concentration at the p-n junction determined by SIMS.

The top view of the contact interface was investigated for contacts fired at 840° C (Fig. 7.6) and 750° C (Fig. 7.7) to support the above model. It is clear that the Ag precipitation is greater at 840° C for the large Ag particle sized paste compared with the

small and ultra-fine pastes. This supports our model because higher temperature increases the Ag dissolution in the glass frit causing larger and/or more frequent Ag crystallite precipitation as shown in the previous chapter. However, comparing Figures 7.6(b) and 7.7(b), the small Ag particle size shows the least change in the distribution and size of Ag precipitation with temperature change. This possibly supports our hypothesis that the sintering and Ag dissolution in the glass frit occur more or less together for the small Ag particle size. The small Ag particle sized paste shows the most regular distribution of Ag crystallite precipitation. Figure 7.8, showing the cross-section SEM of the contact interface for the different particle sized pastes, also confirms this result, as shown in Figure 7.8(b) for the small Ag particle sized paste.

Figures 7.6 and 7.7 show that for large particle size, the contact area fraction is larger for 840° C firing relative to 750° C. However, the series resistance is similar (~0.3-0.4 $\Omega$-cm$^2$) for both firing conditions. This is because the macroscopic specific-contact resistance remains very low (~0.3 m$\Omega$-cm$^2$) (Figs. 7.1 and 7.9) to influence $R_S$ for the large Ag particle sized paste for both firing conditions. Note that for the large particle sized paste fired at 750° C, ultra-thin glass regions or direct connections between the Ag gridline bulk and the Ag crystallites have been observed (Fig. 7.8(c)). This indicates that the frequency of the thin glass layer is equally or more important than the frequency of Ag crystallites. Note that the simultaneous presence of both Ag crystallites and thin glass layer is believed to be necessary for the tunneling process.

The large particle size paste also shows a greater variation in the depth topology of the emitter surface, as shown in the plane-view AFM images in Figure 7.10. An enhanced variation in the surface depth suggests that more Ag dissolved in the glass has

precipitated onto the Si emitter surface. Ag precipitates were etched away before the measurement. For large Ag particle size, Ag crystallites for 750° C firing were only ≤100 nm in depth as opposed to ≤210 nm for the 840° C firing. SIMS measurements showed that Ag concentration near the p-n junction was ~$2\times10^{15}$ $cm^{-3}$ for both (Figs. 7.5 and 7.11), indicating a similar trend for different firing temperatures. Based on these SIMS results and the SEM images of Figures 7.6 and 7.7 the cause of the enhanced Ag diffusion for the large particle size paste could be explained as follows:

1- More Ag precipitation implies that precipitation occurs earlier for this contact (Fig. 7.12). This is because super-saturation during cooling probably occurs faster for the larger Ag particle size contact. Consequently, Ag diffusion will start to take place at a higher temperature, which would enhance the Ag diffusion.

2- The original area where Ag precipitates on the Si emitter surface is larger for large Ag particle size. Thus, the average diffused Ag beneath the contact will be higher since the SIMS beam spot size was 40 μm in diameter.

It is important to note that the results shown in this work may be different for different glass frit chemistry and firing scheme. However, for this study we have used a glass frit that results in good contact quality along with industrial-type rapid firing schemes.

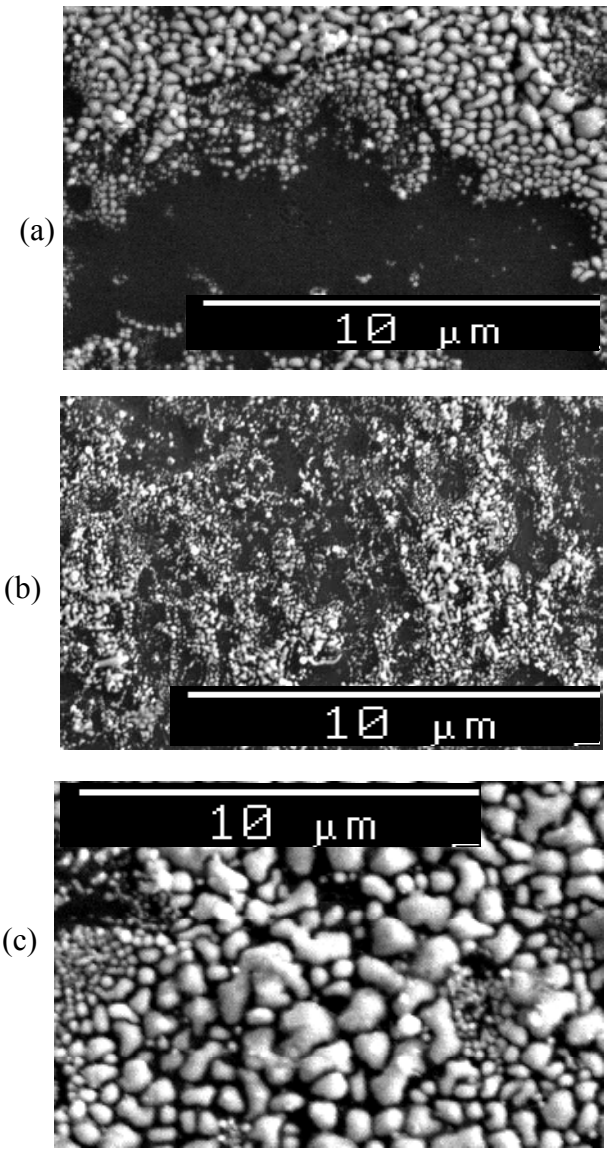


Figure 7.6. Top-view SEM images of the contact interface showing Ag crystallite precipitates after removal of the Ag gridline bulk and glass frit for 840° C/120 ipm firing for (a) ultra-fine, (b) small, and (c) large particle sized pastes.

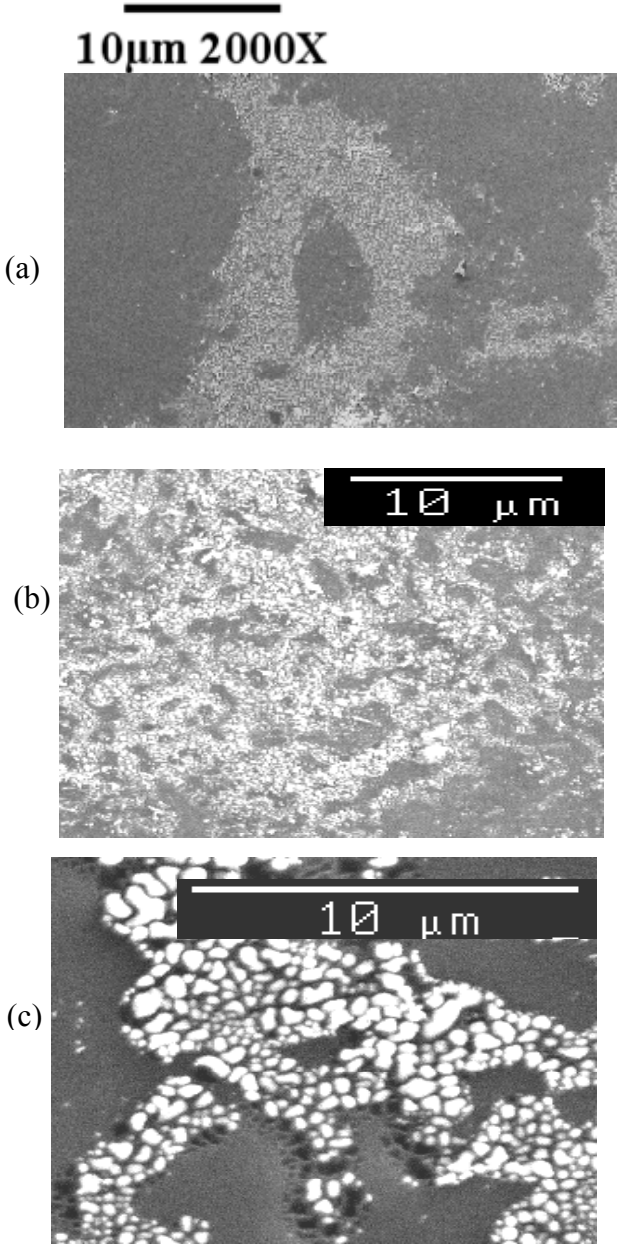


Figure 7.7. Top-view SEM images of the contact interface showing Ag crystallite precipitates after removal of the Ag gridline bulk and glass frit for 750°C/120 ipm firing for (a) ultra-fine, (b) small, and (c) large particle sized pastes.

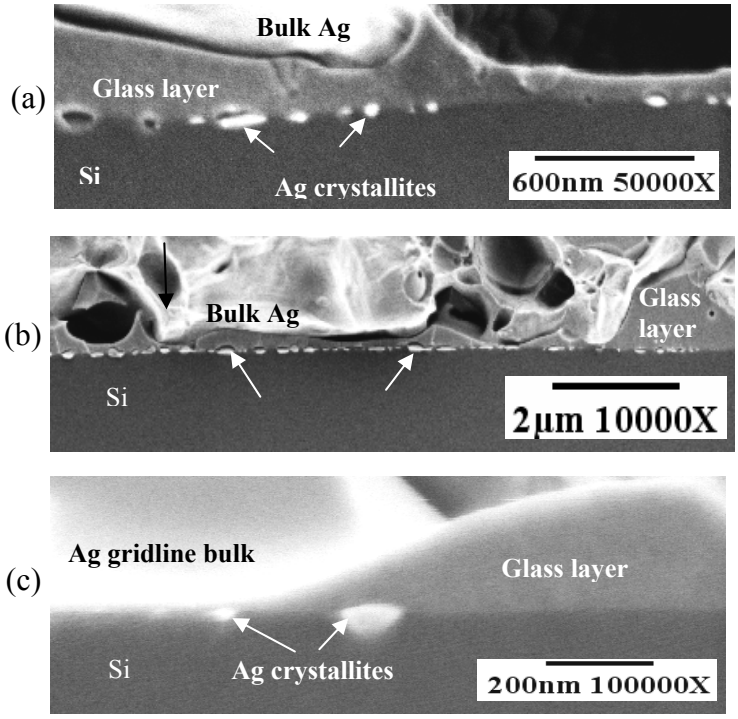


Figure 7.8. SEM images of the Ag-Si contact interface for (a) ultra-fine Ag particle paste, (b) small Ag particle paste, and (c) large Ag particle paste. The contacts were fired at 750° C/120. ipm.

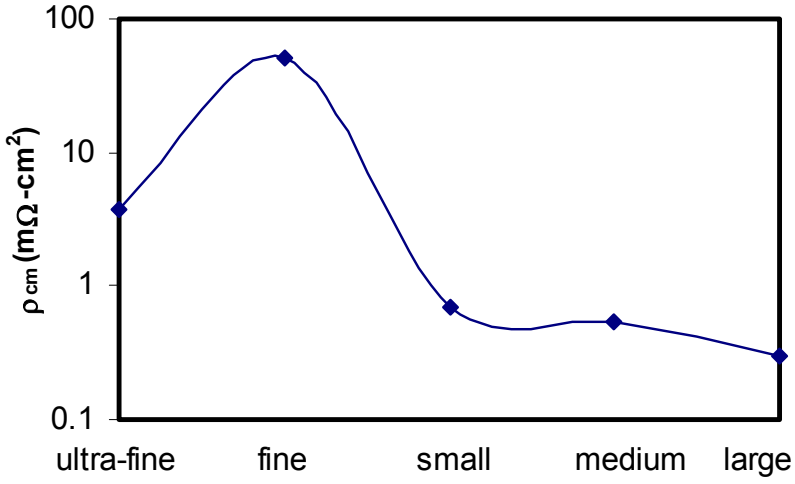


Figure 7.9. Measured specific contact resistance for the different Ag particle sized pastes fired at 750° C/120 ipm.

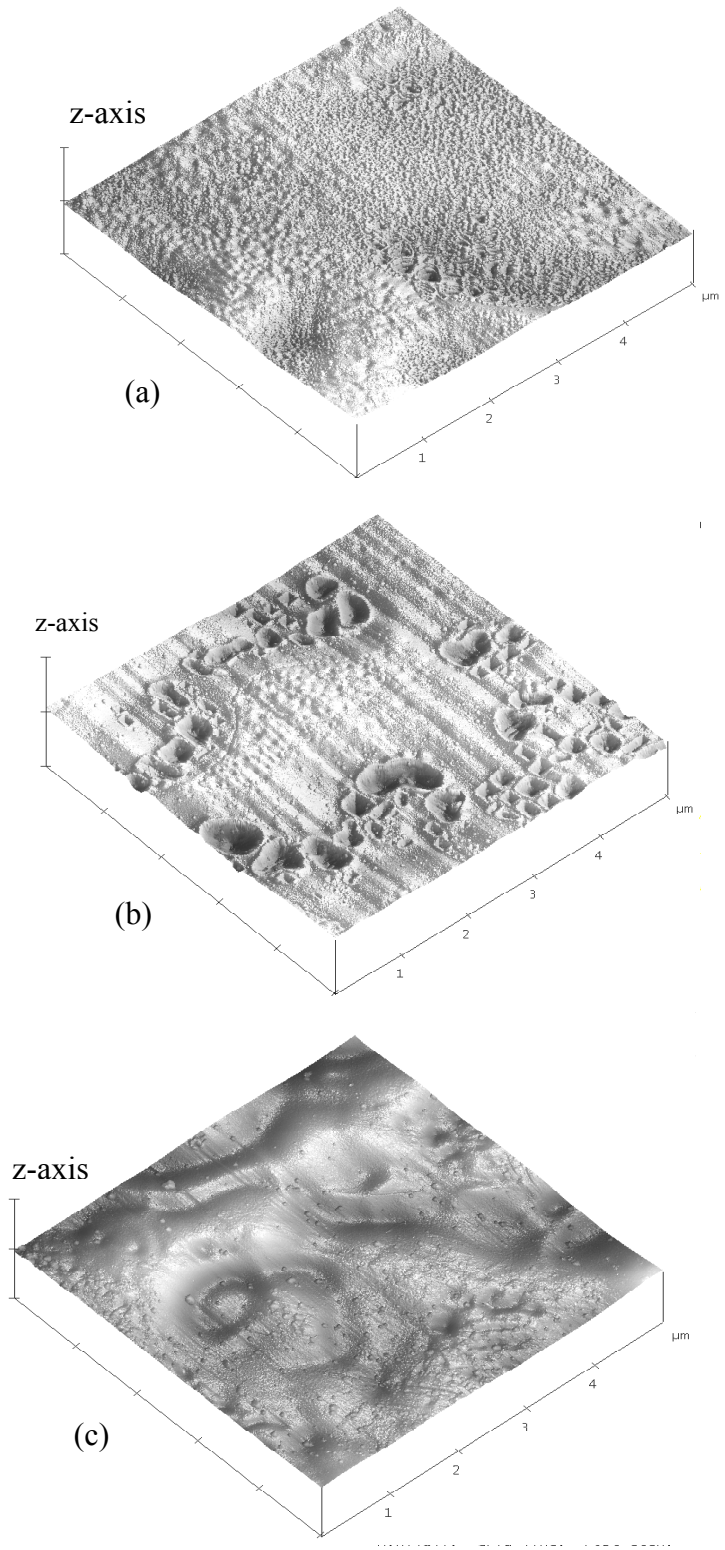


Figure 7.10. Plane-view AFM images of the A-Si contact interface for (a) ultra-fine particle paste, (b) small particle paste, and (c) large particle paste. The Ag gridline bulk, glass frit, and Ag crystallites were removed before the AFM measurement.

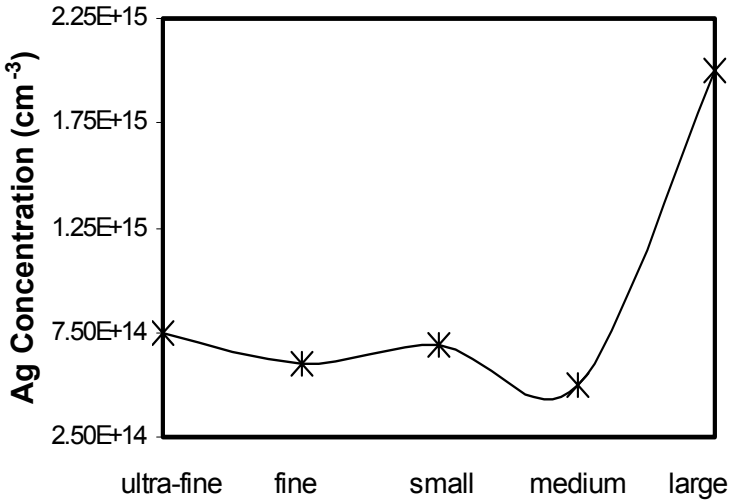


Figure 7.11. Ag concentration close to the p-n junction for the different Ag particle sized pastes fired at 750° C/120 ipm.

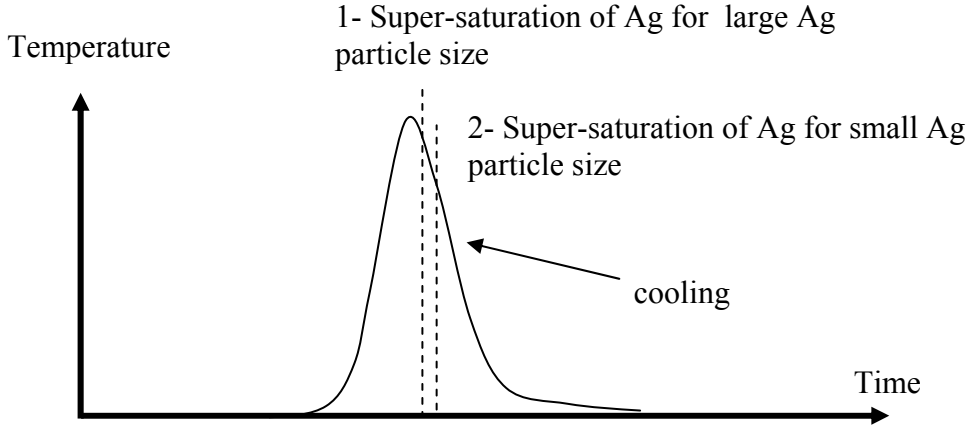


Figure 7.12. A schematic showing the firing cycle and the points where the Ag starts precipitating during cooling.

### 7.3.2 Effect of Ag Particle Morphology on Screen-Printed Contacts and Cell Performance

Pastes 33-456 and 33-462(E) were formulated with identical glass frit chemistry and particle size (large), but a different Ag particle morphology (flake versus spherical). Table 7.3 shows that the flake morphology in paste 33-456 gave higher $V_{oc}$ and FF compared to paste 33-462(E), with large spherical Ag particles for identical firing conditions (840° C/120 ipm or 750° C/120 ipm). This resulted in ~0.7% higher absolute efficiency (17.2%) for the flake morphology compared to 16.5% for the spherical particle paste 33-462 (E), as shown in Table 7.3. Dark-IV analysis revealed a higher junction leakage current ($J_{o2}$) of ~85-120 nA/cm$^2$ and n factor (1.24) for the large spherical particle size of paste 33-462(E) compared to a $J_{o2}$ of ~30 nA/cm$^2$ and n factor of 1.08 for the flake particle morphology. However, regular or medium size spherical particles in paste 33-462(D) gave cell parameters comparable to the flake morphology (Table 7.3), indicating that both size and morphology are important for good ohmic contact.

Table 7.3: Performance of spherical versus flake Ag particle morphology.

| Paste | Morphology/Size | Voc (mV) | FF | Eff(%) | n factor | $\rho_{cm}$ (m$\Omega$-cm$^2$) |
|---|---|---|---|---|---|---|
| 33-456 | flake / large | 642 | 0.771 | 17.2 | 1.08 | 1.34 |
| 33-462(D) | spherical / medium | 639 | 0.780 | 17.3 | 1.07 | 0.36 |
| 33-462 (E) | spherical / large | 635 | 0.757 | 16.6 | 1.29 | 0.24 |

### 7.3.3 Effect of Solids (Ag+frit) Content on Contact Quality and Cell Performance

Pastes 33-455 (HS) and 33-455 (LS) have identical glass frit chemistry and Ag particle shape and size, but different (higher content of ~90% and lower content of ~80%) solids content. We did not observe an appreciable difference in cell performance as a result of solids content. As shown in Table 7.4, the $V_{oc}$, FF, and $\rho_c$ are similar for both

pastes. The firing process used for this study was 750° C with a belt speed of 120 ipm. Notice that very good untextured FZ cell efficiencies of ~17.4% were achieved in both cases (Table 7.4).

Table 7.4: Effect of solids content on cell performance.

| Paste | $V_{oc}$ (mV) | FF | Eff(%) | $\rho_{cm}$ (m$\Omega$-cm$^2$) |
|---|---|---|---|---|
| 33-455 (HS) | 644 | 0.783 | 17.4 | 0.91 |
| 33-455 (LS) | 645 | 0.778 | 17.4 | 0.76 |

### 7.3.4 Effect of Glass frit Chemistry and its Transition Temperature on Contacts and Cell Performance

#### 7.3.4.1 Effect of Glass Transition Temperature on the Contact Behavior for Different Firing Temperatures and Belt Speed

In the previous sections it was established that small to medium size spherical Ag particles (~0.8 mm) are good for the contacts and that the solids content of the paste has no significant influence on contact quality. In this section, a blend of small- to medium-sized Ag particles was selected for the different glass chemistries. The glass transition temperature ($T_g$) was changed to see how it affects the contacts. It is important to realize that a lower $T_g$ glass with low softening point starts to fluidize at lower temperatures and can increase the thickness of the glass. The effect of glass frit in the Ag paste was studied for different firing schemes to understand the interaction of frit chemistry and firing temperature. The effect of 830-840° C firing at a belt speed of 80 ipm on high (90-95 Ω/sq) and low (40-45 Ω/sq) sheet-resistance emitters was studied (Fig. 7.13). On the 90-95 Ω/sq emitter, paste 33-455 with lower Pb content in the glass and a higher $T_g$ gave a FF of less than 0.70 because of high series resistance (2.6 Ω-cm$^2$) and contact resistance (7.5 mΩ-cm$^2$). The same high $T_g$ paste gave $R_s$ of ~0.643 Ω-cm$^2$ on the 40 Ω/sq emitter.

Pastes 33-452 and 33-462, which have low glass transition temperatures but different glass frit viscosity behavior, gave acceptably low $\rho_{cm}$ (0.35-1 m$\Omega$-cm$^2$) on the 90-95 $\Omega$/sq emitter.

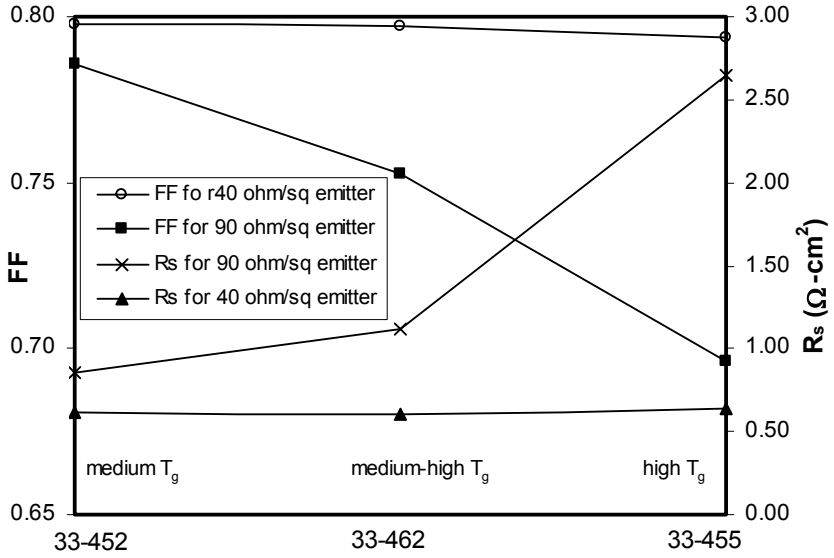


Figure 7.13. Response of Ag pastes with different glass frit $T_g$ on 90-95 $\Omega$/sq emitters fired at ~840° C/80 ipm.

SEM images (Fig. 7.14(b) and (c)) of the Ag-Si interface fired at 840˚C/80 ipmshow an increase in the number and size of Ag crystallites for the lower $T_g$ glass frit (GF2). This is because the lower $T_g$ glass frit dissolves more Ag during the firing process, and produces larger and more frequent Ag precipitates upon cooling. The size of Ag crystallites is much larger for lower $T_g$ frit (~800 nm in width for paste 33-452 and 150 nm for paste 33-455). However, when paste 33-455 is fired at the same condition (840° C/80 ipm) on a 40 $\Omega$/sq emitter, the Ag crystallites at the Ag-Si interface grow up to 600 nm in width. This may suggests that the higher P concentration in the 40 $\Omega$/sq emitter may help enhance the dissolution of Si by the glass frit (Fig. 7.14(a)), which may also aid the precipitation of the Ag crystallites. An increase in the width and number of

Ag crystallites at the interface improves the probability of encountering thin glass regions for tunneling, resulting in lower $\rho_{cm}$ (Fig. 7.14).

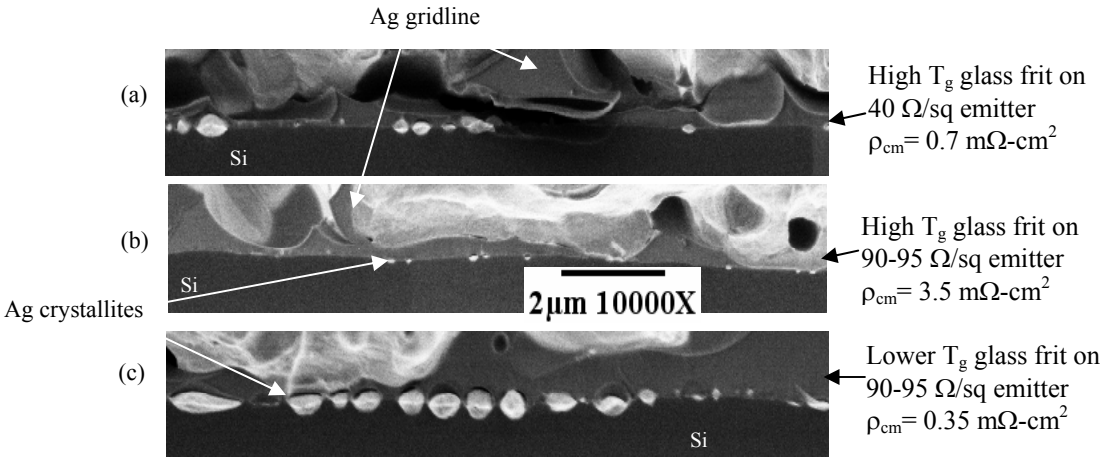


Figure 7.14. SEM images of (a) paste 33-455 fired on a 40 Ω/sq emitter, and pastes (b) 33-455 fired on a 90-95 Ω/sq emitter, and (c) 33-452 fired on a 90-95 Ω/sq emitter.

Next, the use of conventional (750° C) firing with faster belt speed was compared to the above 840° C firing. Figure 7.15 shows that high FFs were achieved on 100 Ω/sq emitters at 840° C with 120 ipm belt speed for all three pastes. However, at 750° C firing, high FF was achieved only for medium-high $T_g$ glass pastes (33-462 and 33-455) from Ferro Corporation. This demonstrates that, unlike the case with the PV168 Ag paste, a high firing temperature of ~835° C is not necessary to achieve a good ohmic contact to the 100 Ω/sq emitter provided high $T_g$ glass and fast belt speed are used. However, glass frits GF1 (33-460) and GF2 (33-452) gave significantly lower FFs for the 750° C firing. Figure 7.15 shows that this is primarily due to higher series resistance resulting from higher macroscopic specific contact resistance. Thus, the glass frit chemistry dictates whether good ohmic contacts can be achieved at the desired firing temperature. Paste 33-460, which has a low $T_g$ glass and is less aggressive, gave poor FFs (0.686) at lower-

temperature firing. However, for the 840° C firing, paste 33-460 gave excellent FFs of 0.789. Paste 33-452, which has a lower $T_g$ compared to paste 33-455, gave a lower FF of 0.710 at 750° C firing temperature, which increased to ~0.777 at 840° C firing (Fig. 7.15). This increase in FF was reflected in a decrease in $\rho_{cm}$ from 9.07 mΩ-cm$^2$ to 1.09 mΩ-cm$^2$. The highest fill factors were achieved for the higher $T_g$ pastes 33-462 and 33-455 due to the low series resistance. Paste 33-455, which has a higher $T_g$ (less fluid) and is less aggressive, also showed a slight improvement in FF, from ~0.777 to ~0.783 when going from the 750°C/120 ipm to the 840°C/120 ipm condition after forming gas anneal. Thus, the combined effect of glass $T_g$, firing temperature, and belt speed can be summarized as follows:

1- Lower $T_g$ glass gives high FFs at 840° C for both faster (120 ipm) and slower (80 ipm) belt speeds because even though low $T_g$ gives a thick glass layer, the high-temperature firing followed by forming gas anneal (FGA) allows more metal precipitates to form in the glass to promote tunneling through the thick glass.

2- High $T_g$ (less fluid) glass gives high FFs only at faster belt speeds (for both 750° C and 840° C firing temperatures) because faster belt speed helps to form thin glass regions, which promotes tunneling.

3- For conventional firing conditions (750° C/120 ipm) the paste should have medium to high $T_g$ glass to achieve good FFs. The low $T_g$ glass (GF1 of paste 33-460) does not work well with conventional (700-750° C) firing temperature because the glass layer is always too thick due to the high fluidity of the glass and there are not enough metal precipitates in the glass for effective tunneling.

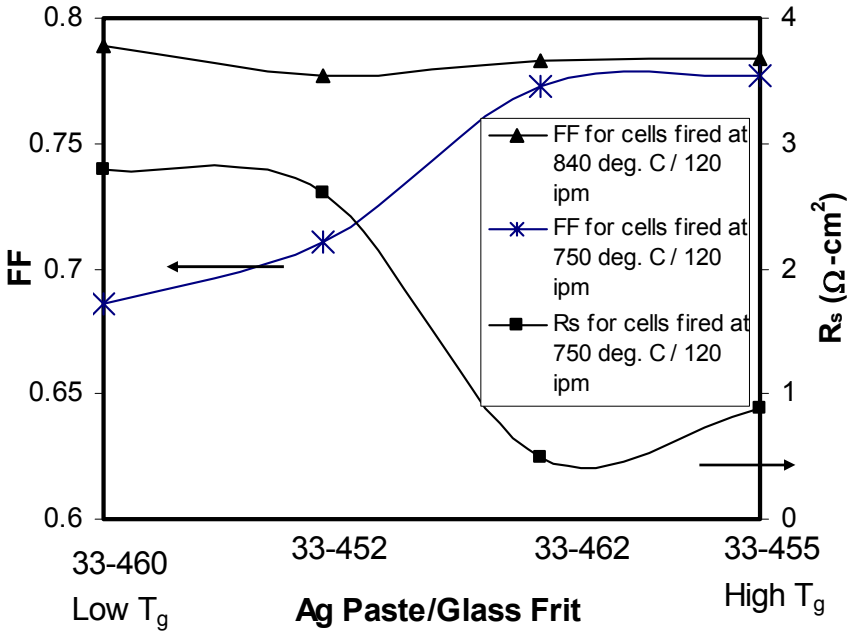


Figure 7.15. Effect of glass frit chemistry and firing temperature on the FF of solar cells.

According to [78], metal precipitates in the glass are only observed in over-fired (~840° C) samples. It is possible that for the lower $T_g$ glass frits (GF1 and GF2), metal precipitates are not present in the glass layer at lower firing temperatures (~750° C, 120 ipm) to assist the current transport, which then takes place via tunneling through ultra-thin glass regions between the Ag crystallites and the bulk Ag. In this case, FGA would not be expected to play an important role. Rather the thickness of the glass layer would become more important for better current transport.

The above study shows that the combination of glass frit ($T_g$) and the firing process plays an important role in achieving good contact to high sheet-resistance emitters because it dictates the thickness and conductivity of the glass layer, Ag precipitates, and multi-step tunneling [120]. The cross-sectional TEM/EDS image in

Figure 7.16 demonstrate the presence of Ag precipitation within the glass layer formed using the Ferro pastes.

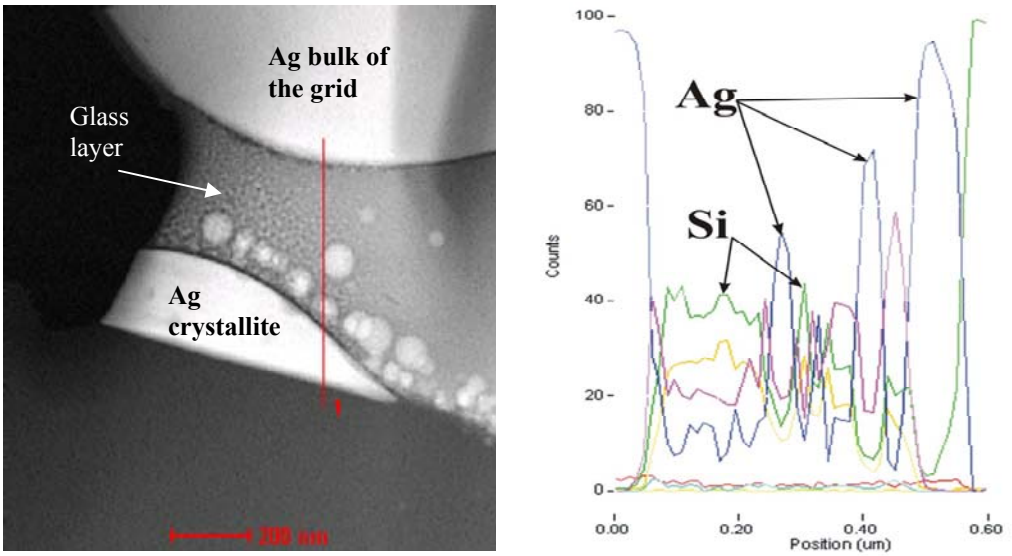


Figure 7.16. TEM/EDS analysis of Ferro paste glass layer at the contact interface showing Ag and Si precipitation. (Courtesy of Ferro Corporation)

To further understand the effect of $T_g$ on the contact formation, SEM images were obtained for the three glass frit types (GF1, GF2, and GF4). Figure 7.17 shows that the glass frit with lower $T_g$ (GF1) gave a thicker glass layer compared to the higher $T_g$ glass frit (GF4). Thinner glass layers should result in lower contact resistance [120, 123, 124], and faster firing is expected to give thinner glass regions by reducing the time for the glass layer to seep to the Si surface.

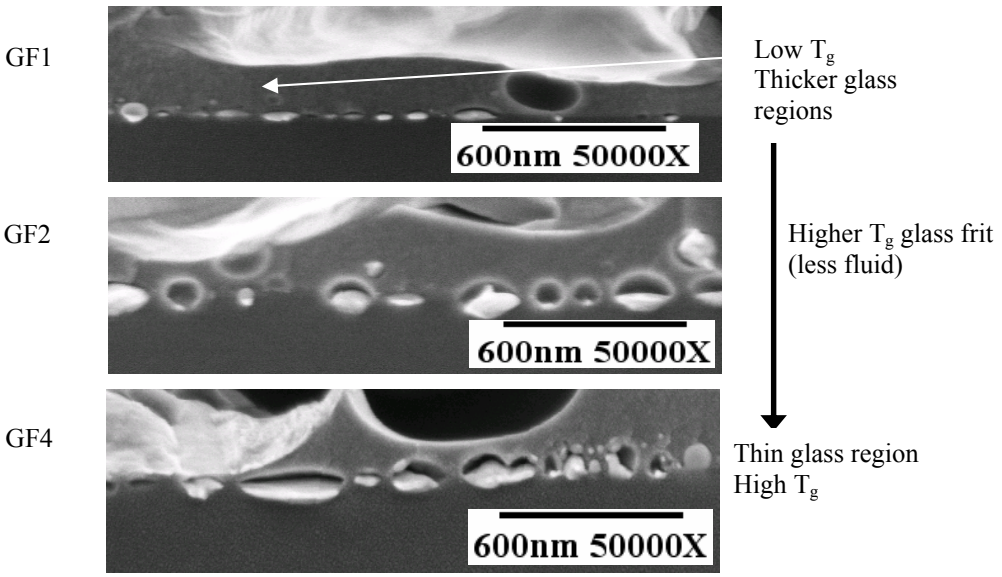


Figure 7.17. SEM images showing the effect of glass $T_g$ on the Ag-Si contact interface.

Figure 7.18 shows that the low $T_g$ glass frit (paste 33-460) resulted in larger and more frequent distribution of Ag crystallites compared with the higher $T_g$ glass frit (paste 33-462). This is because the lower the glass $T_g$, the earlier the glass starts to flow during the firing cycle. This allows the glass to interact with the Ag particles for a longer period of time during firing. Lower $T_g$ also allows the glass to dissolve the Ag before it completely sinters, resulting in more Ag dissolution and hence more precipitated Ag crystallites. The lower $T_g$ glass is thicker after firing because it is more fluid so less of it is retained within the bulk of the bulk Ag grid.

Figure 7.19 also illustrates the formation of very thin glass regions for paste 33-455 with high $T_g$ compared to the 33-460 paste with low $T_g$. The Ag crystallite precipitation on the Si emitter surface is significantly less for the 33-455 paste compared to the 33-460 paste.

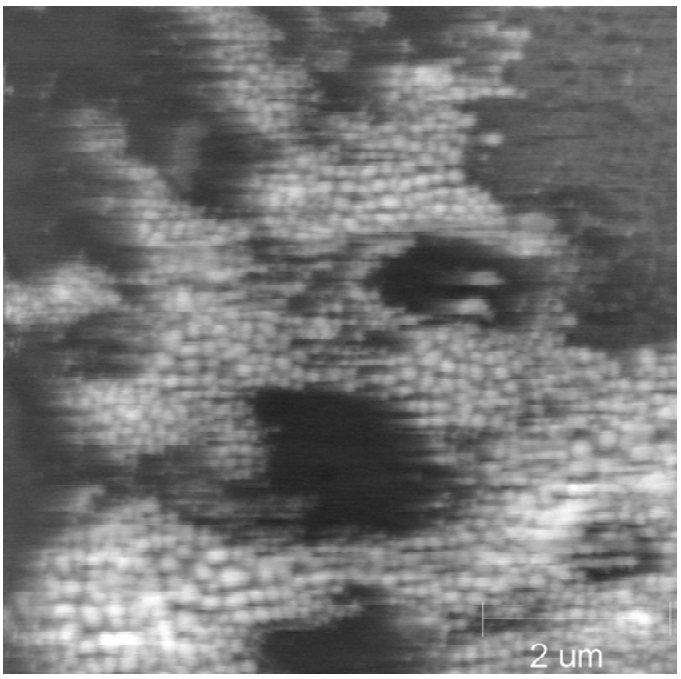


(a)

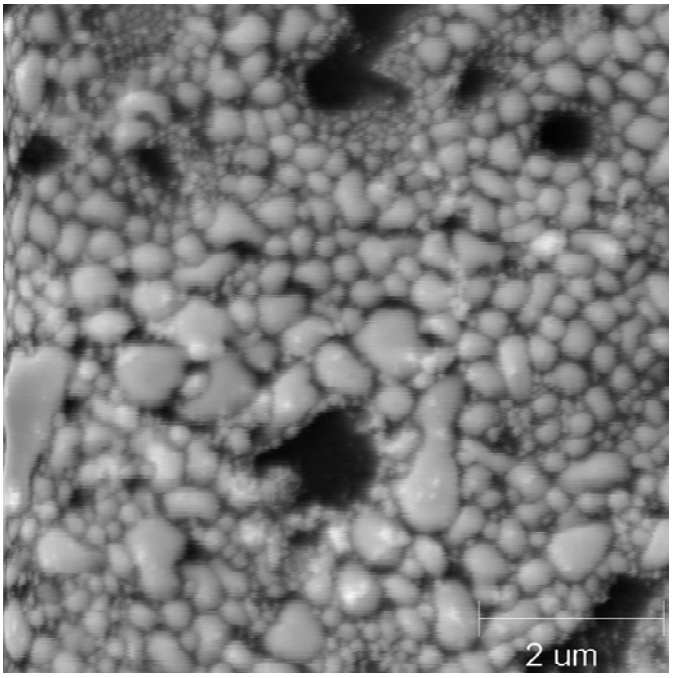


(b)

Figure 7.18. SEM top-view images of the contact interface for (a) higher-$T_g$ glass (33-462) and (b) lowest-$T_g$ glass of paste 33-460.

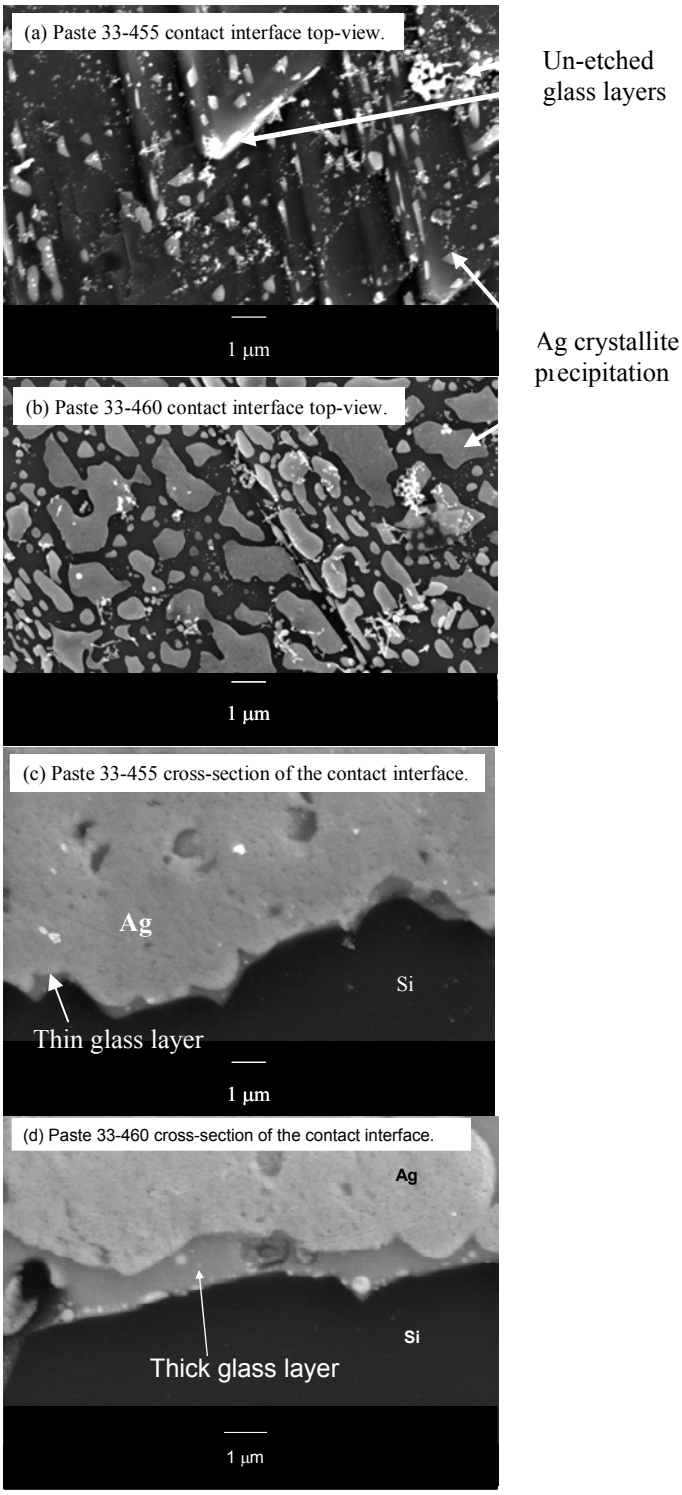


Figure 7.19. SEM images showing the top-view of the contact interface showing Ag crystallites precipitation for pastes (a) 33-455 and (b) 33-460. Low-angle cross-section SEM images of the contact interface showing the glass thickness for pastes (c) 33-455 and (d) 33-460. (Courtesy of Ferro Corporation)

#### 7.3.4.2 Formulation and Investigation of a Novel Fast Crystallizing Glass Frit with High $T_g$

Based on the above understanding, a new paste (33-455) was formulated by Ferro Corp. that has high $T_g$ glass but crystallizes rapidly after reaching high temperatures to produce thinner glass regions. In addition, rapid crystallization of the glass at higher temperatures freezes the glass early so Ag crystallites are not allowed to fully precipitate from the glass. As a result, smaller Ag crystallites and less Ag diffusion are achieved, which reduces the probability of junction shunting. Finally, more Ag precipitates and up in the glass, which could help metal assisted tunneling through the glass layer. Thus, this paste should have most of the ingredients for good contacts. The new paste (33-455) was formulated by adding some modifiers that provide nucleation sites to promote early crystallization near the peak temperature during firing, just before or after the cooling starts. Again solar cells were fabricated and analyzed by electrical and physical characterization tools.

SEM cross-section of the contact interface for this paste in Figure 7.20 shows smaller Ag precipitates on the Si emitter surface, resulted in lower junction leakage current, $J_{o2}$ of 12 nA/cm$^2$, and a higher $V_{oc}$ of ~645 mV compared to $J_{o2}$ of ~25 nA/cm$^2$ and $V_{oc}$ of ~640 mV for the conventional glass of paste 33-462, which produced larger Ag crystallites that contributed to the higher $J_{o2}$.

The contact interface with smaller Ag crystallites and thinner glass layer in Figure 7.20 for paste 33-455 can be explained by a following model. Since the glass crystallizes fast, it becomes less fluid and dissolves less Ag for a shorter period of time compared to the counterpart conventional paste 33-462. More importantly, rapid crystallization reduces the time for Ag precipitation from the glass layer. These two factors lead to

smaller Ag crystallites. More dissolved Ag is probably retained within the glass layer when it crystallizes, fewer precipitates are observed on the Si emitter surface compared to paste 33-462. In fact it was found that it was harder to etch the glass layer of paste 33-455 (Fig. 7.21(a)), which supports the presence of more Ag in the glass.

Rapid crystallization of the glass also results in a reduced flow of the glass, which helps in the formation of thinner glass regions to promote tunneling. This is shown in Figure 7.19 in the previous subsection.

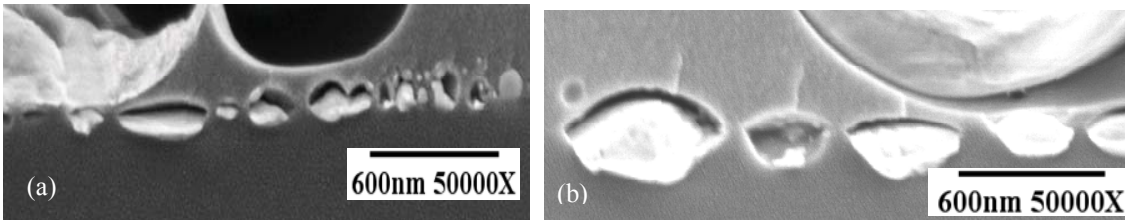

Figure 7.20. SEM cross-section images of the Ag-Si contact interface for (a) high $T_g$ fast crystallizing glass (paste 33-455), and (b) conventional glass (paste 33-462).

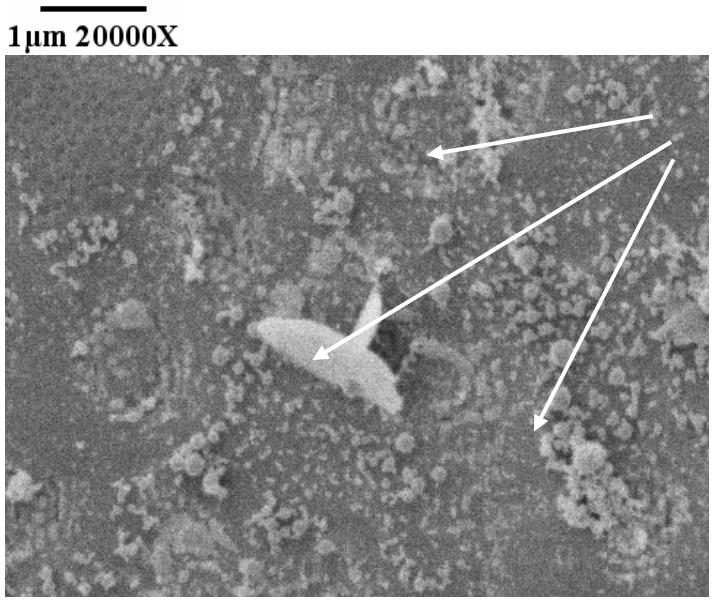


(a)

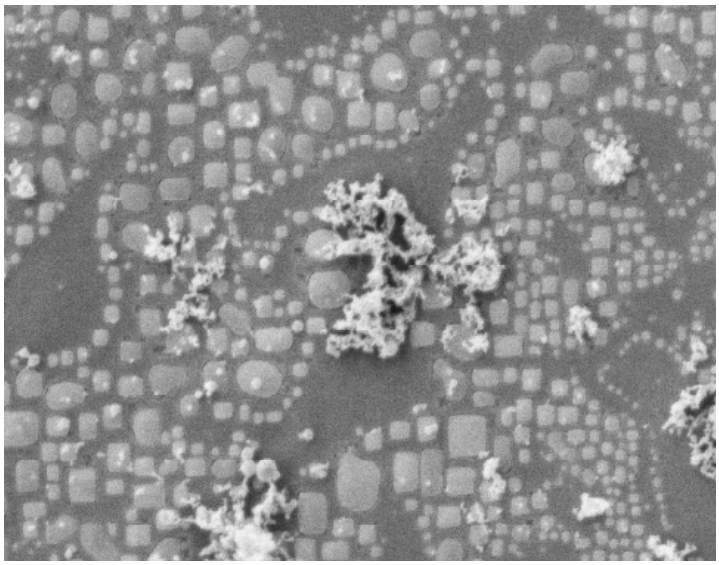

(b)

Figure 7.21. Top-view SEM images of the contact interface after 2.5 % HF solution dipping for 4 min for paste (a) 33-455 and (b) 33-460.

To prove the concept that the rapidly crystallizing glass frit of paste 33-455 helps enhance FF and $V_{oc}$ by decreasing the size of Ag crystallites, another fast crystallizing glass paste (A203-7A) was formed with large Ag particles. Recall that junction shunting degraded the $V_{oc}$ and FF for these large particles, but by converting it into a rapid

crystallization paste reduction of the Ag crystallite size may be possible and higher fill factors may be expected. Indeed, when this was done, FF and $V_{oc}$ increased, resulting in ~0.5% increase in cell efficiency. The enhancement in $V_{oc}$ for the medium and large particle sized pastes resulting from the fast crystallizing glass frit is shown in Figure 7.22. Detailed cell analysis showed that this enhancement in $V_{oc}$ is mainly due to a decrease in $J_{oe}$ from ~500 fA/cm$^2$ to ~320 fA/cm$^2$, probably because of the reduced metal coverage and smaller Ag crystallites. $J_{o2}$ also decreased from ~35 nA/cm$^2$ to ~15 nA/cm$^2$ as a result of the decrease in the size of Ag crystallites.

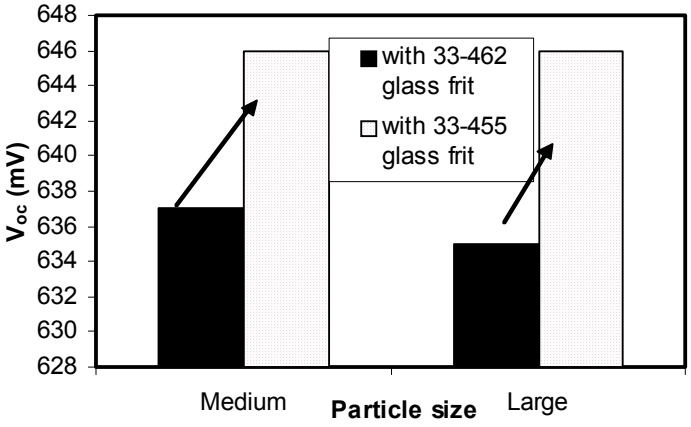


(a)

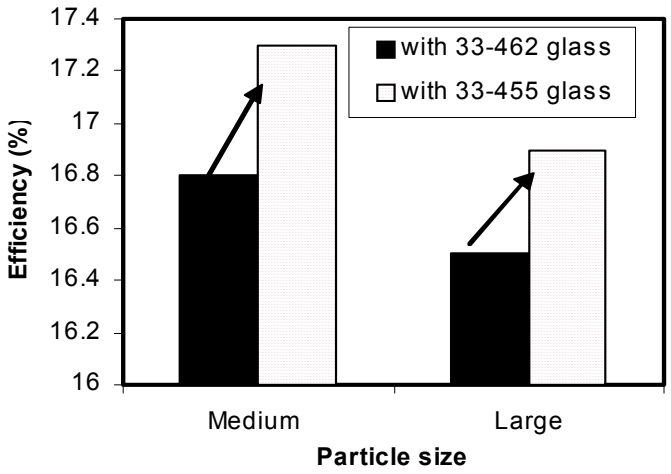


(b)

Figure 7.22. Enhancement of (a) $V_{oc}$ and (b) efficiency for the medium (paste A203-7B) and large particle size (paste A203-7A) pastes by using a fast crystallizing glass of paste 33-455.

### 7.3.4 Effect of P Self-Doping from the Ag Paste

This study was conducted to demonstrate that enhanced performance from paste constituents in the previous sections is not related to phosphorus injection or self-doping from the paste. Instead it is due to the intended functionality of the ingredients. To accomplish this, cells were fabricated on 100 Ω/sq emitters and analyzed to show that self-doping P contained in the paste does not influence the contact quality. The 840° C 120 ipm firing (Table 7.5) was used for this study. Results in Table 7.5 show that low $\rho_c$ (≤1 mΩ-cm$^2$) and high FFs (>0.77) were achieved for pastes with and without P self-doping. Moreover, for lower firing temperature (~750° C, 120 ipm), where P doping is not expected to take place because of the low solubility of P in Si, high FFs (~ 0.78) were achieved. Paste 33-455, which has no P self-doping, gave a FF of 0.783. Thus, P self-doping can be precluded as the cause for the formation of good ohmic contacts to high sheet-resistance emitters.

Table 7.5: Effect of P self-doping on $\rho_c$ and FF.

| Paste | P Self-Doping Property | $\rho_{cm}$ (mΩ-cm$^2$) | Best FF |
|---|---|---|---|
| 33-462 | self-doping | 1..01 | 0.782 |
| 33-456 | self-doping | 1.34 | 0.776 |
| 33-455 | no self-doping | 0.82 | 0.783 |
| 33-452 | no self-doping | 1.09 | 0.777 |
| 33-460 | no self-doping | 0.30 | 0.789 |

### 7.3.5 Fabrication of High-Efficiency Cells on 100 Ω/sq Planar Emitters

This section demonstrates that, consistent with our understanding and analysis of contact interface in the previous sections, high-efficiency cells can be achieved from the two most desirable pastes – 33-462 and 33-455. Figure 7.23 shows that untextured FZ cell efficiencies as high as 17.4% on 100 Ω/sq emitters were achieved. Sometimes there

is a slight scatter or non-uniformity in the cells made on the 100 Ω/sq emitter. Fill factors are generally high for the 40 Ω/sq-emitter cells because of the lower sheet-resistance loss. However, when a good ohmic contact is achieved on 90-100 Ω/sq emitters with a good surface-passivation, a clear improvement of ~0.2-0.4% in absolute efficiency is observed over the ~40 Ω/sq emitter. Tables 7.6 and 7.7 show the best and average cell efficiencies achieved on 100 and 40 Ω/sq emitters using the Ferro paste 33-462. Figure 7.23 shows the best spatial distribution for the nine 4-cm$^2$ cells on a 4-in diameter FZ wafer. This was obtained using the Ferro paste 33-455 and a firing condition of 840° C/120 ipm, followed by forming gas anneal (FGA). These cells had an average FF of 0.779 and an average efficiency of 17.2%. Figure 7.23(b) shows that for the rapidly crystallizing glass in paste 33-455, high-efficiency cells were achieved by 750º C firing conditions. It is also important to note that the glass of paste 33-455 also has a lower lead content (~40% lower) than the other pastes. This is of course better for the environment.

Table 7.6: 90-100 Ω/sq-emitter cells using paste 33-462.

| Cell Name | $V_{oc}$ (mV) | $J_{sc}$ (mA/cm$^2$) | FF | Eff (%) | n factor | $R_s$ (Ω-cm$^2$) | $R_{sh}$ (Ω-cm$^2$) |
|---|---|---|---|---|---|---|---|
| Best Cell | 642 | 34.31 | 0.786 | 17.32 | 1.03 | 0.948 | 27725 |
| Average | 640 | 34.34 | 0.773 | 17.00 | 1.12 | 0.553 | 233546 |
| Standard Dev. | 1 | 0.16 | 0.009 | 0.23 | 0.03 | 0.162 | 599234 |

Table 7.7: 40 Ω/sq-emitter cells using paste 33-462.

| Cell Name | $V_{oc}$ (mV) | $J_{sc}$ (mA/cm$^2$) | FF | Eff (%) | n factor | $R_s$ (Ω-cm$^2$) | $R_{sh}$ (Ω-cm$^2$) |
|---|---|---|---|---|---|---|---|
| Best Cell | 638 | 33.66 | 0.797 | 17.1 | 1.03 | 0.592 | 94677 |
| Average | 637 | 33.50 | 0.790 | 16.87 | 1.05 | 0.719 | 50409 |
| Standard Dev. | 1 | 0.13 | 0.010 | 0.22 | 0.02 | 0.168 | 79500 |

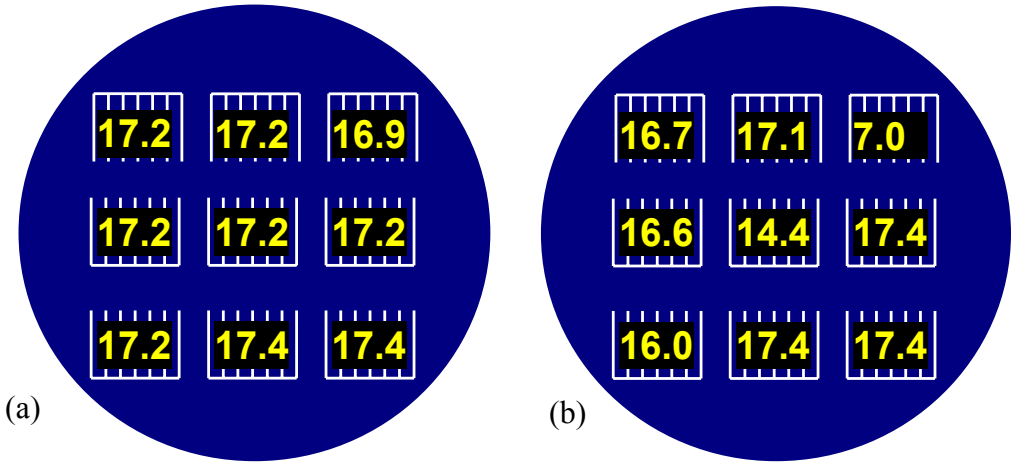


Figure 7.23. The efficiency distribution of nine 4 $cm^2$ cells on a 4 in FZ Si wafer on a 100 Ω/sq emitter using paste 33-455 fired at (a) 840° C/120 ipm and (b) 750° C/120 ipm.

## 7.4 Conclusions

This chapter showed that good ohmic contacts can be achieved directly onto a high sheet-resistance emitter by proper formulation of the glass frit chemistry, particle morphology, and firing condition. The Ag particle size used in the screen-printed Ag paste is found to influence the structure of the contact interface, quality of ohmic contacts, and the $V_{oc}$ and FF of solar cells. Particle size affects the junction leakage current, contact and series resistance, as well as emitter saturation current density. For the five, carefully formulated pastes investigated in this study with different particle size, the Ag-Si contact interface changed dramatically as the Ag particle size was varied from ultra-fine to large. It was found that small spherical Ag particles gave the best fill factor and $V_{oc}$. This is attributed to the lower junction leakage current (~20 $nA/cm^2$) and acceptably low contact resistance (1.7 $m\Omega\text{-}cm^2$) and series resistance (~0.6 $\Omega\text{-}cm^2$). The contact interface showed a large number of small and more uniformly distributed Ag crystallites (≤80 nm) at the interface in conjunction with a fairly thin and uniform glass layer between the Ag crystallites and the grid. This resulted in low series resistance as

well as low junction leakage current. SEM images revealed that the contact interface for large Ag particles contains significant number of large Ag crystallites as well as ultra-thin glass region, resulting in low specific contact resistance (0.24 mΩ-cm$^2$). The enhanced Ag precipitation at the Si emitter surface resulted in a higher Ag diffusion into the Si emitter for the large particle sized paste. Finally, ultra-fine Ag particles showed a fairly uniform and moderately thick glass layer with fewer and more irregularly distributed Ag crystallites. This resulted in higher macroscopic specific-contact resistance (~7 mΩ-cm$^2$) and lower FF (0.754). Ultra-fine particles undergo rapid sintering, thus reducing dissolution of Ag into fluidized glass and leads to the reduced precipitation of Ag crystallites at the interface. Because of tunneling-assisted carrier transport, the fraction of thin glass regions is very critical in reducing the macroscopic contact resistivity. Further understanding of the effect of the paste constituents and firing conditions on the contact interface can lead to the development of even better, more reproducible, and higher-performance screen-printed contacts in the future.

After establishing the role and the requirements for Ag particle size, glass frit chemistry was altered in the paste by changing its aggressiveness or glass transition temperature. Low $T_g$ glass softens early, dissolves more Ag, and flows more easily to form a thicker glass layer. It was found that a glass frit with a high $T_g$ (less fluid) makes better contact to the Si emitter at conventional firing conditions (750° C/120 ipm). Also, a glass frit with a low-medium (more fluid) $T_g$ appears to be less sensitive to firing time. Glass frit primarily determines the optimum firing temperature. A fast crystallizing glass with high $T_g$ was demonstrated to be even better, further enhancing the $V_{oc}$ and cell efficiency because of reduced shunting and junction leakage. It was found that low $T_g$ frit

does not work well with conventional firing temperature of 750° C because it forms a uniform and thick glass layer between Ag crystallites and Ag grid, and there are also not enough metal precipitates in the glass to provide adequate tunneling. However, low $T_g$ glass gave good contact and FF at higher firing temperatures of ~840° C in conjunction with a 400° C forming gas anneal, which helps the formation of enough metal precipitates in the thick glass layer to promote tunneling. High $T_g$ glass works well with higher belt speeds because, even though it forms fewer Ag crystallites, it 'freezes' the glass quickly to give a higher fraction of thin glass regions, which helps the tunneling probability. Based on the understanding of the particle size and frit chemistry, a novel paste was formulated (by Ferro Corporation) that had a blend of small-medium Ag particles, high $T_g$ glass, and modifiers to nucleate rapid crystallization at higher temperatures. This reduces the Ag crystallite size to prevent shunting, increases the fraction of thin glass regions to assist direct connections or tunneling to take place, and increases the metal precipitation within the glass layer to help metal-assisted multi-step tunneling. All these features contributed to a very high FF of 0.783 on 100 Ω/sq emitter with planar cell efficiencies as high as 17.4%. This represents about a 0.4% increase in absolute efficiency over conventional 40 Ω/sq emitter cells.

# CHAPTER 8

# SCREEN-PRINTED HIGH-EFFICIENCY SOLAR CELLS ON LOW-COST SI SUBSTRATES USING100 Ω/SQ EMITTERS

## 8.1 Introduction

In the previous sections only high-lifetime FZ substrates were used for the development and understanding of the screen-printed contacts and solar cells with high sheet-resistance emitters. In this section, low-cost Si substrates, which account for ~60% of the PV modules produced today, are used to study the benefit of the lightly doped emitter. EFG ribbon Si is a promising material for low-cost, high-efficiency solar cells because it eliminates the need for mechanical sawing and damage etching. As a result, kerf loss is eliminated. EFG Si is produced by RWE Schott Solar, Inc., which is the current leader in production volume for Si ribbon solar cells [125]. However, like most low-cost mc-Si materials, EFG Si contains a high concentration of impurities and crystalline defects, which degrade the as-grown minority-carrier lifetime to less than 5 μs. This is not sufficient for high-efficiency cells (>15%). Hence, it is essential to enhance the bulk lifetime during cell fabrication to obtain high-efficiency screen-printed EFG Si cells. High sheet-resistance emitter cells were also fabricated in this chapter on CZ and cast multicrystalline HEM substrates with 1.3 Ω-cm base resistivity. Screen This chapter describes the development and implementation of a simple and rapid firing process that produced for the first time screen-printed EFG Si ribbon cells with efficiency greater than

16% through the development of high-quality screen-printed contacts on a 100 Ω/sq emitter with high bulk lifetime in finished devices exceeding 100 μs.

## 8.2 Experimental Method

In this study, 2×2 cm EFG Si ribbon cells were fabricated by a co-firing process on a 100 Ω/sq emitter using screen-printing technology and belt-line processing. A simple $n^+$-p-$p^+$ cell design was used with a single-layer AR coating and no surface texturing. Cells were fabricated on p-type, 300-μm thick, 3 Ω-cm EFG Si. EFG Si wafers were provided by RWE Schott Solar, Inc. Cell fabrication involved phosphorus diffusion in a $POCl_3$ furnace to form a 100 Ω/sq emitter. A single-layer $SiN_x$ AR coating was deposited on top of the $n^+$ emitter in a commercial low-frequency PECVD reactor. A commercial Al paste (Ferro FX 53-038) was screen printed on the entire back side and dried at 200° C. The front metal grid was then screen printed on top of the $SiN_x$ AR coating using PV168 Ag paste from DuPont, which gave high-efficiency cells on the 100 Ω/sq emitter in Chapter 5. The samples were then co-fired rapidly in a three-zone lamp-heated belt furnace at a set temperature of > 900° C and belt speed of 120 ipm to simultaneously form the Al-BSF and front grid metallization. The firing process was modified slightly, relative to the one developed in Section 5.2. The firing process involved a faster belt speed of 120 ipm instead of 80 ipm, while the peak temperature was ~840° C. This thermal cycle had faster ramp-up and cooling rates to promote and enhance the PECVD $SiN_x$-induced hydrogen passivation of defects in EFG Si [126, 127]. The rapid and high-temperature firing may also help in the formation of good-quality ohmic contacts to a 100 Ω/sq emitter and prevent high leakage current through the use of

a paste like PV168 or the improved Ferro pastes investigated in Section 4.4. At the end of the process, cells were annealed in forming gas at 400$^{o}$ C for 15 min. The final bulk lifetime in the cell was measured using a photo-conductive decay minority-carrier lifetime tester after etching the metal contacts, back-surface field, the AR coating, and the emitter region.

## 8.3 Results and Discussion

EFG cells were fabricated with the above co-firing process on a 100 Ω/sq emitter. Table 8.1 shows the lighted current-voltage (I-V) parameters for the screen-printed 16.1% EFG Si cell achieved in this study with a single-layer AR coating and no surface texturing. These results were confirmed by National Renewable Energy Laboratory (Golden, CO). The 3 Ω-cm EFG Si cell had a $V_{oc}$ of 601.5 mV, $J_{sc}$ of 35.0 mA/cm$^2$, and FF of 0.764. The fast contact co-firing in the belt furnace helped to achieve very effective defect hydrogenation in EFG Si, which is supported by a very high average lifetime of 103 μs with standard deviation of 43 μs in the EFG Si cell. The as-grown lifetime in EFG Si was only ~2 μs. Nine 4 cm$^2$ cells fabricated on a 10×10 cm$^2$ EFG wafer were stripped down to bare Si after cell testing to assess the minority-carrier lifetime in the finished devices. Figure 8.1 shows the results of quasi-steady-state photo-conductance lifetime measurements at several different locations on the wafer containing ~16.1% cells. These measurements were taken at an injection level of $1.0\times10^{15}$ cm$^{-3}$ using an iodine/methanol solution for surface passivation [128]. Such a high lifetime is attributed to the increased retention of hydrogen at defect sites since rapid firing prevents the release of hydrogen from defects.

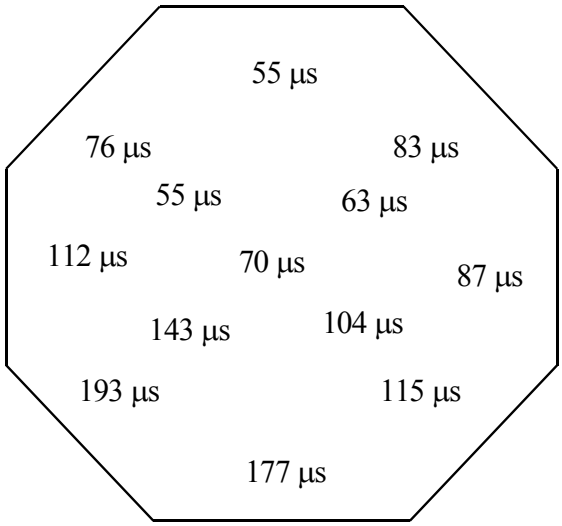


Figure 8.1. Lifetime distribution in the belt co-fired EFG Si wafer containing the 16.1% cell.

Figure 8.2 shows the internal quantum efficiency (IQE) and reflectance of the 16.1% EFG Si cell. To evaluate the benefit of the high sheet-resistance emitter, IQE measurements were taken. Figure 8.3 demonstrates that the IQE in the short-wavelength region for EFG cells improved appreciably because of the successful implementation of a lightly doped emitter compared to the conventional 45 Ω/sq emitter cells, which gave a $V_{oc}$ of 597 mV, $J_{sc}$ of 32.5 mA/cm$^2$, FF of 0.770, and efficiency of 15.0%. These results demonstrate that high-efficiency screen-printed cells can also be achieved on low-cost defective materials using a lightly doped emitter along with simple, rapid, and manufacturable cell fabrication processing. A few cells were also fabricated on cast multicrystalline Si and monocrystalline Cz Si. Table 8.1 shows that the 100 Ω/sq emitter resulted in EFG, multicrystalline HEM, and Cz cell efficiencies of ~16.4%. The detailed processing conditions for both monocrystalline and multicrystalline screen-printed cells (fabricated on the 100 Ω/sq emitters) are given in Appendix D.

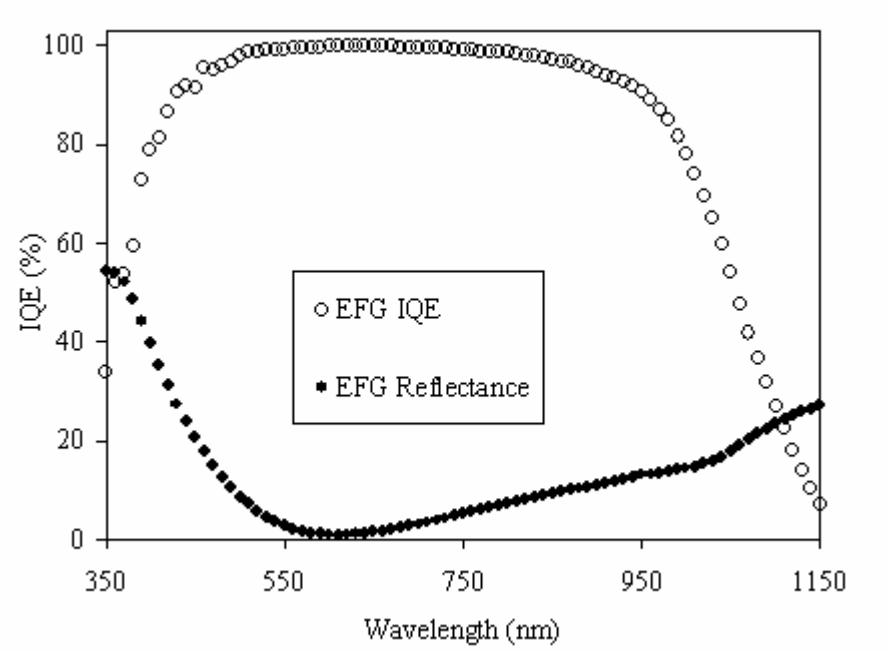


Figure 8.2. IQE and reflectance of the 16.1% EFG cell.

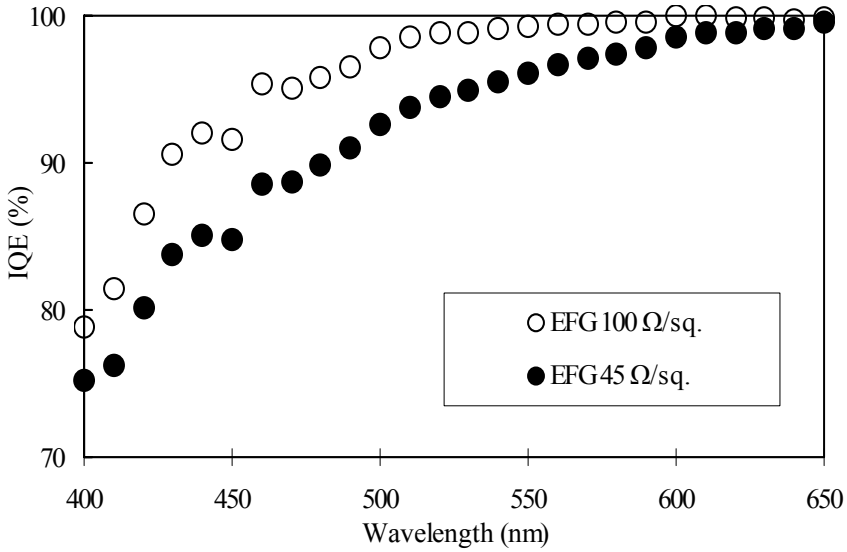


Figure 8.3. Short-wavelength response for 100 and 45 Ω/sq-emitter cells.

Table 8.1. High-efficiency cells on 95-100 Ω/sq emitters for EFG and other low-cost Materials using PV168 Ag paste from DuPont.

| Substrate | $V_{oc}$ (mV) | $J_{sc}$ (mA/cm²) | FF | Eff (%) | n factor | $R_s$ (Ω-cm²) | $R_{sh}$ (Ω-cm²) |
|---|---|---|---|---|---|---|---|
| EFG | 602 | 35 | 0.764 | 16.1 | 1.08 | 0.77 | 86,225 |
| HEM | 633 | 34.9 | 0.746 | 16.49 | 1.18 | 1.348 | 31,469 |
| Cz | 622 | 33.6 | 0.783 | 16.35 | 1.07 | 0.754 | 162,229 |

In addition to the PV168 paste, we also investigated Ferro 33-456 paste for EFG Si cells because it has the right particle size and glass transition temperature, but it has flake morphology instead of spherical. The cross-section SEM study in Figure 8.4 shows that this paste also gives a large number of small Ag crystallites and ultra-thin glass regions, which are desirable for a good contact. An efficiency >16.1% was also obtained for paste 33-456 from Ferro Corporation as well, with higher uniformity and higher $V_{oc}$ (617 mV) compared to Ag paste PV168 from DuPont. The glass frit and Ag particle morphology behavior of paste 33-456 has been studied in Section 7.3.2 and was found to give a comparable performance to the medium spherical particle size paste with the same medium-high $T_g$ glass frit. Table 8.2 shows the cell performance data for the EFG cells with 100 Ω/sq emitters. Paste 33-456 was found to be the best paste for achieving good-quality contacts to the EFG Si ribbon emitter surface, indicating that flake morphology may be more suitable for ribbon material surfaces.

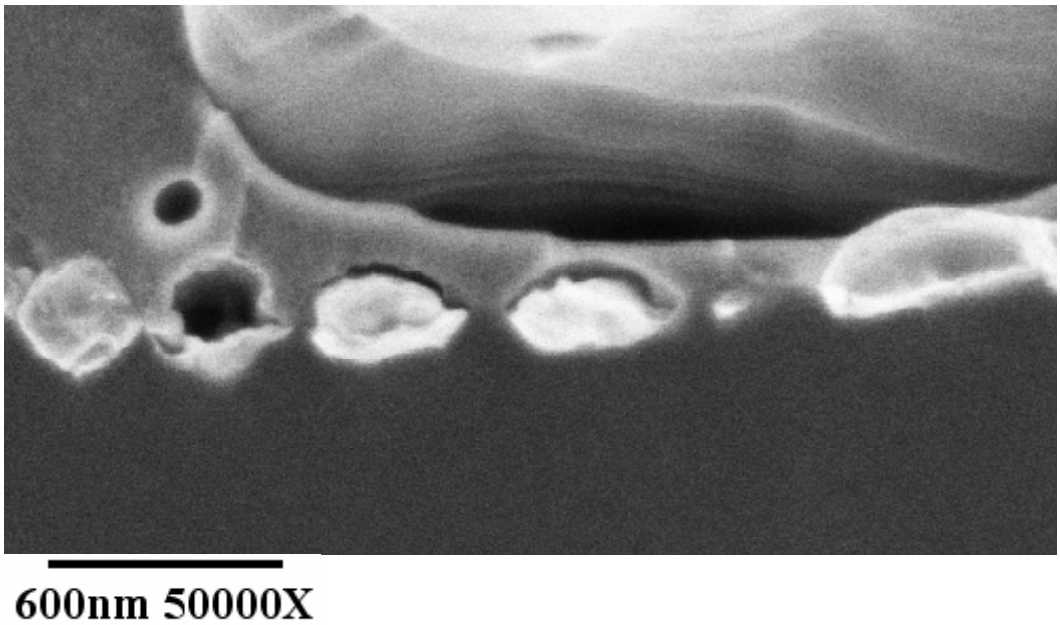


Figure 8.4. Cross-sectional SEM of the contact interface for paste 33-456.

Table 8.2: High-efficiency cells on 95-100 Ω/sq emitters for EFG using 33-456 Ag paste from Ferro Corporation.

| Cell Name | $V_{oc}$ (mV) | $J_{sc}$ (mA/cm²) | FF | Eff (%) | n factor | $R_s$ (Ω-cm²) | $R_{sh}$ (Ω-cm²) |
|---|---|---|---|---|---|---|---|
| efg3-18-9 | 617 | 34.90 | 0.751 | 16.17 | 1.31 | 0.830 | 83795 |
| Average | 604 | 34.69 | 0.754 | 15.81 | 1.24 | 0.899 | 91094 |
| STDEV | 9 | 0.23 | 0.004 | 0.25 | 0.07 | 0.109 | 55827 |

## 8.4 Conclusions

The results of this study show that it is possible to achieve good contact quality on high sheet-resistance emitters even for low-cost multicrystalline and ribbon Si materials. This is achieved in conjunction with bulk lifetime enhancement. Lifetimes >100 μs were achieved along with the FFs greater than 0.76. The firing process developed in this section involved a fast firing speed (120 ipm), with peak temperature of ~840° C, which is similar to the process developed for FZ in Section 5.3. This prevented junction

shunting and resulted in high lifetime, indicating enhanced hydrogen retention at defects during this firing process. Cell efficiencies of 16.1% and ~16.2% on EFG ribbon substrates using both PV168 Ag paste from DuPont and 33-456 Ag paste from Ferro Corporation, respectively, confirmed the robustness of the firing process. High efficiencies of >16.3% and >17.5% were also achieved on high sheet-resistance planar and textured single-crystal Cz substrates, respectively.

# CHAPTER 9

# UNDERSTANDING, MODELING, FABRICATION, AND ANALYSIS OF RECORD HIGH-EFFICIENCY SCREEN-PRINTED TEXTURED CELLS ON HIGH SHEET-RESISTANCE EMITTERS

## 9.1 Introduction

The cost and performance targets of Si photovoltaics can be reached simultaneously by enhancing cell efficiency while utilizing low-cost high throughput processing [15]. It is well known that front-surface texturing and high sheet-resistance emitters can significantly enhance solar cell performance [129-131]. However, prior to this research they have not been implemented together using direct screen-printed contact to high sheet-resistance emitters (i.e., single-step diffusion and co-firing of the screen-printed contacts). Therefore, in this chapter, we combine the benefit of high sheet-resistance emitters and surface texturing to achieve record high efficiency screen-printed Si cells. In Chapters 5 and 7 high fill factors (>0.78) were achieved on high sheet-resistance planar emitters through the understanding and optimization of the Ag paste and firing recipe. This led to the fabrication of ≥17.4%-efficient solar cells on float-zone Si with screen-printed contacts on an untextured 100 Ω/sq phosphorus-doped emitter. In this chapter an investigation of textured high sheet-resistance emitters is conducted. Detailed

modeling of the cell parameters is performed to understand the source of efficiency enhancement.

## 9.2 Experimental Method

In this study, screen-printed (SP) $n^+$-p-$p^+$ solar cells (4 $cm^2$) are fabricated on single-crystal p-type, 300-μm thick (100) float-zone (FZ) substrates. First, textured and planar FZ silicon wafers received a standard RCA clean, followed by $POCl_3$ diffusion to form the $n^+$-emitter. A diffusion temperature of 843° C was used for the 100 Ω/sq emitter, while 878° C was used for the 45 Ω/sq. After the phosphorus-glass removal and another clean, a 50 kHz PECVD $SiN_x$ AR coating was deposited on the emitter. Next, an Al paste was screen-printed on the back side and dried at 200° C. The Ag grid was then screen printed on top of the $SiN_x$ film and then the Ag and Al contacts were co-fired (single firing step) in a lamp-heated three-zone infra-red belt furnace. Cells were then isolated using a dicing saw and subjected to a 400° C 15-min forming-gas anneal. Cell performance was characterized by light I-V as well as internal quantum efficiency (IQE) measurements for the short-wavelength response. Textured cells were used with a planar back to ensure that the base properties were the same when comparing planar and textured cells. Cells with surface texturing on both sides were also fabricated.

## 9.3 Results and Discussion

### 9.3.1 Understanding the Difference in Enhancement Due to the High Sheet-Resistance Emitter in Textured Cells Compared to Planar Cells

After cell fabrication on textured and planar FZ substrates, IQE and reflectance measurements were taken. It was found (Figure 9.1) that the short-wavelength response for a textured emitter cell was lower than that for the planar emitter cell. This is largely attributed to the higher front-surface recombination velocity because of the ~70% increase in surface area resulting from the regular pyramid texturing on the surface. However, the lower surface reflectance (Fig. 9.2) resulting from texturing produced a 8.4% reduction in average weighted reflectance, which corresponds to an increase of 3.94 $mA/cm^2$ in transmitted current over the planar surface, calculated from the incident photon flux and reflectance curves in Figure 9.2. Therefore, the loss in the short-wavelength response shown in Figure 9.1 is more than compensated by the improved surface reflectance to provide appreciable enhancement of 2.7 $mA/cm^2$ in $J_{sc}$ and 1.2% in absolute cell efficiency (Table 9.1) because of texturing on 100 Ω/sq emitter cells. However, improvement due to texturing was somewhat less (2.4 $mA/cm^2$ in $J_{sc}$ and 0.7% in absolute efficiency) on the 45 Ω/sq emitter. Model calculations and cell analysis were used to investigate the reason for this difference.

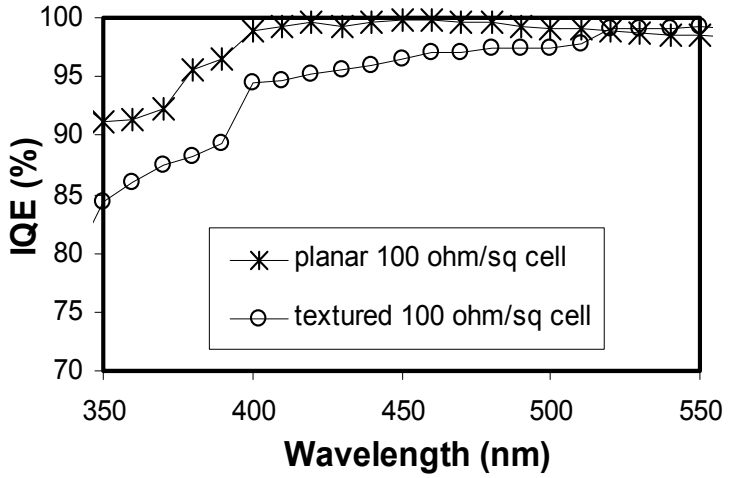


Figure 9.1. Short-wavelength response of planar versus textured 100 Ω/sq emitters.

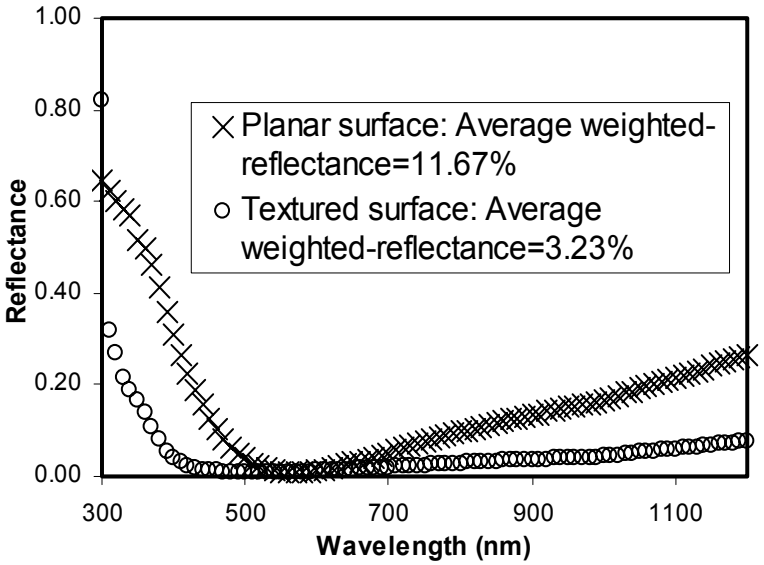


Figure 9.2. Reflectance of planar and textured emitter surface with $SiN_x$ single-layer antireflection coating.

Cell data in Table 9.1 shows that the ~0.4-0.5% higher increase in efficiency for textured cells results primarily from a higher $\Delta J_{sc}$ of ~0.3 mA/cm$^2$ for the textured cells on the high and low sheet-resistance emitter compared to the planar counterpart (1.1 mA/cm$^2$ versus 0.8 mA/cm$^2$). The $V_{oc}$ enhancement due to the high sheet-resistance emitter was same (10 mV) for textured and planar cells. The enhancement in $J_{sc}$ is also ~0.3 mA/cm$^2$ higher for textured cells compared to planar cells with the high sheet-resistance emitter compared with the low sheet-resistance emitter counterpart (2.7 mA/cm$^2$ versus 2.4 mA/cm$^2$). There was some scatter in fill factors, but it was comparable for the textured and planar cells for both sheet resistances.

The IQE as well as the spectral response (SR) of all four cells in Table 9.1 was analyzed in detail to explain the greater difference in $\Delta J_{sc}$ resulting for the high sheet-resistance emitter. The short-circuit current is proportional to the spectral response (SR), which is expressed as [132] $SR(\lambda)=IQE(\lambda)(1-R(\lambda))\cdot(\lambda/1.24)$, where IQE is the internal quantum efficiency, R is the reflectance of the cell, $\lambda$ is the wavelength in μm, and $\lambda/1.24$ is the photon energy in eV.

Table 9.1: Light I-V parameters of 0.6 Ω-cm textured and planar best cells with 45 and 100 Ω/sq emitters.

| Emitter Surface | Emitter (Ω/sq) | $V_{oc}$ (mV) | $\Delta V_{oc}$ (mV) | $J_{sc}$ (mA/cm$^2$) | $\Delta J_{sc}$ (mA/cm$^2$) | FF | η (%) | Δη (%) | n factor | $R_s$ (Ω-cm$^2$) | $R_{sh}$ (Ω-cm$^2$) |
|---|---|---|---|---|---|---|---|---|---|---|---|
| Textured | 45 | 631 | 10 | 36.19 | 1.09 | 0.777 | 17.7 | 0.87 | 1.13 | 0.702 | 89,026 |
| | 100 | 641 | | 37.28 | | 0.778 | 18.6 | | 1.09 | 0.733 | 68,114 |
| Planar | 45 | 636 | 10 | 33.8 | 0.8 | 0.789 | 17.0 | 0.4 | 1.03 | 0.805 | 658,549 |
| | 100 | 646 | | 34.6 | | 0.780 | 17.4 | | 1.09 | 0.789 | 281,975 |

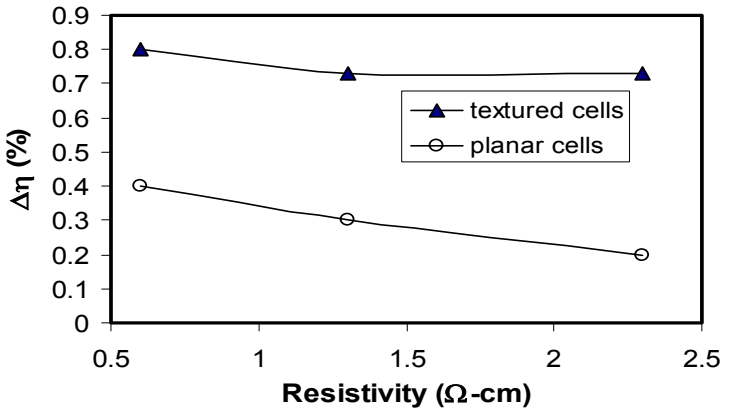


Figure 9.3. Measured enhancement in efficiency resulting from a 100 Ω/sq over a 45 Ω/sq emitter in textured and planar cells fabricated on different base resistivity.

It is important to realize that IQE is strongly influenced by bulk lifetime and surface recombination velocity. Thus, there are three factors that can contribute to a greater enhancement in $J_{sc}$ for the textured high sheet-resistance emitter compared with the low sheet-resistance emitter: the greater enhancement in IQE, the greater reduction in reflectance, and the greater difference in FSRV. Texturing results in oblique light penetration into the cell which increases the path length and could contribute to enhancement in IQE due to texturing. The increased path length increases absorption for a textured surface according to $\alpha_{tex}=\alpha_{pl}/\cos(\theta,)$ where $\alpha_{pl}$ is the absorption for a planar surface and θ is the refracted angle [133]. The effect of the increased optical path length due to texturing was simulated in PC1D for 45 Ω/sq and 100 Ω/sq cells. Cell parameters including IQE were calculated and compared. Figure 9.4 shows that the short-wavelength IQE was almost identical for the 100 Ω/sq textured and planar cells when other device parameters (including FSRV) were assumed to be the same. Similarly, the simulated short-wavelength IQE was nearly identical for the 45 Ω/sq planar and textured emitter,

assuming the same FSRV. Therefore, the difference in the short-wavelength response due to path-length enhancement is negligible if FSRV is assumed to be the same. However, if the change in FSRV is different due to texturing for high and low sheet-resistance emitters then it could influence the change in IQE due to texturing. This can happen because FSRV is known to be a function of surface dopant concentration. Thus, FSRV may be very different for the high and low sheet-resistance cells before and after texturing.

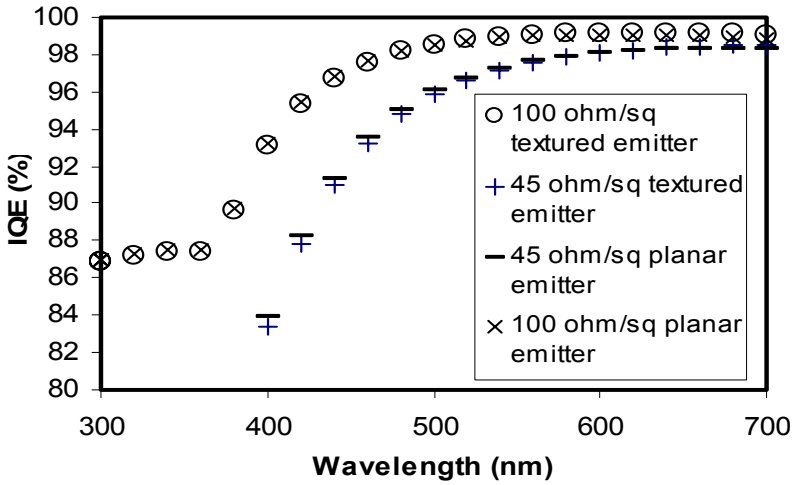


Figure 9.4. PC1D-simulated short-wavelength response for textured and planar 100 and 45 Ω/sq emitter cells. FSRV is the same for all cases.

Therefore, the FSRV difference was investigated in detail to explain the enhancement difference between textured and planar cells for 45 and 100 Ω/sq emitter cells. The change in FSRV for the 45 Ω/sq emitter is expected to be greater as a result of texturing because FSRV should increase by a factor of ~1.73 in both cases. As a result of the 1.73 times increase in the surface area, the 45 Ω/sq emitter is expected to have a higher FSRV due to higher emitter surface concentration. To prove this point, the FSRV

was extracted by matching the measured short-wavelength IQE with the PC1D-modeled IQE for planar and textured cells. An example of the FSRV extraction is shown in Fig. 9.5, which shows an excellent match between the measured and simulated short-wavelength IQE for a FZ cell with a 100 Ω/sq textured emitter is shown in Figure 9.5. The short-wavelength IQE response for all the four cases (100 and 45 Ω/sq emitters for textured and planar surfaces) is shown in Fig. 9.6. The extracted FSRV values for each case are shown in Table 9.2. The extracted FSRV values in Table 9.2 validate an increase of 1.7 times in FSRV due to texturing for both the emitters. However, Table 9.2 shows that the FSRV change is much greater for the textured devices when switching from the 45 Ω/sq emitter to the 100 Ω/sq emitter (35,000 cm/s to 60,000 cm/s for the 100 Ω/sq emitter, and 90,000 cm/s to 150,000 cm/s for the 45 Ω/sq emitter). Using the FSRV values in Table 9.2, PC1D simulations were performed (Fig. 9.7), which showed that texturing provides an additional enhancement of 0.4% in $\Delta\eta$ in favor of the high sheet-resistance emitter, which supports the experimental results in Figure 9.3.

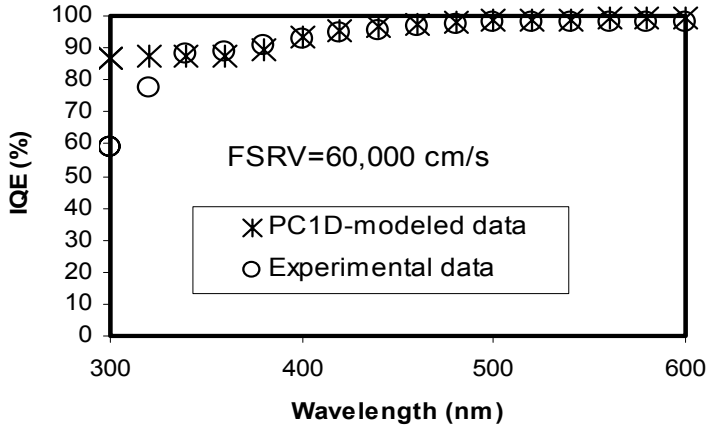


Figure 9.5. IQE matching of experimental short-wavelength response data using PC1D-modeled data for 100 Ω/sq emitter textured cell.

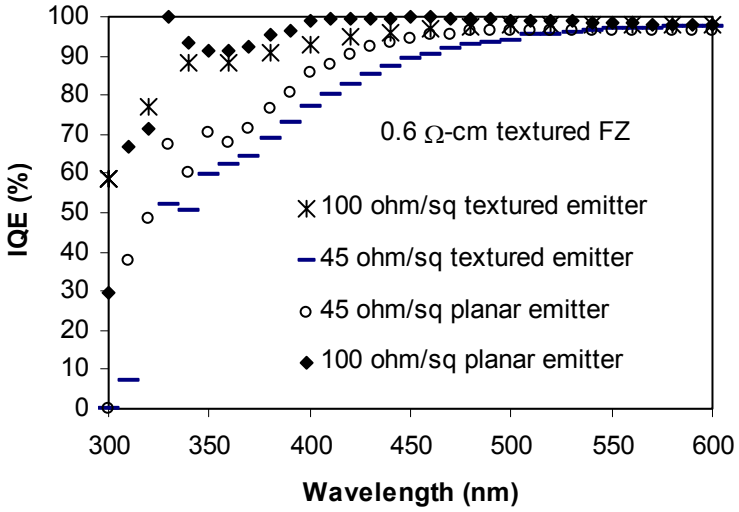


Figure 9.6. Short-wavelength IQE response of the 45 and 100 ohm/sq planar and textured emitter cells.

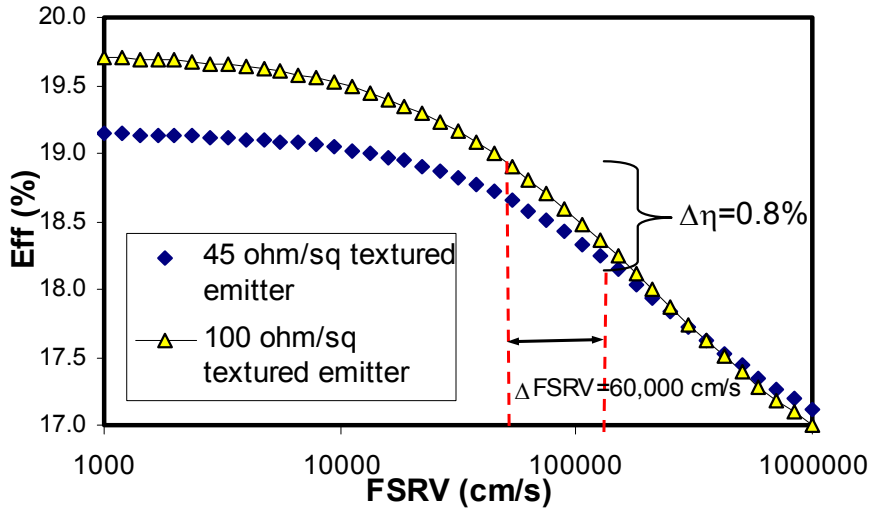


(a) Textured high and low sheet-resistance emitter cells.

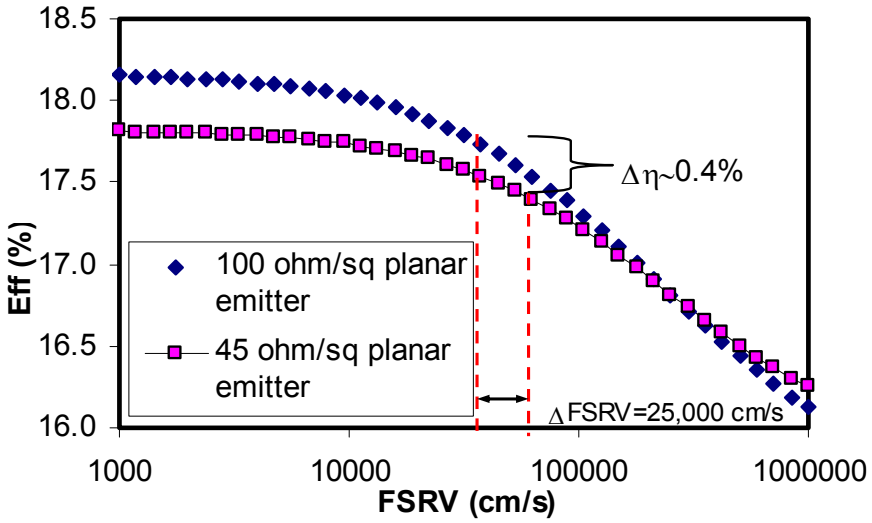


(b) Planar high and low sheet-resistance emitter cells.

Figure 9.7. PC1D modeling of the efficiency versus FSRV for (a) textured and (b) planar cells with high and low sheet-resistance emitters.

Table 9.2:. Extracted FSRV values for 45 and 100 Ω/sq textured and planar emitters.

| Emitter $\rho_s$ (Ω/sq) | Textured/Planar | FSRV (cm/s) | FSRV Factor Due to Textured Surface |
|---|---|---|---|
| 45 | planar | 90,000 | 1.67 |
| 45 | textured | 150,000 | |
| 100 | planar | 35,000 | 1.71 |
| 100 | textured | 60,000 | |

### 9.3.2 Study of Contact Interface Difference for Textured and Planar Cells

We have also investigated the contact interface for both textured and planar high sheet-resistance emitter cells. Figure 9.8 shows top-view SEM images of the area underneath the Ag gridline (~25×25 μm) after etching away the bulk metal of the gridline and the glass layer. As shown in Figure 9.8(a), the planar surface has a more irregular distribution of Ag crystallite precipitation compared with the textured emitter surface in Figure 9.8(b). Ag crystallites represent the current pick-up points from the Si emitter to the Ag grid [78]. Figure 9.8(b) shows that there is Ag precipitation mainly at the peaks and edges of the texture pyramids, even in regions where the Ag crystallite precipitation is sparse. However, this is not the case for the planar surface, where many regions are devoid of Ag crystallite precipitation. This results in a less regular distribution of Ag crystallites for the planar emitter surface as opposed to the textured emitter surface. This may explain the smaller standard deviation of 0.48 Ω-cm$^2$ in the series resistance for textured emitter cells compared with a standard deviation of 1.19 Ω-cm$^2$ for planar emitter cells. In addition, the macroscopic specific-contact resistance for the planar cells was measured to be ~2 mΩ-cm$^2$, and for the textured cells it is ~0.63 mΩ-cm$^2$. However, the fill factors achieved on the high-performance textured and planar 100 Ω/sq cells are very close because the specific contact resistance is less than 3 mΩ-cm$^2$ in both cases,

below which it has a negligible effect on FF.

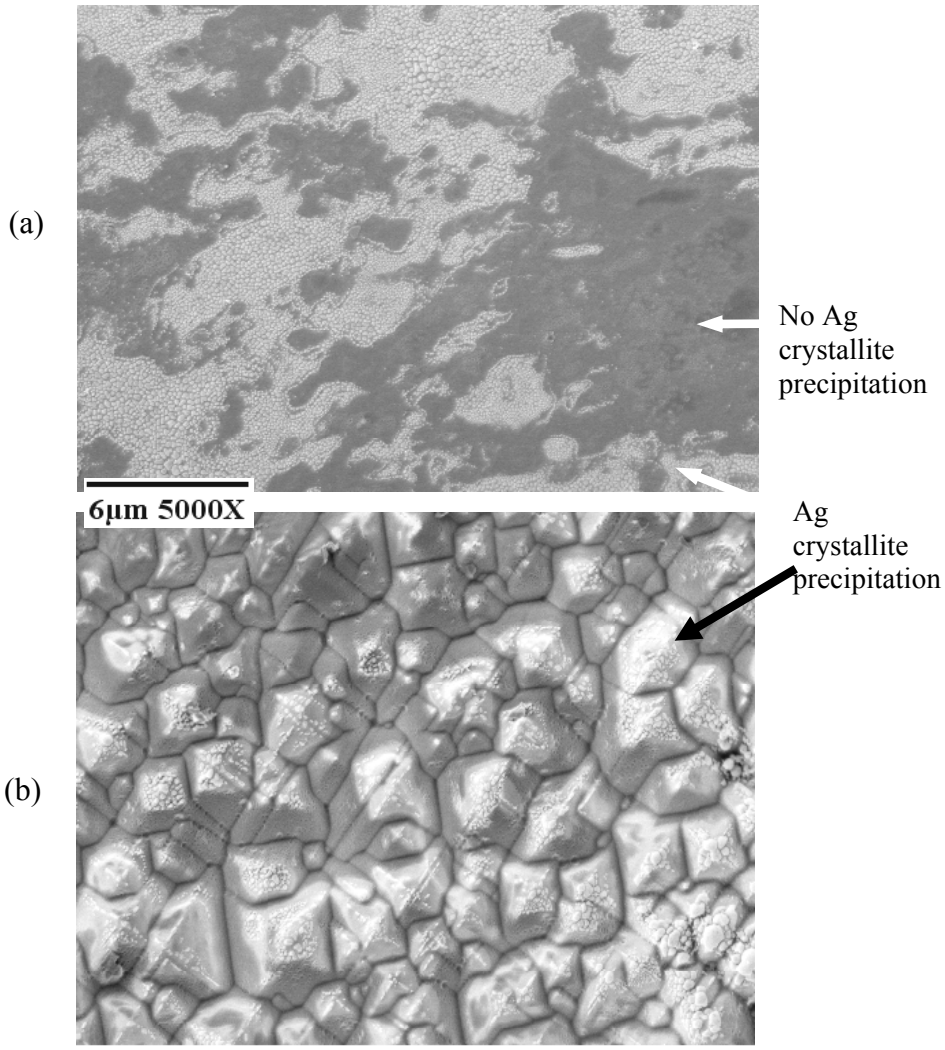


Figure 9.8. SEM top-view images of the region underneath the screen-printed contact for (a) planar emitter and (b) textured emitter.

Ag precipitates are regularly observed on the textured emitter, particularly at the tips and edges of the pyramids. One possible reason is that the surface area per unit volume is greater at the tips and edges of the pyramids so there is a higher probability of precipitation. In addition, Si etching is more rapid and easy at the tips because when the (111) plane is etched off by the frit, the exposed (100) plane etches even more rapidly and results in rounding of the tip (Fig. 9.9). Finally, as shown in Figure 9.10, there are

more Ag precipitates on the (111) plane, which forms the sides of the texture pyramids. This is consistent with the observations of Mertens et al. [57].

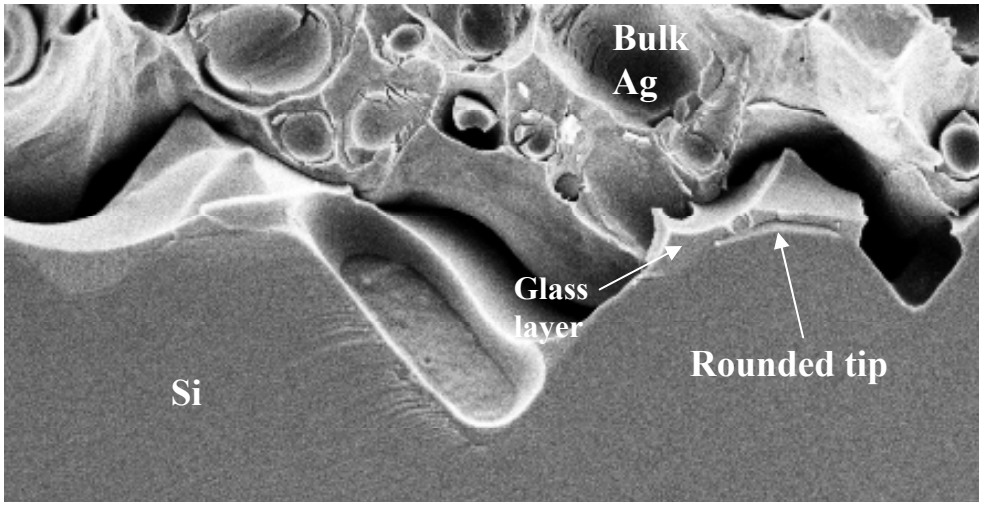


Figure 9.9. SEM cross-section of the textured Ag-Si contact interface.

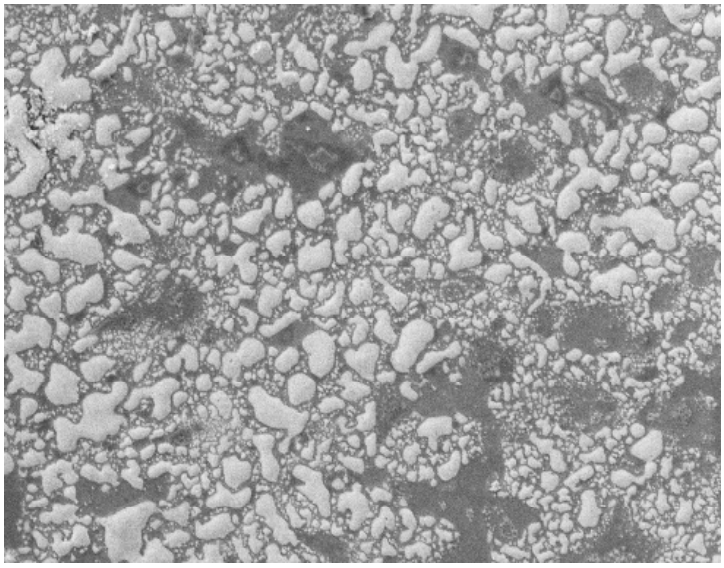

Figure 9.10. Ag precipitation on the (111) Si emitter surface after firing the paste through the $SiN_x$ film.

### 9.3.3 Record High-Efficiency Screen-Printed Textured Cells with 100 Ω/sq Emitters

Through the understanding and implementation of all of the above effects associated with paste, firing, and texturing, record high-efficiency 19% screen-printed cells were achieved on 0.6 Ω-cm FZ Si with a textured 100 Ω/sq emitter and a single-layer PECVD ARC. This efficiency was independently confirmed by NREL (Fig. 9.11). Figure 9.12 shows the simple low-cost process sequence used for fabricating the cell. This cell has 0.6 Ω-cm base resistivity and a single-layer antireflection coating (PECVD $SiN_x$). The best cell had an excellent FF of ~0.78 and high current of ~37.5 mA/cm$^2$ as a result of texturing, in addition to a high $V_{oc}$ of 643 mV. Figure 9.13 shows that most of the textured cells fabricated on 100 Ω/sq emitters had efficiencies greater than 17.0% and about half had efficiencies in the range of 18-19%. The poor efficiencies for some of the cells shown in Figure 9.13 generally resulted from the high series resistance. This was reflected in a high contact resistance and very low FF. Thus, more work needs to be done to improve the uniformity of high-efficiency cells with high sheet- resistance emitters. Figure 9.14 shows a distribution of nine 4 cm$^2$ cells on one 4-in diameter FZ wafer with front and back surface texture. These cells were measured at NREL using a mask with an aperture area of 3.8 cm$^2$. The $V_{oc}$ of these cells was ~643 mV, which demonstrates high-quality screen-printed contacts without shunting of the shallow high sheet-resistance emitter.

The 19% cell achieved in this research represents the highest-efficiency screen-printed cell to date. Figure 9.15 shows the progress of high-efficiency screen-printed cells since 1980. The cell fabricated in this research work had an area of 4 cm$^2$. Prior to this

Munzer et al. [128] reported on 18.2% efficient cells on large-area (106 $cm^2$) CZ wafers but with a longer process sequence. Figure 9.16 shows the distribution of a large number of high-efficiency textured cells fabricated in this research with 100 Ω/sq emitter using (a) 1.3 and (b) 0.6 Ω-cm base resistivity. Most of the cells were fabricated with PV168 Ag paste from DuPont. However, 1.3 Ω-cm base resistivity cells with efficiencies greater than 18% were also achieved using Ag paste 33-455 from Ferro. The $V_{oc}$, $J_{sc}$, FF, and cell efficiency (%) of a large number of 17-18%- and 18-19%-eficient cells are shown in Tables 9.3 and 9.4, respectively.

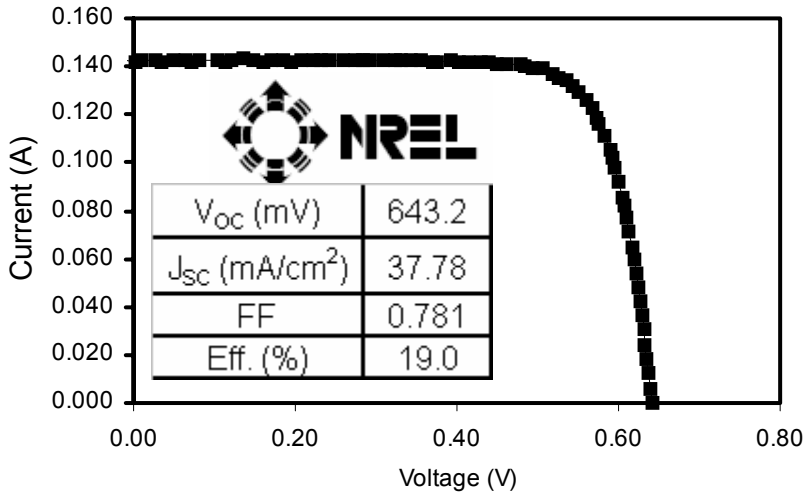


Figure 9.11. I-V measurement by NREL for the 19.0% textured front and back 100-Ω/sq emitter cell.

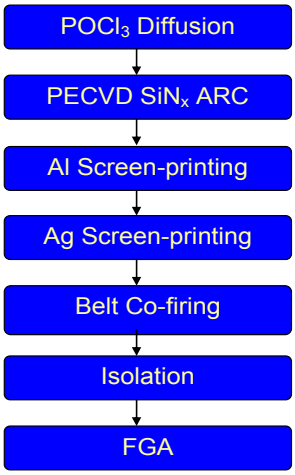


Figure 9.12. Process sequence for the 19% textured cell with 100 Ω/sq emitter.

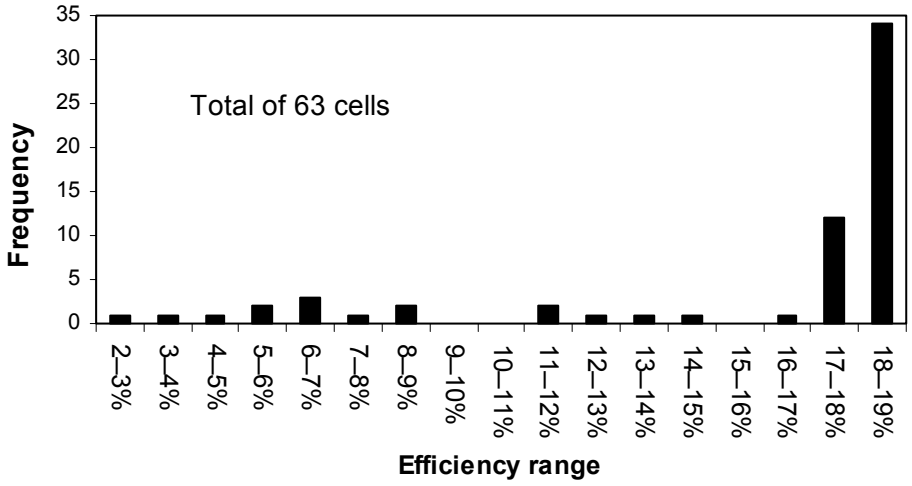


Figure 9.13. Efficiency distribution of 63 textured (0.6 and 1.3 Ω-cm base resistivity) cells with 100 Ω/sq emitters.

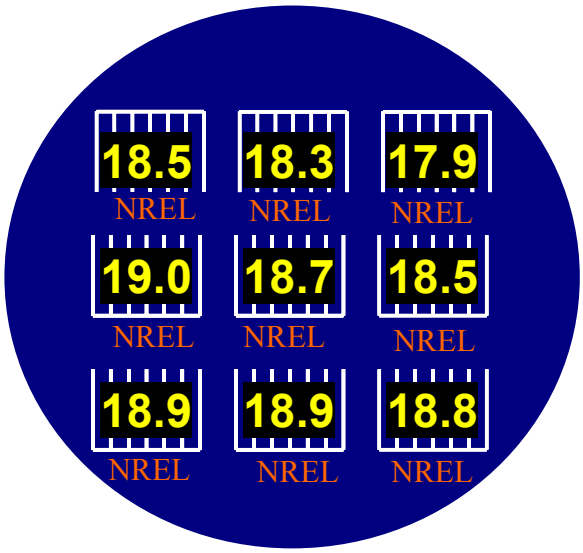


Figure 9.14. The distribution of nine 4 $cm^2$ cells with a 3.8 $cm^2$ mask on a 4 in. 0.6 Ω-cm FZ wafer textured on both sides. The $V_{oc}$ ranged form 641-644 mV (measured at NREL).

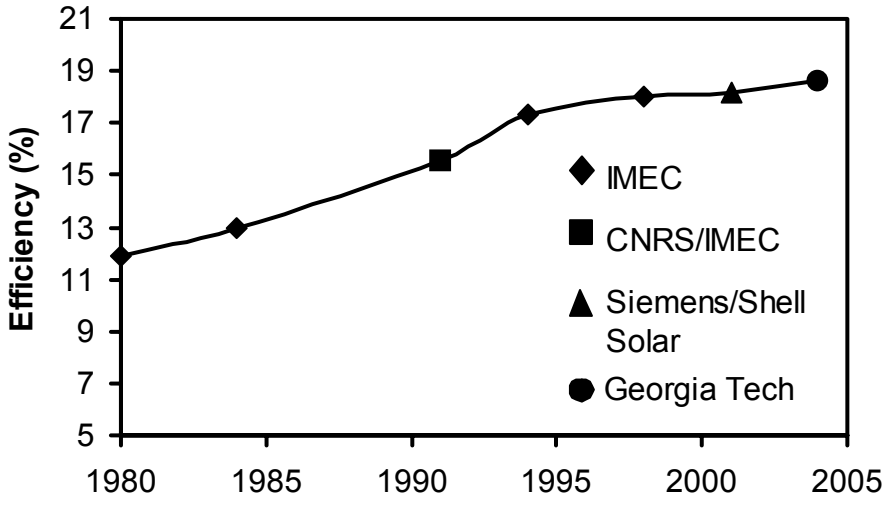


Figure 9.15. Record high-efficiency screen-printed cells over the past 25 years.

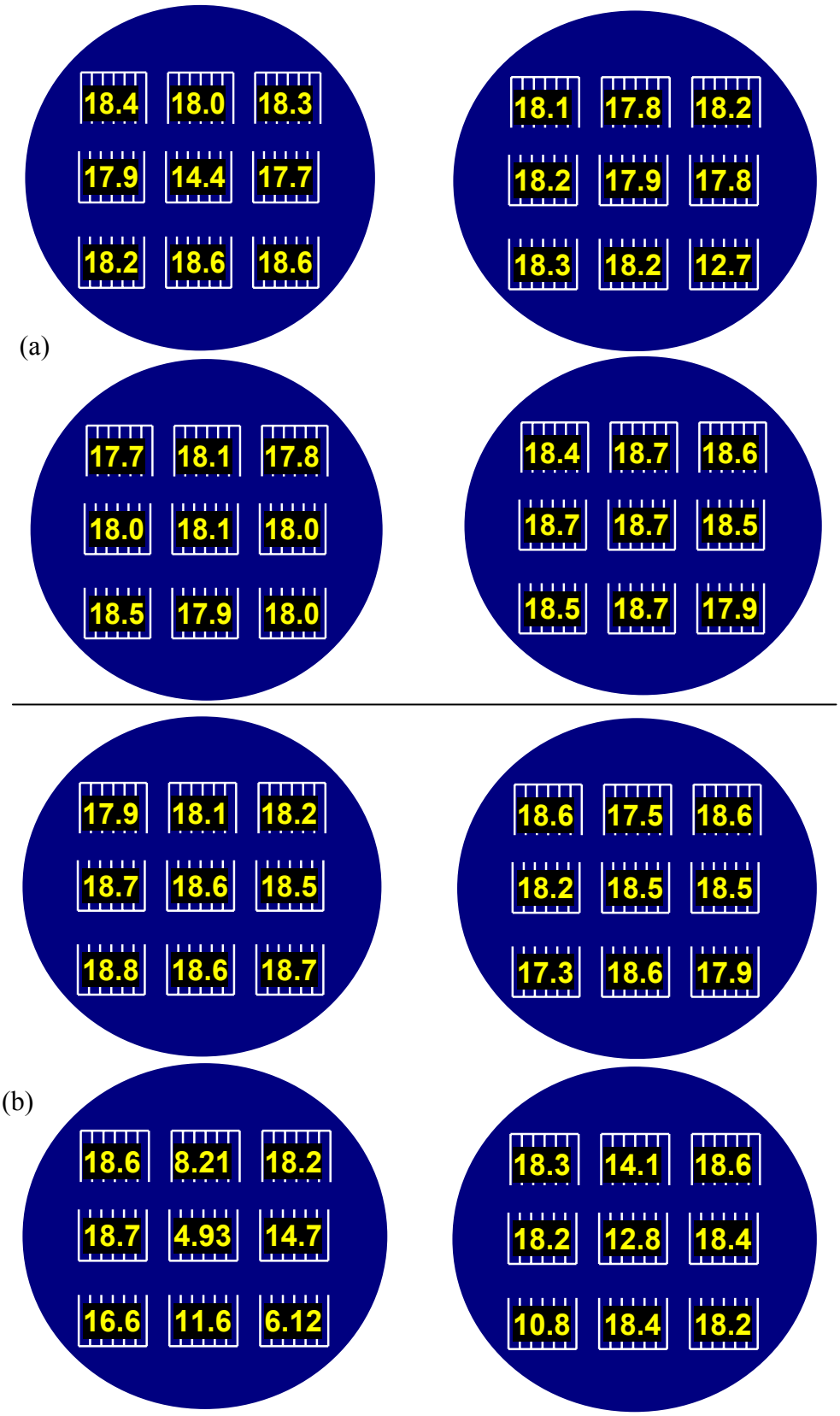


Figure 9.16. The distribution of cell efficiency of textured 100 Ω/sq emitter cells on (a) 1.3 Ω-cm and (b) 0.6 Ω-cm FZ Si substrates.

Table 9.3: Measured $V_{oc}$, $J_{sc}$ and FF for 100 Ω/sq emitter textured cells with 17-18% efficiencies.

| Cell ID | $V_{oc}$ (mV) | $J_{sc}$ (mA/cm$^2$) | FF | Eff (%) |
|---|---|---|---|---|
| T06-100-1-2-1 | 638 | 37.30 | 0.751 | 17.88 |
| A1-7-8 | 639 | 38.06 | 0.747 | 17.96 |
| A1-7-1 | 639 | 38.16 | 0.750 | 17.92 |
| A1-10-8 | 637 | 37.78 | 0.739 | 17.78 |
| A1-8-1 | 638 | 37.73 | 0.747 | 17.90 |
| A1-8-8 | 635 | 37.52 | 0.743 | 17.78 |
| A1-9-2 | 638 | 37.82 | 0.752 | 17.84 |
| A1-9-4 | 639 | 38.09 | 0.745 | 17.76 |
| A1-9-5 | 636 | 38.27 | 0.749 | 17.85 |
| A1-3-1 | 633 | 36.24 | 0.770 | 17.67 |
| A1-3-3 | 635 | 36.98 | 0.755 | 17.72 |
| A1-3-4 | 634 | 36.79 | 0.771 | 17.97 |
| A1-3-7 | 634 | 36.95 | 0.767 | 17.96 |
| A1-3-8 | 635 | 37.12 | 0.761 | 17.94 |
| A1-4-7 | 638 | 38.42 | 0.730 | 17.89 |
| A1-1-4 | 637 | 37.81 | 0.735 | 17.71 |
| A1-1-6 | 637 | 37.78 | 0.742 | 17.85 |

Table 9.4: Measured $V_{oc}$, $J_{sc}$ and FF for 100 Ω/sq emitter textured cells with 18-19% efficiencies.

| Cell ID | $V_{oc}$(mV) | $J_{sc}$(mA/cm$^2$) | FF | Eff (%) |
|---|---|---|---|---|
| T06-100-1-2-2 | 641 | 37.07 | 0.763 | 18.13 |
| T06-100-1-2-3 | 640 | 37.14 | 0.767 | 18.23 |
| T06-100-1-2-4 | 641 | 37.41 | 0.772 | 18.51 |
| T06-100-1-2-5 | 642 | 37.45 | 0.772 | 18.58 |
| T06-100-1-2-6 | 643 | 37.30 | 0.780 | 18.70 |
| T06-100-1-2-3 | 641 | 37.00 | 0.769 | 18.23 |
| T06-100-1-2-7 | 643 | 37.31 | 0.780 | 18.69 |
| T06-100-1-2-8 | 644 | 37.27 | 0.774 | 18.56 |
| T06-100-1-2-9 | 643 | 37.48 | 0.781 | 18.83 |
| T06-100-1-1-1 | 642 | 37.30 | 0.779 | 18.64 |
| T06-100-1-1-3 | 642 | 37.08 | 0.781 | 18.59 |
| T06-100-1-1-4 | 642 | 37.21 | 0.775 | 18.52 |
| T06-100-1-1-5 | 642 | 37.22 | 0.774 | 18.48 |
| T06-100-1-1-8 | 642 | 37.30 | 0.776 | 18.57 |
| p06-100-1-1-1 | 639 | 37.44 | 0.759 | 18.16 |
| p06-100-1-1-3 | 641 | 37.32 | 0.777 | 18.57 |
| p06-100-1-1-6 | 641 | 37.45 | 0.779 | 18.69 |
| Tx06-1-1 | 645 | 37.67 | 0.766 | 18.60 |
| Tx06-1-3 | 640 | 37.61 | 0.762 | 18.35 |
| Tx06-1-4 | 640 | 37.92 | 0.759 | 18.40 |
| Tx06-1-6 | 639 | 38.07 | 0.747 | 18.17 |
| Tx06-1-7 | 638 | 37.66 | 0.757 | 18.19 |
| Tx06-1-8 | 641 | 38.04 | 0.757 | 18.44 |
| A1-9-6 | 634 | 37.53 | 0.764 | 18.16 |
| A1-9-8 | 635 | 37.58 | 0.763 | 18.21 |
| A1-9-9 | 635 | 37.70 | 0.762 | 18.25 |
| A1-10-1 | 635 | 37.68 | 0.768 | 18.36 |
| A1-10-3 | 635 | 37.53 | 0.768 | 18.29 |
| A1-10-7 | 635 | 37.62 | 0.767 | 18.31 |
| A1-10-9 | 634 | 37.74 | 0.763 | 18.27 |
| A1-4-1 | 638 | 37.95 | 0.766 | 18.55 |
| A1-4-2 | 639 | 38.16 | 0.767 | 18.72 |
| A1-4-3 | 638 | 38.13 | 0.755 | 18.39 |
| A1-4-4 | 637 | 38.00 | 0.766 | 18.54 |
| A1-4-5 | 638 | 38.04 | 0.772 | 18.74 |
| A1-4-6 | 638 | 38.14 | 0.767 | 18.66 |
| A1-4-8 | 639 | 38.29 | 0.764 | 18.67 |
| A1-4-9 | 639 | 37.81 | 0.767 | 18.53 |
| A1-1-1 | 638 | 37.67 | 0.760 | 18.27 |
| A1-1-2 | 638 | 37.62 | 0.751 | 18.02 |
| A1-1-3 | 638 | 37.73 | 0.763 | 18.35 |
| A1-1-7 | 638 | 38.01 | 0.765 | 18.56 |
| A1-1-8 | 637 | 37.76 | 0.771 | 18.55 |
| A1-1-9 | 639 | 38.06 | 0.748 | 18.19 |
| A1-3-2 | 635 | 37.13 | 0.768 | 18.09 |
| A1-3-5 | 634 | 36.95 | 0.773 | 18.12 |
| A1-3-6 | 634 | 36.69 | 0.775 | 18.01 |
| A1-3-9 | 635 | 37.52 | 0.765 | 18.24 |
| A1-6-1 | 636 | 38.31 | 0.754 | 18.37 |
| A1-6-2 | 637 | 38.25 | 0.754 | 18.37 |
| A1-6-3 | 638 | 37.82 | 0.767 | 18.52 |
| A1-6-4 | 637 | 38.53 | 0.755 | 18.52 |
| A1-6-6 | 639 | 38.09 | 0.741 | 18.02 |
| A1-6-8 | 636 | 38.27 | 0.755 | 18.39 |
| A1-6-9 | 638 | 38.60 | 0.761 | 18.74 |
| A1-7-2 | 638 | 38.13 | 0.764 | 18.38 |
| A1-7-4 | 638 | 38.04 | 0.770 | 18.53 |
| A1-7-5 | 638 | 38.14 | 0.764 | 18.33 |
| A1-7-7 | 639 | 37.81 | 0.768 | 18.35 |
| A1-8-5 | 635 | 37.13 | 0.768 | 18.28 |
| A1-8-6 | 634 | 36.95 | 0.769 | 18.29 |
| A1-8-7 | 634 | 36.69 | 0.761 | 18.19 |
| A1-8-9 | 636 | 38.31 | 0.759 | 18.16 |
| A1-9-1 | 637 | 38.25 | 0.764 | 18.18 |
| A1-9-3 | 637 | 38.53 | 0.762 | 18.11 |

### 9.3.4 Modeling of the High-Efficiency Textured Cell and Investigation of the $V_{oc}$ Limiting Factors

The 19% screen-printed cell was thoroughly characterized and modeled to explain its high performance. The FSRV and BSRV were extracted by matching the measured IQE with the PC1D simulated IQE (Fig. 9.17) using the inputs shown in Table 9.5. The FSRV was found to be 60,000 cm/s from the matching of the short-wavelength response, and the IQE match in the long-wavelength response gave a back-surface recombination velocity (BSRV) of 600 cm/s (Fig. 9.17). Cells textured on both sides as well as only on the front side only with a planar back gave the same BSRV of ~600 cm/s, which indicates that the textured back does not appreciably degrade the back-surface field quality. The minority-carrier lifetime ($\tau_B$) in the 0.6 Ω-cm finished cell was measured after etching the emitter and the Al BSF of the cell. The junction leakage current ($J_{o2}$) of 2 nA/cm$^2$ and second-diode ideality factor ($n_2$) of 1.65 were extracted using the suns-$V_{oc}$ technique discussed in Chapter 2 [29]. The exact emitter profile was measured using spreading resistance on a planar 100 Ω/sq emitter and was used in the PC1D modeling of the textured cell. The back reflectance was extracted to be ~61.5% using an extended spectral analysis of the cell IQE, which involves matching the IQE and escape reflectance in the wavelength regime of 1050-1200 nm [133]. The grid shading was obtained by measuring the printed line width of ~80-μm gridlines on the 2 cm × 2 cm cell. Using these parameters, the PC1D cell modeling gave a cell efficiency of 19.0%, with $V_{oc}$=640.3 mV and $J_{sc}$=37.3 mA/cm$^2$, which agreed well with the measured data. PC1D modeling was extended on the textured 45 Ω/sq and 100 Ω/sq emitter cells using the measured inputs, and it is found that the simulated enhancement in $V_{oc}$, $J_{sc,}$ and cell efficiency, resulting from the high sheet-resistance emitter, was very close to the

measured enhancement, as shown in Figure 9.18. The extracted FSRV for the textured 45 Ω/sq emitter cell was ~150,000 cm/s as opposed to 60,000 cm/s for the textured 100 Ω/sq emitter.

Table 9.5: Modeling parameters for the 19% textured 100 Ω/sq cell.

| Cell Parameters | Textured FZ Cell |
|---|---|
| Base Resistivity (Ω-cm) | 0.6 |
| $R_s$ (Ω-cm$^2$) | 0.79 |
| $R_{sh}$ (Ω-cm$^2$) | 68,157 |
| $n_2$ | 1.65 |
| $J_{o2}$(nA/cm$^2$) | 2 |
| Emitter sheet resistance (Ω/sq) | 100 |
| Surface Conc. (cm$^{-3}$) | 1.5x10$^{20}$ |
| Texture angle (degrees) | 54.7 |
| Texture depth (μm) | 3 |
| $\tau_{bulk}$(μs) | 250 |
| BSRV (cm/s) | 600 |
| $R_{back}$(%) | 61.5 |
| FSRV (cm/s) | 60,000 |
| grid shading (%) | ~4% (for 75-85 μm gridlines) |
| modeled $V_{oc}$ (mV) | 640.3 |
| modeled $J_{sc}$(mA/cm$^2$) | 37.3 |
| modeled FF | 0.796 |
| modeled η (%) | 19.0 |

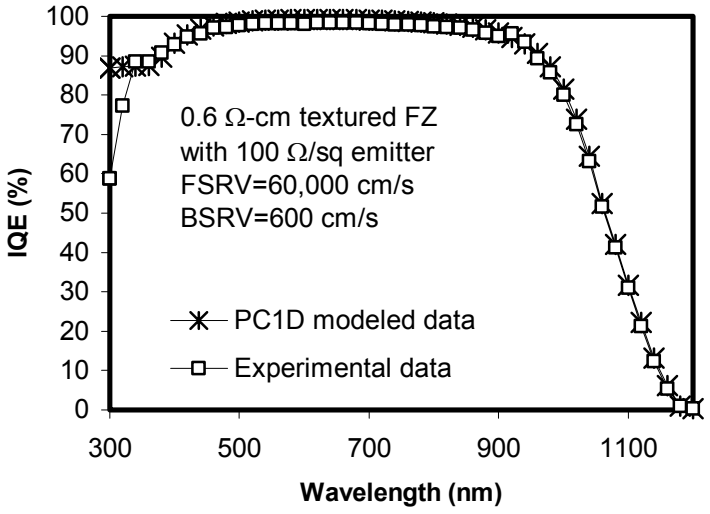


Figure 9.17. Experimental and PC1D-modeled IQE plots.

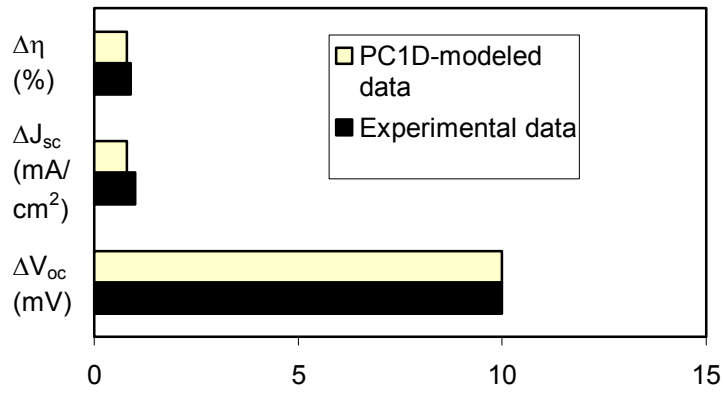


Figure 9.18 Experimental and PC1D-modeled data of the enhancement in efficiency, $J_{sc}$, and $V_{oc}$ resulting from the 100 Ω/sq emitter textured cell.

#### 9.3.4.1 Extraction of the Emitter and Base Saturation Current Densities in the 19% Efficient Cells

The emitter and base saturation current densities $J_{oe}$ and $J_{ob}$ can be found by biasing the cell in the dark in the PC1D device modeling program. $J_{ob}$ can also be found from the following equation:

$$J_{ob} = \frac{qn_i^2}{N_A}\frac{D}{L_{eff}}F \tag{9.1}$$

where $q$ is the elementary charge, $n_i$ is the intrinsic carrier density, $N_A$ is the acceptor carrier density, $D$ is the diffusivity of minority carriers, $L_{eff}$ is the effective (including the surface effect) minority-carrier diffusion length, and $F$ is described in Section 4.1.

To find the emitter saturation current density using dark bias in PC1D, the electric field across the depletion region is simulated and plotted to obtain the depletion region edges and doping concentration there. $J_{oe}$ is found from the following equation:

$$J_{oe} = \left.\frac{J_p}{\left(np/n_i^2\right)}\right|_{x_{jn}} = \left.\frac{J_p}{e^{qV/kT}}\right|_{x_{jn}} \tag{9.2}$$

where $J_p$ is the minority-carrier current in the emitter region. All parameters were determined at $x_{jn}$ which represents the junction edge or the width of the depletion region on the n-side (emitter side) of the p-n junction at the applied bias. $T$ is room temperature and $k$ is the Boltzmann constant. V is the applied bias voltage, which was set to 0.4 V, so that it is in a region where the shunt resistance and series resistance do not come into play. $J_p(x_{jn})$ is obtained from the PC1D simulation output. $J_{oe}$ is found to be ~230 fA/cm$^2$ for the 100 Ω/sq textured high-efficiency cell, for an FSRV of 60,000 cm/s and the PC1D inputs in Table 9.5. Similarly, $J_{ob}$ was found using the following equation:

$$J_{ob} = \left.\frac{J_n}{\left(np/n_i^2\right)}\right|_{x_{jp}} = \left.\frac{J_n}{e^{qV/kT}}\right|_{x_{jp}} \tag{9.3}$$

$J_{ob}$ was found to be ~170 fA/cm$^2$ for a textured cell using a p-type 0.6 Ω-cm base resistivity wafer with a BSRV of 600 cm/s and a bulk lifetime of ~250 μs. Since $J_{o1}=J_{oe}+J_{ob}$, the total $J_{o1}$ value of 400 fA/cm$^2$ is obtained from the above analysis. To validate this analysis, suns-$V_{oc}$ was used to directly measure $J_{o1}$ (refer to Chapter 2).

The measured $J_{o1}$ was found to be 433 fA/cm$^2$, which is in good agreement with the simulated results. This analysis shows that the $J_{oe}$ is higher than $J_{ob}$, which indicates that cell performance and $V_{oc}$ are still affected by $J_{oe}$ in spite of the high sheet-resistance emitter. In addition, $V_{oc}$ can also be improved further by lowering the $J_{ob}$.

### 9.3.4.2 The Effect of the Metal Grid Coverage on the Emitter Saturation Current Density and the Open-Circuit Voltage

The previous section revealed that even in the 19% efficient cell, $J_{oe}$ partly limits the $V_{oc}$ of the device. This could be the result of the grid coverage of the screen-printed contact, which could increase the effective FSRV and lower the $V_{oc}$. Therefore, in this section, an attempt is made to quantify the impact of the metal grid on $J_{oe}$ and $V_{oc}$. This was done with the help of the extracted and measured parameters in the previous section, $J_{oe}$ measurement by the PCD technique (refer to Chapter 2) without the grid, and the measured metal area fraction.

The total emitter saturation current density of the finished cell can be expressed as

$$J_{oe} = F_m J_{oem} + (1 - F_m) J_{oeSiN} \tag{9.4}$$

where $F_m$ is the metal grid coverage and $J_{oem}$ is the emitter saturation current density underneath the metal grid. $J_{oeSiN}$ is the emitter saturation current density between the gridlines and underneath the silicon nitride film. This was measured using the PCD lifetime tester (refer to Chapter 2). And was found to be 115 fA/cm$^2$. $F_m$ was estimated at ~4% for the 10-line grid formed by PV168 paste, which gave 75- to 85-μm wide gridlines on a 2 cm × 2 cm cell.

$J_{oem}$ was calculated from equation (9.4) using the estimated value of $J_{oe}$ ($J_{o1(measured)}$-$J_{ob(extracted)}$), metal area coverage, $F_m$, of 4%, and $J_{oeSiN}$ of 115 fA/cm$^2$ for the 100 Ω/sq textured emitter. $J_{oem}$ was found to be 3915 fA/cm$^2$ for the textured 19% high-efficiency cells. This result is in good agreement with the $J_{oem}$ of 4000 fA/cm$^2$ obtained by Lenkeit et al. for a 100 Ω/sq planar emitter [113]. After determining the $J_{oem}$, it is now possible to plot the total emitter recombination current density, $J_{oe}$, as a function of the metal grid area fraction, $F_m$, for the textured cells, as shown in Figure 9.19. Figure 9.19

also shows the effect of the metal grid coverage on $V_{oc}$, calculated using the single- diode model equation without the effect of $J_{o2}$, ($V_{oc}=kT/q \cdot ln(J_{sc}/J_{o1} + 1)$). Recall that $J_{o1}=J_{oe}+J_{ob}$ and $J_{ob}$=170 fA/cm$^2$ and $J_{sc}$=37.3 mA/cm$^2$ for this cell. For the grid area coverage of ~4%, the calculations give a $V_{oc}$ of 651 mV, which is in good agreement with the experimental value of $V_{oc}\cong$644 mV. The difference should be accounted for by incorporating the $J_{o2}$ term. Notice that the maximum $V_{oc}$ without any metal front grid, calculated from $J_{oSiN}$, is ~663 mV for the textured 100 Ω/sq emitter cells. This shows that the front metal grid is responsible for ~20 mV loss in $V_{oc}$ (663-644=19 mV). Thus, incorporating finer gridlines using techniques like hot-melt printing can improve cell efficiency further.

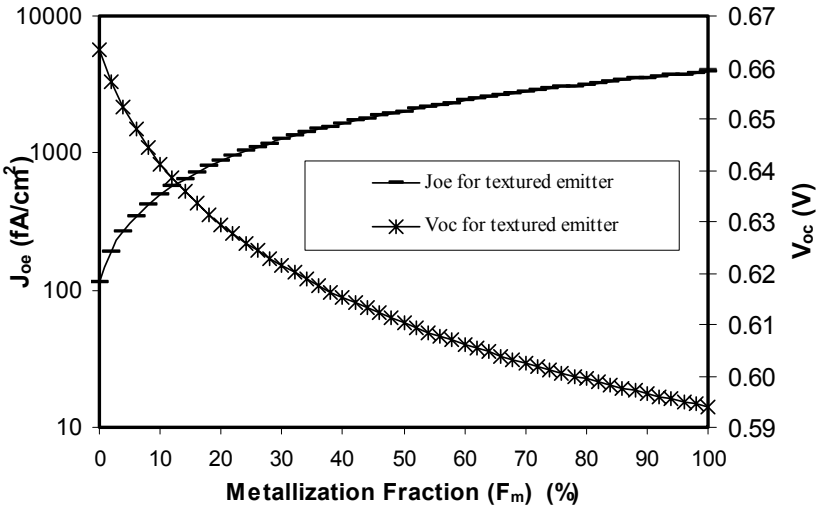


Figure 9.19. The effect of the metal grid percent coverage on the emitter saturation current density for textured 100 Ω/sq emitter cells.

## 9.4 Conclusions

Surface texturing produced greater enhancement in cells with high emitter sheet-resistance. This is mainly attributed to the smaller increase in FSRV due to texturing of the lightly doped emitters. Optimized co-firing was developed for textured cells which provided a high FF of 0.784 on a 100 Ω/sq emitter along with a record efficiency of 19.0%. This was primarily due to the high-quality contacts, resulting in a low series resistance and junction leakage. High $V_{oc}$ of 640-644 mV indicates high-quality contacts with low junction recombination as well as acceptable front-surface passivation. The textured surface also shows more robustness in achieving consistently low series resistance compared with the planar emitter surface as a result of the ease of the Ag crystallite precipitation and contact formation at the edges and tips of the pyramids. Our modeling results show that improving the FSRV from 60,000 cm/s to 30,000 cm/s could increase cell efficiency to ~19.3%. The use of a 95% back reflector as well as a lower BSRV (~150 cm/s) can further improve the efficiency to >20%.

# CHAPTER 10

# GUIDELINES FOR FUTURE WORK

In this chapter, guidelines are provided to achieve greater than 19% efficient FZ Si cells while maintaining cost effectiveness by using low-cost processes. To do this, model calculations were performed using the record high-efficiency 19% cell as a starting point. The results of these calculations are illustrated in Figure 10.1, where key variables were changed to provide guidelines for taking this efficiency beyond 20%. The results indicate that this can be achieved mainly by reducing the back-surface recombination velocity, improving the back-surface reflectance, and reducing the FSRV. Figure 10.1 shows that the reduction in BSRV from 600 to ~50 cm/s can enhance cell performance from 19-19.6%. However, this is not a trivial task using conventional passivating dielectrics, while maintaining a high throughput manufacturing process. The widely used aluminum back-surface field today gives much higher BSRV values. Also, Al firing could cause bowing, especially for thin cells. Therefore, other back passivation techniques need to be employed to achieve ≤50 cm/s BSRV.

Even though wet/dry thermal oxide is known to provide excellent passivation [134], the oxide passivation quality degrades when screen-printed contacts are fired in the atmosphere at high temperatures. Silicon nitride films are known to have a lot of positive charge, which induces an inversion layer and parasitic shunting at the back of the solar cell when deposited on bare Si. This degrades the passivation quality and the open-circuit voltage [135]. Hence, improving the back-surface field may require an amorphous Si (a-

Si) film on the back side of the cell similar to that has been developed for the HIT solar cells [136]. The amorphous Si has a wider bandgap, which acts as a barrier to carrier recombination at the surface. The amorphous Si can be deposited on the crystalline Si by CVD. It has been demonstrated that a recombination velocity of less than 50 cm/s can be achieved at the a-Si/crystalline-Si interface. However, implementation of this in conventional screen-printed cells could be challenging.

Figure 10.1 shows that once a low BSRV of ~50 cm/s has been achieved, a back reflector of 95%, as opposed to ~62% in the 19% cell, can raise the efficiency to 20.3%. This is possible by using a metal reflector on top of a dielectric layer (e.g., silicon nitride) on the back of the cell. However, the challenge will be to fire point contacts through the silicon nitride film and still achieve a good ohmic contact. This can be done by laser grooving through the nitride or by using a screen-printed paste that dissolves the $SiN_x$ film at selected points. Finally, reducing the FSRV from 60,000 cm/s to 20,000 cm/s can drive the efficiency up to 21% for a textured cell. This may require very fine gridlines and excellent surface passivation.

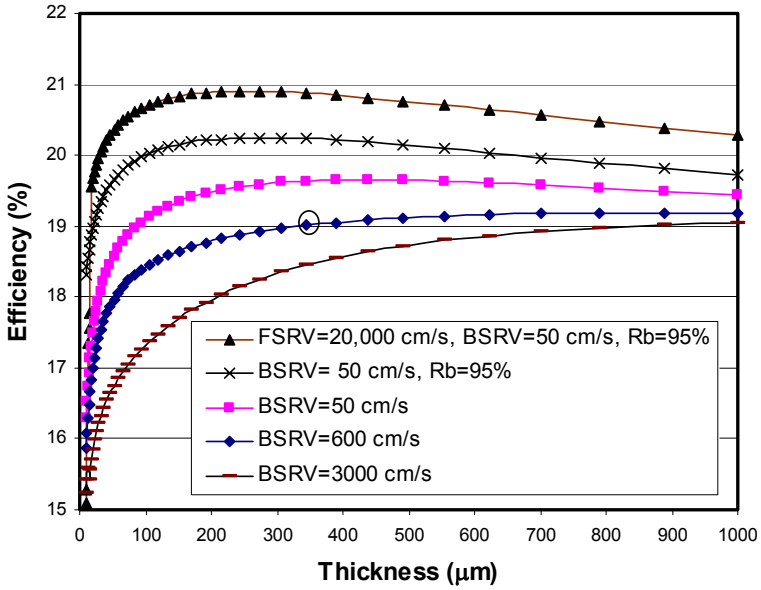


Figure 10.1. Efficiency versus cell thickness for different BSRV values for a textured cell. Results are also shown when the FSRV is reduced from 60,000 cm/s to 20,000 cm/s. The circle indicates the current status of 19% cell.

Some cells were fabricated in this research with photolithography (PL) front contacts (see Appendix E for the process sequence), while the rest of the cell structure was identical to the screen-printed (SP) cells. The front grid metallization was the last step in the fabrication process. These cells were compared to the fully screen-printed planar cells developed in Chapter 5. Table 10.1 shows a difference of ~0.4% between the co-fired screen-printed cell and the PL cell. This difference is attributed to the lower series resistance, ~0.4 Ω-cm$^2$ for the PL cell, as opposed to 0.85 Ω-cm$^2$ for the SP cell. In addition, the lower shading of ~3% resulting from the finer PL fingers gave a higher current density of 34.9mA/cm$^2$. Figure 10.2 shows that an optimized grid with finer lines and closer grid spacing (S) gives a lower loss in FF because of the decrease in sheet

resistance loss. This brings the resistive loss in 100 and 45 Ω/sq cells much closer; thus, enhancing the benefit of the 100 Ω/sq emitter.

Based on the above results, future work should involve printing finer gridlines. This could be done by using the hotmelt technique [137], where the viscosity of the paste is controlled by the screen temperature rather than by the shear rate of the squeegee movement and original rheology of the paste alone. This allows for the possibility of printing finer lines at fast squeegee speeds. The other advantage of the hotmelt paste is that it "freezes" (the viscosity rapidly increases) as it comes in contact with the cooler wafer and therefore there is less chance for the gridline to spread and more shading. The hotmelt paste does not require a drying step. Continuous gridlines of ~60 μm have been printed using a hotmelt paste. It is probably possible to print 50 μm lines to reduce the shadowing loss from ~4-4.5% to ~3.25%.

Table 10.1: Screen-printed (SP-PV168) versus photolithography (PL) front metallization cells with single-layer $SiN_x$ ARC.

| CELL | $V_{oc}$(mV) | $J_{sc}$(mA/cm$^2$) | FF | Eff(%) | n factor | $R_s$(Ω-cm$^2$) | $R_{sh}$(Ω-cm$^2$) |
|---|---|---|---|---|---|---|---|
| **PL** | 640 | 34.90 | 0.797 | 17.80 | 1.12 | 0.41 | 57577 |
| **SP-PV168** | 646 | 34.48 | 0.782 | 17.42 | 1.08 | 0.85 | 131404 |

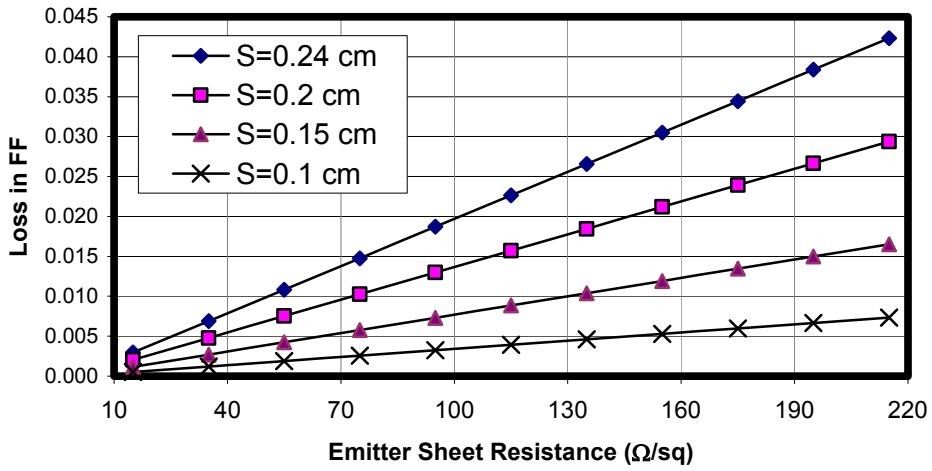


Figure 10.2. The loss in fill factor resulting from the emitter sheet resistance for different gridline spacing(S).

# APPENDIX A

# DERIVATION AND UNDERSTANDING OF LOSSES DUE TO THE FRONT METAL GRID AND EMITTER SHEET RESISTANCE

The power loss mechanisms resulting from resistive and shadow losses are given below. The equations below describe the losses resulting from the front metal grid and can be used for optimizing the grid design [34]. These losses are given for the gridline structure shown in Figure A.1.

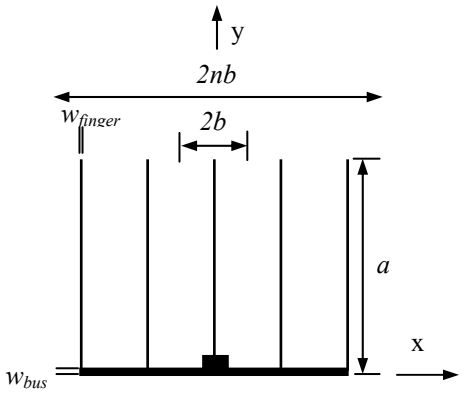


Figure A.1. Gridline structure of the cell used for deriving the power losses.

The power loss resulting from the lateral sheet resistance, resistance of the metal fingers and bus are obtained by integrating the current $I^2dR$, where $dR$ is the resistance of a strip $dx$ or $dy$ (depending on the geometry of each case) wide and $I$ is the current passing through the corresponding strip.

The power loss resulting from the emitter sheet resistance is

$$P_{lateral-sheet} = \frac{2}{3} J_L{}^2 nab^3 R_e \qquad \text{(A.1)}$$

where $J_L$ is the light-generated current density and $R_e$ is the semiconductor sheet-resistance. The power loss associated with the contact resistance is

$$P_{contact-front} = 2J_L^2 nab^2 \left(\rho_c \cdot R_e\right)^{1/2} \tag{A.2}$$

where $\rho_c$ is the contact resistivity or specific contact resistance.

The power loss associated with the current flow along the gridlines is

$$P_{finger} = \frac{4}{3}\left(J_L^2 na^3 b^2 \rho_{metal}\right) \Big/ \left(t \cdot w_{finger}\right) \tag{A.3}$$

The power loss associated with the busbar is given as

$$P_{bus} = \frac{2}{3}\left(J_L^2 a^2 n^3 b^3 \rho_{metal}\right) \Big/ \left(t \cdot w_{bus}\right) \tag{A.4}$$

where $\rho_{metal}$ is the resistivity of the grid metal, $t$ is the thickness of the finger lines and busbar, $w_{busbar}$ is the width of the busbar, and $w_{finger}$ is width of the finger. The current flow through the base or bulk of the cell results in the following power loss:

$$P_{bulk} = 2J_L^2 nab\rho_{bulk} l \tag{A.5}$$

where $\rho_{bulk}$ is the resistivity of the semiconductor base and $l$ is the thickness of the base region. Finally, the power loss resulting from shadowing of the emitter surface by the gridlines and the busbar is

$$P_{shadow} = P_L \eta n\left(aw_{finger} + 2bw_{busbar}\right) \tag{A.6}$$

where $P_L$ is the power density of the incident light and $\eta$ is the energy conversion efficiency of the cell.

It is normally more convenient to express the power loss terms as normalized to the unit cell area. This is done by dividing the power loss expressions in equations (A.1) to (A.6) by *2nab*, the area of the cell. The normalized power loss equations are given in Table A.1 below:

Table A.1: Expressions for power loss from various sources, normalized to unit area of the cell.

| **Source of loss** | **Expression** |
|---|---|
| Emitter sheet | $P_{Nlateral-sheet} = \frac{1}{3} J_L{}^2 b^2 R_e$ |
| Grid contact interface | $P_{Ncontact-front} = J_L{}^2 b(\rho_c \cdot R_e)^{1/2}$ |
| Grid finger | $P_{Nfinger} = \frac{2}{3}\left(J_L{}^2 a^2 b \rho_{metal}\right) / \left(t \cdot w_{finger}\right)$ |
| Grid busbar | $P_{Nbus} = \frac{1}{3}\left(J_L{}^2 a n^2 b^2 \rho_{metal}\right) / \left(t \cdot w_{bus}\right)$ |
| Device bulk | $P_{Nbulk} = J_L{}^2 \rho_{bulk} l$ |
| Shadowing | $P_{Nshadow} = P_L \eta \left( \frac{w_{finger}}{2b} + \frac{w_{busbar}}{a} \right)$ |

The cell series resistance normalized to unit area can be estimated as

$$R_s = P_{Ntotal} / J_L{}^2 \qquad \text{(A.7)}$$

where

$$P_{Ntotal} = P_{Nsheet} + P_{Ncontact} + P_{Nfinger} + P_{Nbus} + P_{Nbase} \qquad \text{(A.8)}$$

# APPENDIX B

# DESIGN OF THE METAL GRID OF THE SOLAR CELL

Generally, the width of the metal fingers is determined by technological constraints, typically ~100 μm for screen-printed metallization and 20-30 μm for photolithography contacts. Thus, the design of the metal grid is practically restricted to optimizing the separation between the gridlines that yields optimum compromise between resistive and shading losses. All the power loss mechanisms described in Appendix A are considered. Considering a rectangular solar cell as in Figure A.1, the fractional power losses normalized to unit area are obtained by dividing the power loss, equation (A.8), by the maximum power output $J_{mp}V_{mp}$ ($V_{mp}$ is the voltage at the maximum power point) and substituting the light-generated current by the maximum operation current $J_{mp}$. $J_{mp}$ used in the grid optimization includes all resistive losses but not the grid shading [27]. The method for finding the optimum gridline spacing is based on suggestions by Green [27] and Cuevas [104]. Considering half of the cell in Fig. A.1 with a gridline separation $S=2b$ we then have the following fractional power losses:

- Losses resulting from the lateral current flow in the diffused layer between the gridlines:

$$p_e = \frac{R_e J_{mp}}{12 V_{mp}} S^2 \tag{B.1}$$

- Losses resulting from the series resistance of the gridlines:

$$p_m = \frac{1}{3} a^2 R_m \frac{J_{mp}}{V_{mp}} \frac{S}{W_f} \tag{B.2}$$

where $a$ is the length of the gridline and $R_m$ is the sheet resistance of the metal gridlines and is equal to $\rho_{metal}/t$.

❖ Losses resulting from the contact resistance between the gridlines and the semiconductor:

$$p_c = \rho_c \frac{J_{mp}}{V_{mp}} \frac{S}{W_f} \tag{B.3}$$

❖ Losses resulting from the shadowing by the gridlines:

$$p_s = \frac{W_f}{S} \tag{B.4}$$

The optimization procedure is to sum up all the losses and to obtain the minimum by taking the partial derivative of the total loss with respect to the gridline separation and equating this to zero. This does not yield a direct closed-form analytical formula, and hence an iterative method is needed. The approach used here is to assume that the contact resistance losses, $p_c$, and finger resistive losses, $p_m$, are both equal to zero. This gives an initial estimate for the separation between the gridlines:

$$S_1 = \left( 6 \frac{W_f}{R_e \frac{J_{mp}}{V_{mp}}} \right)^{1/3} \tag{B.5}$$

This approximation is very close to the final converged value except in cases where the metal or contact resistances are very high. Improved accuracy can be obtained by differentiating the expression for the power loss ($p_e$+$p_c$+$p_m$+$p_s$) with respect to $S$. The derivative must equal zero for the optimum value of $S$. This optimum $S$ is found using the Newton-Raphson method and iterating a few times for finding the roots of the non-linear equation [104].

$$S_{n+1} = S_n \frac{2(p_e + p_s)}{(p_m + 4p_e + p_c + p_s)} \tag{B.6}$$

# APPENDIX C

# DERIVATION OF THE CHANGE IN FILL FACTOR WITH SPECIFIC CONTACT RESISTANCE AND SERIES RESISTANCE

## C.1 The Effect of Specific Contact Resistance on Power Loss and Fill Factor

Since the metal grid covers only a fraction of the cell area (~5%), the grid area fraction-related specific-contact resistance ($\rho_{cm}$) is given by

$$\rho_{cm} = \frac{\rho_c}{A_f} \tag{C.1}$$

where $\rho_c$ is the specific contact resistance (see equation (6.1) in Chapter 6) for a given grid area fraction:

$$A_f = \frac{A_m}{A_T} = \frac{W_f}{S} \tag{C.2}$$

$A_T$ is the area of the unit cell and $A_m$ is the area of metal coverage. S is the spacing between the metal gridlines, and $W_f$ is the gridline or finger width. The fractional power loss resulting from the contact resistance loss of metal fingers only (ignoring the busbar) is given by

$$p_{cf} = \frac{\text{power loss due to contact resistance}}{\text{maximum power output of the unit cell}} = \frac{J_{mp}{}^2 \rho_{cm}}{J_{mp} V_{mp}} \tag{C.3}$$

$$p_{cf} = \frac{J_{mp}^2 \rho_c A_f}{J_{mp} V_{mp}} = \rho_c \frac{J_{mp}}{V_{mp}} \frac{S}{W_f} \tag{C.4}$$

which is equation (B.3) in Appendix B.

Now, the fill factor is directly proportional to the maximum power output:

$$FF = \frac{J_{mp} V_{mp}}{V_{oc} J_{sc}} \tag{C.5}$$

Hence, a resistive loss in the maximum power output would result in a directly proportional loss in fill factor. When studying the effect of contact resistance on fill factor, only the change in power loss resulting from the contact resistance effect on the maximum power output was considered. Thus, the following equation was used for the loss in FF due to the increase in specific contact resistance

$$\Delta FF = \Delta p_{cf} \cdot FF \,. \tag{C.6}$$

## C.2 The Change in Fill Factor with Series Resistance

An expression for the fill factor in the presence of series resistance is given by

$$FF = FF_0 (1 - r_s) \tag{C.7}$$

$$r_S = \frac{R_S}{R_{CH}} \tag{C.8}$$

$$R_{CH} = \frac{V_{oc}}{I_{sc}} \tag{C.9}$$

$R_{CH}$ is the characteristic resistance of a solar cell; $FF_0$ represents the ideal fill factor in the absence of parasitic resistance and is given by the following empirical equation [27]:

$$FF_0 = \frac{\upsilon_{oc} - \ln(\upsilon_{oc} + 0.72)}{\upsilon_{oc} + 1}, \tag{C.10}$$

where $v_{oc}$ is the normalized voltage described as $V_{oc}/(nkT/q)$ for a single-diode solar cell model, $n$ is the diode ideality factor. Equations (C.7) to (C.9) result in the following relation for typical solar cell values of $V_{oc}$ and $I_{sc}$ assuming the shunt resistance is very high [115]:

$$\Delta FF \approx 0.042\ \Delta R_s \tag{C.11}$$

Thus, for a 1 Ω-cm increase in series resistance, the FF increases by ~0.042 for a typical solar cell.

# APPENDIX D

# DETAILED PROCESS SEQUENCE FOR SCREEN-PRINTED MONOCRYSTALLINE AND MULTICRYSTALLINE SI SOLAR CELLS WITH HIGH SHEET-RESISTANCE EMITTERS

**1. Initial Cleaning**

- DI rinse, 5 min.
- HF Dip (10:1 HF) 1 min.
- DI rinse, 2 min.
- DI $H_2O$: $H_2O_2$ :$H_2SO_4$ = 2 : 1 : 1, 5 min.
- DI rinse, 3 min.
- HF Dip (10:1 HF) 1 min (for FZ and dendritic-web wafers).
- For cast mc-Si use an etching solution: $HNO_3$ : Acetic acid : HF in the following ratio is approximately 15:5:2 for 8-10 min (2-3 min for Cz and EFG materials). Alternatively an alkaline etch may be used.
- DI rinse, 2 min.
- DI $H_2O$: HCl : $H_2O_2$ : ratio 2 : 1 : 1, 10 min.
- Final DI rinse, 3 min.
- HF Dip (10:1 HF) for 30 sec.
- $N_2$ dry and visual inspection.

**2. $POCl_3$ Furnace Diffusion for $N^+$ Emitter**

Set temperature: 847$^o$ C for planar emitters to achieve sheet resistance of 95-105 Ω/sq and 877° C to achieve emitters with sheet resistance of 40-45 Ω/sq (20 min drive-in time in both cases). The $POCl_3$ tube furnace (Tystar) recipe is shown in Table D.1. It is important to note that for a textured surface, the diffusion temperature should be lower (843° C) to obtain the same emitter-sheet resistance of 95-100 Ω/sq.

***The conventional furnace oxidation (CFO) procedure is shown in Table D.2 (if needed before the $SiN_x$ deposition for better passivation (stack passivation)).***

**3. Glass Removal and Post-Diffusion Cleaning**

DI rinse, 2-3 min.

- 10:1 HF dip, 2 min.
- DI rinse
- Check *Hydrophobic (no water on the wafer surface).*
- $N_2$ Dry.
- Measure emitter-sheet resistance.
- DI rinse, 2 min.
- DI $H_2O$: HCl : $H_2O_2$ : ratio 2 : 1 : 1, 10 min.
- Final DI rinse, 3 min.
- HF Dip (10:1 HF) for 30 sec.
- $N_2$ dry and visual inspection.

**4. PECVD $SiN_x$ Deposition**

a) High-frequency (HF) $SiN_x$ (13.56 MHz)

Target: ~830 Å, 1.98 (finally 750 Å, 2.04 after 850° C firing). The deposition rate is normally ~2.1 Å/sec. Textured surfaces take about 4/3 times longer to deposit.

- First, chamber cleaning for 60 min.

Gas flow rate: $N_2$ ( 900 sccm), $NH_3$ (11) sccm, and $SiH_4$ ( 320 sccm).

Pressure : 900 mTorr, Plasma power : 30 W (RF power). DC power should be zero. If not, run PECVD a couple of times for a dummy deposition of $SiN_x$ for a few minutes until the DC power reaches zero.

OR

b) Low-frequency (LF) $SiN_x$ (50 KHz)

Target: ~750-780 Å, 2.02 (no densification after firing). The deposition rate for the Coyote LF PECVD $SiN_x$ is ~3 Å/s for planar wafers and ~2.2 Å/s for textured wafers.

First, ammonia pretreatment while plasma is on.

Gas flow rate: No $N_2$ flow, $NH_3$ (3000) sccm, and $Si_3H_4$ (300 sccm).

Pressure : 2 Torr, Plasma power : 150 W (RF power).

**5. Screen Printing of Al**

Before starting the printing Al on the back, make sure the dry belt is on and check the gas flow and temperature (~200° C).

Paste: Al Paste FX53-038 from Ferro Corp.

Stir paste gently for 3-5 min.

Check the house vacuum, working with an appropriate level of strength in the printer.

- IPA cleaning of screen, printer, tweezers, squeegee, spatula, and workbench.
- Printer setting: Snap-off distance (40 mils) + wafer thickness (~12 mils) + Texwipe (5 mils) (generally ~55 mils).
- Squeegee pressure ~ 25 psi.
- Dummy printing on dummy FZ wafers.
- Main run printing (*should be done on the back side*).
- Dry in the dry belt at ~200 $^{o}$C for 2 min.

**6. Screen Printing of Ag**

- Turn on the dry belt and check the gas flow and temperature (~200$^{o}$ C).
- Stir paste for 3-5 min.
- Check the house vacuum, working with an appropriate level of strength in the printer.
- IPA cleaning of screen, printer, squeegee, tweezers, spatula, and workbench.
- Screen height ≈65 mils: Snap-off distance (30 mils) + wafer thickness (~12 mils) + Texwipe (5 mils) + alloyed Al (~20 mils).
- Squeegee pressure should be ~25 psi, squeegee height should be lowered until continuous gridlines without disconnections are achieved. Lowering the squeegee too much will result in wafer breakage as well as line spreading on the wafer underneath the emulsion.
- Print first on dummy FZ.
- Main run printing should be done on top of the $SiN_x$.
- Dry in the dry belt at ~200 $^{o}$C for 2 min.

**7. Belt Furnace Co-Firing**

***a) Contacting High Sheet-Resistance Emitters (>80 Ω/sq) using PV168 Ag Paste from DuPont for Mono-crystalline (mainly planar and Textured FZ and Cz):***

- First burn-out step (essential for PV168 paste) with conditions shown in Table D.3.
- The actual co-firing process uses recipe *mhsdp80* shown in Table D.4. (This recipe is not suitable for mc-Si wafers). It is important to note that the $SiN_x$ thickness should be less than or equal to 750 Á.

***b) Contacting High Sheet-Resistance Emitters (>80 Ω/sq) using Ferro Pastes (33-455, 33- 462) for Mono- and Multi-crystalline wafers:***

- Burn-out step is found unnecessary for paste 33-455, 33-462, and 33-49.
- Recipe *mhcofire* (~746° C/1 sec actual peak temperature) shown in Table D.5. However, this recipe is <u>not</u> suitable for pastes 33-460 and 33-452. This recipe also works for large area cells without forming gas anneal.

OR

- Recipe *mhsdp120* (~840°C/1 sec actual peak temperature) shown in Table D.6. This recipe is suitable for all the pastes listed above.

The left power is 23% and the right power is 17% for all firing conditions in the belt furnace.

**8. Cell Isolation**

Check dicing system: wheel, vacuum, air, and water flow.

Wheel height setting: ~11 mils for isolation and ~2 mils for cutting.

Make sure no Al beads on the back side.

After dicing, remove Si dust from the cells using DI water and soft Alpha-wipe.

**9. Forming Gas Anneal**

Check the forming gas flow meter and make sure enough gas is flowing.

Turn on forming gas and let it flow for 5-10 min before loading samples.

- Forming gas anneal at $400^{o}$ C for 10 min for less than 10 wafers; 15 min for more than 10 wafers.

**10. Cell Test for Lighted and Dark I-V Characteristics**

Check the I-V tester, cooling system, etc.

Turn on light and adjust current level to obtain one-sun intensity; then, leave the light for 10-15 min for the lamp to stabilize.

- Standard cell test.
- Main cell test.

**11. Data Analysis and Documentation**

Table D.1: Recipe 6. Phosphorous Diffusion ($POCl_3$ Liquid Source, tube#3). Parameters not included in the table (e.g., Hi $O_2$) are off as a default. Dep=deposition.
Target Sheet ρ = 95-100 Ω/sq.

| Step | Time Hr:min:sec | Temp C | Function | $N_2$ L/m | $O_2$ lo Sccm | $N_2$ carr Sccm | Source On/Off | Boat in In/min | Boat out In/min |
|---|---|---|---|---|---|---|---|---|---|
| 0 | 00:00:02 | 800 | Default | 3.0 | 150 | | | 15.0 | |
| 1 | 00:05:00 | 800 | Boat in | 5.0 | | | | 15.0 | |
| 2 | 00:30:00 | 845* | Ramp to 845 | 3.0 | | | | 15.0 | |
| 3 | 00:05:00 | 845* | Pre Dep | 1.8 | 500 | 200 | Off | 15.0 | |
| 4 | 00:20:00 | 847* | Dep | 1.8 | 500 | 200 | On | 15.0 | |
| 5 | 00:05:00 | 847* | Purge | 1.8 | 500 | 200 | Off | 15.0 | |
| 6 | 00:12:00 | 847* | Drive | 3.0 | | | | 15.0 | |
| 7 | 00:15:00 | 800* | Ramp down | 3.0 | | | | 15.0 | |
| 8 | 00:10:00 | 800 | Boat out | 5.0 | | | | | 10.0 |

* Controlled Ramp

Table D.2: Recipe 9. Oxidation (~100-120 Å) on 100 Ω/sq n-doped Si.

| Step | Time Hr:min:sec | Temp. ˚C | Function | $N_2$ L/m | $N_2$ carr (sccm) | $O_2$ Hi (sccm) | Boat in In/min | Boat out In/min |
|---|---|---|---|---|---|---|---|---|
| 0 | 00:05:00 | 800 | Default | 5.0 | | | 15.0 | |
| 1 | 00:05:00 | 800 | Boat in | 1.0 | | | 15.0 | |
| 2 | 00:30:00 | 925* | Ramp to 925 | 1.0 | Off | Off | 15.0 | |
| 3 | 00:06:00 | 925* | Oxidation | Off | 200 | 3000 | 15.0 | |
| 4 | 00:05:00 | 925* | Anneal | 3.0 | Off | Off | 15.0 | |
| 5 | 00:30:00 | 800* | Purge | 3.0 | | Off | 15.0 | |
| 8 | 00:10:00 | 800 | Boat out | 5.0 | | | | 10.0 |

* Controlled Ramp

Table D.3: Burnout process conditions.

| **Furnace Segments** | **Entrance Eductor** | **Entrance Baffle** | **Zone 1** | **Zone 2** | **Zone 3** | **Exit Baffle** | **Exit Eductor** | **Plenum** | **Cooling Tunnel** |
|---|---|---|---|---|---|---|---|---|---|
| Gas Flow Rates (sccm) | *55* | *75* | *60* | *60* | *60* | *40* | *90* | *50* | *10* |
| Set Temperature (°C) | | | 500 | 435 | 425 | Belt speed = 25 IPM | | | |

Table D.4: Process conditions for belt furnace recipe *mhsdp80.*

| **Furnace Segments** | **Entrance Eductor** | **Entrance Baffle** | **Zone 1** | **Zone 2** | **Zone 3** | **Exit Baffle** | **Exit Eductor** | **Plenum** | **Cooling Tunnel** |
|---|---|---|---|---|---|---|---|---|---|
| Gas Flow Rates (sccm) | *10* | *25* | *50* | *50* | *50* | *40* | *90* | *50* | *200* |
| Set Temperature (°C) | | | 965 | 920 | 650 | Belt speed = 80 IPM | | | |

Table D.5: Process conditions for belt furnace recipe *mhsdp120.*

| Furnace Segments | Entrance Eductor | Entrance Baffle | Zone 1 | Zone 2 | Zone 3 | Exit Baffle | Exit Eductor | Plenum | Cooling Tunnel |
|---|---|---|---|---|---|---|---|---|---|
| Gas Flow Rates (sccm) | *10* | *25* | *50* | *50* | *50* | *40* | *90* | *50* | *200* |
| Set Temperature (°C) | | | 980 | 965 | 650 | Belt speed = 120 IPM | | | |

Table D.6: Process conditions for belt furnace recipe *mhcofire.*

| Furnace Segments | Entrance Eductor | Entrance Baffle | Zone 1 | Zone 2 | Zone 3 | Exit Baffle | Exit Eductor | Plenum | Cooling Tunnel |
|---|---|---|---|---|---|---|---|---|---|
| Gas Flow Rates (sccm) | *10* | *25* | *50* | *50* | *50* | *40* | *90* | *50* | *200* |
| Set Temperature (°C) | | | 955 | 935 | 575 | Belt speed = 120 IPM | | | |

Table D.7: Process conditions for belt furnace recipe *mhtex* for textured high sheet-resistance emitters.

| Furnace Segments | Entrance Eductor | Entrance Baffle | Zone 1 | Zone 2 | Zone 3 | Exit Baffle | Exit Eductor | Plenum | Cooling Tunnel |
|---|---|---|---|---|---|---|---|---|---|
| Gas Flow Rates (sccm) | *10* | *25* | *50* | *50* | *50* | *40* | *25* | *50* | *200* |
| Set Temperature (°C) | | | 965 | 920 | 900 | Belt speed = 80 IPM | | | |

# APPENDIX E

# HYBRID SCREEN-PRINTED AL BACK AND FRONT PHOTOLITHOGRAPHY GRID METALLIZATION

**1. Spin-on Doping and Baking**

- Source: $P_5 0_7$-6%.
- Spin speed: 3000 rpm.
- Spin time: 30 s.
- Bake: 200$^o$ C, 10 min using the oven; 200$^o$ C, 2 min using either a hot plate or dry belt.

**2. Belt Diffusion for $N^+$ Emitter Using Spin-on Dopant Source)**

***For a sheet resistance of 45±5 Ω/sq.***

Set temperature: 925$^o$ C (for low humidity ambient) in all three heating zones. For high humidity (>40%) ~945$^o$ C was used.

Belt speed: 5 ipm (inches per min).

***For a sheet resistance of 100±5 Ω/sq***

Set temperature: 890$^o$ C in all three heating zones.

Belt speed: 10 ipm (for low humidity ambient). For a high humidity ambient 5 ipm was used.

### 3. Phosphorus Glass Etch and Post-Diffusion Clean

This has been already described in Appendix D.

### 4. PECVD Single-Layer Antireflection Coating (SLAR) $SiN_x$ Deposition

This step is added here in the cell process sequence only if no double-layer antireflection coating will be used.

### 5. Al Back-Surface Field and ~80 Å Oxide Formation

Table E.1: Recipe for RTP/RTO.

| | Type | Time/rate (s or C/s) | Temp( ˚C ) | $N_2$ | $O_2$ |
|---|---|---|---|---|---|
| 1 | Delay | 10 | | On | |
| 2 | Ramp | 20 | 400 | On | |
| 3 | SS | 5 | 400 | | On |
| 4 | SS | 30 | 400 | | On |
| 5 | Ramp | 100 | 850 | | On |
| 6 | SS | 120 | 850 | | On |
| 7 | SS | 5 | 850 | | On |
| 8 | Ramp | 1 | 800 | On | |
| 9 | Ramp | 10 | 500 | On | |

### 6. Photolithography Metallization Sequence

THIN LIFT-OFF & PLATING

**A- Resist application**

1. Bake 80º C, 30 min (water drive off step)
2. Spin speed to 3000 rpm and time for 30 sec.
3. Center wafer on chuck front side up and turn on the vacuum.
4. Flood surface of wafer with HMDS (Hexamethyldisilizane) primer. Let stand for 10 sec. Then start the spin cycle.

5. Using Shipley 1818 photo-resist pipette enough resist on the surface of the wafer to cover approximately two thirds of the wafer surface.
6. Spin at 3000 rpm for 30 sec.
7. Repeat Steps 5 & 6 again; this will give total of two layers.
8. Bake the wafer at 85-90° C for 20 min This bake time is important to the success of the process; do not try to shorten it.

## B- Exposure & Development

9. Expose (light intensity 12.5 $mW/cm^2$) for 25-30 sec.
10. Make up a developing solution consisting of three parts $H_2O$ to one part Shipley 351 developer.
11. Develop ~ 1 to 1 ½ min. until windows are clear. Make sure development is complete (by observing under microscope) before going to next step.
12. Rinse well in DI water 5 min with multiple dumps.
13. Make sure the buffered-oxide etch solution (BOE) bottle does not have any crystals in it; otherwise, use new bottle. Make sure the water sheaths off the wafer after BOE etch.

- For etching off the passivation oxide BOE, etch the wafer by dipping rinsed wafers in the BOE solution for 40-60 sec.

**In case no DLAR ($ZnS/Mg_2F$) will be used (only SLAR):**

- For etching off an annealed high-frequency PECVD $SiN_x$: ~20 min of BOE etching is needed (for a single-layer antireflection coating (SLAR)).
- For etching off an annealed low-frequency PECVD $SiN_x$: ~45 min of BOE

etching is needed.

14. Rinse in running DI water for 5 min with multiple dumps.

15. Blow dry with dry $N_2$ gun.

## C- Metallization

16. Apply metal using CVC evaporator. Evaporate 600 Å Ti, 400 Å Pd, and 1000 Å Ag. Allow 5 min for cooling before each rotation of hearth. This is important to avoid baking the resist to point where it will not dissolve in acetone during lift off.

## D- Lift-off

17. After removing wafers from evaporator, place in a beaker full of acetone. Place beaker in an ultrasonic bath for 40 min.

18. Remove wafers from acetone one at a time and blow dry excess metal. If all metal is not removed, allow another few minutes in ultrasonic bath and blow off remaining metal.

19. Some wafers may lift off sooner than others and should be removed from acetone and kept aside. Metal that is very difficult to remove can be lifted off using tape to pull the metal off the surface.

20. After lift off is completed, clean the wafers by placing in two consecutive baths of two acetone followed by one IPA and one methanol for about 30 sec each. Then rinse in running DI water for 5 min with multiple dumps.

21. Blow dry with the $N_2$ gun.

## E- Silver Electroplating for Thin Lift-off

22. **Never use acids near plating bath to prevent the release of cyanide**.
23. Turn on agitator for at least 15 min prior to use to mix the solution thoroughly.
24. Check PH--should be around 13.
25. Turn off the agitator before putting the sample in the solution.
26. Connect plating clip to sample and turn on power supply and submerge the sample in plating solution.
27. Set current to 150 mA and maintain it constant at this value.
28. Check the wafer every 2 min. Monitor total time on first two wafers until desired thickness is reached. Shining light for photo-plating may also be used to possibly enhance uniformity.
29. Turn off power supply and DI rinse wafer thoroughly for 5 min with multiple dumps.
30. Blow dry with $N_2$.
31. The thickness of plated silver should be 7 or 8 um for 2x2 cells.
32. Refer to Table E.2 below for the next steps.

Table E.2: PL front metallization process.

| Process | Procedure |
|---|---|
| Front Contact Lift-off | THIN Lift off & Plating |
| Isolation | Using a dicing saw |
| Test | Light and Dark I-V; |
| Anneal | Temp: 400° C<br>Time: 10 min.<br>Forming Gas Flow Rate: 5L/min Input furnace control settings: |
| Test | Light and Dark I-V |
| In case of double-layer antireflection coating (DLAR), coat | 1- $MgF_2$ ~35 Å, 2- ZnS ~500 Å, 3- ~450 Å of $MgF_2$, (thickness calculated based on oxide thickness of ~100 Å).<br>(no PECVD $SiN_x$ has been deposited in this case) |
| *Anneal* ***(Optional)*** | *Temp: 400° C*<br>*Time: 10 min.*<br>*Forming Gas Flow Rate: 5L/min.* |
| Test | Light I-V, Dark I-V/Suns-$V_{oc}$ and Spectral Response |

# APPENDIX F

# DETERMINATION OF THE BEST-FIT LINE

The least-squares method gives the best-fitting straight line, which is the line that minimizes the sum of squares of lengths of the vertical line segments, as shown in Figure F.1, drawn from the measured data points to the fitted line. The smaller the deviations of the measured values from the line, and hence the smaller the sum of the squares of the deviations, the closer the best-fit line will be to the measured data.

Mathematically, the least-squares method can be described as follows. Let $\hat{Y}_i=\hat{C}_0+\hat{A}_1X_{i,}$ where $\hat{C}_0$ and $\hat{A}_1$ are the intercept and the slope of the fitted line, respectively. The vertical distance between the experimental data point $(X_i\ ,\hat{Y}_i)$ and the corresponding point of the fitted line is given by the absolute value $\left|\ Y_i\text{-}\hat{Y}_i\ \right|$. Thus, the sum of the squares of all these distances is given as [138]

$$\Sigma_{i=1}^{n}\left(Y_i-\hat{Y}_i\right)^2=\Sigma_{i=1}^{n}\left(Y_i-\hat{C}_0-\hat{A}_1X_i\right)^2 \qquad \text{(F.1)}$$

The least-squares solution is defined to be the choice of $\hat{C}_0$ and $\hat{A}_1$ for which the sum of the squares is a minimum. The minimum sum of squares corresponding to the least-squares estimates $\hat{C}_0$ and $\hat{A}_1$ is the sum of squares about the regression line, or the sum of squares resulting from error (SSE), also known as the residual sum of squares.

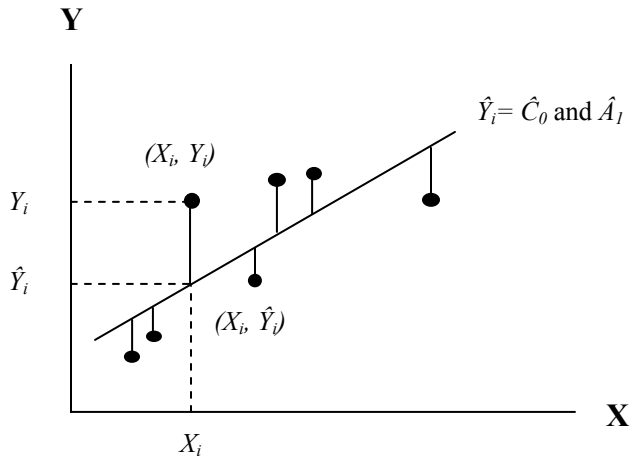


Figure F.1. Deviations of the observed points from the fitted regression line.

For fitting the suns-$V_{oc}$ (Section 2.2.3), data is scaled using a scaling factor of the ratio of the fitting suns points $suns_i/suns_k$, where $i<k$; without this scaling, even a difference factor of two in the fit at low suns has no effect on the fit, because the square of the difference is negligible compared to the data at high suns. So, if the least squares are not scaled, one will obtain a good fit only to the high suns data.

When using dark-IV analysis (Section 2.2.2), the residual incorporates the natural logarithm of the currents (the measured currents and the fitted current). This results in an already scaled best-line fit, as the fit is sensitive that way to both high and low currents and no scaling factor is needed.

# APPENDIX G

# DERIVATION OF THE SPECIFIC CONTACT RESISTANCE FOR A DEGENERATE SEMICONDUCTOR

The current density $J_{sm}$ from the semiconductor to the metal is given by the concentration of electrons with energies sufficient to overcome the potential barrier traversing in the $x$ direction [110]:

$$J_{sm} = \int_{E_F+q\phi_B}^{\infty} qv_x dn \tag{G.1}$$

where $E_F+q\phi_B$ is the minimum energy required for thermionic emission into the metal, and $v_x$ is the carrier velocity in the direction of transport. For a heavily doped semiconductor or for operation at low temperature, the tunneling current could become the dominant transport process. Thus, equation (G.1) will be modified to include the thermionic emission and tunneling components [139]. The expression for $J_{sm}$ (at a bias voltage V) is proportional to the quantum transmission coefficient $T(\eta)$ multiplied by the occupational probability in the semiconductor $F_s$ and the unoccupied probability in the metal; hence, $J_{sm}$ is given by

$$J_{sm}(V) = \frac{A^*T}{k}\int_0^{\infty} T(\xi)\exp\left[\frac{-q(V_b+V_n+\xi-\Delta\phi)}{kT}\right]d\xi + \frac{A^*T}{k}\int_0^{q(V_b-\Delta\phi)} F_s(V)T(\eta)(1-F_m)d\eta \tag{G.2}$$

A similar expression can be given to the current $J_{ms}$ traversing the metal to the semiconductor [110]:

$$J_{ms}(V) = -\frac{A^* T}{k}\exp\left[\frac{-q\phi_{Bn}}{kT}\right]\int_0^{\infty} T(\xi)\exp\left[-\frac{\xi}{kT}\right]d\xi - \frac{A^* T}{k}\int_0^{q(V_b-\Delta\phi)} F_m T(\eta)(1-F_s)d\eta \qquad \text{(G.3)}$$

The first term on the right hand side of equations (G.2) and (G.3) represents the contribution from the thermionic emission of carriers, while the second term is the tunneling component. $A^*$ is the effective Richardson constant, T is the temperature in °K, and $\phi_{Bn}$ is the metal-semiconductor barrier height. $F_s$ and $F_m$ are the Fermi-Dirac distribution functions for the semiconductor and for the metal, respectively. $\xi$ and $\eta$ are measured upward and downward from the potential maximum, as shown in Figure G.1. Figure G.1 shows the energy band diagram of a metal-semiconductor contact. For the bias voltage V=0, the metal-semiconductor contact will be in thermal equilibrium. $T(\xi)$ and $T(\eta)$ are the quantum transmission coefficients above and below the potential maximum. The total current density is the algebraic sum of equations (G.2) and (G.3) [139]:

$$J = J_{sm} + J_{ms} \qquad \text{(G.4)}$$

$$J = J_S\left[\exp\left(qV/nkT\right) - 1\right] \qquad \text{(G.5)}$$

$$J \approx J_S \exp\left(qV/nkT\right) \qquad \text{for V >> } kT/q \qquad \text{(G.6)}$$

where $J_S$ is the saturation current density obtained by extrapolating the current density from the log-linear region to V=0 and n is the ideality factor, defined as

$$n = \frac{q}{kT}\frac{\partial V}{\partial(\ln J)} \qquad \text{(G.7)}$$

This ideality factor is very close to unity at low doping concentrations and high temperatures. However, it can depart from unity if the doping is increased or the temperature is lowered. $J_s$ is constant for low doping concentrations but increases rapidly for $N_D > 10^{17}$ cm$^{-3}$ [110].

The specific-contact resistance is the reciprocal of the derivative of the current density with respect to the voltage. For a zero bias, the specific contact resistance is an important figure of merit for ohmic contacts [33, 110, 139]:

$$\rho_c = \left( \frac{\partial J}{\partial V} \right)^{-1}_{V=0} \tag{G.8}$$

The relative magnitude for the thermionic emission and tunneling components depends on the barrier height, temperature, and doping concentration. These factors are implicit in the quantum transmission functions or coefficients. For samples with higher doping concentrations, the tunneling component dominates the current flow (high doping and low temperature) and the first term on the right hand side of equations (G.2) and (G.3) can be neglected. Using the WKB approximation for the transmission coefficient, we have [139]

$$T(\eta) = \exp\left( - q(\phi_{Bn} - V) \Big/ E_{00} \right) \tag{G.9}$$

where

$$E_{00} \equiv \frac{q\hbar}{2} \sqrt{\frac{N_D}{\varepsilon_s m^*}} \tag{G.10}$$

Substituting equation (G.9) into equation (G.2) ($F_s \rightarrow 1$ for $E_F >> E$ and $F_m \rightarrow 0$ for $E >> E_F$):

$$J_{sm} \approx \frac{A^* T}{k} E_{00} \exp\left( -q(\phi_{Bn} - V) \Big/ E_{00} \right) \tag{G.11}$$

Now, substituting into equation (G.8) for V=0 (no bias, thermal equilibrium) gives

$$\rho_c = \frac{k}{qTA^*} \exp\left( q\phi_{Bn} \Big/ E_{00} \right) \tag{G.12}$$

The elementary charge q in the denominator of equation (G.12) is for the unit conversion to obtain units of Ω-cm$^2$ for the specific contact resistance; the barrier height, $\phi_{Bn,}$ has units of volts. $A^*$ is 200 Amp/cm$^2$°K$^2$ for <100> n-type Si [139].

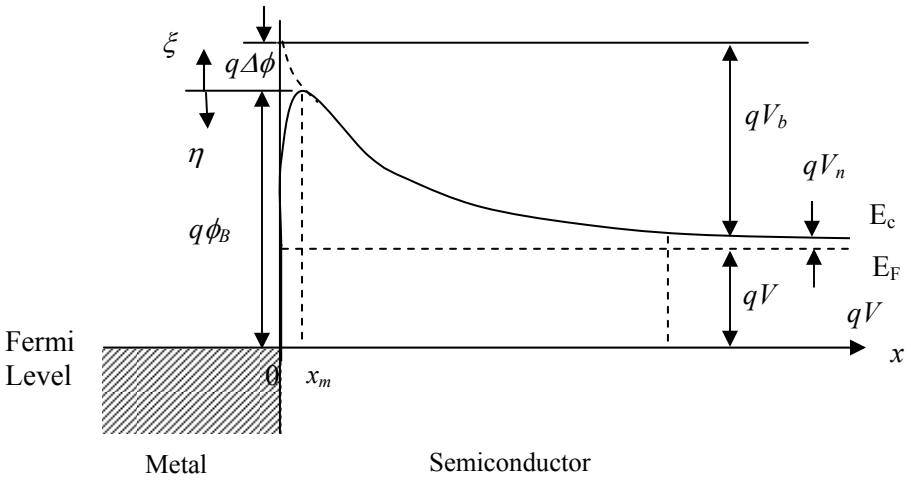


Figure G.1. Energy-band diagram of the metal semiconductor contact.

# APPENDIX H

# DERIVATION OF THE QUANTUM TUNNELING PROBABILITY

Starting from the time-independent one-dimensional Schrödinger equation,

$$\frac{-\hbar^2}{2m^*}\frac{\partial^2\psi(x)}{\partial x^2}+V(x)\psi(x)=E\psi(x) \tag{H.1}$$

$$\frac{\partial^2\psi(x)}{\partial x^2}=\frac{2m^*(V(x)-E)}{\hbar^2}\psi(x) \tag{H.2}$$

where $\psi(x)$ is the wave equation, $E$ is the incoming electron energy, $V(x)$ is the potential energy of the electron, $m^*$ is the mass of an electron, and $\hbar$ is the reduced Planck constant. Assuming $V(x)-E$ is independent of position between $x$ and $x+dx$ and solving the differential equation,

$$\psi(x+dx)=\psi(x)\exp(-kdx) \tag{H.3}$$

where the wave vector

$$k=\frac{\sqrt{2m^*[V(x)-E]}}{\hbar} \tag{H.4}$$

The amplitude of the wave function at $x=L$ can be related to that at $x=0$ by the following Equation:

$$\psi(L)=\psi(0)\exp\left[-\int_0^L k(x)dx\right] \tag{H.5}$$

This equation is known as the Wentzel-Kramers-Brillouin (WKB) approximation [110]. From this, the tunneling probability can be obtained:

$$\Theta = \frac{\psi(L)\psi^*(L)}{\psi(0)\psi^*(0)} \approx \exp\left[-2\int_0^L |k(x)|dx\right] \tag{H.6}$$

Assuming a parabolic potential energy barrier *PE(x)* or *V(x)* (Figure H.1), the metal oxide glass barrier could be represented by the following algebraic form [110]:

$$V(x) - E = \frac{\left(\left(L/2\right)^2 - x^2\right)}{L^2} \cdot \left(q\phi_B\right) \tag{H.7}$$

where $q\phi_B$ is the barrier potential energy with a barrier width L. The energy of the electron is measured from the center of the band.

$$\Theta = \exp\left[-2\int_{-L/2}^{L/2} \frac{\sqrt{2m^*\left(V(x)-E\right)}}{\hbar}dx\right] \tag{H.8}$$

$$= \exp\left[-\frac{\sqrt{2m^* q\phi_B}}{\hbar L}\left(\frac{1}{2}x\sqrt{\left(L/2\right)^2 - x^2} + \frac{1}{2}\left(\frac{L}{2}\right)^2 \sin^{-1}\left(\frac{x}{L/2}\right)\right)\right]_{-L/2}^{L/2}$$

$$= \exp\left[-\frac{\sqrt{2m^* q\phi_B}}{\hbar L}\left(\frac{\pi L^2}{4}\right)\right]$$

$$\Theta = \exp\left(\frac{-\pi\sqrt{m^* q\phi_B}}{2\sqrt{2}\hbar}L\right) \tag{H.9}$$

The electric field $\xi = \phi_B/L$; hence

$$\Theta = \exp\left(-\frac{\pi\sqrt{qm^*}\left(\phi_B\right)^{3/2}}{2\sqrt{2}\hbar\xi}\right) \tag{H.10}$$

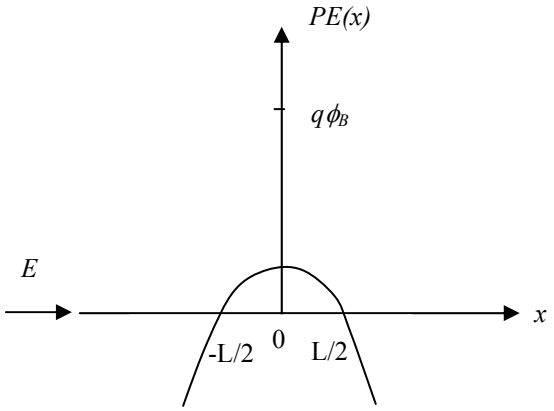

Figure H.1. Parabolic potential barrier.

# REFERENCES


[1] Key World Energy Statistics, 2003*, International Energy Agency (IEA),* 2003 Edition.

[2] A. Rohatgi, "Road to Cost-Effective Crystalline Silicon Photovoltaics" *Proceedings of the 3rd World Conference on Photovoltaic Energy Conversion*, Osaka, Japan 2003.

[3] J. Johnson, "Power from the Sun," *Chemical and Engineering News,* Vol. 82, No. 25, June 21, 2004 pp. 25-28

[4] Paul D. Maycock, *PV News*, Vol. 24, No. 4, April 2005.

[5] Paul D. Maycock, *PV News*, Vol. 23, No. 3, March 2004.

[6] I. Chambouleyron, "Photovoltaics in the Developing World," *Energy*, Vol. 21, No. 5, 1996, pp. 385-394.

[7] K. Kurokawa, T. Takashima, T. Hirasawa, T. Kichimi, T. Imura, T. Nishioka, H. Iitsuka, and N. Tashiro, "Case Studies of Large-Scale PV Systems Distributed Around Desert Area of the World," *Solar energy Materials and Solar Cells*, Vol. 47, 1997, pp. 189-196.

[8] Monthly Energy Review, *Energy Information Administration (EIA)*, June 2004.

[9] M. A. Green, "Photovoltaics Technology Overview," *Energy Policy*, 2000, pp. 989-998.

[10] S. J. Strong, "World Overview of Building-Integrated Photovoltaics," *25th IEEE Photovoltaic Specialists Conference*, Washington, May, 1996, pp. 1197-1202.

[11] M. J. Factoran, "Silicon's Usefulness in Photovoltaics," *IEEE Potentials*, 1995, pp. 8-12.

[12] M. A. K. Lodhi, "Photovoltaics and Hydrogen: Future Energy Options," *Energy Conversion Management*, Vol. 38, No. 18, 1997, pp. 1881-1893.

[13] J. L. Strong, "Photovoltaics: Unlimited Electrical Energy from the Sun," *Physics Today*, September, 1993, pp. 22-29.

[14] R. M. Swanson, "A Vision for Crystalline Silicon Solar Cells," 19th *European Photovoltaic Solar Energy Conference*, Paris, France, June, 2004, pp. 1078-1081.

[15] J. Szlufcik, F. Duerinckx, E. Van Kerschaver, and J. Nijs, "Advanced Industrial Technologies for Multicrystalline Silicon Solar Cells," *17th European Photovoltaic Solar Energy Conference*, Munich, Germany, October, 2001, pp. 1271-1276.

[16] D. Margadonna and F. Ferrazza, "The Status of Crystalline Si Modules," *Renewable Energy*, Vol. 15, 1998, pp.83-88.

[17] G. Schubert, F. Huster, and P. Fath "Physical Understanding of Printed Thick Film Contacts of Crystalline Si Solar Cells: Review of Existing Models and Recent Developments," *Technical Digest of the International PVSEC-14*, Bangkok, Thailand, 2003, pp. 441-442.

[18] D. R. Baselt, "The Tip-Sample Interaction in Atomic Force Microscopy and its Implications for Biological Applications," *Ph.D. Thesis*, California Institute of Technology, Pasadena, California, 1993.

[19] A. W. Czandernna, *Overview of Ion Spectroscopies for Surface Compositional Analysis*. In *Methods of Surface Characterization: Ion Spectroscopies for Surface Analysis*, Vol. 2, edited by A. W. Czanderna and D. M. Hercules, Plenum Press: New York, 1991.

[20] D. P. Woodruff and T. A. Delchar, *Modern Techniques of Surface Science*, Cambridge University Press: Cambridge, 1986.

[21] J. C. Vickerman and A. J. Swift. *Secondary Ion Mass Spectrometry —the Surface Mass Spectrometry*. In *Surface Analysis: The Principal Techniques*, edited by J. C. Vickerman, John Wiley & Sons: New York, 1997.

[22] J. Goldstein, D. Newbury, D. Joy, C. Lyman, P. Echlin, E. Lifshin, L. Sawyer, and J. Michael, *Scanning Electron Microscopy and X-Ray Microanalysis*, 3rd ed. Kluwer Academic / Plenum Publishers: New York, 2003.

[23] Z. L. Wang, *Elastic and Inelastic Scattering in Electron Diffraction and Imaging*, Plenum Press: New York, 1995.

[24] J. M. Cowley, *Imaging*. In *High-Resolution Transmission Electron Microscopy and Associated Technologies*, edited by P. Buseck, J. Cowley, and L. Eyring, Oxford University Press: New York, 1988.

[25] S. Horiuchi, Fundamentals *of High-Resolution Transmission Electron Microscopy*, North-Holland: Amsterdam, 1994.

[26] S. Bowden, and A. Rohatgi, "Rapid and Accurate Determination of Series Resistance and Fill Factor Losses in Industrial Silicon Solar Cells," *Proceedings of the 17th European Photovoltaic Solar Energy Conference*, Munich, Germany, Oct. 2001, pp. 1802-1806.

[27] M. A. Green, *Solar Cells: Operating Principles. Technology and System Applications*, The University of New South Wales: Kensington, N.S.W, 1992.

[28] D. L. King, R. Hansen, J. A. Kratochvil, and M. A. Quintana, "Dark Current-Voltage Measurements on Photovoltaic Modules as a Diagnostic or Manufacturing Tool," *Proceedings of the 26th IEEE Photovoltaic Specialists Conference*, 1997, pp. 1125-1128.

[29] R. A. Sinton, A. Cuevas, "A Quasi-Steady Open-Circuit Voltage Method for Solar Cell Characterization," *Proceedings of the 16th European Solar Energy Conference*, Vol. II, Glasgow, United Kingdom, 2000, pp.1152-1155.

[30] A. Goetzberger, *Crystalline Silicon Solar Cells*, New York: John Wiley & Sons, Inc., 1998.

[31] M. J. Kerr, "Surface, Emitter and Bulk Recombination in Silicon and Development of Silicon Nitride Passivated Solar Cells," *Ph.D. Thesis,* The Australian National University, Canberra, 2002.

[32] W. Schockley, A. Goetzberger, and R. M. Scarlett, "Research and Investigation of Inverse Epitaxial UHF Power Transistors," Report No. AFAL-TDR-64-207, Air Force Avionics Lab, Wright-Patterson Air Force Base, OH, Sept. 1964.

[33] D. K. Schroder, *Semiconductor Material and Device Characterization*, New York: John Wiley & Sons, Inc., 1990.

[34] D. L. Meier and D. K. Schroder, "Contact Resistance: Its Measurement and Relative Importance to Power Loss in a Solar Cell", *IEEE Transactions on Electron Devices*, Vol. ED-31, No. 5, May 1984, pp. 647-653.

[35] Ji-Weon Jeong, "Hydrogen Passivation of Defects and Rapid Thermal Processing for High-Efficiency Ribbon Silicon Solar Cells," *Ph.D. Thesis*, Georgia Institute of Technology, Atlanta, Georgia, 2002.

[36] D. J. Griffiths, *Introduction to Electrodynamics*, 3rd ed. Prentice-Hall, Inc.: New Jersey, USA, 1999.

[37] V. Yelundur, "Understanding and Implementation of Hydrogen Passivation of Defects in String Ribbon Silicon for High-Efficiency, Manufacturable, Silicon Solar Cells," *Ph.D. Thesis*, Georgia Institute of Technology, Atlanta, Georgia, 2003

[38] R. A. Sinton, "Quasi-Steady-State Photoconductance, A New Method for Solar Cell Material and Device Characterization," *Proceedings of the 25th IEEE Photovoltaic Specialists Conference,* Washington D.C, 1996, pp.457-460.

[39] S. S. Li, *Semiconductor Physical Electronics*, Plenum Press: New York, 1993.

[40] D. E. Kane and R. M. Swanson, "Measurement of the Emitter Saturation Current by a Contactless Photoconductivity Decay Method," *Proceedings of the 18th IEEE Photovoltaic Specialists Conference*, Las Vegas, NV, 1985, pp. 578-583.

[41] F. L. Pedrotti, S.J. and L. S. Pedrotti, *Introduction to Optics*, 2nd ed. Prentice Hall: New Jersey, 1993.

[42] Technical Guide, "A Guide to Integrating Sphere Theory and Applications," Labsphere Inc.

[43] J. H. Wohlgemuth, S. Narayanan, and R. Brenneman, "Cost Effectiveness of High-Efficiency Cell Processes as Applied to Cast Polycrystalline Silicon*," Proceedings of the 21st IEEE Photovoltaic Specialists Conference*, 1990, pp. 221-226.

[44] D. L. Meier and D. K. Schroder, "Contact Resistance: Its Measurement and Relative Importance to Power Loss in a Solar Cell", *IEEE Transactions on Electron Devices*, Vol. ED-31, No. 5, May 1984, pp. 647-653.

[45] A. Ebong, Y. H. Cho, M. Hilali, A. Rohatgi, and D. Ruby, "Rapid Thermal Technologies for High-Efficiency Silicon Solar Cells," *Solar Energy Materials and Solar Cells*, Vol. 74, 2002, pp. 51-55.

[46] A. Rohatgi, D. S. Kim, K. Nakayashiki, V. Yelundur, and B. Rounsaville, "High-Efficiency Solar Cells on Edge-Defined Film-Fed Grown (18.2%) and String Ribbon (17.8%) Silicon by Rapid Thermal Processing," *Applied Physics Letters*, Vol. 84, No. 1, January 2004, pp.145-147.

[47] J. Zhao, A. Wang, and M. A. Green, "24.5% Efficiency PERT Silicon Solar Cells on SEH MCZ Substrates and Cell Performance on Other SEH CZ and FZ Substrates," *Solar Energy Materials and Solar Cells*, Vol. 66, 2001, pp. 27-36.

[48] O. Schultz, S.W. Glunz, J. C. Goldschmidt, H. Lautenschlager, A. Laimenstoll, E. Schneiderlöchner, and G. P. Willeke, "Thermal Oxidation Processes for High-Efficiency Multicrystalline Silicon Solar Cells," *Proceedings of the 19th European Photovoltaic Solar Energy Conference,* Paris, June 2004, pp. 604-607.

[49] S. Wenham, "Buried-Contact Si Solar Cells," *Progress in Photovoltaics: Research and Applications*, Vol. 1, 1993, pp. 3-10.

[50] D. Jordan and J. P. Nagle, "New Generation of High-Efficiency Solar Cells: Development, Processing and Marketing," *Progress in Photovoltaics: Research and Applications*, Vol. 2, 1994, pp. 171-176.

[51] C. M. Chong, S. R. Wenham, and M. A. Green, "High-Efficiency, Laser Grooved, Buried-Contact Silicon Solar Cells," *Applied Physics Letters*, Vol. 52, February 1988, pp. 407-409.

[52] W. Jooss, P. Fath, and E. Bucher, "Large Area Multicrystalline Silicon Buried Contact Solar Cells with Bulk Passivation and Efficiency of 17.5%," *Proceedings of the 29th IEEE Photovoltaic Specialists Conference*, 2002, pp. 202-205.

[53] L. Pirozzi, G. Arabito, F. Artuso, V. Barbarossa, U. Besi-Vetrella, S. Loreti, P. Mangiapane, and E. Salza, "Selective Emitters in Buried Contact Silicon Solar Cells: Some Low-Cost Solutions," *Solar Energy Materials and Solar Cells*, Vol. 65, 2001, pp. 287-295.

[54] L. Frisson, G. Cheek, R. Mertens, and R. Van Overstraeten, "The Integral Screen Printing Solar Cell Technology in an Industrial Environment," *Commission of the European Communities Report EUR*, 1984, pp. 1002-1006.

[55] D. E. Riemer, "Evaluation of Thick Film Materials for use as Solar Cell Contacts," *Proceedings of the 13th IEEE Photovoltaic Specialists Conference*, 1978, pp. 603-608.

[56] H. H. C. de Moor, A. W. Weeber, J. Hoornstra, and W. C. Sinke, "Fine-line Screen Printing For Silicon Solar Cells," *6th Workshop on Crystalline Silicon Solar Cell Materials and Processes*, Snowmass, Colorado, Oct. 1996, pp.154-170.

[57] R. Mertens, M. Eyckmans, G. Cheek, M. Honore, and R. Van Overstraten, "Critical Processing Parameter Optimization for Screen-Printed Semicrystalline Silicon Solar Cells," *Proceedings of the 17th IEEE Photovoltaic Specialists Conference*, 1984, pp.1347-1351.

[58] A. S. Shaikh, S. Vasudevan, and C. S. Khadilkar, *Ceramics and Glasses in Microelectronics*, In *Handbook of Ceramics, Glasses, and Diamonds*, edited by C. A. Harper, McGraw-Hill: New York, 2001.

[59] R. J. Bacher, "High-Resolution Thick-Film Printing," *Proceedings of the 1986 International Symposium on Microelectronics*, 1986, pp. 576-581.

[60] D. C. Hughes, "Screens for Fine-Line Printing," *Presented at the International Microelectronics and Packaging Symposium,* Nov. 2002.

[61] A. Dziedzic, J. Nijs, and J. Szlufcik, "Thick-film fine-line fabrication techniques-application to front metallisation of solar cells," *Hybrid Circuits*, No. 30, Jan. 1993, pp. 18-22.

[62] H. El Omari, J. P. Boyeaux and A. Laugier, "Screen-Printed Contacts Formation by Rapid Thermal Annealing in Multicrystalline Silicon Solar Cells," *Proceedings of the 25th Photovoltaic Specialists Conference*, Washington D.C., May 1996, pp. 585-588.

[63] B. E. Taylor and W. A. Craig, "Thick Film Palladium Silver Conductors: A Processing and Performance Study," *Proceedings of the 1986 International Symposium on Microelectronics*, 1986, pp. 124-131.

[64] G. C. Cheek, R. P. Mertens, R. Van Overstraeten, and L. Frisson, "Thick-film Metallization for Solar Cell Applications," *IEEE Transactions on Electron Devices*, Vol. ED-31, May 1984, pp. 602-609.

[65] A. K. Varshneya and T. P. Seward III, *Inorganic Glasses—Structure, Composition and Properties*, In *Handbook of Ceramics, Glasses, and Diamonds*, edited by C. A. Harper, McGraw-Hill: New York, 2001.

[66] W. D. Kingery, H. K. Bowen, and D. R. Uhlmann, *Introduction to Ceramics*, 2nd ed., John Wiley & Sons, Inc.: New York, 1976.

[67] J. S. Hirschhorn, *Introduction to Powder Metallurgy*, American Powder Metallurgy Institute: New York, 1969.

[68] R. M. German, *Powder Metallurgy Science*, Metal Powder Industries Federation: Princeton, New Jersey, 1984.

[69] J. C. Lin, and C. Y. Wang, "Effect of Surface Properties of Silver Powder on the Sintering of its Thick-Film Conductor," *Materials Chemistry and Physics*, Vol. 45, 1996, pp. 253-261.

[70] J. C. Lin and C. Y. Wang, "Effects of Surfactant Treatment of Silver Powder on the Rheology of its Thick-Film Paste," *Materials Chemistry and Physics*, Vol. 45, 1996, pp. 136-144.

[71] S. B. Rane, T. Seth, G. J. Phatak, D. P. Amalnerkar, and B. K. Das, "Influence of Surfactants Treatment on Silver Powder and its Thick Films," *Materials Letters*, Vol. 57, 2003, pp. 3096-3100.

[72] S. B. Rane, P. K. Khanna, T. Seth, G. J. Phatak, D. P. Amalnerkar, and B. K. Das, "Firing and Processing Effects on Microstructure of Fritted Silver Thick Film Electrode Materials for Solar Cells," *Materials Chemistry and Physics*, Vol. 82, 2003, pp. 237-245.

[73] J. Savage. *Conductor Materials*. In *Handbook of Thick Film Technology*, edited by P. J. Holmes and R. G. Loasby, Isle of Man, Great Britain: Electrochemical Publications Ltd., 1976.

[74] S. Narasimha, "Understanding and Application of Screen-Printed Metallization, Aluminum Back Surface Fields and Dielectric Surface Passivation for High Efficiency Silicon Solar Cells," *Ph.D. Thesis*, Georgia Institute of Technology, Atlanta, Georgia, 1999.

[75] P. Doshi, J. Mejia, K. Tate, and A. Rohatgi, "Modeling and Characterization of High-Efficiency Silicon Solar Cells Fabricated by Rapid Thermal Processing, Screen Printing , and Plasma-Enhanced Chemical Vapor Deposition*," IEEE Transactions on Electron Devices*, Vol. 44, No. 9, September, 1997, pp. 1417-1424.

[76] M. Prudenziati, L. Moro, B. Morten, F. Sirotti, and L. Sardi, "Ag-Based Thick-Film Front Metallization of Silicon Solar Cells," *Active and Passive Electronic Components*, Vol. 13, 1989, pp. 133-150.

[77] R. J. S. Young and Alan F. Carroll, "Advances in Front-side Thick Film Metallizations for Silicon Solar Cells," *Proceedings of the 16th European Photovoltaic Energy Conference*, Vol. II, Glasgow, UK, May 2000, pp. 1731-1734.

[78] C. Ballif, D. M. Huljić, G. Willeke, and A. Hessler-Wysser, "Silver Thick-Film Contacts on Highly Doped N-type Silicon Emitters: Structural and Electronic Properties of the Interface," *Applied. Physics Lett*ers, Vol. 82, No. 12, March 2003, pp. 1878-1880.

[79] G. Schubert, B. Fischer, and P. Fath, "Formation and Nature of Ag Thick Film Front Contacts on Crystalline Silicon Solar Cells," *Proceedings of the Photovoltaics in Europe Conference*, Rome, 2002.

[80] C. Ballif, D. M. Huljić, A. Hessler-Wysser, and G. Willeke, "Nature of the Ag-Si Interface in Screen-Printed Contacts: A Detailed Transmission Electron Microscopy Study of Cross-Sectional Structures," *Proceedings of the 29th IEEE Photovoltaic Specialists Conference*, New Orleans, LA, 2002, pp. 360-363.

[81] G. Schubert, F. Huster, and P. Fath, "Current Transport Mechanism in Printed Ag Thick Fim Contacts to an N-Type Emitter of a Crystalline Silicon Solar Cell," *Proceedings* of the *19th European Photovoltaic Solar Energy Conference*, Paris, June 2004, pp. 813-816.

[82] K. Firor, S. J. Hogan, J. M. Barrett, and R. T. Coyle, "Series Resistance Associated with Thick-Film Contacts to Solar Cells" *Proceedings of the 16th IEEE Photovoltaic Specialists Conference*, 1982, pp. 824-827.

[83] T. Nakajima, A. Kawakami, and A. Tada, "Ohmic Contact of Conductive Ag Paste to Silicon Solar Cells," *International Journal of Hybrid Microelectronics*, Vol. 6, 1983, pp. 580-586.

[84] Sivothaman, J. Horzel, W. Laureys, F. Durinckx, P. De Schepper, J. Szlufcik, J. Nijs, and R. Mertens, "Towards a Fast and Cost-Effective Production of Industrial Size Silicon Solar Cells Using Rapid Thermal Processing and Screenprinting," *Proceedings of the 14th European Photovoltaic Solar Energy Conference*, Barcelona, Spain, July 1997, pp. 400-403.

[85] J. Horzel, C. Allebe, J. Szlufcik, and S. Sivoththaman, "Development of RTP for Industrial Solar Cell Processing," *Solar Energy Materials and Solar Cells*, Vol. 72, 2002, p. 263-269.

[86] D. M. Huljić, Gűnther Grupp, Jörg Horzel, and Ralf Preu, "Comprehensive Study of Rapid Thermal Firing for Industrial Production of Crystalline Silicon Thick-Film Solar Cells," *Proceedings* of the *19th European Photovoltaic Solar Energy Conference*, June 2004, Paris, pp. 580-5833.

[87] J. Szlufcik, F. Duerinckx, J. Horzel, E. Van Kerschaver, H. Dekkers, S. De Wolf, P. Choulat, C. Allebe, and J. Nijs, "High-Efficiency Low-Cost Integral Screen-Printing Multicrystalline Silicon Solar Cells," *Solar Energy Materials and Solar Cells*, Vol. 74, 2002, pp. 155-163.

[88] A. Rohatgi, S. Narasimha, A. U. Ebong, and P. Doshi, "Understanding and Implementation of Rapid Thermal Technologies for High-Efficiency Silicon Solar Cells," *IEEE Transactions on Electron Devices*, Vol. 46, No. 10, October 1999, pp. 1970-1977.

[89] J.-W. Jeong, A. Rohatgi, V. Yelundur, A. Ebong, M. D. Rosenblum, and J. P. Kalejs, "Enhanced Silicon Solar Cell Performance by Rapid Thermal Firing of Screen-Printed Metals," *IEEE Transactions on Electron Devices*, Vol. 48, No. 12, December 2001, pp. 2836-2841.

[90] A. Rohatgi and J.-W. Jeong, "High-Efficiency Screen-Printed Silicon Ribbon Solar Cells by Effective Defect Passivation and Rapid Thermal Processing," *Applied Physics Letters*, Vol. 82, No. 2, January 2003, pp. 224-226.

[91] J. Szlufcik, H. E. Elgamel, M. Ghannam, J. Nijs, and R. Mertens, "Simple Integral Screenprinting Process for Selective Emitter Polycrystalline Silicon Solar Cells*,"* *Applied Physics Letters*, Vol. 59, No. 13, September 1991, pp. 1583-1584.

[92] R. Einhaus, E. Van Kerschaver, F. Duerinckx, A. Ziebowski, J. Szlufcik, J. Nijs, and R. Mertens, "Optimization of a Selective Emitter Process for Multicrystalline Silicon Solar Cells To Meet Industrial Requirements," 14th *European Photovoltaic Solar Energy Conference*, Barcelona, Spain, July 1997, pp. 187-190.

[93] D. S. Ruby, P. Yang, M. Roy, and S. Narayanan, "Recent Progress on the Self-Aligned, Selective-Emitter Silicon Solar Cell," Proceedings of the 26th *IEEE Photovoltaic Specialists Conference*, Anaheim, CA, October 1997, pp. 39-42.

[94] L. Debarge, J. Boudaden, D. Ballutaud, R. Monna, and J. C. Muller, "Phosphorus Emitter Etch Back and Bulk Hydrogenation by Means of an ECR-Hydrogen Plasma Applied to Form a Selective Emitter Structure on mc-Si," *Solar Energy Materials and Solar Cells*, Vol. 72, 2002, pp. 247-254.

[95] J. Horzel, J. Szlufcik, J. Nijs, and R. Mertens, "A Simple Processing Sequence for Selective Emitters," 26th *IEEE Photovoltaic Specialists Conference*, Anaheim, CA, October 1997, pp. 139-142.

[96] L. Debarge, M. Schott, J. C. Muller, and R. Monna, "Selective-Emitter Formation with a Single Screen-Printed P-doped Paste Deposition Using Out-diffusion in an RTP-step," *Solar Energy Materials and Solar Cells*, Vol. 74, 2002, pp. 71-75.

[97] D.L Meier H. P. Davis, R. A. Garcia, J. A. Jessup, and A. F. Carroll, "Self-Doping Contacts to Silicon Using Silver Coated with a Dopant Source," 28th *IEEE Photovoltaic Specialists Conference*, Anchorage, Alaska, 2000, pp. 69-74.

[98] D. L. Meier, H. P. Davis, A. Shitiba, T. Abe, and K. Kinoshita, "Self-Doping Contacts and Associated Silicon Solar Cell Structures," *Proceedings of the 2nd World Conference on Photovoltaic Solar Energy Conversion*, July 1998, Vienna, Austria, pp. 1491-1494.

[99] D. L. Meier, H. P. Davis, P. Hacke, R. A. Garcia, S. Yamanaka, J. Salami, and J. Jessup, "Self-Doing, Screen-Printed Silver Contacts Applied to IBC and PhosTop Dendritic Web Silicon Solar Cells," *Proceedings of the 17th European Solar Energy Conference,* Munich, Germany, October 2001, pp. 1323-1326.

[100] F. Rollert, N. A. Stolwijk, and H. Mehrer, "Solubility, Diffusion and Thermodynamic Properties of Silver in Silicon," *Journal of Physics D: Applied Physics*, Vol. 20, 1987, pp. 1148-1155.

[101] Stephen A. Campbell, *The Science and Engineering of MicroelectronicFabrication*, Oxford University Press: New York, 1996.

[102] P.A. Basore and D.A. Clugston, "PC1D Version 4 for Windows: from Analysis to Design," *Proceedings of the 25th IEEE Photovoltaic Specialists Conf*erence, Washington, D.C., May 13-17, 1996, pp. 449-452.

[103] A. Rohatgi, P. Doshi, J. Moschner, T. Lauinger, A. G. Aberle, and D. S. Ruby, "Comprehensive Study of Rapid, Low-cost Silicon Surface Passivation Technologies," *IEEE Transactions on Electron Devices*, Vol. 47, No. 5, May 2000, pp. 987-993.

[104] A. Cuevas and D. A. Russell, "Co-Optimisation of the Emitter Region and the Metal Grid of Silicon Solar Cells," *Progress in Photovoltaics: Research and Applications,* Vol. 8, 2000, pp. 603-616.

[105] J. F. Nijs, J. Sclufcik, J. Poortmans, S. Sivoththaman, and R. P. Mertens, "Advanced Manufacturing Concepts for Crystalline Silicon Solar Cells", *IEEE Transactions on Electron Devices*, Vol. 46, No. 10, October 1999, pp.1948-1969.

[106] L. M. Porter, A. Teicher, and D. L. Meier, "Phosphorus-Doped, Silver-Based pastes for Self-Doping Ohmic Contacts for Crystalline Silicon Solar Cells," *Solar Energy Materials and Solar Cells*, Vol. 73, 2002, pp. 209-219.

[107] H. J. Hovel, "The Effect of Depletion Region Recombination Currents on the Efficiencies of Si and GaAs Solar Cells," *Conference Record of the 10th IEEE Photovoltaic Specialists Conference*, Palo Alto, CA, Nov. 1973, pp. 34-39.

[108] A. Y. C. YU, "Electron Tunneling and Contact Resistance of Metal-Silicon Contact Barriers," *Solid-State Electronics*, 1970, Vol. 13, pp. 239-247.

[109] Dieter K. Schroder and Daniel L. Meier, "Solar Cell Contact Resistance — A Review," *IEEE Transactions on Electron Devices*, Vol. ED-31, No. 5, May 1984, pp. 637-647.

[110] S. M. Sze, *Physics of Semiconductor Devices*, 2nd ed. John Wiley and Sons: New York, 1981.

[111] M. Van Craen, L. Frisson, and F. C. Adams, "SIMS Study of the Penetration of Metallic Secondary Impurities in Screen-Printed Silicon Solar Cells," *Surface and Interface Analysis*, Vol. 6, No. 6, 1984, pp. 257-260.

[112] M. J. Kerr, J. Schmidt, and A. Cuevas, J. H. Bultman, "Surface Recombination Velocity of Phosphorus –Diffused Silicon Solar Cell Emitters Passivated with Plasma Enhanced Chemical Vapor Deposited Silicon Nitride and Thermal Silicon Oxide," *Journal of Applied Physics*, Vol. 89, No. 7, 2001, pp. 3821-3826.

[113] B. Lenkeit, T. Lauinger, A. G. Aberle, and R. Hezel, "Comparison of Remote Versus Direct PECVD Silicon Nitride Passivation of Phosphorus-Diffused Emitters of Silicon Solar Cells," in *Proceedings of the 2nd World Conf. on Photovoltaic Solar Energy Conversion* July 1998, Vienna, Austria, pp. 1434-1437.

[114] J. Schmidt, J. D. Moschner, J. Henze, S. Dauwe, and R. Hezel, "Recent Progress in the Surface Passivation of Silicon Solar Cells using Silicon Nitride," *Proceedings* of the *19th European Photovoltaic Solar Energy Conference*, Paris, June 2004, pp. 391-396.

[115] A. L. Fahrenbach and R. H. Bube, *Fundamentals of Solar Cells: Photovoltaic Solar Energy Conversion*, Academic Press: New York, 1983.

[116] S. Narasimha, A. Rohatgi, and A. W. Weeber, "An Optimized Rapid Aluminum Back Surface Field Technique for Silicon Solar Cells," *IEEE Transactions on Electron Devices*, Vol. 46, No. 7, July 1999, pp. 1363-1370.

[117] R. W. Olesinski and G. K. Abbaschian, in *Binary Alloy Phase Diagrams*, 2nd ed., edited by T. B. Massalski, (American Society for Metals, Materials Park, OH, 1990) pp. 92-94.

[118] D. L. Meier, Hubert P. Davis, Ruth A. Garcia, and Joyce A. Jessup, "Method and Apparatus for Self-Doping Contacts to a Semiconductor," Ebara Corporation, US patent #6,703,295, March, 2004.

[119] O Growski, L. Murawski, and K. Trzebiatowsky, "The Surface Conductivity of Lead Glasses," *Journal of Physics D: Applied Physics*, Vol. 15, 1982, pp. 1097-1101.

[120] C. Khadilkar, S. Kim, T. Pham, A. Shaikh, and S. Sridharan, "Characterization of Silver Front Contact in a Silicon Solar Cell," *Presented at the14th International Photovoltaic Specialists Energy Conference,* Bangkok, Thailand, 2004, pp. 443-444.

[121] J. L. Barton and M. Morain, "Hydrogen Diffusion in Silicate Glasses," *Journal of Non-Crystalline Solids*, Vol. 3, 1970, pp. 115-126.

[122] R. W. Vest, "Conduction Mechanisms in Thick-Film Microcircuits," *Final Technical Report, Grant Number: DAHC-15-70-G7 and DAHC-15-73-G8 (ARPA)*, Purdue University, West Lafayette, Indiana, Dec. 1975.

[123] A. Shaikh, S. Sridharan, T. Pham, and C. Khadilkar, "Designing a Front Contact Ink for $SiN_x$ Coated Si Solar Cells," *3rd World Conference on Photovoltaic Energy Conversion*, Osaka, Japan, May, 2003, pp. 1500-1503.

[124] S. Sridharan, C. Khadilkar, T. Pham, and A. Shaikh "Characterization of Silver/Glasss/Silicon Front Contact Interface in a Silicon Solar Cell" *presented at the 13th Workshop on Crystalline Silicon Solar Cell Materials and Processes*, Vail, Colorado, August, 2003, pp. 162-165.

[125] J. Kalejs, B. Mackintosh, W. Schmidt, and B. Woesten, "Advances in High Throughput Wafer and Solar Cell Technology for EFG Ribbon," *Proceedings of the 29th IEEE Photovoltaic Specialists Conference*, New Orleans, LA, 2002, pp. 74-77.

[126] A. Rohatgi, V. Yelundur, J. Jeong, A. Ebong, M. D. Rosenblum, and J. I. Hanoka, *Proceedings of the 12th International Photovoltaic Science and Engineering Conference*, Cheju, South Korea, 2001, p. 23-26.

[127] J. Jeong, Y. H. Cho, A. Rohatgi, M. D. Rosenblum, B. R. Bathey, and J. P. Kalejs, "Rapid Thermal Processing to Enhance PECVD SiN-Induced Hydrogenation in High-Efficiency EFG Silicon Solar Cells," *Proceedings of the 29th IEEE Photovoltaic Specialists Conference*, New Orleans, LA, 2002, pp. 250-253.

[128] D. Macdonald and A. Cuevas, "Trapping of Minority Carriers in Multicrystalline Silicon," *Applied Physics Letters*, Vol. 74, 1999, pp. 1710-1712.

[129] K. A. Münzer, K. H. Eisenthrith, R. E. Schlosser, and M. G. Winstel, "18%-PEBSCO-Silicon Solar Cells for Manufacturing," *Proceedings of the 17th European Solar Energy Conference,* Munich, Germany, October 2001, pp. 1363- 1366.

[130] J. Nijs, E. Demesmaeker, J. Szlufcik, J. Poortmans, L. Frisson, K. De Clerq, M. Ghannam, R. Mertens, and R. Van Overstraeten, "Latest Efficiency Results with the Screen-printing Technology and Comparison with the Buried-Contact Structure," *Proceedings of the 1st World Conference on Photovoltaic Solar Energy Conversion*, 1994, pp. 1242-1249.

[131] C. Schmiga, J. Schmidt, A. Metz, A. Endrös, and R. Hezel, "17.6% Efficient Tricrystalline Silicon Solar Cells with Spatially Uniform Texture," *Progress in. Photovoltaics: Research and Application*., Vol. 11, 2003, pp. 33-38.

[132] M. A. Green, *Silicon Solar Cells: Advanced Principles and Practice*, Center of Photovoltaic Devices and Systems, University of New South Wales: Sydney, N.S.W, 1995.

[133] P. A. Basore, "Extended Spectral Analysis of Internal Quantum Efficiency," *Proceedings of the 23rd IEEE Photovoltaic Specialists Conference*, 1993, pp.147-152.

[134] J. Zhao, A. Wang, and M. A. Green, "24% Efficient PERL Structure Silicon Solar Cells," *Proceedings of the 21st IEEE Photovoltaic Specialists Conference*, 1990, pp. 333-335.

[135] S. Dauwe, L. Mittelstädt, A. Metz, and R. Hezel, "Experimental Evidence of Parasitic Shunting in Silicon Nitride Rear Surface Passivated Solar Cells," Progress *in Photovoltaics: Research and Applications*, Vol. 10, pp. 271-278.

[136] H. Sakata, T. Nakai, T. Baba, and M. Taguchi, "20.7% Highest Efficiency Large Area (100.5 $cm^2$) HIT™ Cell," *Proceedings of the 28th IEEE Photovoltaic Specialists Conference*, Anchorage, Alaska, 2000, pp. 7-12.

[137] Todd Williams, Kristins McVicker, Aziz Shaikh, Tim Koval, Stephen Shea, Bonnie Kinsey and Dave Hetzer, "Hot Melt Ink Technology for Crystalline Silicon Solar Cells," Proceedings of the *29th IEEE Photovoltaic Specialists Conference*, New Orleans, 2002, pp. 352-355.

[138] D. G. Kleinbaum, L. L. Kupper, K. E. Muller, and A. Nizam, *Applied Regression Analysis and Other Multivariable Methods*, 3rd. ed., Duxbury Press: Pacific Grove, CA, 1998.

[139] C. Y. Chang, Y. K. Fang, and S. M. Sze, "Specific Contact Resistance of Metal-Semiconductor Barriers," Vol. 14, 1971, pp. 541-550.

# PUBLICATIONS FROM THIS WORK

## Refereed International Journal Publications

[1] **Mohamed M. Hilali**, Ajeet Rohatgi, and Sally Asher. "Development of Screen-Printed Silicon Solar Cells with High Fill Factors on 100 Ohms/sq Emitters," *IEEE Transactions on Electron Devices*, **Vol. 51**, No. 6, June 2004, pp. 948-955. ***Received Georgia Institute of Technology best paper award sponsored by Science Application International Corporation (SAIC).***

[2] **M. Hilali**, A. Ebong, A. Rohatgi, and D. L. Meier, "Resistivity Dependence of Minority Carrier Lifetime and Cell Performance in P-type Dendritic Web Silicon Ribbon," *Solid-State Electronics* **45**(2001) pp. 1973-1978.

[3] **M. M. Hilali**, M. M. Al-Jassim, B. To, H. Moutinho, A. Rohatgi, and S. Asher, "Understanding and Formation of High-Quality Thick-Film Ag Contacts on High Sheet-Resistance Si Emitters for Solar Cells," accepted for publication in *Journal of the Electrochemical Society*, April 2005.

[4] **M. M. Hilali**, K. Nakayashiki, C. Khadilkar, R. C. Reedy, A. Rohatgi, A. Shaikh, S. Kim, and S. Sridharan, "The Effect of Ag Particle Size in Thick-Film Ag Paste on the Electrical and Physical Properties of Screen-Printed Contacts and Silicon Solar Cells," accepted with revisions in *Journal of the Electrochemical Society*, July 2005.

[5] A. Rohatgi, **M. M. Hilali**, and K. Nakayashiki, "Screen-printed Solar Cell on Edge-Defined Film-Fed Grown Ribbon Si Through Optimized Rapid Belt Co-firing of Contacts and High Sheet Resistance Emitter," *Applied Physics Letters,* **Vol. 84**, No. 17, April 26$^{th}$, 2004, pp.3409-3411.

[6] A. Ebong, **M. Hilali**, A. Rohatgi, D. Meier and D. S. Ruby, "Belt Furnace Gettering and Passivation of n-Web Silicon for High-Efficiency Screen-Printed Front-Surface-Field Solar Cells," *Progress in Photovoltaics: Research and Applications*, 2001, **9**, pp. 327-332.

[7] A. Ebong, Y.H. Cho, **M. Hilali**, A. Rohatgi, and D. Ruby, "Rapid Thermal Technologies for High-Efficiency silicon Solar Cells," *Solar Energy Materials & Solar Cells*, Vol. **74**, 2002, pp. 51-55.

[8] A. Rohatgi, D. S. Kim, V. Yelundur, K. Nakayashiki, A. Upadhyaya, **M. Hilali**, V. Meemongkolkiat, "Record-High-Efficiency Solar Cells on Multicrystalline Materials Through Understanding and Implementation of RTP-Enhanced $SiN_x$-induced Defect Hydrogenation," *Solar Energy Materials & Solar Cells, in press.*

[9] V. Meemongkolkiat, **M. Hilali**, K. Nakayashiki, and A. Rohatgi, "Process and Material Dependence of Al-BSF in Crystalline Si Solar Cells," *Solar Energy Materials & Solar Cells, in press*.

[10] D.S. Kim, **M. M. Hilali,** A. Rohatgi, K. Nakano, A. Hariharan and K. Matthei "Development of a Novel Phosphorus Spray Diffusion System for Low Cost Silicon Solar Cells," submitted to *Journal of the Electrochemical Society*, June 2005.

## Refereed International Conference Publications

[1] **M. Hilali**, J. –W. Jeong, A. Rohatgi, D. L. Meier, and A. F. Carroll, "Optimization of Self-Doping Ag Paste Firing to Achieve High Fill Factors on Screen-Printed Silicon Solar Cells with 100 Ω/sq. Emitter," *Proceedings of the 29th IEEE PVSC,* New Orleans, LA, May 2002, pp. 356-359. ***Received Best Poster Paper Award***.

[2] **M. M. Hilali**, A. Rohatgi, C. Khadilkar, S. Kim, T. Pham, J. Salami, A. Shaikh, and S. Sridharan, "Understanding and Development of Ag Pastes for Silicon Solar Cells with High-Sheet-Resistance Emitters," *Proceedings of the 19th European PVSEC*, Paris, France, June 7-11, 2004, pp. 1300-1303.

[3] B. Damiani, **M. Hilali**, and A. Rohatgi,"High Temperature Light Induce Degradation", *Proceedings of the 29th IEEE PVSC*, New Orleans, May 2002, pp. 348-351.

[4] A. Ristow, **M. Hilali**, A. Ebong, and A. Rohatgi, "Screen-Printed Back Surface Reflector for Light Trapping in Crystalline Silicon Solar Cells," *Proceedings of the 17th European PVSEC*, Munich, Germany, 2001, pp. 1335-1338.

[5] Rohatgi, **M. Hilali**, D. L. Meier, A. Ebong, C. Honsberg, A. F. Carroll, and P. Hacke, "Self-Aligned Self-Doping Selective Emitter for Screen-Printed Silicon Solar Cells," *Proceedings of the 17th European PVSEC*, Munich, Germany, 2001, 1307-1310.

[6] A. Ebong, Y. H. Cho, **M. Hilali**, A. Rohatgi, and D. Ruby, "Rapid Thermal Technologies for High Efficiency Silicon Solar Cells," *12th International Photovoltaic Science and Engineering Conference*, June 11-15, 2001, Cheju Island, Korea, P-37.

[7] A. Ebong, **M. Hilali** and A. Rohatgi, "Rapid Photo-Assisted Forming Gas Anneal (FGA) for High Quality Screen-Printed Contacts for Silicon Solar Cells," *Proc. of the 28th IEEE PVSC*, Anchorage, Alaska, 2000, pp. 264-267.

[8] V. Meemongkolkiat, **M. Hilali,** K. Nakayashiki**,** and A. Rohatgi, "Process and Material Dependence of Al-BSF in Crystalline Si Solar Cells," *Technical Digest of the International PVSEC-14*, Bangkok, Thailand, 2004, pp. 401-402.

[9] A. Rohatgi, D. S. Kim, V. Yelundur, K. Nakayashiki, A. Upadhyaya, **M. Hilali,** and V. Meemongkolkiat**,** "Record-High- Efficiency Solar Cells on Multicrystalline Materials Through Understanding and Implementation of RTP-enhanced SiN-induced Defect Hydrogenation,"*Technical Digest of the International PVSEC-14*, Bangkok, Thailand, 2004, pp. 635-638. ***Invited paper***.

[10] V. Meemongkolkiat, **M. Hilali,** and A. Rohatgi, "Investigation of RTP and Belt-Fired Screen-Printed Al-BSF on Textured and Planar-Back-Surfaces of Silicon Solar Cells*," Proceedings of the 3rd World Conference on Photovoltaic Energy Conversion*, Osaka, Japan, May 2003, Volume B, pp. 1467-1470.

[11] **M. M. Hilali**, K.Nakayashiki, A.Ebong, and A.Rohatgi, "Investigation of High-Efficiency Solar Cells with High Sheet-Resistance Emitters," *Proceedings of the 31st IEEE Photovoltaic Specialists Conference*, Orlando, Jan 2005, pp. 1185-1188.

[12] A. Ebong, **M. Hilali**, V. Upadhyaya, B. Rounsaville, I. Ebong, and A. Rohatgi, **"***High Efficiency Screen-Printed Planar Solar Cells On Single Crystalline Silicon* Materials**"** *Proc. of the 31st IEEE Photovoltaic Specialists Conference*, Orlando, Jan 2005, pp. 1173-1176.

[13] V. Yelundur, K. Nakayashiki, **M. Hilali**, and A. Rohatgi, "Implementation of a Homogeneous High-Sheet-Resistance Emitter in Multicrystalline Si Solar Cells," *Proc. of the 31st IEEE Photovoltaic Specialists Conference*, Orlando, Jan 2005, pp. 959-962.

## Workshop Conference Publications

[1] **Mohamed M. Hilali**, Bobby To, and A. Rohatgi, "A Review nd Understanding of Scree-Printed Contacts and Selective-Emitter Formation," *14th Workshop on Crystalline Si Solar Cell Materials and Processes* (National Renewable Energy Lab), Winter Park, Colorado, August 8-11, 2004, pp. 109-116. ***Invited talk***.

[2] **M. Hilali**, V. Meemongkolkiat, and A. Rohatgi, "Advances in Screen-Printed High-Sheet-Resistance Emitter Cells", *13th Workshop on Crystalline Si Solar Cell Mat. and Processes (National Renewable Energy Lab)*, Vail, Colorado, August 11-14, 2003, pp.211. ***Graduate Student Award***

[3] **M. Hilali**, J. –W. Jeong, and A. Rohatgi, "A Study of Contact Resistance and Cell Performance of Selective-Emitter Screen-Printed Silicon Solar Cells Using a Self-Doping Paste", *12th Workshop on Crystalline Si Solar Cell Mat. and Processes* (National Renewable Energy Lab), Breckenridge, Colorado, August 11-14, 2002, pp.286-90. ***Graduate Student Award***

[4] **M. Hilali**, B. Damiani, and A. Rohatgi, "Lifetime Enhancement During Processing of Porous Si Solar Cells", *11th Workshop on Crystalline Si Solar Cell Mat. and Processes* (National Renewable Energy Lab), Estes Park, Colorado, August 19-22, 2001, pp.235-239. ***Graduate Student Award***

[5] B. Damiani, **M. Hilali**, and A. Rohatgi, "Light Induced Degradation in Manufacturable Multicrystalline Silicon Solar Cells", *11th Workshop on Crystalline Si Solar Cell Mat. and Processes* (National Renewable Energy Lab, Estes Park, Colorado, August 19-22, 2001, pp.229-234.

[6] A. Ebong, **M. Hilali**, A. Rohatgi, D. Meier, and D.S. Ruby, "Belt Furnace Gettering and Passivation of n-Web Silicon for High-Efficiency Screen-Printed Front-Surface-Field Solar Cells," *10th Workshop on Crystalline Silicon Solar Cell Materials and Processes* (National Renewable Energy Lab), Copper Mountain, August 13-16, 2000, pp. 234-237. ***Invited Paper***.

[7] A. Rohatgi, V. Yelundur, J. Jeong, A. Ristow, **M. Hilali**, and B. Damiani, "Recent Advances and Approach towards Low-Cost High-Efficiency Multicrystalline Silicon Solar Cells," in *Proc. 11th International Workshop on the Physics of Semiconductor Devices*, Vol. **I**, India, 2001, pp. 73-80.

[8] A. Ebong, V. Meemongkolkiat, **M. Hilali**, V. Upadhyaya, B. Rounsaville, I. Ebong, A. Rohatgi, G. Crabtree, J. Nickerson, and T. L. Jester, "Variation of Screen-Printed Solar Cell Performance Along Commercially Grown Ga- and B-Doped Czochralski Ingots," *14th Workshop on Crystalline Si Solar Cell Materials and Processes* (National Renewable Energy Lab), Winter Park, Colorado, August 8-11, 2004, pp. 254-258.

# VITA

Mohamed M. Hilali was born on August 28, 1976 in Giza, Egypt. He earned his Bachelor's of Science in Engineering Degree in Electrical/Electronics Engineering from Vrije Universiteit Brussel (VUB) in 1995. He obtained his Master's of Engineering degree from the University of Florida in 1997. During 1997 and 1998 he was a lab instructor and teaching assistant at the Department of Electrical and Computer Engineering, University of Florida. He is currently pursuing the Doctorate of Philosophy from the Georgia Institute of Technology in the School of Electrical and Computer Engineering, under the supervision of Dr. Ajeet Rohatgi in the University Center of Excellence for Photovoltaic Research and Education. His graduate research has focused on the understanding and development of screen-printed contacts to high sheet-resistance emitters. This work resulted in over 30 publications in professional journals, international refereed conference proceedings, and workshop conference proceedings.